

**MECHANICAL CHARACTERISTICS OF  
FRESH AND HARDENED ALUMINOUS  
CEMENT PASTES**

by

**ASSEM MOSTAFA KAMAL ABDELALIM**

**A Thesis  
Submitted for the Degree of  
Doctor of Philosophy  
of the University of Aston in Birmingham**

**September 1980**

## SUMMARY

Assem Mostafa Kamal ABDELALIM

Doctor of Philosophy 1980

In this research the rheological properties of fresh aluminous cement pastes were investigated mainly by means of a coaxial rotational viscometer. The effect of conversion on the pore structure of the hardened high alumina cement (HAC) pastes was monitored using a mercury intrusion porosimeter. A scanning electron microscope / KEVEX energy dispersive X-ray analysis combination, and in some instances a differential thermal analyser, were used to study the morphological changes in the interfacial zone between HAC pastes and various substrates. A brief study was made of the feasibility of using by-product phosphogypsum as a cheap additive to eliminate conversion effects in HAC pastes.

The consistency of HAC fresh pastes was highly dependent on mixing time and temperature. The development of a thixotropic structure on mixing involves a thermally activated process for which the activation energy was estimated to be  $43 \pm 1$  KJ/mole. The sensitivity of HAC pastes to mixing and storage conditions made it essential to develop stringent procedures for specimen preparation, curing, and testing.

Mineralogical and pore size distribution studies on hardened HAC pastes have revealed a number of relationships between these two factors and the strength of the material. In addition, the shape of the pore size distribution curves was found to be directly related to the mechanical and mineralogical conditions of the paste.

Analytical and morphological studies of the interfacial zone developed between HAC pastes and various substrates indicated that this zone is seriously affected by the conversion process. In general, the paste side of the interface, which was initially largely made up of small platelets of probable composition  $C_2(A,F)H_8$ , was converted to gibbsite crystals of high variability of size and shape.

Crude phosphogypsum was found to be an unsuitable additive in HAC because of its acidity. The purified form, however, was comparable to natural gypsum in producing a cementitious material of slow setting properties at a relatively low ambient temperature, but which has proved to be reliable on subsequent exposure to a higher temperature.

KEY WORDS

aluminous cement, rheology, porosity, conversion, scanning electron microscopy

**TO MY PARENTS**

## ACKNOWLEDGEMENTS

The author would like to thank Dr C L Page, Senior Lecturer in the Department of Construction and Environmental Health, for his appreciation, supervision, help and support.

Thanks are also due to Professor A W Pratt, head of the department for providing facilities for conducting this research and allocating studentship to the author.

Special thanks are due to Mr C J Thompson for his technical assistance, especially with the scanning electron microscope. Mr R Newman was of enormous help in all the photographic work presented in this thesis.

The excellent typing of this work was done by Mrs M Creighton to whom the author is grateful for her patience and accuracy.

The author wishes to thank his parents for their moral and financial support and all his friends who helped in any way they could.

Finally, the author would like to mention with deep respect Mr I Hussin for his invaluable help during the period of stay of the author in Birmingham.

## LIST OF CONTENTS

	Page
TITLE PAGE	
SUMMARY	
DEDICATION	
ACKNOWLEDGEMENTS	
LIST OF CONTENTS	V
LIST OF FIGURES AND TABLES	IX
CHAPTER 1 INTRODUCTION	1
1.1 Background	1
1.2 Purpose of Investigation	7
1.3 Plan of Presentation	8
CHAPTER 2 MATERIALS AND EXPERIMENTAL TECHNIQUES	9
2.1 Materials	9
2.2 Preparation of Cement Paste Samples	10
2.3 Compressive Strength Measurements	11
2.4 Differential Thermal Analysis	12
2.5 Porosity Measurement	14
2.5.1 Determination of Total Porosity	14
2.5.2 Pore Size Distribution Measurements	16
2.6 Morphological Studies	19
CHAPTER 3 THE RHEOLOGICAL CHARACTERISTICS OF FRESH ALUMINOUS CEMENT PASTES	31
3.1 Introduction	31
3.2 The Influence of Interparticle Forces on the Physical Properties of Hydrosols and Cement Pastes	33
3.3 Rheological Systems and their Flow Curves	35
3.4 Methods of Measurement	38

3.5	Experimental	40
3.5.1	The Penetration Test	40
3.5.2	The Coaxial Cylinders Viscometer Method	41
3.5.3	The Effect of Temperature	42
3.6	Results and Discussion	43
3.6.1	The Effect of Mixing of the Consistency of the Pastes	43
3.6.1.1	The Penetration Test Results	43
3.6.1.2	The Viscometer Results	44
3.6.2	The Effect of Mixing Efficiency	44
3.6.2.1	The Viscometer Results	45
3.6.3	The Effect of Mixing on the Thixotropic Properties	45
3.6.3.1	The Penetration Results	45
3.6.3.2	The Viscometer Results	46
3.6.4	The Effect of Temperature	47
3.6.4.1	The Penetration Results	47
3.6.4.2	The Viscometer Results	48
3.6.4.3	The Activation Energy Calculations	49
3.7	Conclusions	50
CHAPTER 4	THE EFFECT OF MIXING, CURING AND TESTING CONDITIONS ON SUBSEQUENT RESULTS	75
4.1	Heat of Hydration	75
4.2	Surface Moisture	77
4.3	Conclusions	79
CHAPTER 5	STRENGTH, MINERALOGY, AND PORE STRUCTURE OF SET HIGH ALUMINA CEMENT PASTES	87
5.1	Introduction	87

5.2	The Effect of Porosity on the Mechanical Properties of Cement Paste and Related Materials	87
5.3	The Influence of Pore Size on Strength	93
5.4	Experimental	95
5.5	Results and Discussion	96
	5.5.1 First Set	96
	5.5.2 Second Set	98
5.6	Conclusions	102
CHAPTER 6	THE EFFECT OF CONVERSION ON THE CONTACT ZONE BETWEEN HIGH ALUMINA CEMENT PASTE AND EMBEDDED MATERIALS	129
6.1	Introduction	129
6.2	Experimental Procedures	132
	6.2.1 Substrate Preparation	132
	6.2.2 Specimen Preparation and Test Conditions	133
	6.2.3 Paste Separation and Analysis	133
6.3	Results and Discussion	134
	6.3.1 Unconverted Specimens	134
	6.3.2 Fully Converted Specimens	136
	6.3.2.1 Cement-Glass Interface	136
	6.3.2.2 Cement-Aggregate Interface	138
	6.3.3 The Conversion Process at the Interface	141
	6.3.3.1 Morphological Analysis	141
	6.3.3.2 Elemental Analysis	141
6.4	Conclusions	142
CHAPTER 7	PHOSPHOGYPSUM AS AN ADDITIVE TO HIGH ALUMINA CEMENT PASTES	192
7.1	Introduction	192
7.2	Experimental	194
7.3	Results and Discussion	195

	7.3.1	Setting Time	195
	7.3.2	Compressive Strength	196
	7.3.3	Thermal Analysis	197
	7.4	Conclusions	198
CHAPTER 8		GENERAL CONCLUSIONS AND RECOMMENDATIONS FOR FURTHER WORK	205
	8.1	General Conclusions	205
	8.2	Recommendations for Further Work	210
APPENDIX 1		POROSITY MEASUREMENTS	212
	A.1.1	Total Porosity Determination	212
		A.1.1.1 Apparent Density	212
		A.1.1.2 True Density	212
		A.1.1.3 Total Porosity	213
	A.1.2	Calculation of Pore Size Distribution	213
APPENDIX 2		THE WASHBURN FORMULA OF THE INTRUSION OF A NON-WETTING LIQUID INTO A SPHERICAL PORE	215
APPENDIX 3		THE REINER AND RIWLIN EQUATION OF PLASTIC FLOW IN A ROTATIONAL VISCOMETER	216
APPENDIX 4		DIFFERENTIAL THERMAL ANALYSIS THERMOGRAMS	218
REFERENCES			220

LIST OF FIGURES AND TABLES

Figure 2.1	Incubator Curing	22
Figure 2.2	Water Bath Curing	22
Figure 2.3	The Avery-Denison Universal Testing Machine Model 7152	23
Figure 2.4	Ball Bearing Mounted Plate for testing small Cylindrical Specimens	24
Figure 2.5	A Stanton Redcroft Differential Thermal Analyser Model 673-4	25
Figure 2.6	Apparent density bottle	26
Figure 2.7	A Micromeritics instrument corporation porosimeter, Model 900/910 series	27
	Table 2.1 Chemical composition of cement (% by weight) as supplied by Lafarge Aluminous Cement Company Limited	28
Figure 2.8	The loss of water from hydrated calcium aluminates on ignition <sup>(46)</sup>	28
Figure 2.9	A glass manifold with ten branches for vacuum drying	29
Figure 2.10	A Cambridge Stereoscan - 150 Scanning Electron Microscope/EDXA Unit Combination	30
Figure 3.1	Representation of electrical double layer <sup>(70)</sup>	52
Figure 3.2	The influences of electrolyte concentration $\kappa$ on the total potential energy of interaction of two spherical particles <sup>(72)</sup>	52
Figure 3.3	The influence of the surface potential $\psi_0$ on the total potential energy of interaction of two spherical particles <sup>(72)</sup>	52
Figure 3.4	Consistency Curves	53

Figure 3.5	Experimental ( $\tau, \dot{\gamma}$ ) curves for a range of water-cement ratios and a range of mixing times for OPC pastes <sup>(79)</sup>	54
Figure 3.6	Effect of pH on the rheological properties of 43% quartz powder suspension <sup>(81)</sup>	54
Figure 3.7	Breakdown curve for a 0.30 w/c paste at 386 rev/min <sup>(77)</sup>	55
Figure 3.8	The Penetration method	56
Figure 3.9	A Ferranti portable viscometer	57
Table 3.1	The temperature of the samples during mixing	58
Figure 3.10	Effect of mixing on the consistency of Fondu cement paste of water-cement ratio 0.55	59
Figure 3.11	Behaviour of Fondu cement pastes under shear stress at various water-cement ratios	60
Figure 3.12	Behaviour of Secar cement pastes under shear stress at various water-cement ratios	61
Figure 3.13	Behaviour of Fondu cement pastes of water-cement ratio 0.55 under shear stress at various rates of shear	62
Figure 3.14	Behaviour of Secar cement pastes of water-cement ratio 1.00 under shear stress at various rates of shear	63
Figure 3.15	Effect of mixing procedure on the structure of Fondu cement pastes of water-cement ratio 0.55	64
Figure 3.16	Thixotropic Hysteresis loop for Fondu cement paste of water-cement ratio 0.6	65
Figure 3.17	Thixotropic Hysteresis loop for chrome-yellow ink <sup>(86)</sup>	66
Figure 3.18	Effect of mixing temperature on the consistency of Fondu cement paste (Penetration test)	67

Figure 3.19	Effect of mixing temperature on the consistency of Fondu cement pastes of water-cement ratio 0.55	68
Figure 3.20	Effect of mixing temperature on the consistency of Fondu cement pastes of water-cement ratio 0.6	69
Figure 3.21	Effect of mixing temperature on the consistency of Secar cement pastes of water-cement ratio 1.00	70
Figure 3.22	Energy of activation	71
Table 3.2	Data of plots of $\log_{10} \left( \frac{1}{t_{\max}} \right)$ against $\left( \frac{1}{T} \right)$	72
Table 3.3	Activation energy values	72
Figure 3.23	Development of Thixotropic structure of Fondu cement pastes (Penetration test results)	73
Figure 3.24	Development of Thixotropic structure of Fondu and Secar cement pastes (Viscometric results)	74
Figure 4.1	A method for monitoring the temperature changes within cement pastes during hardening	81
Figure 4.2	Time-temperature curves of HAC pastes during hardening at three different temperatures	82
Figure 4.3	The effect of self-generated heat on the strength results	83
Table 4.1	The effect of surface moisture on the strength results	84
Table 4.2	The effect of mixing time on the strength results	84
Figure 4.4	The effect of insufficient mixing on DTA measurements	85
Table 4.3	The proportions of HAC pastes mixes	86
Figure 5.1	Effect of porosity on compressive strength of alumina and zirconia <sup>(88)</sup>	103
Figure 5.2	Hardness vs porosity for the cement systems <sup>(29)</sup>	103

Figure 5.3	Proposed effect of micromechanical stress concentrations on the strength of a porous brittle material: Case I, flaw size $\ll$ pore size; Case III, flaw size $\gg$ pore size; and Case II flaw size $\approx$ pore size <sup>(108)</sup>	104
Figure 5.4	Strength of HAC pastes as a function of water-cement ratio	105
Figure 5.5	Influence of the water-cement ratio on the compressive strength of fully converted HAC paste expressed as a percentage of 1-day strength at 10°C	106
Figure 5.6	Porosity of HAC paste as a function of water-cement ratio	107
	Table 5.1 Specific gravity of HAC pastes	108
	Table 5.2 Apparent density of HAC pastes	108
	Table 5.3 Total porosity of HAC pastes	108
Figure 5.7	Pore size distribution curves of unconverted HAC cement pastes of various water-cement ratios	109
Figure 5.8	Pore size distribution curves of fully converted HAC cement pastes of various water-cement ratios	110
Figure 5.9	The effect of conversion on the pore structure of HAC pastes of water-cement ratio 0.25	111
Figure 5.10	The effect of conversion on the pore structure of HAC pastes of water-cement ratio 0.4	112
Figure 5.11	The effect of conversion on the pore structure of HAC pastes of water-cement ratio 0.55	113
Figure 5.12	Strength of HAC paste as a function of total porosity	114
Figure 5.13	Strength of converted HAC paste as a function of total porosity (Cottin's results <sup>(44)</sup> )	115
Figure 5.14	The effect of water-cement ratio and curing conditions on the strength of HAC pastes	116
Figure 5.15	The effect of water-cement ratio and curing conditions on the mineralogy of HAC pastes	117

Figure 5.16	Strength of HAC paste as a function of degree of conversion.	118
Figure 5.17a	Pore size distribution curves of HAC pastes of water-cement ratio 0.4 during the first stage of the conversion process at 40°C and 100% R.H.	119
Figure 5.17b	Pore size distribution curves of HAC pastes of water-cement ratio 0.4 during the second stage of the conversion process at 45°C and 100% R.H.	120
Figure 5.18a	Pore size distribution curves of HAC pastes of water-cement ratio 0.4 during the first stage of the conversion process at 35°C and 100% R.H.	121
Figure 5.18b	Pore size distribution curves of HAC pastes of water-cement ratio 0.4 during the second stage of the conversion process at 35°C and 100% R.H.	122
Figure 5.19a	Pore size distribution curves of HAC pastes of water-cement ratio 0.4 during the first stage of the conversion process in water at 45°C	123
Figure 5.19b	Pore size distribution curves of HAC pastes of water-cement ratio 0.4 during the second stage of the conversion process in water at 45°C	124
Figure 5.20a	Pore size distribution curves of HAC pastes of water-cement ratios 0.55 during the first stage of the conversion process at 45°C and 100% R.H.	125
Figure 5.20b	Pore size distribution curves of HAC pastes of water-cement ratio 0.55 during the second stage of the conversion process at 45°C and 100% R.H.	126
Figure 5.21	Relationship between strength and total porosity of HAC pastes with change in water-cement ratio and curing conditions	127
Figure 5.22	The effect of conversion on the shape of the pore size distribution curves of HAC pastes	128

Figure 6.1	The different types of substrates	144
Figure 6.2	Specimen preparation for morphological studies	145
Figure 6.3	The general features of the unconverted paste side of the interface with a glass slide	146
Figure 6.4	X-ray spectrum of the surface in Figure 6.3	146
Figure 6.5	A higher magnification of the interfacial film in Figure 6.3	147
Figure 6.6	The general features of a window observed on the unconverted paste side of the interface with a glass slide	147
Figure 6.7	A higher magnification of a window similar to that of Figure 6.6	148
Figure 6.8	Small platelets of the unconverted paste side of the interface with glass	148
Figure 6.9	X-ray spectrum of the white platelets in Figure 6.8	149
Figure 6.10	X-ray spectrum of the dark background in Figure 6.8	149
Figure 6.11	The general features of the unconverted paste side of the interface with a polished section of limestone	150
Figure 6.12	X-ray spectrum of the area marked by a triangle in Figure 6.11	150
Figure 6.13	Typical features of the continuous regions observed on the unconverted paste side of the interface with limestone	151
Figure 6.14	A close-up of the surface shown in Figure 6.13	151
Figure 6.15	The general appearance of the limestone side of the interface with an unconverted paste	152
Figure 6.16	X-ray spectrum of the area marked by a triangle in Figure 6.15	153
Figure 6.17	X-ray spectrum of the area marked by a square in Figure 6.15	153

Figure 6.18	The converted paste side of the interface with a glass slide	154
Figure 6.19	A close-up of the large crystals in Figure 6.18	154
Figure 6.20	A close-up of the small crystals in Figure 6.18	155
Figure 6.21	X-ray spectrum of the crystallised alumina in Figure 6.18	155
Figure 6.22	Scanning electron micrograph of the specimen in Figure 6.27	156
Figure 6.23	The distribution of aluminium on the two surfaces of Figure 6.22	156
Figure 6.24	The calcium distribution for the two surfaces of Figure 6.22	157
Figure 6.25	X-ray spectrum of the vertical edge in Figure 6.22	158
Figure 6.26	X-ray spectrum of the fractured paste in Figure 6.22	158
Figure 6.27	Preparation of the cross-section specimen and its orientation in the SEM	159
Figure 6.28	The edge of the fractured surface in Figure 6.22	160
Figure 6.29	A higher magnification of Figure 6.28	160
Figure 6.30	The aluminium distribution for the fractured surface of Figure 6.29	161
Figure 6.31	The calcium distribution for the fractured surface of Figure 6.29	161
Figure 6.32	DTA thermograms of the converted paste side of the interface with a glass slide	162
Figure 6.33	X-ray spectrum of the area marked by a triangle in Figure 6.34	163
Figure 6.34	A close-up of the converted paste side of the interface with a glass slide	163
Figure 6.35	The glass side of the interface with a fully converted paste	164
Figure 6.36	A higher magnification of the adhering film in Figure 6.35	164

Figure 6.37	Crystallised alumina scattered on the top of the film adhering to the glass surface	165
Figure 6.38	X-ray spectrum of the area marked by a triangle in Figure 6.36	165
Figure 6.39	The general features of the converted paste side of the interface with Alag aggregate	166
Figure 6.40	The general features of the converted paste side of the interface with granite	166
Figure 6.41	The general features of the converted paste side of the interface with limestone	167
Figure 6.42	X-ray spectrum of the converted paste side of the interface with aggregates	167
Figure 6.43	One of the shapes of gibbsite crystals on the converted paste side of the interface with Alag aggregate	168
Figure 6.44	Another shape of gibbsite on the converted paste side of the interface with Alag aggregate	168
Figure 6.45	A close-up of the centre of Figure 6.39	169
Figure 6.46	A different shape of gibbsite on the converted paste side of the interface with Alag aggregate	169
Figure 6.47	A close-up of the centre of Figure 6.40	170
Figure 6.48	A close-up of the centre of Figure 6.41	170
Figure 6.49	The general features of a polished surface of Alag aggregate	171
Figure 6.50	A higher magnification of the Alag surface in in Figure 6.49	171
Figure 6.51	X-ray spectrum of the area marked by a triangle in Figure 6.50	172
Figure 6.52	X-ray spectrum of the area marked by a square in Figure 6.50	172
Figure 6.53	Alag side of the interface with a fully converted paste	173

Figure 6.54	A close-up of the Alag side of the interface with a fully converted paste in Figure 6.53	173
Figure 6.55	Crystallised alumina on the Alag side of the interface with a fully converted paste	174
Figure 6.56	X-ray spectrum of the Alag side of the interface with a fully converted paste	174
Figure 6.57	Different features of the Alag side of the interface with a fully converted paste	175
Figure 6.58	Fragments from the layer marked by a triangle in Figure 6.57 on the paste side of the interface with Alag aggregate	175
Figure 6.59	X-ray spectrum of the area marked by a triangle in Figure 6.57	176
Figure 6.60	The general features of the limestone side of the interface with a fully converted paste	177
Figure 6.61	A close-up of the ettringite needles on the limestone surface	177
Figure 6.62	Attached crystallised alumina on the ettringite needles	178
Figure 6.63	Needles of ettringite on the converted paste side of the interface with limestone	178
Figure 6.64	X-ray spectrum of ettringite needles	179
Figure 6.65	X-ray spectrum of the area marked by a triangle in Figure 6.60	179
Figure 6.66	The granite side of the interface with a fully converted paste	180
Figure 6.67	X-ray spectrum of the granite surface	180
Figure 6.68	The converted paste side of the interface of a specimen from a 20 year old HAC concrete bridge	181
Figure 6.69	A close-up of the paste side of the interface in Figure 6.68	181

Figure 6.70	Another area of the paste side of the interface shown in Figure 6.68	182
Figure 6.71	A close-up of the paste side of the interface in Figure 6.70	182
Figure 6.72	X-ray spectrum of the area marked by a triangle in Figures 6.69 and 6.71	183
Figure 6.73	X-ray spectrum of the area marked by a square in Figures 6.69 and 6.71	183
Figure 6.74	The aggregate side of the interface with a converted paste in a 20 year old HAC concrete bridge	184
Figure 6.75	A close-up of the centre of Figure 6.74	184
Figure 6.76	DTA thermograms of the paste side of a specimen from a 20 year old HAC concrete bridge	185
Figure 6.77	The morphology of the paste side of the interface with a glass slide after 2 days of curing at 45°C	186
Figure 6.78	A close-up of the interfacial film in Figure 6.77	186
Figure 6.79	The general features of the paste side of the interface with a glass slide after 4 days of curing at 45°C	187
Figure 6.80	A close-up of the crystals in Figure 6.79	187
Figure 6.81	The general appearance of the paste side of the interface with a glass slide after 6 days of curing at 45°C	188
Figure 6.82	A close-up of the gibbiste crystals in Figure 6.81	188
Figure 6.83	The morphology of the paste side of the interface with a glass slide after 10 days of curing at 45°C	189
Figure 6.84	A close-up of the gibbsite crystals in Figure 6.83	189
Figure 6.85	X-ray spectrum of the crystals in Figure 6.78	190
Figure 6.86	X-ray spectrum of the crystals in Figure 6.80	190
Figure 6.87	X-ray spectrum of the crystals in Figure 6.82	191
Figure 6.88	X-ray spectrum of the area marked by a triangle in Figure 6.80	191

Table 7.1	Effect of additions on the setting time of HAC pastes	199
Table 7.2	Effect of washing on phosphogypsum	200
Figure 7.1	The effect of adding gypsum or purified phosphogypsum on the strength of HAC pastes	201
Figure 7.2	The effect of adding natural or chemical anhydrite on the strength of HAC pastes	202
Figure 7.3	DTA of HAC with additions of gypsum or purified phosphogypsum	203
Figure 7.4	DTA of HAC with additions of natural or chemical anhydrite	204

CHAPTER 1  
INTRODUCTION

1.1 BACKGROUND

The commercial aluminous cements, or high alumina cements (HAC), are all made by fusing together a carefully controlled mixture of aluminous and calcareous materials, usually bauxite and limestone of fairly low silica content, to a completely molten state and grinding the resulting product to cement fineness<sup>(1)</sup>.

The particular cementitious properties of aluminous cements, which are distinctly different from those of portland cements, are derived primarily from the hydration product of monocalcium aluminate (CA)\* which is by far the main anhydrous constituent of HAC. This compound is relatively slow setting but it hardens so rapidly that mixes made with HAC achieve virtually full strength within 24 hours. The other compounds, usually present in smaller proportions, are  $C_{12}A_7$ ,  $CA_2$ ,  $C_2AS$ ,  $C_2S$ , CT, and  $C_4AF$ .

The variable amounts of these compounds cause colour differences to range from very dark to very light grey and the alumina content from 36% to over 50%; the latter may influence the refractoriness of the cement since the melting-points of the various calcium aluminates rise with increasing alumina content. The white HAC made by fusing

---

\* Throughout this dissertation, cement chemist's shorthand notation will be employed e.g.  $CaO = C$ ,  $Al_2O_3 = A$ ,  $SiO_2 = S$ ,  $Fe_2O_3 = F$ ,  $TiO_2 = T$ , and  $H_2O = H$ . Thus CA represents  $CaO \cdot Al_2O_3$ .

pure grade alumina with calcium carbonate is widely employed for special refractory applications at temperatures in excess of  $1350^{\circ}\text{C}$  which is the maximum service temperature for ordinary HAC. This special type of HAC contains 72-80% alumina, and is mainly composed of monocalcium aluminate which melts at  $1608^{\circ}\text{C}$ , together with a fair amount of  $\text{CA}_2$  which has a fusion point of about  $1770^{\circ}\text{C}$ <sup>(2)</sup>.

Apart from their satisfactory service at fairly high temperatures, HAC mixes made with appropriate aggregates are resistant to sulphates, to certain hydroxylic substances, and to low levels of acidity. One reason for this is the absence of free calcium hydroxide which is directly responsible for the disintegration and instability of ordinary portland-type cements in corrosive waters. In fact, HAC was originally developed as a sulphate resisting cement in 1908 by a Frenchman M J Bied who realised that the decomposition of portland cement structures in sea water and heavily sulphated grounds was due to the attack of the concrete by sulphate ion. Bied devoted many years to the search for a cement based on calcium aluminate instead of calcium silicate as the former would be, according to earlier work by Vicat in 1846, resistant to sulphate action<sup>(3)</sup>.

The commercial manufacture of HAC was not started until 1913 and, following extensive tests on the product, it was finally placed on the market in 1918-1920. During the first world war the ultra-rapid hardening of the cement was already utilised in the construction of gun emplacements and shelters. Since 1924 the manufacture of HAC was extended to the USA, Japan, and many European countries. Subsequently,

the cement was used in the precast industry particularly for the fabrication of prestressed concrete beams, and in all types of emergency work on bridges, airfields, busy roads, etc, as well as in aggressive situations and as a binder in refractory concrete<sup>(4)</sup>.

HAC has also shown certain advantages for winter and cold weather concreting without auxiliary heating equipment or cement additives, since the total heat liberated during the hardening period is quite sufficient to protect the concrete from severe frost. Although this self-generated heat is very useful when working at remarkably low temperatures, a number of precautions may be required to prevent the concrete from over-heating during hardening at relatively higher ambient temperatures; otherwise, strength and durability may be reduced<sup>(5)</sup>. But such precautions in placing and curing do not necessarily guarantee that the concrete properties would not be seriously affected if the concrete is subsequently exposed to warm humid conditions<sup>(6)</sup>.

The adverse effect of such conditions on HAC structures has been known for many years<sup>(7)</sup>, and, following a number of failures in France, Tunisia, Algeria, and other countries, the structural use of the cement was banned for public work in France by 1943. In the mid-1950's the manufacture of HAC was stopped in Hungary. The use of the cement for structural purposes was also forbidden in Germany by 1962 after a series of structural collapses in agricultural buildings in Bavaria in 1961.

In recent years, three failures have been experienced in the United Kingdom; the first was the roof of the Bennett Building at the University of Leicester in June 1973, followed a day later by the collapse

of the roof of the assembly hall at the Camden School for Girls, and the third was the roof of the Sir John Cass's Foundations and Red Coat Church of England Secondary School in Stepney in February 1974<sup>(8)</sup>. Because of these troubles, recommendations for the use of HAC in all BS structural codes have been removed, and this could mean the end for the use of this type of cement in structures in this country where the main concern has been to assess the safety of existing buildings with precast prestressed concrete beams made with HAC<sup>(9, 10)</sup>.

The deterioration of HAC, accompanied sometimes by a change in colour from grey-black to yellow-brown, is usually attributed to chemical change known as "conversion". This involves the transformation of the initial metastable hexagonal hydrates,  $CAH_{10}$  and  $C_2AH_8$ , into the more stable hydrate,  $C_3AH_6$ , with water and gibbsite ( $AH_3$ ) as by-products, and the aging of the alumina gel produced during the very early stages of hydration to fully crystallised gibbsite<sup>(11)</sup>. The process of conversion appears to be favoured by raising the temperature of hydration and the presence of free water within the cement micro-structure which increases either as the original water-cement ratio or the ambient humidity is increased. It is suggested that the process takes place by a "through solution" mechanism, with the dissolution of the initial hydrates and the final crystallisation of the conversion products which are believed to be more dense than the metastable hydrates<sup>(12)</sup>. The subject is rather complex and not fully understood but there is evidence to show that, unless the water-cement ratio is sufficiently low<sup>(13, 14)</sup>, the conversion may be accompanied by a

substantial increase in porosity resulting from the decreased volume of solids<sup>(15)</sup> and the formation of large cubic crystals of low specific surface area<sup>(16, 17)</sup>. This is compatible with the reduction in strength and the increased vulnerability to chemical attack.

Generally, the strength-time curves for HAC mixes follow a characteristic pattern of an increase to a maximum strength, then a decrease to a minimum strength, followed by a very slow increase in strength with age, the time required to reach the minimum strength being dependent upon the temperature and the water-cement ratio<sup>(18)</sup>. The residual strength after conversion, which has been reported to be dependent almost uniquely on the water-cement ratio<sup>(19)</sup>, appears to be dependent on the rate at which the conversion reaction takes place as well<sup>(18, 20)</sup>. Investigations showed that the loss of strength of any particular mix is the same regardless of the age at which the higher temperature acts<sup>(21)</sup>.

Conversion may also influence the bond between the cement and the aggregate material. It was found that, when a neat cement paste is cast against most substrates under normal temperature conditions, an interfacial film presenting the appearance of gel is usually formed at the paste-solid interface<sup>(22)</sup>. However, observations made on highly converted HAC concrete samples obtained from a six-year-old roof beam illustrated the formation of a very porous structure consisting of rounded clusters typical of the conversion product at the interfacial zone between the converted matrix and aggregates causing decohesion between the two materials<sup>(12)</sup>.

Several measures have been proposed by different investigators to prevent the conversion process, and these have been described by Robson<sup>(23)</sup> who reported in 1962 that 'so far it cannot be said that any reliable and effective method has been discovered which will greatly retard or prevent the conversion process when the conditions for for the latter are specially favourable'.

More recent work associated with the same problem showed that the most promising method is the addition of calcium sulphoaluminate or calcium sulphate with the result that calcium sulphoaluminate hydrate is produced instead of calcium aluminate hydrate in HAC<sup>(24, 25)</sup>. This may confirm the finding of Budnikov in 1960<sup>(26)</sup> but it seems probable that the experimental conditions and the materials used may influence considerably the outcome of these attempts<sup>(24)</sup>. Another approach was tried by French, Montgomery, and Robson<sup>(27)</sup> in 1970; HAC mixes having low water-cement ratios were cured at elevated temperatures for relatively short periods which proved to be sufficient to yield a stable hardened concrete even under conditions which are highly favourable to conversion. In the same year the use of HAC for government buildings in France was permitted with severe restriction on mix design and control, but since then and until 1975 no applications were made to use the cement in buildings.

However, the use of HAC for structural purposes remains questionable until the basic features of conversion are fully understood and until well-established measures are achieved either to prevent the conversion of the metastable hydrates or to replace such compounds with more stable ones. This could mean the development of new types of cement to fill the gap left by HAC in construction materials.

## 1.2 PURPOSE OF INVESTIGATION

In this investigation, cement pastes were chosen for study instead of mortars or concretes to obtain precise information about the microstructure of the hardened cement without the interference which is expected due to the presence of aggregates or sand.

The main objectives of the present investigation were:

1. To interpret strength variations accompanying the conversion reaction under various conditions in terms of mineralogical changes, porosity, and pore size distribution.
2. To study the effect of conversion on the microstructural features of the interface between various aggregate materials and HAC pastes and to deduce its effect on the paste-aggregate bond.
3. To examine the possibility of using phosphogypsum (impure gypsum in the form of a cheap industrial by-product) as an additive to replace calcium aluminate hydrate in HAC with calcium sulphoaluminate hydrate.

Although not part of the original plan, the study of the rheological properties of fresh HAC paste had to be undertaken to overcome unexpected irregularities in the flow behaviour of the pastes which resulted in considerable experimental difficulties. Such studies were found to be of the utmost importance to achieve uniform and reproducible pastes, and *provide an* essential reference to any further

investigation to be carried out on HAC pastes. As a result, however, other aspects of conversion could not be studied as comprehensively as planned.

### 1.3 PLAN OF PRESENTATION

The thesis is introduced by background information relating to the properties of hardened HAC concretes and the problems attendant upon its use in constructions, followed by the scope of this research. In chapter 2, the materials and experimental techniques employed in studying the set pastes are described. The rheological study of fresh HAC pastes occupies chapter 3; a review introduces the chapter, followed by the methods of measurements and the experimental results. Chapter 4 discusses the effect of mixing, curing, and testing conditions on subsequent results. In chapter 5, the change in the pore structure and the mineralogical properties throughout the conversion process were followed and related to strength variations. The microstructural features of the interfacial zone between the hydrated constituents of HAC and aggregates were studied in chapter 6. In chapter 7, a brief attempt is made to explore the possibility of using phosphogypsum as an additive in HAC. The general conclusions and recommendations for further work can be found in chapter 8.

## CHAPTER 2

### MATERIALS AND EXPERIMENTAL TECHNIQUES

#### 2.1 MATERIALS

##### CEMENTS

The majority of specimens used in this research were prepared from 'Fondu' high alumina cement. However, 'Secar 250' cement, which is a relatively pure material based on calcium aluminates was used in part of the work described in chapter 3. A single batch of each cement was supplied in bags by the Lafarge Aluminous Cement Company Limited, and stored in airtight drums until required. Chemical analysis of representative samples of the two types of cement is given in table 2.1.

##### AGGREGATES

The use of aggregates was limited to the investigations of chapter 6. Alag aggregates, the clinker of HAC, were supplied in large pieces by the Lafarge Aluminous Cement Company Limited, while granite and limestone were provided in large chunks from Shap in Cumbria and Mendip in Somerset, UK.

##### SITE CONCRETE

Concrete samples obtained from a parapet unit of a demolished 20 year old footbridge at Wishaw, Scotland, were also examined in work described in chapter 6.

## PHOSPHOGYPSUM

Three types of phosphogypsum (PG) supplied from different sources were investigated in chapter 7.

PG I (S)	Scottish Agricultural Industries Ltd.
PG II (IC)	ICI
PG III (F)	Albright & Wilson Ltd - Whitehaven

PG I and III were provided in wet conditions, but type II was dry.

## NATURAL GYPSUM

Natural gypsum was supplied by British Gypsum Limited.

## 2.2 PREPARATION OF CEMENT PASTE SAMPLES

Neat cement pastes were made up with different water-cement ratios; deionised water was used throughout. Owing to the anomalous behaviour of fresh aluminous cement pastes, details of mixes and mixing procedures used in the various pastes of the investigation are given in chapter 4, whilst the experimental procedures followed in studying the rheological characteristics of fresh pastes are given in full in chapter 3.

To examine the properties of mature cement pastes at a given water-cement ratio, fresh pastes of constant consistency were cast in small glass tubes of 23mm diameter and 50mm height. After casting, each group of four tubes was placed for 24 hrs in an airtight plastic box of dimensions 120mm x 240mm x 80mm at 10°C and 100% relative humidity. The tubes were then smashed and the specimens were transferred to storage in saturated air within large plastic boxes at the desired temperatures and for the required lengths of time. The boxes were kept either in an incubator or in a water bath, Figures 2.1 and 2.2. For the investigations described in chapter 6, cement paste specimens in contact with glass slides and aggregate sections were subjected to the same curing conditions as above.

### 2.3 COMPRESSIVE STRENGTH MEASUREMENTS

The strength of hydrated cement may be determined by various methods. such as compression, flexure, penetration resistance and ultrasonic pulse velocity tests<sup>(28)</sup>. Indentation hardness has been also used as a measure of strength of cement pastes<sup>(29)</sup>.

In this present investigation, the Avery-Denison Universal Testing Machine model 7152 with maximum capacity of 600 KN was used for testing the compressive strength of set high alumina cement pastes, Figure 2.3. In this test, the specimen is placed between two compression platens and the load is applied through a straining frame coupled to a hydraulic piston. Two load ranges were available, 0-600 KN and 0-60 KN, the latter was usually employed and the load rate of 4.3N/mm<sup>2</sup>/min was maintained throughout. The chosen rate was suitable for the specimens which, beside being small were, in some cases, very weak.

## PROCEDURES

At the end of each period of curing, the paste samples (mentioned in section 2.2) were cut to the same length of 35mm with a diamond saw using water as a lubricant. The specimens were then air-dried at room temperature for 6 h before testing. The influence of surface moisture on the measurements is discussed in chapter 4. To determine the compressive strength of the paste, three specimens were tested for each condition, so that a mean value could be obtained. To ensure the uniformity of the load on the small cylindrical specimens, the upper spherically seated platen was replaced by a specially designed ball bearing mounted plate with a 25mm diameter recess to secure the specimens centrally in the compression space, Figure 2.4.

## 2.4 DIFFERENTIAL THERMAL ANALYSIS

Dynamic thermal methods involve measuring the physicochemical changes in a substance while it is being heated or cooled at a controlled rate. In differential thermal analysis (DTA) and differential scanning calorimetry (DSC), the energy changes are recorded, whilst in derivative thermogravimetry (DTG) weight changes are measured.

DTA and DTG have been widely used in the analysis of hydrated cement<sup>(30-32)</sup> and building products<sup>(33)</sup>. The use of DTA in the field of cement and related materials was reviewed by Ramachandran<sup>(34)</sup>. In several published investigations, the mineralogical changes of

hydrated aluminous cement have been studied by DTA<sup>(11, 12, 18, 35)</sup>. DSC, which is a related technique, was also used to study the hydration of monocalcium aluminate<sup>(13)</sup>. DTA, besides being considered the most convenient method in characterising the main compounds of hydrated aluminous cement<sup>(11)</sup>, will also identify chemical attack or impurities in HAC concrete samples<sup>(36)</sup>.

It was convenient, therefore, to use DTA throughout the present studies. In this technique, the temperature difference ( $\Delta T$ ) between the sample to be studied and a thermally inert material is plotted against temperature. When phase changes or chemical reactions take place in the sample under study, either exo- or endothermic, the chart of  $\Delta T$  against temperature will show upward or downward peaks respectively. Alumina gel and  $CAH_{10}$  may be recognised by endothermic peaks at about 110-120°C, whilst  $C_3AH_6$  and  $AH_3$  (gibbsite) have almost equal endothermic peaks in the region of 300°C.

The peak heights of the DTA thermograms are used as a measure of the relative amounts of  $CAH_{10}$  and  $C_3AH_6$  in calculating the degree of conversion which was originally defined by Midgley<sup>(20)</sup> in percentage terms as

$$\frac{\text{amount of } C_3AH_6 \times 100}{\text{amount of } C_3AH_6 + \text{amount of } CAH_{10}}$$

But, as the amount of  $C_3AH_6$  is usually influenced by carbonation, the degree of conversion (DOC) may be determined on the basis of gibbsite which is not subjected to the same effect. Thus:

$$DOC = \frac{\text{amount of } AH_3 \times 100}{\text{amount of } AH_3 + \text{amount of } CAH_{10}}$$

The present analyses were carried out on a Stanton Redcroft differential thermal analyser model 673-4, Figure 2.5. The system comprises four basic modules; analyser module including sample holder, platinum v 13% platinum-rhodium thermocouples and furnace, temperature programmer, DC amplifier module and potentiometric recorder. Dimpled platinum-rhodium crucibles were used and tests were carried out in static air atmospheres.

## PROCEDURES

Cement pastes to be subjected to DTA were ground by hand using a pestle and mortar and then screened over a 150  $\mu$ m sieve. The ground specimens were dried over silica gel in a CO<sub>2</sub>-free system at ambient temperature. Calcined alumina was used as a reference material and the same packing procedure was carried out each time to ensure reproducibility between successive experiments. The heating rate of 20°C/minute was maintained throughout. The whole procedure was consistent with the general recommendation for testing high alumina cement concrete samples<sup>(36)</sup>.

### 2.5 POROSITY MEASUREMENT

#### 2.5.1 DETERMINATION OF TOTAL POROSITY

The determination of this property involves the measurements of the true specific gravity and the apparent density of a dry cement paste<sup>(37, 38)</sup>. The drying procedure is to be discussed in section 2.5.2.

The true specific gravity is determined pycnometrically; the paste is ground to powder whose volume is determined by the mass difference between a pycnometer filled with a wetting liquid (paraffin) and the same pycnometer with the powder in it filled up with the same liquid. The filling operation is done under vacuum to ensure that the liquid completely wets the powder.

The apparent density can be obtained by knowing the weight of a dry specimen and its external volume by the displacement of non-wetting liquid (mercury).

A specially designed 'bottle and top' was used which was capable of reproducing a fixed volume of mercury. The top was levelled with a glass slide, Figure 2.6. The 'bottle' was filled with mercury, and the 'top' inserted and the meniscus of mercury levelled with the glass slide. The outside was carefully cleaned with a brush and the whole thing placed in a clean previously weighed beaker. The 'top' was opened and the weighed dry sample inserted. The 'top' was replaced and the exuded mercury carefully collected in the beaker. The 'top' was levelled and the outside carefully brushed so that all displaced mercury was collected. The beaker was reweighed and the weight of mercury noted.

The calculation procedure for the total porosity is given in Appendix 1.

## 2.5.2 PORE SIZE DISTRIBUTION MEASUREMENTS

Porosity and pore-size-distribution of hardened cement paste may be determined by capillary condensation techniques<sup>(39-41)</sup>. However, the alternative mercury intrusion method seems to give a considerably coarser size distribution with mean diameters of the order of several hundred  $\text{Å}$ , which is consistent with evidence obtained from other techniques, whilst the capillary condensation methods are limited to much finer pores<sup>(42)</sup>. Mercury intrusion pore-size-distribution data for hydrated HAC have been reported by Tsukayama<sup>(43)</sup>, and Cottin and Reif<sup>(44)</sup>.

In this present work, a Micromeritics Instrument Corporation porosimeter, model 900/910 series, of 50,000psi ( $351 \text{ N/mm}^2$ ) pressuring capacity was used to study the pore system of hardened aluminous cement pastes, Figure 2.7.

The principle of the instrument is to determine the quantity of nonwetting liquid, mercury, that may be forced into the pores of the material under various pressures. The system is first evacuated to remove adsorbed gases and vapours, then the mercury penetrates the pores in proportion to their size and the pressure applied. The porosimeter consists of a means for generating a pressure and a means for determining the volume of the mercury intruded. A vacuum pump and indicator are required to evacuate the system. A sample cell and reservoirs for the mercury and pressure transmitting fluid are also essential parts of the system.

The pressure at which mercury enters a pore of given size can be calculated by the Washburn pressure displacement equation<sup>(45)</sup>

$$P = -4 \gamma \cos\theta/d$$

where P is the pressure applied, d is the pore diameter,  $\gamma$  is the surface tension of the mercury ( $485 \times 10^{-6}$  N/mm), and  $\theta$  is the contact angle between mercury and the material. The proof of the equation is given in Appendix 2.

Corrections were made for compressibility of the mercury and duplicate runs were made on each sample.

The penetration technique requires the specimen and the system to be evacuated prior to a test, so that the mercury is free to penetrate without additional obstructions. It is essential, therefore, to have the specimens dried, but hydration products of high alumina cement such as  $CAH_{10}$  and  $C_2AH_8$  are easily influenced by the drying conditions;  $CAH_{10}$ , for example, loses  $3H_2O$  on drying at 45 per cent relative humidity or over solid NaOH and  $7.5 H_2O$  on more intensive drying over  $P_2O_5$  or at  $100-105^\circ C$ <sup>(46)</sup>. The influence of ignition on hydrated calcium aluminates is illustrated in Figure 2.8.

Several investigators used vacuum drying technique for preparing HAC specimens for various applications<sup>(13, 44, 46)</sup>. Mention for the level of vacuum reached was reported only by Chatterji and Jeffrey<sup>(47)</sup> who used a pressure of  $1 \times 10^{-4}$  mm Hg. Although this drying procedure is suitable for the stability of the hydrate  $CAH_{10}$ <sup>(44)</sup>,

pastes dried under vacuum could contain some residual surface water at the end of the process<sup>(48)</sup>. The oven drying method could result in drier samples, but it may cause a complete conversion of the hydrated calcium aluminate. However, this method is widely used for pastes made of portland cement. Previous investigations on vacuum dried specimens of aluminous cement indicated that mercury penetrates practically all the pores intruded by methanol or acetone<sup>(13, 44)</sup>.

The dependence of the contact angle between mercury and cement pastes on the drying method was discussed by Winslow and Diamond<sup>(48)</sup>. Contact angles of 117 and 130 degrees were obtained for oven dried and P dried (equilibration over magnesium perchlorate hydrates) portland cement pastes respectively.

## PROCEDURES

It was clear that objections could be raised to whatever procedures were used for preparation and drying of pastes. The methods adopted in the present work were therefore selected on the basis that they appeared to avoid major pitfalls and would provide a means of obtaining consistent and comparable results.

For each condition to be studied, 1mm thin sections were sliced from the cylindrical sample using a diamond cutting wheel. The slices were then broken by hand into small pieces, approximately 5mm wide and 10mm long. The specimens were immediately transferred to a small glass cell and evacuated over a liquid nitrogen water trap, until the pressure dropped to  $2 \times 10^{-3}$  mm Hg and was maintained at that level for at least 4 days. A special glass manifold with 10 branches was

built to allow continuous evacuation of 10 specimens at the same time, Figure 2.9. The dried specimens were then stored <sup>under vacuum</sup> (in a vacuum desiccator containing silica gel and CO<sub>2</sub> absorbent until needed for test. The contact angle between mercury and the paste surface was assumed to be 130 degrees throughout the calculations since the specimens were vacuum dried.

The chosen specimen size and shape were most suitable for the vacuum drying technique. Large sizes require evacuation for a much longer period, whilst if small grains are used, considerable care has to be exercised in interpreting the results of mercury porosimetry because interparticle void space is included in the measurements as well as the true porosity<sup>(49)</sup>. Moreover, the intrusion curves for small sizes are considered to be the closest to the true pore-size-distribution function<sup>(50)</sup>.

## 2.6 MORPHOLOGICAL STUDIES

The morphology and microstructure of hydrating cement have been studied by optical and electron microscopic methods. Although cement paste consists of materials which are too small for resolution in the optical microscope<sup>(51)</sup>, the technique has revealed valuable information on which the earlier knowledge of Le Chatelier<sup>(52)</sup> in the field of cementitious materials was based. More recent optical observations using petrographic thin sections<sup>(53, 54)</sup> have been mentioned by Williamson<sup>(55)</sup> and used to identify the microstructural zones in cement pastes and to interpret the features revealed by scanning electron microscopy of the pastes. Farran<sup>(22)</sup> used optical microscopy techniques to investigate the interfacial zone developed between various types of cement and several aggregates.

Recently, substantial progress in understanding the micro-structure of hydrated cement systems has been made as a direct result of using scanning electron microscopy (SEM)<sup>(55-57)</sup>. SEM has a large depth of field which permits the examination of fractured peices as well as smooth surfaces in a three-dimensional arrangement.

In a number of studies, morphological changes which occur during the hydration of high alumina cement have been followed by SEM<sup>(16, 47)</sup>. Moreover, SEM has been used to study the morphology of the contact zone between portland cement pastes and glass, steel and aggregates<sup>(58-60)</sup>. Some of the studies were carried out using a scanning electron microscope-energy dispersive X-ray spectrometer combination for rapid identification of the major elements present in the different micro-structural features observed by SEM<sup>(59-62)</sup>.

Transmission electron microscopy (TEM) could be used in studying the microstructure of hardened cement pastes<sup>(63, 64)</sup>. However, the technique appears to be mainly limited to ultra-thin sections or replicas which may result in a considerable distortion and loss of topography in the fracture surface<sup>(65)</sup>. This view is supported by the published work of Mori et al<sup>(66)</sup> and Berger et al<sup>(67)</sup> in which SEM and replica TEM micrographs are presented.

Scanning electron microscopy was considered, therefore, to be the most useful technique for the morphological studies to be carried out in this research. The observations were made with a Cambridge Stereoscan-150 Scanning Electron Microscope equipped with a KEVEX energy dispersive X-ray analysis (EDXA) unit with a display screen and X-Y recorder, Figure 2.10.

In this technique, the sample to be studied is dried, mounted on an SEM stub and coated with a thin conducting layer. The sample is then scanned with a narrow electron beam, which could be focussed on a selected spot or area, to generate X-ray photons which interact with a silicon detector to produce electrical pulses. The count of pulses is then accumulated by a multi-channel analyser for elemental analyses<sup>(61)</sup>.

#### PROCEDURES

Vacuum-dried specimens were mounted on aluminium SEM stubs, and coated with a 250Å<sup>0</sup> carbon conducting layer to prevent charging in the SEM. Observations were carried out with an acceleration voltage of 20 KV to restrict the penetration of the electron beam into the surface under study. The multi-channel analyser was allowed to accumulate counts of pulses over a range of 0-10 Kev.

Photographs were taken at various magnifications over the range of (1000x) to (5000x), whilst EDXA results were plotted on an X-Y recorder.

*No corrections for excitation and absorption effects on EDXA results were made.*



Figure 2.1 Incubator Curing

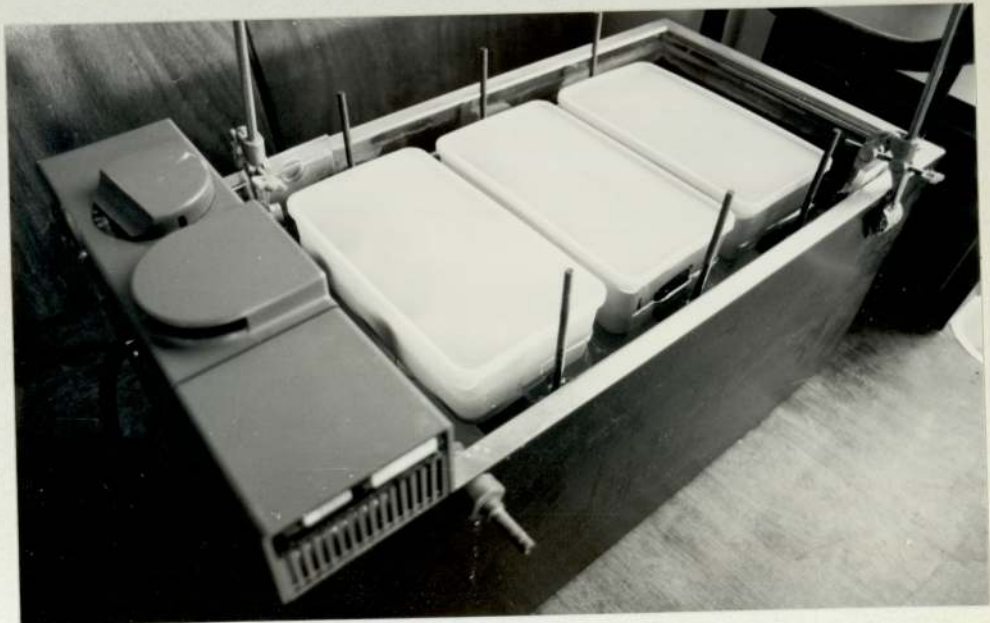


Figure 2.2 Water Bath Curing



Figure 2.3 The Avery-Denison Universal Testing Machine Model 7152



**Figure 2.4** Ball Bearing Mounted Plate for testing small Cylindrical Specimens



Figure 2.5 A Stanton Redcroft Differential Thermal Analyser Model 673-4

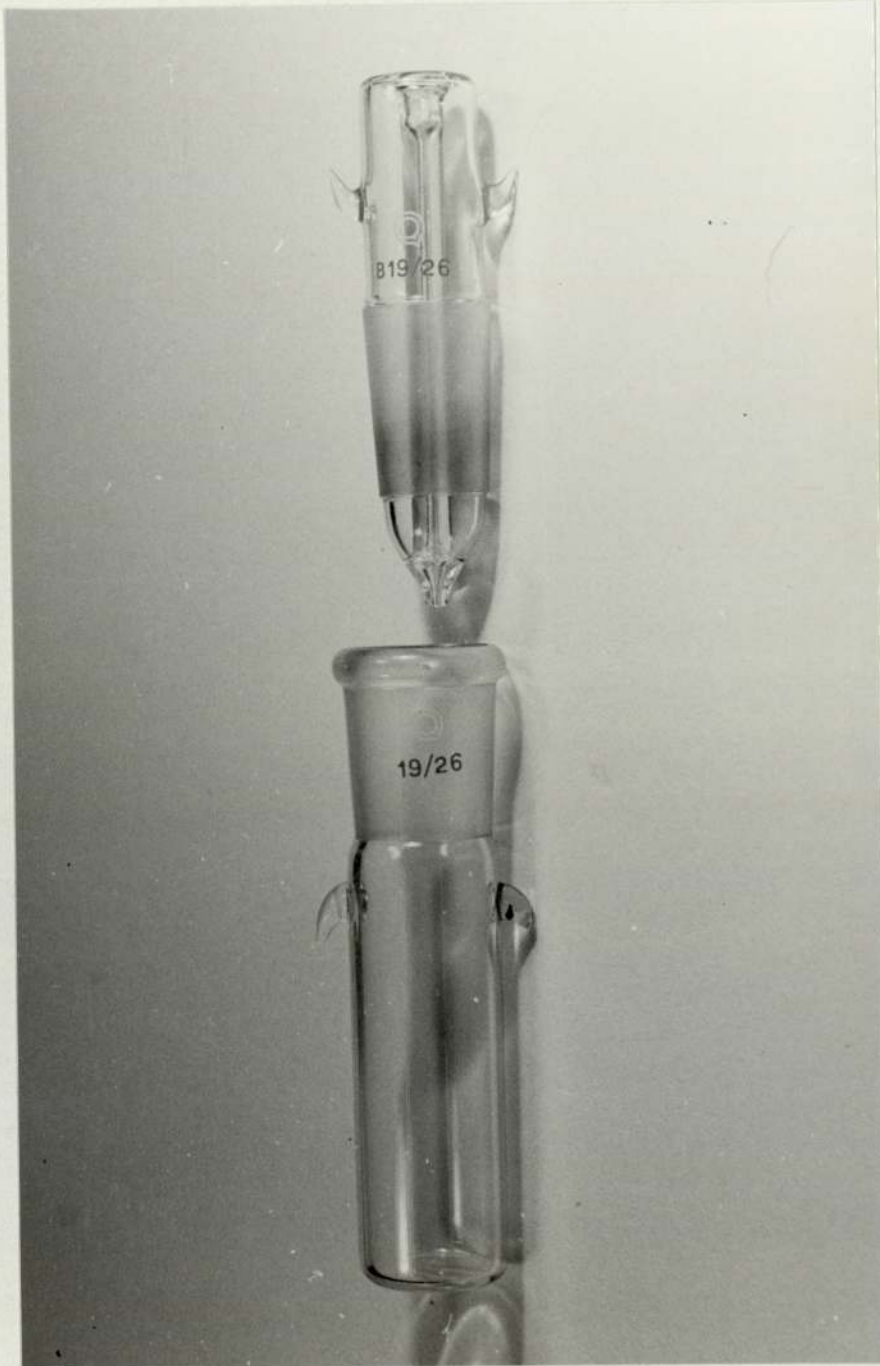


Figure 2.6 Apparent density bottle



Figure 2.7 A Micromeritics instrument corporation porosimeter, Model 900/910 series

Constituents	Fondu	Secar 250
CaO	37.50	27.10
Al <sub>2</sub> O <sub>3</sub>	39.48	71.00
SiO <sub>2</sub>	4.75	0.46
Fe <sub>2</sub> O <sub>3</sub>	11.43	0.18
FeO	4.18	
TiO <sub>2</sub>	2.03	
MgO	Trace	Trace
K <sub>2</sub> O	0.39	0.05
Na <sub>2</sub> O		0.21
Na <sub>2</sub> O <sub>3</sub>	0.18	
CO <sub>2</sub>	0.18	
SO <sub>3</sub>		0.02
SO <sub>4</sub>	0.1	
Loss of ignition	0.18	0.24

Table 2.1 Chemical composition of cement (% by weight) as supplied by Lafarge Aluminous Cement Company Limited

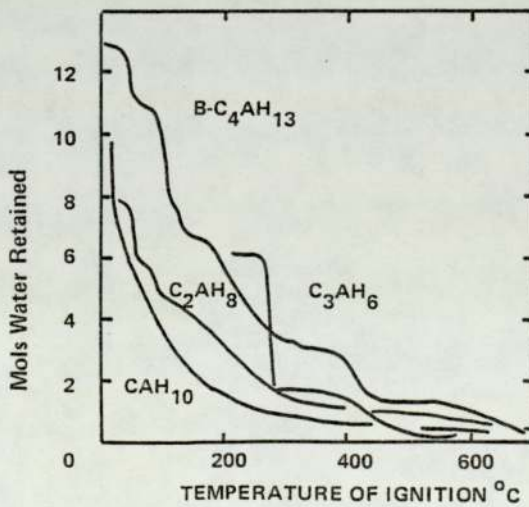


Figure 2.8 The loss of water from hydrated calcium aluminates on ignition<sup>(46)</sup>

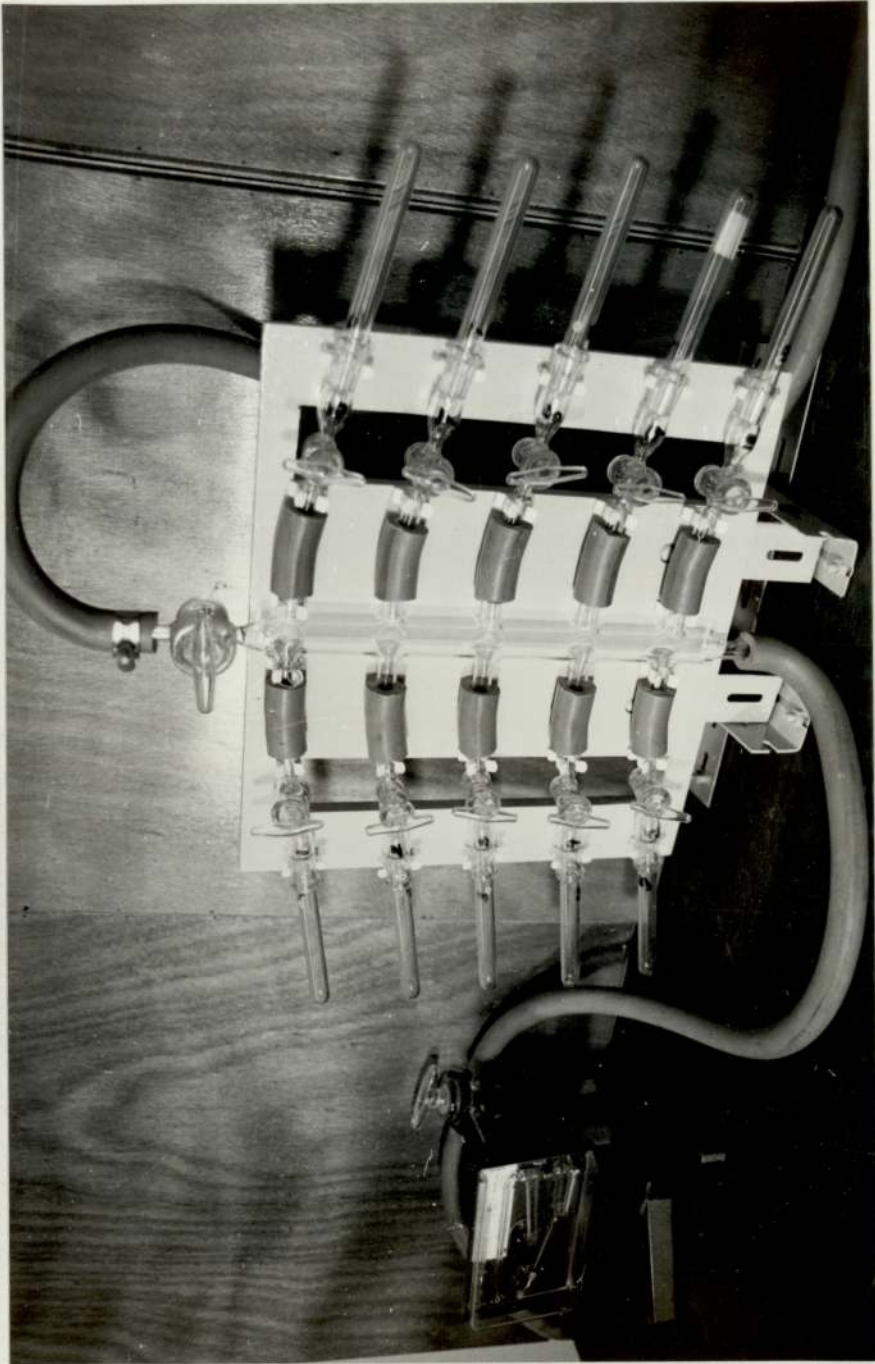


Figure 2.9 A glass manifold with ten branches for vacuum drying

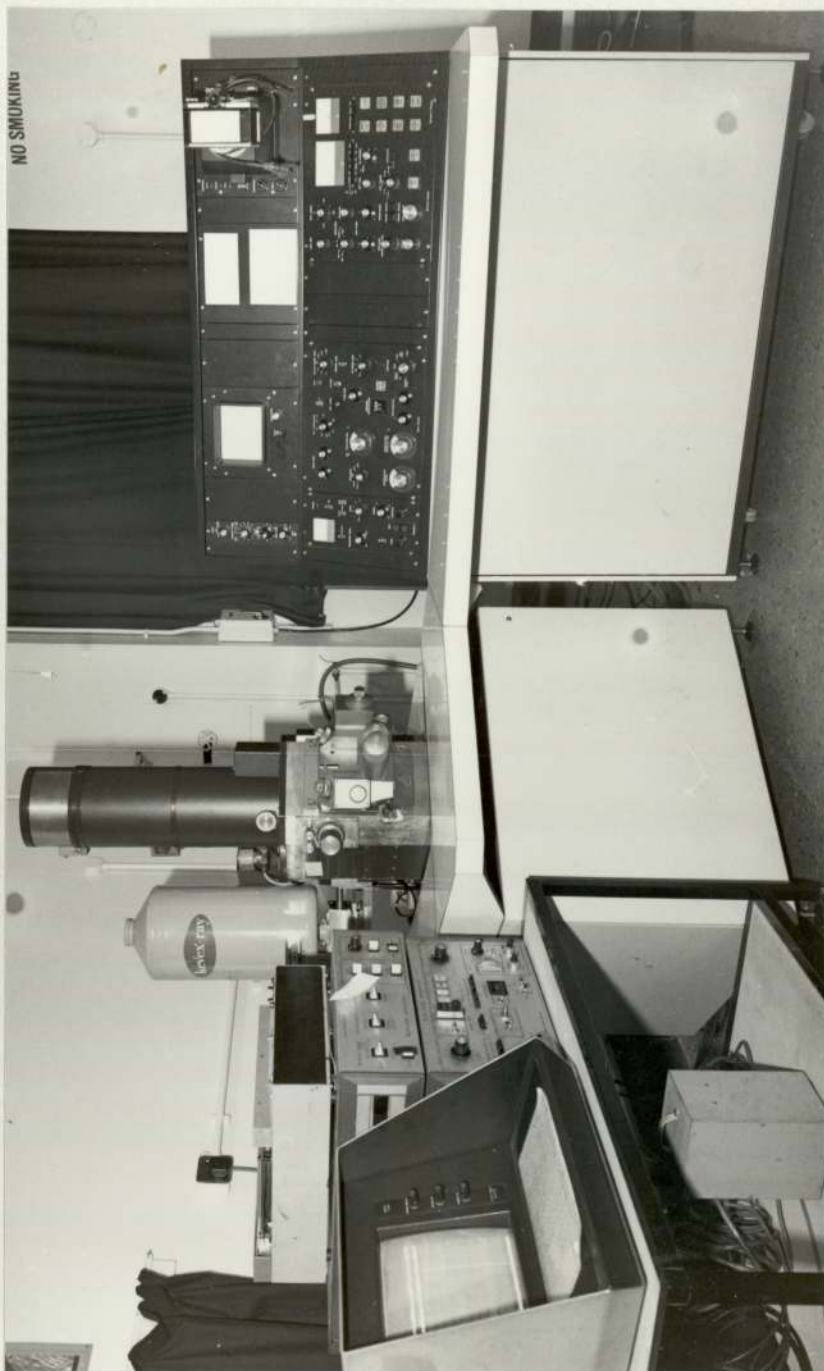


Figure 2.10 A Cambridge Stereoscan - 150 Scanning Electron Microscope/EDXA Unit Combination

## CHAPTER 3

### THE RHEOLOGICAL CHARACTERISTICS OF FRESH ALUMINOUS CEMENT PASTES

#### 3.1 INTRODUCTION

The experimental work carried out in this chapter is based on observations that were made during the early experiments of this recent research on the properties of hardened aluminous cement pastes. Unexpected variations in compressive strength and degrees of conversion measurements occurred for specimens of constant water-cement ratio and maturity. In some cases, under the same casting and curing conditions, the strength varied from  $38 \text{ N/mm}^2$  to  $27 \text{ N/mm}^2$ . The degree of conversion determined on the same sample ranged from 50% to 80%, the higher value being found in the upper region of samples.

Such variations could lead to a complete misunderstanding of any future results. Therefore, it was considered important to find out the causes of these problems and possible methods of eliminating them.

During mixing of 'Fondu' cement pastes of water-cement ratio 0.55, it was observed that the consistency of such pastes altered markedly with mixing time, causing a great deal of sedimentation on some occasions. A simple method of observing this was to determine the volume of sediment in the glass tubes which were used as casting moulds. The maximum sediment volume (i.e. the maximum consistency) was obtained after a certain period of mixing, but as the mixing continued, the consistency reduced again. Therefore the optimum time of mixing required to produce mixes having the same consistency was selected on this basis. However, it was noticed later that at the optimum time, pastes of different consistency were produced.

It was thought, at the time, that the method of mixing was responsible for these variations, and a considerable amount of effort was directed at improving the mixing technique, but the differences remained.

Later, it appeared from the room temperature record that the times required to reach the point of highest consistency might be dependent to some extent on mixing temperature. It was also observed that if 'Fondu' cement pastes were mixed long enough and left undisturbed, they became very thick and resistant to flow unless they were remixed.

Such irregularities in the behaviour of fresh 'Fondu' cement pastes could have resulted in the production of nonuniform samples which, in turn, may have been the cause of some of the variations observed earlier in the measurements of compressive strength and degree of conversion.

The above observations made it essential to examine the rheology of fresh aluminous cement pastes, as understanding the properties and the flow-behaviour of the material appeared to be the logical approach to achieve uniform, reliable and reproducible samples.

Apart from observations that HAC pastes appear wetter than OPC pastes with the same water content<sup>(68)</sup>, no detailed studies were published on the rheological properties of the aluminous cement system.

The available material concerning the field of rheology in general and about the behaviour of OPC pastes in particular provided a useful background to the work which was to be undertaken with aluminous cement pastes.

### 3.2 THE INFLUENCE OF INTERPARTICLE FORCES ON THE PHYSICAL PROPERTIES OF HYDROSOLS AND CEMENT PASTES

Hydrosols are two phase systems consisting of a disperse phase which forms the solid particles and the aqueous medium in which the particles are dispersed. The surface areas of the particles are relatively large and therefore characteristic surface properties are expected to play a very important part in determining the physical properties of the system as a whole. In such sols, if the aqueous medium is strongly adsorbed, the solid may be called hydrophilic (water loving); if it is not, it may be termed hydrophobic (water hating). This terminology is used to describe the tendency of a surface or functional group to become wetted or solvated<sup>(69)</sup>.

Hydrophobic particles in water are electrically charged; at the solid-water interface, an electrical double layer of positive and negative charge is generally formed that is made up of two regions: an inner region which includes adsorbed ions firmly held to the solid and a more diffuse region in which ions are distributed, Figure 3.1. Because of the electrical charges, there is a difference of potential between the fixed and diffuse double layer boundary and the bulk of the dispersion medium; the potential is called the zeta potential or electrokinetic potential<sup>(70)</sup>.

The presence of the electrical double layers surrounding all the particles is essential to the stability of the system, as the mutual repulsion of these layers prevents the particles from approaching each other sufficiently closely to aggregate and form a visible precipitate. While the complete removal of all electrolyte leads to instability of the sol, the adsorption of ions of opposite charge to that of the particles, decreases the double layer's zeta potential and causes the particles to flocculate. This effect is more significant the higher the valence of the added counter ions<sup>(71)</sup>. Figures 3.2 and 3.3 show the influence of the electrolyte concentration and the surface potential of the total potential energy of interaction of two spherical particles.<sup>(72)</sup>

In sols made of hydrophilic particles, the water is strongly attracted to the solid surface, forming a stabilizing layer of water molecules. If the hydration is decreased by the removal of this layer, the sol becomes sensitive to electrolytes; therefore, the stability of such systems is determined by the layer of water molecules and the electric charge<sup>(70)</sup>.

It has been found that zeta potential plays a significant part in determining the rheological properties of cement pastes<sup>(73)</sup>. In addition to this, Powers<sup>(71)</sup> observed that the properties of a suspension of cement in water are due mainly to the electrolytically controlled zeta potential and the strongly adhering film of water; if either the zeta potential or the film is altered, the interparticle forces are also altered. Therefore, cement may be regarded as a hydrophilic solid.<sup>(71)</sup>

While the disjoining pressure due to the adsorbed molecules of water and the electrostatic repulsion due to the double layers represent the forces of repulsion between particles, forces of attraction known as Van der Waals forces are the principal cause of flocculation in such suspensions. These universal attraction forces predominate at small and at large interparticle distances<sup>(74)</sup>; therefore, flocculation could occur while the particles are separated from each other by relatively short interparticle distances.

In fresh cement pastes, if the attraction forces fail to draw the particles together, they tend to disperse and are mutually repelled; this causes the large particles to settle down under their own weight, and the very small particles to suspend in the water experiencing a high degree of random motion known as Brownian motion. The settlement of the large particles reduces the interparticle distances principally in the vertical direction to produce a dense sediment at the lower region thus creating a nonuniform paste. On the other hand, if the cement particles are able to aggregate, they may form separate floccules; the packing of such floccules may result in the formation of a paste structure which encloses more water the higher the original water cement ratio<sup>(71)</sup>.

### 3.3 RHEOLOGICAL SYSTEMS AND THEIR FLOW CURVES

Green<sup>(75)</sup> divided rheological systems into loose structures and connected structures. Dilatant materials and Newtonians such as simple liquids, highly diluted suspensions and deflocculated

suspensions are examples of the former type, while connected structures include plastic materials, Bingham bodies and thixotropic suspensions.

The loose structure of Newtonians allows flow to occur under any stress however small it may be, but the continuous structure of flocculated particles in Bingham bodies imparts a yield value to the system. Such suspensions begin to flow only when this yield value is reached, and the more strongly the particles are flocculated, the greater would be the yield value.

For Newtonians, the rate of shear is directly proportional to the shear stress, and the consistency curve relating stress to rate of shear is a straight line passing through the origin (case a Figure 3.4). The flow curve of a Bingham body is also linear, but only for stresses above the yield value (case b Figure 3.4).

Loose structures, such as deflocculated suspensions with high solid concentration which are expected to show Newtonian behaviour, produce flow curves similar to those of Bingham bodies, but with slight yield values (case c Figure 3.4).

There are materials that flow neither like Newtonians nor like Bingham bodies. Dilatant materials are Newtonian at low rates of shear and are shear thickening at higher rates, the consistency curve being concave towards the stress axis. The material increases its resistance to flow as the shear rate increases (case d Figure 3.4).

Another type of materials is shear thinning. Such substances flow more easily as the shear rate increases, producing flow curves that are convex toward the stress axis (case e Figure 3.4). If the departure from linearity arises from thixotropic breakdown, the material is called thixotropic.

The apparent viscosity of a thixotropic material decreases under shear stress and recovers gradually when the stress is removed<sup>(76)</sup>, the complete reaction taking place isothermally. Such structures give rise to hysteresis loops when the 'up' and 'down' flow curves are plotted together; the 'down' curve is usually a straight line to the left of the 'up' curve. (case f Figure 3.4). The loop area coincides with the extent of thixotropic breakdown, a large area loop implying a large thixotropic breakdown and no loop meaning the absence of thixotropy.

In the case of OPC pastes, even though the predominant kind of flow curve is thixotropic, such pastes give Bingham body consistency curves at low shear rates<sup>(77, 78)</sup>. It has been found also that pastes of low water-cement ratios could produce a shear thickening consistency curve<sup>(78, 79)</sup> Figure 3.5. Antithixotropic and reversible types of flow were reported after various periods of hydration<sup>(80)</sup>. Pastes made of quartz powder and water show Newtonian behaviour, but by raising the pH value, such pastes could be changed to forms which exhibit rheological characteristics of Bingham thixotropic structures<sup>(81)</sup>, Figure 3.6. This serves to illustrate the effect of electrolyte composition on double-layer interactions and hence on the tendency for particle aggregations in sols.

### 3.4 METHODS OF MEASUREMENT

There are many different ways of studying the flow behaviour of rheological systems. The devices used for such studies are termed viscometers and a brief account of the more commonly used forms is given below.

In the capillary tube viscometer, the sample material is forced to flow through a capillary tube under a constant pressure difference and the rate of flow is measured.

The coaxial cylinders viscometer is one example of a rotational viscometer in which the suspension under test fills the gap between two cylinders, the outer of which is rotated at constant speed. The torque required to prevent the inner cylinder from turning is measured. The cone-and-plate viscometer is another example of the rotational viscometers, but the material is placed between the cone and the plate.

Viscosities of Newtonian fluids are easily measured in both the extrusion and the rotational viscometers, but there is an essential difference in the application of these viscometers to Bingham bodies, because such materials start to flow only when the shearing stress equals or exceeds the yield stress.

In the capillary tube, the yield stress is first reached at the outer layer next to the wall of the tube and the flow starts in all layers simultaneously; because there is a very small region around the

axis in which the yield stress can never be attained, however, the material forms a solid cylinder no matter how great is the velocity. As a result of this plug flow, it is not possible to obtain the straight part of the consistency curve.

In the coaxial rotational viscometer, the flow starts at the wall of the inner cylinder, then, with increasing the rate of shear, the stress at the wall of the outer cylinder reaches the yield value and the material as a whole undergoes laminar flow. Therefore, for shear stress in excess of the yield value, the experimental results give a linear flow curve. It should be mentioned here that difficulties may arise because the rate of shear varies across the gap in the coaxial cylinders viscometer. This was discussed by Tattersall<sup>(77)</sup> who stressed the importance of using a narrow annulus to overcome this problem. The advantage of the cone-and-plate viscometer is that the shear rate is constant across the gap between the cone and the plate provided that the cone angle is small<sup>(78)</sup>.

Thixotropic hysteresis loops, which are characteristic features of thixotropic structure, can be formed with the rotational viscometer only, because the loop is obtained by increasing the speed of rotation until the point of highest shearing rate is attained and then decreasing it gradually. Capillary tube viscometers are reported to be unsuitable for the study of thixotropy, because the material under test is extruded and, therefore, cannot be remeasured in its broken-down-state<sup>(82)</sup>.

A great deal of work on OPC pastes has been conducted using coaxial cylinders viscometers running at constant speeds. This method allows any change in the plastic viscosity due to thixotropy of the paste

to be observed continuously with time<sup>(83, 84)</sup> Figure 3.7. Pastes have been examined under dynamic conditions by using the cone-and-plate viscometer with oscillatory shear<sup>(78)</sup>.

### 3.5 EXPERIMENTAL

The flow behaviour of fresh aluminous cement pastes made with both 'Fondu' and 'Secar' cements was examined in this work. Initially a simple penetration test was used to get a general idea about fresh 'Fondu' cement pastes. Later, a coaxial cylinders viscometer with a narrow gap was considered to be the most convenient type of apparatus to give more quantitative information about both cements.

#### 3.5.1 THE PENETRATION TEST

In this test a 0.29 g plastic rod was allowed to sink into the cement paste gradually under its own weight for (5)s; the measured penetration depth in mm was found to represent reasonably the paste condition. In order to study the effect of mixing time on the consistency of fresh 'Fondu' cement pastes, the mixing had to be interrupted to allow the penetration measurements to be made. A different method of measurement was adopted to investigate the thixotropic properties of 'Fondu' cement pastes. Some pastes were mixed for various periods and left undisturbed, the penetration depth being measured over a period of up to 5 mins. Another group of samples was subjected to mix-rest-mix cycles and readings were taken as previously after every mixing period. This method made it possible to follow the reconstruction of the broken structure of the paste.

'Fondu' cement pastes of water-cement ratio of 0.55 were tested using this method, 95g of cement and 52.25 ml of water were mixed in a 100 ml glass beaker rotated mechanically clockwise at 70 rev/min; a spatula was used in a counter rotation manner to ensure thorough mixing, Figure 3.8.

### 3.5.2 THE COAXIAL CYLINDERS VISCOMETER METHOD

The experimental work was carried out with a Ferranti portable viscometer. A low viscosities model was used. The viscometer consists of a rotating smooth outer cylinder driven by a small motor with a second smooth cylinder located coaxially within it. The outer cylinder rotates at the following speeds: 99.5, 148.6, 196.4, 248.2 and 297.3 rev/min. The inner cylinder is free to rotate against a calibrated spring with a pointer to show the angular deflection which is proportional to the viscosity, Figure 3.9. The outer cylinder is 23.75 mm in radius and two inner cylinders of radii 23.00 and 21.50 mm are used. A wide range of shear rates can be achieved by changing the rotating speed and the inner cylinder diameter. The gap widths of 0.75 and 2.25 mm make it possible to obtain shear rates ranging from 110 to  $328 \text{ sec}^{-1}$  and from 318 to  $950 \text{ sec}^{-1}$  respectively. The design of the instrument ensures that the whole of the sample is under uniform shear conditions during measurements, by eliminating the drag on the ends of the inner cylinder. In this particular type of viscometer the apparent viscosity of non-Newtonians is obtained directly, and for a given shear rate, the shear stress at the inner cylinder surface could be calculated from the product of the apparent viscosity and the shear rate.

The Reiner and Rivlin equation of plastic flow in a rotational viscometer was reported by Green<sup>(85)</sup>. The equation may be presented in the following form:

$$\Omega = \frac{T}{4\pi\mu h} \left( \frac{1}{R_b^2} - \frac{1}{R_c^2} \right) - \frac{\tau_0}{\mu} \ln \frac{R_c}{R_b}$$

where  $\Omega$  is the angular speed  
 $h$  is the inner cylinder length  
 $R_b$  is the radius of the inner cylinder  
 $R_c$  is the radius of the outer cylinder  
 $T$  is the torque  
 $\tau_0$  is the yield value  
 $\mu$  is the plastic viscosity

The proof of the equation is given in Appendix 3.

To follow the behaviour of pastes under shear stress, experiments were carried out with the viscometer running at constant speeds. All pastes were mechanically mixed as described in section 3.5.1 for 1.5 min, and were then transferred to a larger beaker to accommodate the viscometer cylinders.

### 3.5.3 THE EFFECT OF TEMPERATURE

The effect of temperature on the consistency of pastes was studied at 13, 17, 20 & 23°C, using both the penetration method and the rotational viscometer. Cement and water containers, glass beakers and viscometer cylinders were stored in an incubator at the desired temperature prior to the preparation of each mix, the temperature of the paste before, during and after mixing being measured (table 3.1).

At an incubation temperature of 17, 20 & 23°C, the temperature of the paste at the point of maximum viscosity did not appreciably differ from the initial value. However, when a temperature of 13°C was used, it was considerably difficult to maintain the mix within reasonable limits from the starting temperature while the mixing was taking place at the room temperature, so that a final temperature of 15°C was attained. The temperature of the mix at its maximum viscosity of 14.5°C is the one which will be employed in any further graphical or numerical manipulation of the data and it reasonably represents the average temperature during the run.

### 3.6 RESULTS AND DISCUSSION

#### 3.6.1 THE EFFECT OF MIXING ON THE CONSISTENCY OF THE PASTES

##### 3.6.1.1 THE PENETRATION TEST RESULTS

The curve in Figure 3.10 is a plot of penetration depth against mixing time at 20°C for 'Fondu' cement pastes of water-cement ratio 0.55. The penetration depth decreased from 43 mm to 14 mm after 4.25 min of mixing and increased again to 36mm after 6 min of continuous mixing. These results indicate considerable changes in the consistency of the paste. It is clear that, under continuous mixing, the viscosity of 'Fondu' cement paste increases as mixing time increases until it reaches a maximum value; this is followed by a gradual decrease in the viscosity of the paste towards a value which is slightly higher than the initial viscosity.

### 3.6.1.2 THE VISCOMETER RESULTS

The effect of shear stress on the consistency of both 'Fondu' and 'Secar' cement pastes was examined at various water-cement ratios. It was observed that 'Secar' cement produces much thicker pastes than those produced by 'Fondu' cement at the same water-cement ratio. Therefore, the range of water-cement ratios used was chosen so that the effect could be investigated within the available range of shearing rates. Curves in Figure 3.11 are plots of the apparent viscosity against time for 'Fondu' cement pastes of water-cement ratio of 0.5, 0.55 & 0.6 at 20°C and shear rate of 109.7 sec<sup>-1</sup>. Secar cement pastes of water-cement ratio of 0.9, 1 & 1.1 produced similar curves at the rate of shear of 163.9 sec<sup>-1</sup>, Figure 3.12. The sudden change in the consistency of the pastes is clear in all curves for both cements at different water-cement ratios. The results show that the lower the water content, the higher the consistency and the shorter the time required to reach the most viscous condition.

It is also apparent from the viscometer results and those obtained earlier from the penetration test that, the mechanical act of mixing causes changes in the interparticle forces. The effect of interparticle forces on the structure of cement pastes is discussed in section 3.2.

### 3.6.2 THE EFFECT OF MIXING EFFICIENCY

The difference in mixing shearing rate would be expected to cause differences in the flow properties of fresh aluminous cement pastes. In order to study this influence, 'Fondu' and 'Secar'

cement pastes of water-cement ratios of 0.55 and 1.00 respectively were subjected to the following rates of shear: 109.7, 163.9, 216.9, 318, 475 and 627.8  $\text{sec}^{-1}$ . All experiments were carried out in the coaxial cylinders viscometer at 20°C.

The use of the viscometer to simulate mixer action is justified by the results obtained in section 3.6.1 which show the curves from penetration tests and viscometer results.

### 3.6.2.1 THE VISCOMETER RESULTS

The results are shown in Figures 3.13 and 3.14. In both 'Fondu' and 'Secar' cement pastes, varying the rate of shear has no significant effect on the time required to reach the point of highest viscosity. This suggests that the process involved in causing stiffening of the pastes is not diffusion controlled and may be the result of a dissolution reaction. The results show also that stiffer pastes are produced at low rates of shear.

### 3.6.3 THE EFFECT OF MIXING ON THE THIXOTROPIC PROPERTIES

#### 3.6.3.1 THE PENETRATION RESULTS

Curves A, B, C and D in Figure 3.15 are plots of penetration depth against time for 'Fondu' cement pastes of water-cement ratio of 0.55 which were subjected to different mixing regimes at 23°C. In all cases, timing was started as soon as the final stage of mixing was completed. Data for a paste which was mixed for two minutes are plotted in curve A from which it is seen that very little change in the structure of the paste took place. This slight decrease in penetration measurements

with time seems to be due to sedimentation, and this behaviour is expected from such a loose structure because the larger particles settle down to form a dense layer which increases the resistance to penetration. Therefore, after 2 minutes of mixing, the condition of the paste was not yet that of a broken thixotropic structure but of a loose structure.

By contrast, pastes which were mixed for 5 or 8 minutes show a considerable tendency to rebuild their broken structure when undisturbed (curves B and C). Such behaviour which is characteristic of thixotropic materials was also recorded for pastes which, after being mixed initially for 5 or 8 minutes, were subjected to one or more cycles of alternate periods of storage undisturbed for 6 minutes followed by mixing for 1.5 minutes (Curve D). The last three curves show that some pastes rebuild their broken structure faster than others, but in all cases, similar structure is retained in just 5 minutes.

### 3.6.3.2 THE VISCOMETER RESULTS

Thixotropic hysteresis loops appear to be difficult to obtain for aluminous cement pastes which are mixed for a time insufficient to make them achieve the point of highest viscosity, because to obtain such curves, the material must be continuously broken down until it reaches the point of highest shearing rate. Aluminous cement pastes in such a condition have no gel-type structure to be broken; on the contrary, they gain this structure during the operation of the viscometer.

In Figure 3.16 is shown the consistency curve for 'Fondu' cement paste of water-cement ratio of 0.6 after being mechanically mixed for 8 minutes. Two inner cylinders and five rotating speeds were used to provide the required range of shear rates. Two loops were obtained, a smaller loop with a top shear rate of  $328 \text{ sec}^{-1}$  and a second loop with a top shear rate of  $791 \text{ sec}^{-1}$ . Such hysteresis loops are typical of thixotropic bodies. Similar thixotropic consistency curves for light chrome-yellow printing ink are shown in Figure 3.17<sup>(86)</sup>.

All these results, therefore, confirm that, under the action of mixing, 'Fondu' cement paste eventually acquires reproducible thixotropic properties, but this condition is not achieved unless mixing is continued beyond the point at which the paste attains its highest consistency.

#### 3.6.4 THE EFFECT OF TEMPERATURE

In this section, all studies were carried out under continuous mixing at four different temperatures: 14.5, 17, 20 and  $23^{\circ}\text{C}$  (see section 3.5.2)

##### 3.6.4.1 THE PENETRATION RESULTS

The results are shown in Figure 3.18. The penetration resistances of 'Fondu' cement pastes of water-cement ratio of 0.55 exhibited generally similar time-dependent variations, but the mixing time required to achieve the maximum consistency tended to increase considerably with decreases in the mixing temperature.

#### 3.6.4.2 THE VISCOMETER RESULTS

'Fondu' cement pastes of water-cement ratio of 0.55 and 0.6 and 'Secar' cement pastes of water-cement ratio of 1.00, were used in these viscometric studies of the influence of temperature on the flow behaviour of aluminous cement pastes. All experiments were performed at a shearing rate of  $163.9 \text{ sec}^{-1}$ . Plots of the apparent viscosity against mixing time given in Figure 3.19 are in agreement with results obtained earlier from the penetration test. The same trend is shown in figures 3.20 and 3.21.

The dependence of the rate of stiffening of the pastes on temperatures suggested that the mechanism of formation of a thixotropic structure might involve a thermally activated process such as the dissolution of certain ions into the electrolyte to promote flocculation of the cement particles.

According to the classic theory of rate processes<sup>(87)</sup> such a change is visualised as involving the passage of thermally activated particles through a transition state represented by the maximum of the free energy curve shown in Figure 3.22 during progress from the initial state to the final state. The thermodynamic driving force for the process is measured by the free energy different ( $\Delta G_{\text{net}}$ ) between the initial and final states and the proportion of particles possessing sufficient thermal energy to surmount the activation free energy barrier ( $\Delta G_a$ ) is given by the Maxwell-Boltzmann distribution law. It is thus proportional to  $\exp(-\Delta G_a/RT)$  where R is the universal gas constant

and T the absolute temperature. This leads to the well known Arrhenius equation  $k = A \exp(-\Delta G_a/RT)$ , where k is the specific reaction rate and A is a constant related to the frequency of the required arrangements of particles. From this it follows that a plot of  $\log_{10}(\text{rate})$  against  $\frac{1}{T}$  for an activated process is a straight line of the slope  $\left(\frac{-\Delta G_a}{2.303R}\right)$ .

With regard to the observed stiffening of aluminous cement pastes, it seems likely that the points of maximum viscosity represent similar structural conditions within the pastes. This implies a similar degree of flocculation in each case which, in turn, may be associated with the attainment of particular levels of dissolved ions in the electrical double-layer region of the electrolyte surrounding the cement grains. Thus assuming the rate of dissolution of the ions concerned to be constant at a given temperature during the period of stiffening, an approximate relative measure of this rate is provided by the reciprocal of the time taken to reach the maximum viscosity  $\left(\frac{1}{t_{\max}}\right)$ . Plots of  $\log_{10}\left(\frac{1}{t_{\max}}\right)$  against  $\left(\frac{1}{T}\right)$  should therefore conform to a linear Arrhenius plot and yield a slope of  $\left(\frac{-\Delta G_a}{2.303R}\right)$  where  $\Delta G_a$  represents the activation free energy of the rate-controlling process.

### 3.6.4.3 THE ACTIVATION ENERGY CALCULATIONS

The data obtained from Figures 3.18, 3.19, 3.20 and 3.21 with the relevant calculations are summarized in Table 3.2. Figures 3.23 and 3.24 show that the plots of  $\log_{10}\left(\frac{1}{t_{\max}}\right)$  against  $\left(\frac{1}{T}\right)$  are straight lines in all cases. The slopes of the lines and the activation energy values are given in Table 3.3. R was taken as 8.32 Joules/mole

The activation energy was calculated from the viscometric results to be  $43 \pm 1$  KJ/mole for both 'Fondu' cement pastes of water-cement ratio of 0.55 and 0.6 and 'Secar' cement pastes of water-cement ratio of 1.00. However, a slightly higher value in the order of  $48 \pm 1$  KJ/mole was obtained from the penetration results for Fondu cement pastes of water-cement ratio 0.55. The lower value was obtained under continuous mixing in the viscometer, but in the case of higher value the mixing was interrupted for performing the penetration tests. For this reason the value of  $43 \pm 1$  KJ/mole is thought to be the more reasonable of the two.

It is apparent, therefore, that changes that take place in aluminous cement pastes under the action of mixing are the result of an activated process. Changing the water-cement ratio and the type of cement do not apparently influence such a process.

### 3.7 CONCLUSIONS

1. The action of mixing causes considerable changes in the consistency of aluminous cement pastes. The consistency increases as mixing time increases until it reaches a maximum value, this is followed by a gradual decrease toward a steady plateau.
2. A thixotropic state could be achieved if the mixing continued beyond the point of highest consistency.
3. Varying the rate of shear has no significant effect on the time required to attain the most viscous condition, but to reach such a state, the mixing time should vary according to the mixing temperature and the water-cement ratio.

4. The development of the thixotropic structure appears to involve a thermally activated process such as the dissolution of counter ions to reduce the zeta potential and cause the particles to flocculate. The activation free energy of the rate controlling process was estimated to be  $43 \pm 1$  KJ/mole for pastes of various water cement ratios and different types of aluminous cement.

5. The similarity in the behaviour of fresh HAC and 'Secar 250' cement pastes indicates that the observed rheological properties are in fact characteristics of calcium aluminate compounds. However, the only difference spotted between the two types of aluminous cement (i.e. the higher consistency of 'Secar 250' cement suspensions) may be attributed to the increased  $Al_2O_3$  content in 'Secar 250' cement. This high proportion of alumina is expected to have a significant role in determining the composition and electrolyte concentration of the solution produced under the action of mixing and hence the consistency and stability of the system.

It seems clear, therefore, that varying the time of mixing could influence the structure of the fresh paste and the way in which the particles are arranged. As a direct result, the pore system of the mature paste is affected as well, because the location of unhydrated particles in the paste determines the sizes of water-filled spaces which are gradually to be filled with solid hydration products. The effects of the properties of fresh aluminous cement pastes on the compressive strength and degree of conversion measurements are considered in the following chapter.

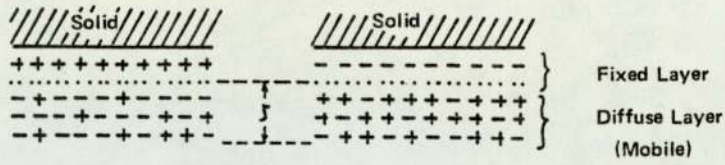


Figure 3.1 Representation of electrical double layer<sup>(70)</sup>

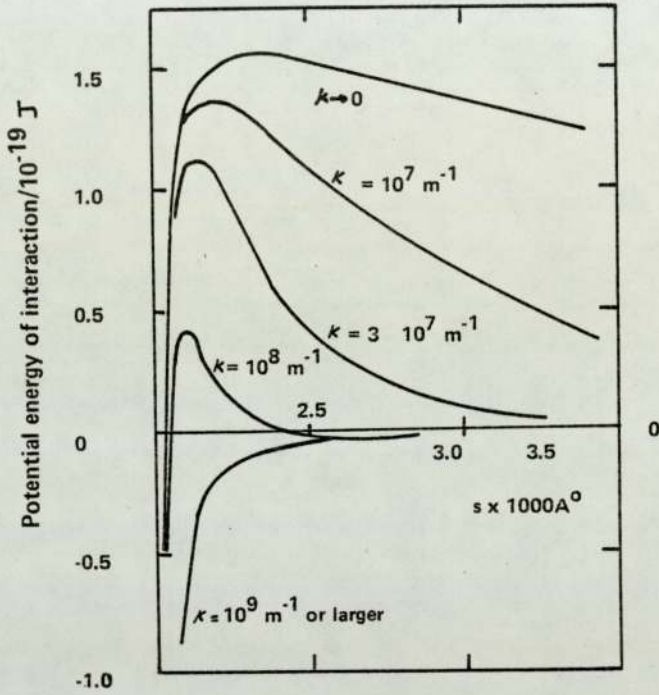


Figure 3.2 The influence of electrolyte concentration  $\kappa$  on the total potential energy of interaction of two spherical particles<sup>(72)</sup>

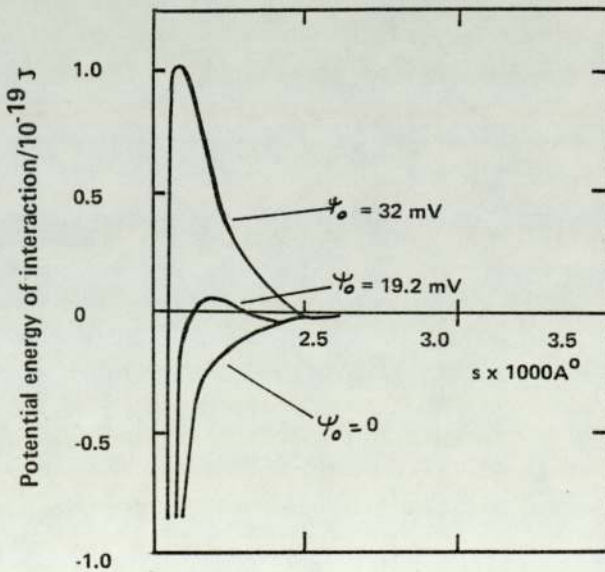


Figure 3.3 The influence of the surface potential  $\psi_0$  on the total potential energy of interaction of two spherical particles<sup>(72)</sup>

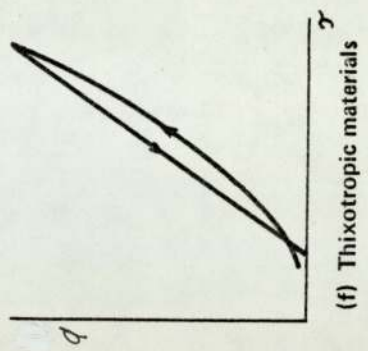
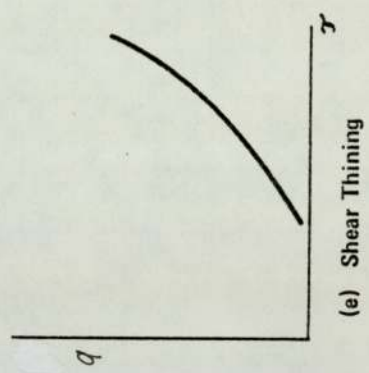
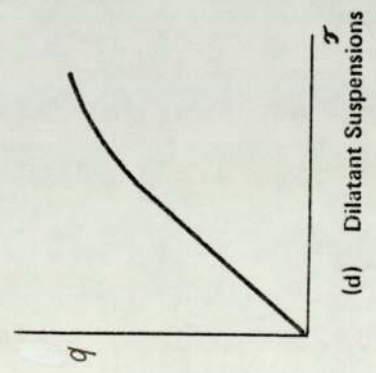
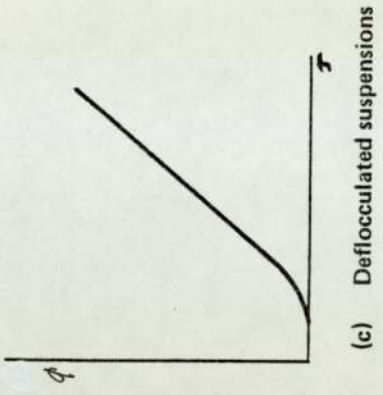
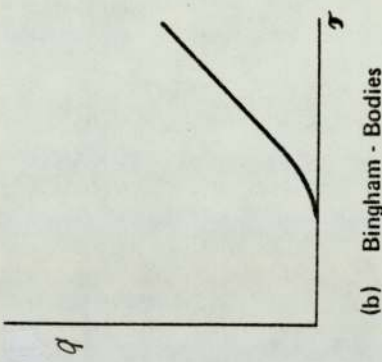
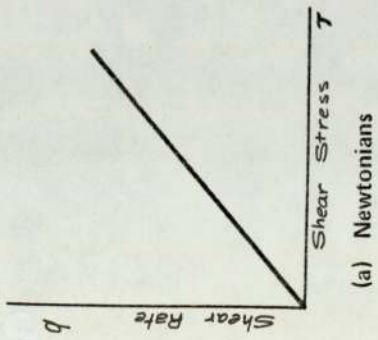


Figure 3.4 Consistency Curves

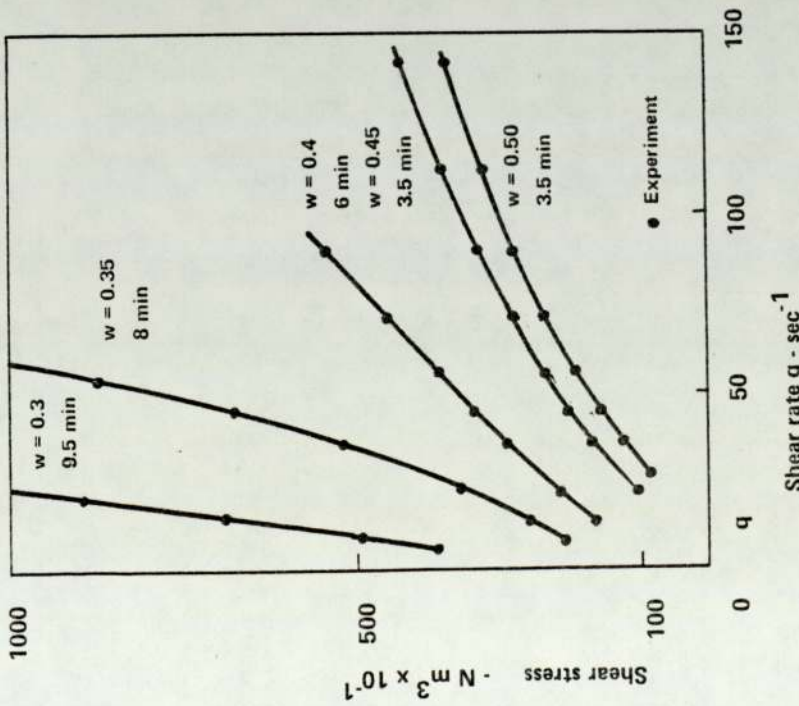


Figure 3.5 Experimental ( $\tau, q$ ) curves for a range of water-cement ratios and a range of mixing times for OPC pastes<sup>(79)</sup>

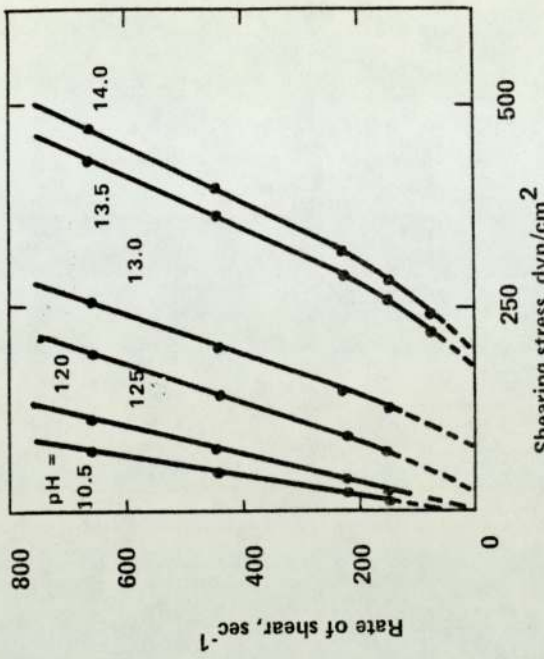


Figure 3.6 Effect of pH on the rheological properties of 43% quartz powder suspension<sup>(81)</sup>

( Axes are reversed of other figures )

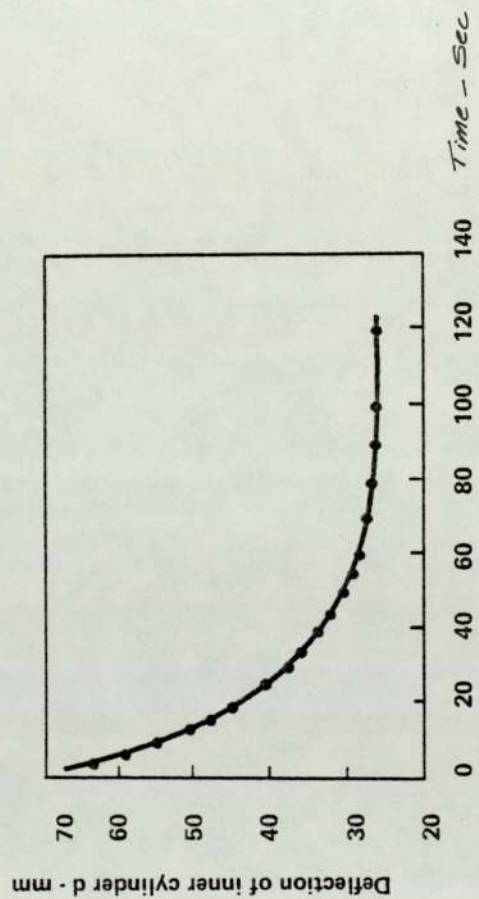


Figure 3.7 Breakdown curve for a 0.30 w/c paste at 386 rev/min (77)

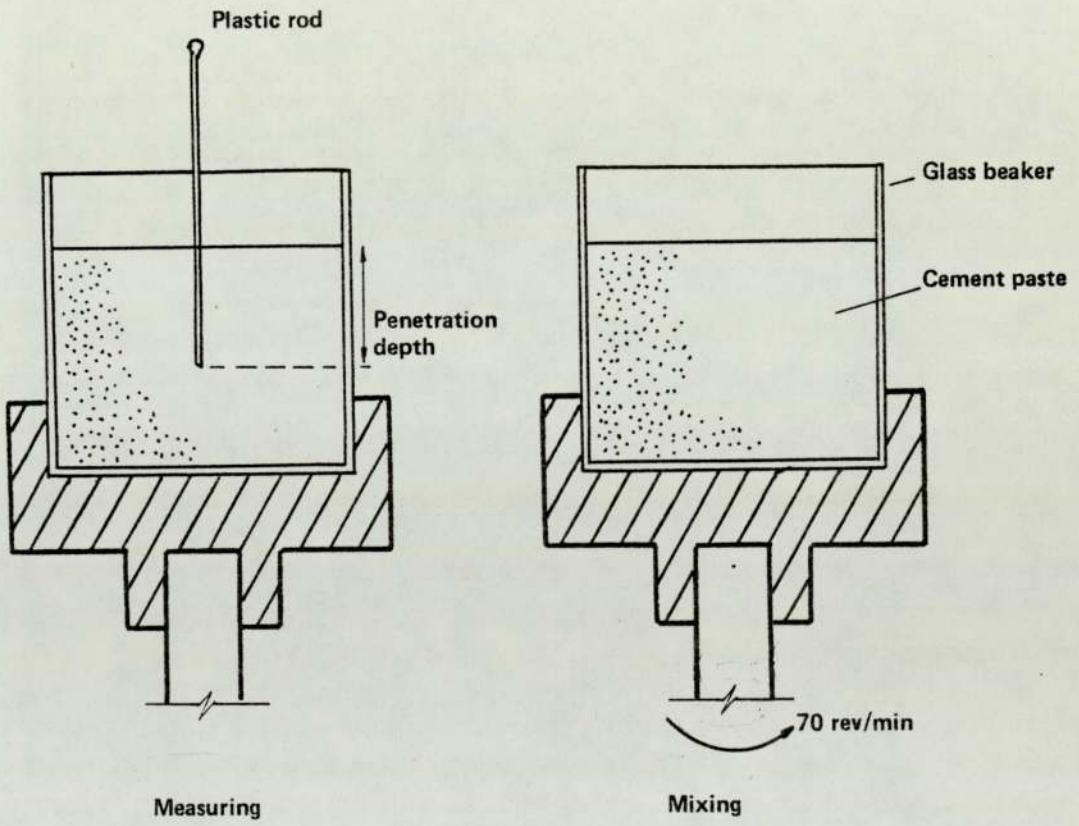


Figure 3.8 The penetration method



Figure 3.9 A Ferranti portable viscometer

Incubation temperature °C	Initial temperature °C	Maximum Consistency temperature °C	Final temperature °C
13	13.5	14.5	15.0
17	17	17	17.5
20	20	20	20
23	23	23	23

Table 3.1 The temperature of the samples during mixing

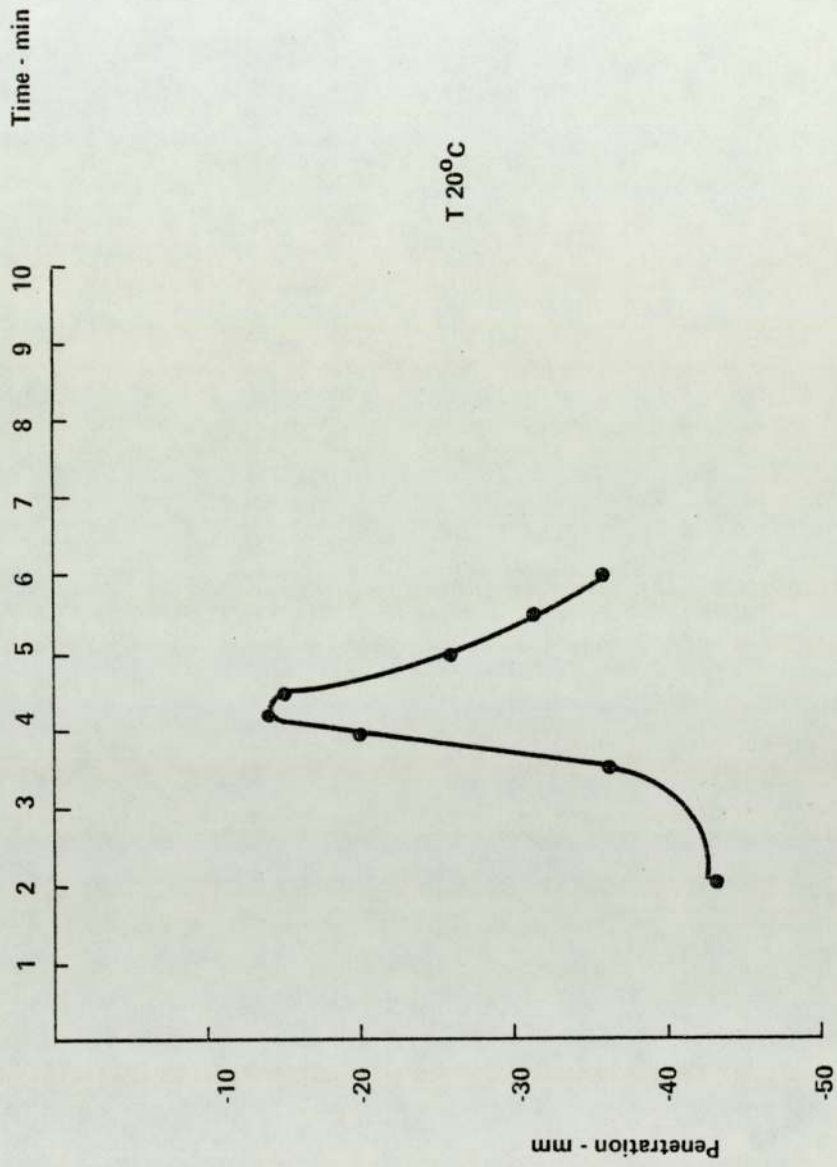


Figure 3.10 Effect of mixing on the consistency of Fondu cement paste of water-cement ratio 0.55

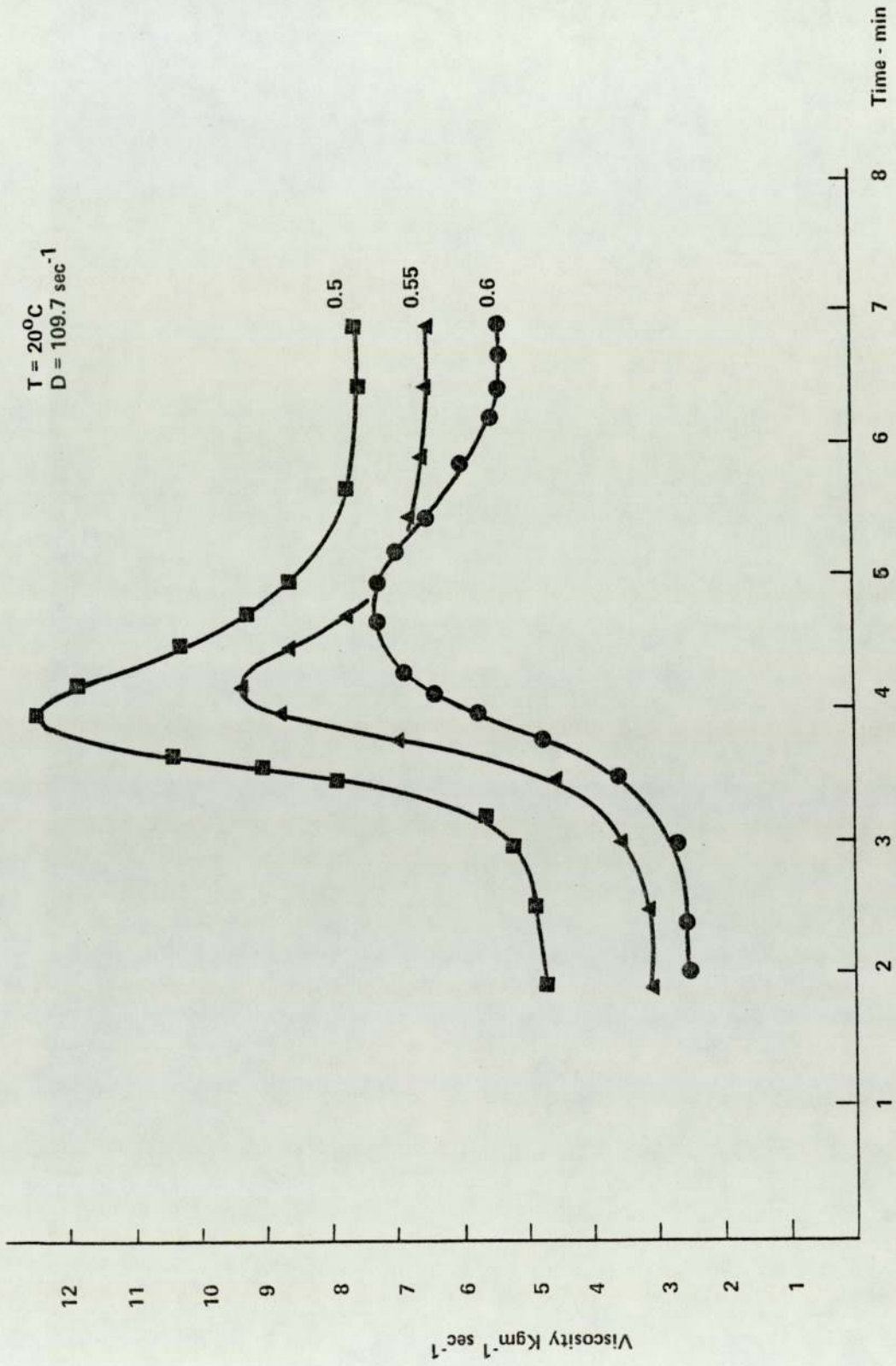


Figure 3.11 Behaviour of Fondu cement pastes under shear stress at various water-cement ratios

T = 20°C  
D = 163.9 sec<sup>-1</sup>

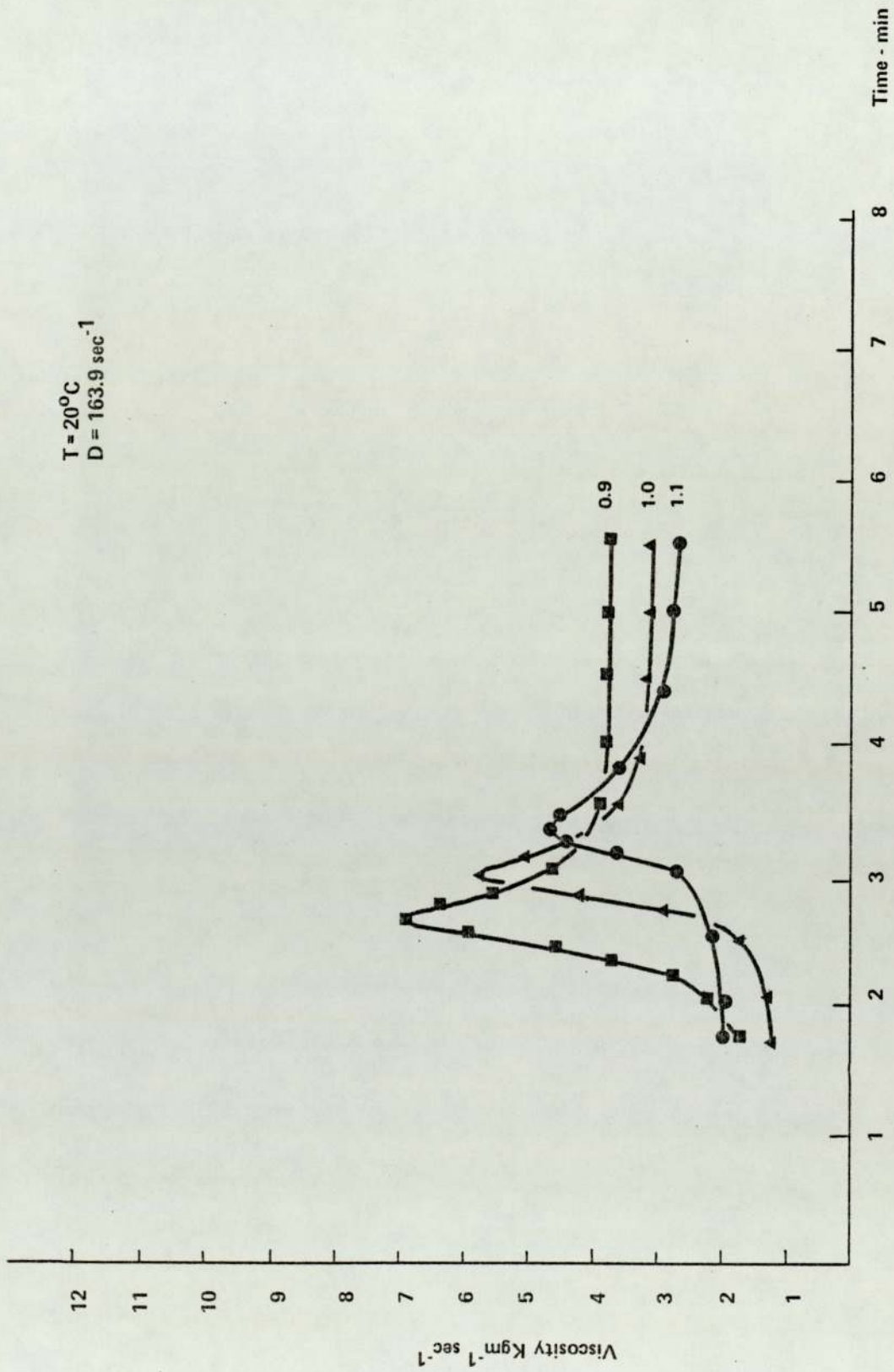


Figure 3.12 Behaviour of Secar cement pastes under shear stress at various water-cement ratios

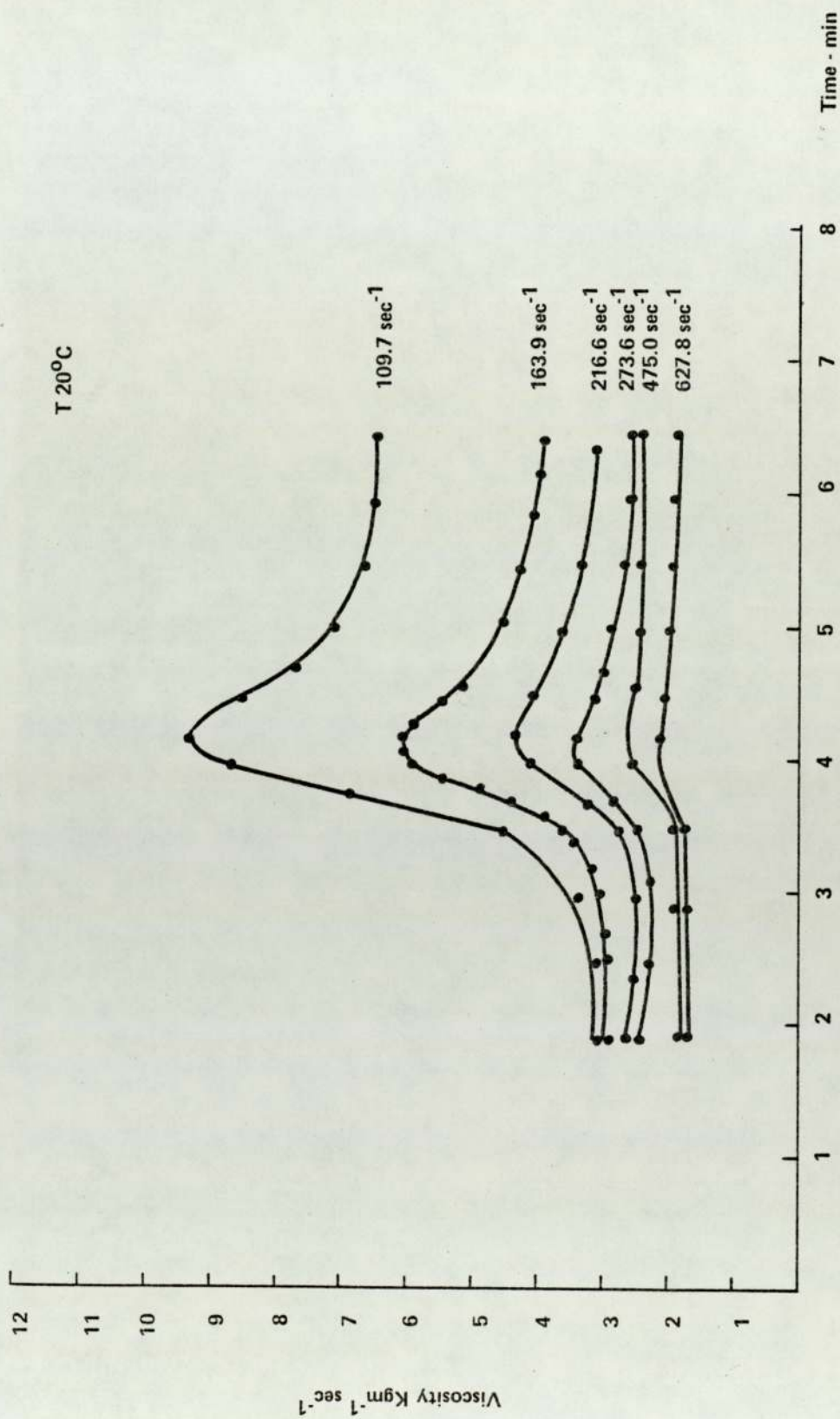


Figure 3.13 Behaviour of Fondu cement pastes of water-cement ratio 0.55 under shear stress at various rates of shear

T 20°C

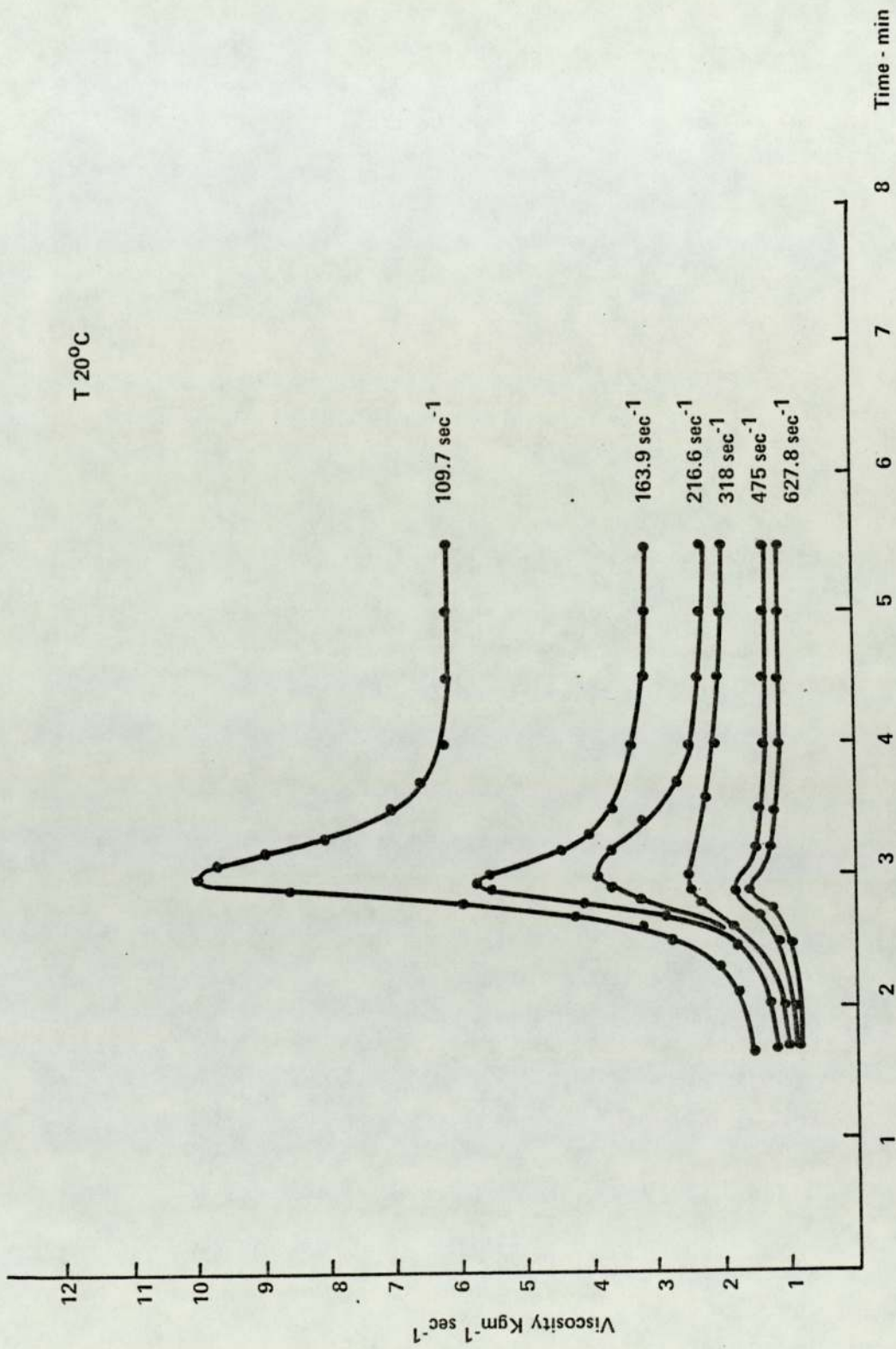


Figure 3.14 Behaviour of Secar cement pastes of water-cement ratio 1.00 under shear stress at various rates of shear

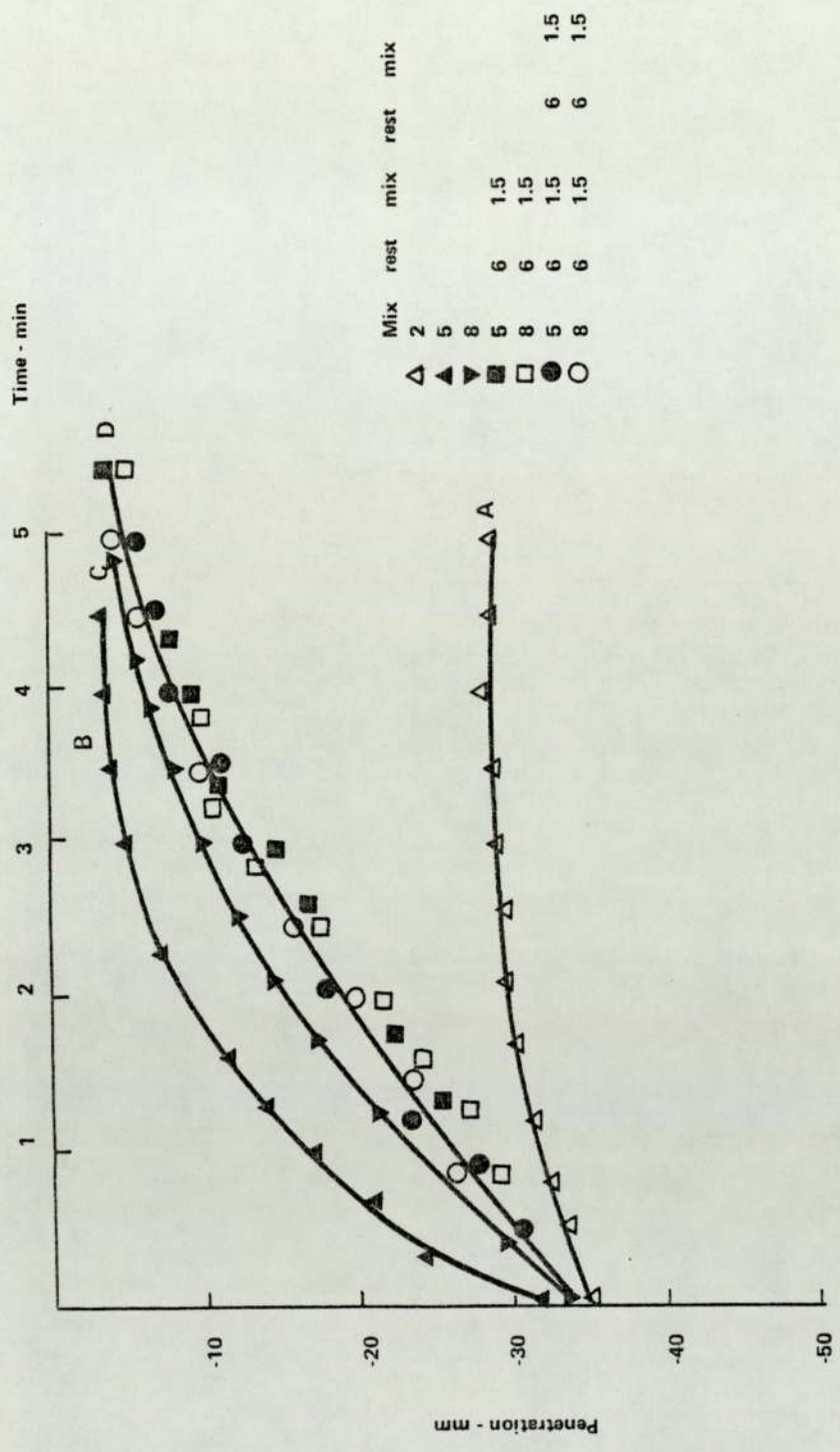


Figure 3.15 Effect of mixing procedure on the structure of Fondu cement pastes of water-cement ratio 0.55

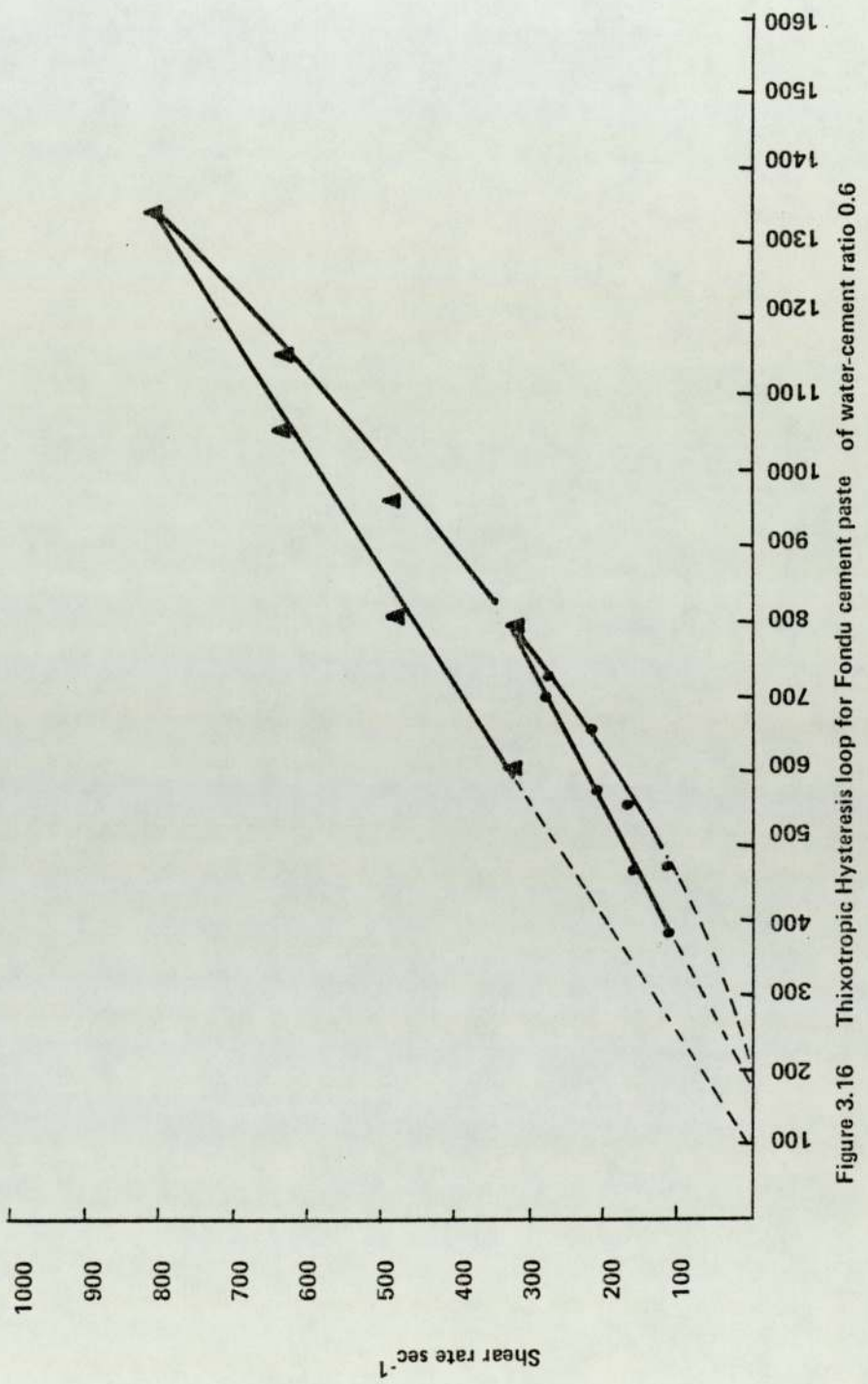


Figure 3.16 Thixotropic Hysteresis loop for Fondur cement paste of water-cement ratio 0.6

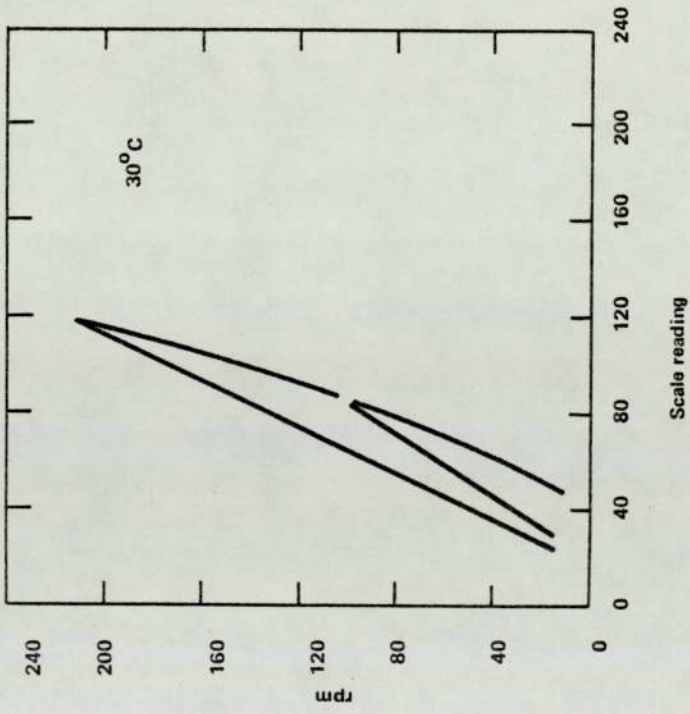


Figure 3.17 Thixotropic Hysteresis loop for light chrome-yellow ink (86)

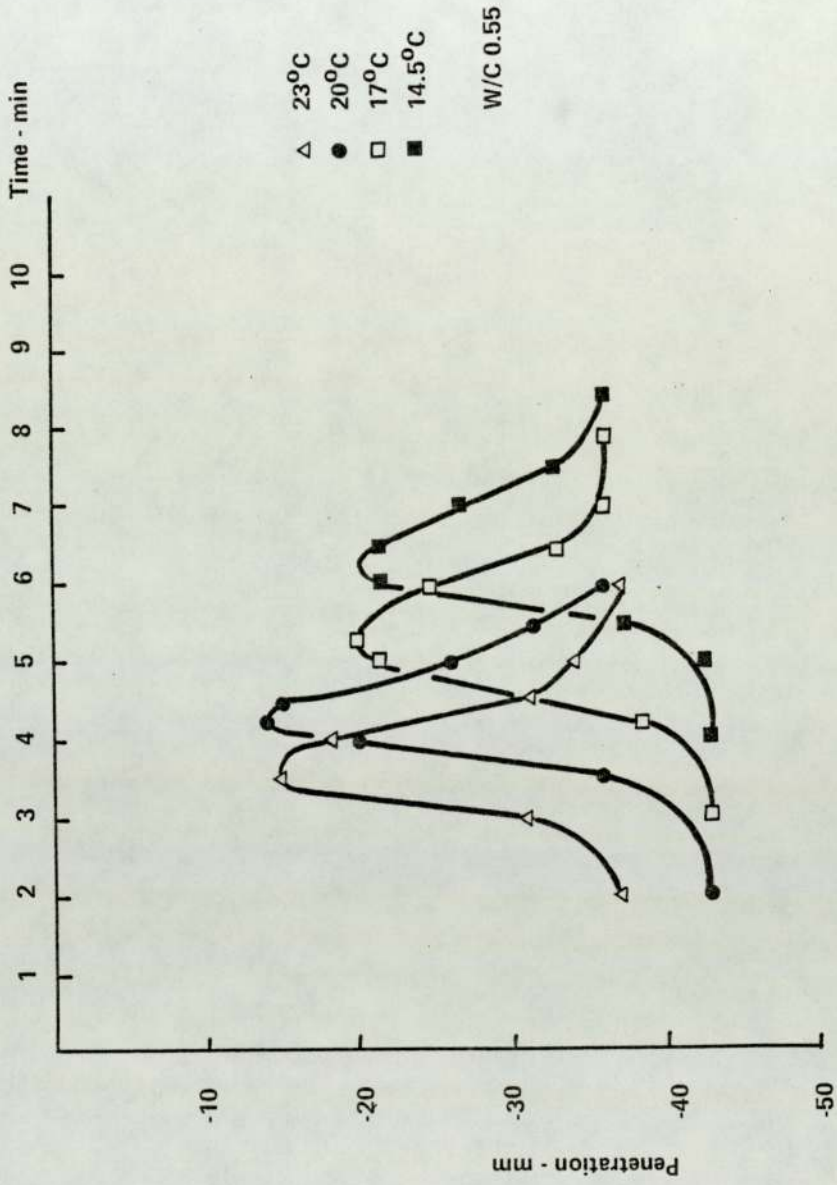


Figure 3.18 Effect of mixing temperature on the consistency of Fondur cement paste (Penetration test)



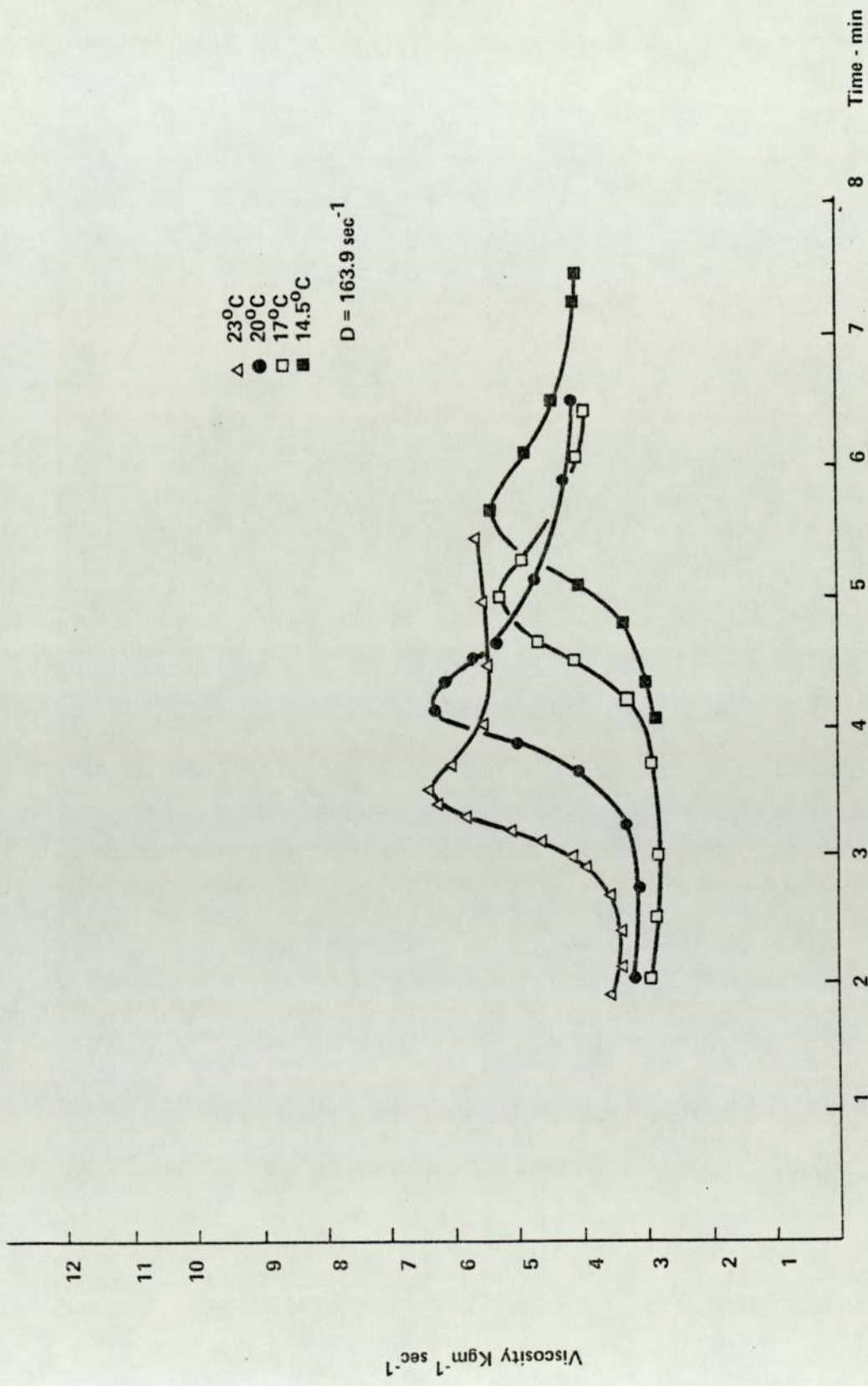


Figure 3.19 Effect of mixing temperature on the consistency of Fondu cement pastes of water-cement ratio 0.55

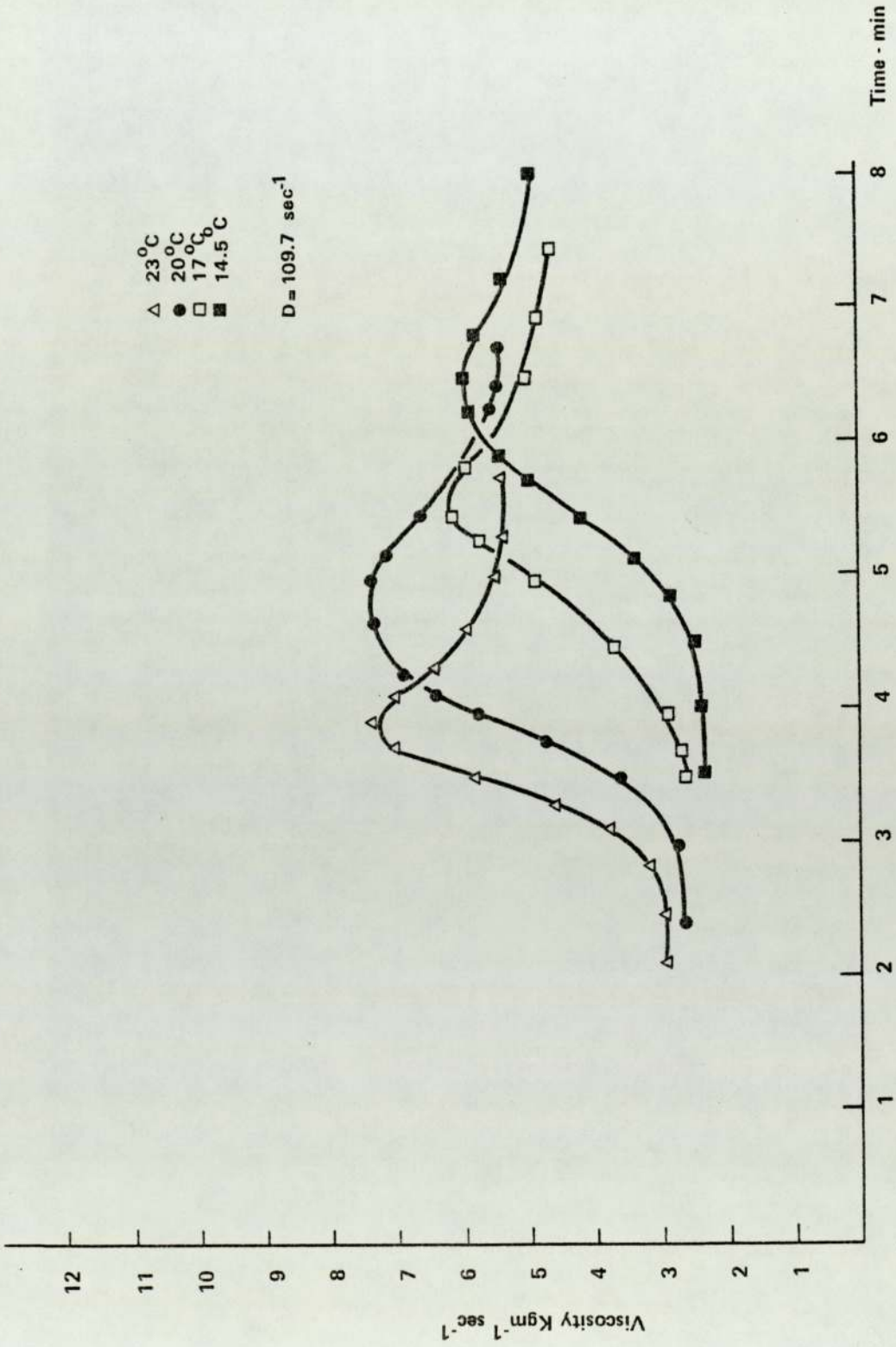


Figure 3.20 Effect of mixing temperature on the consistency of Fondu cement pastes of water-cement ratio 0.6

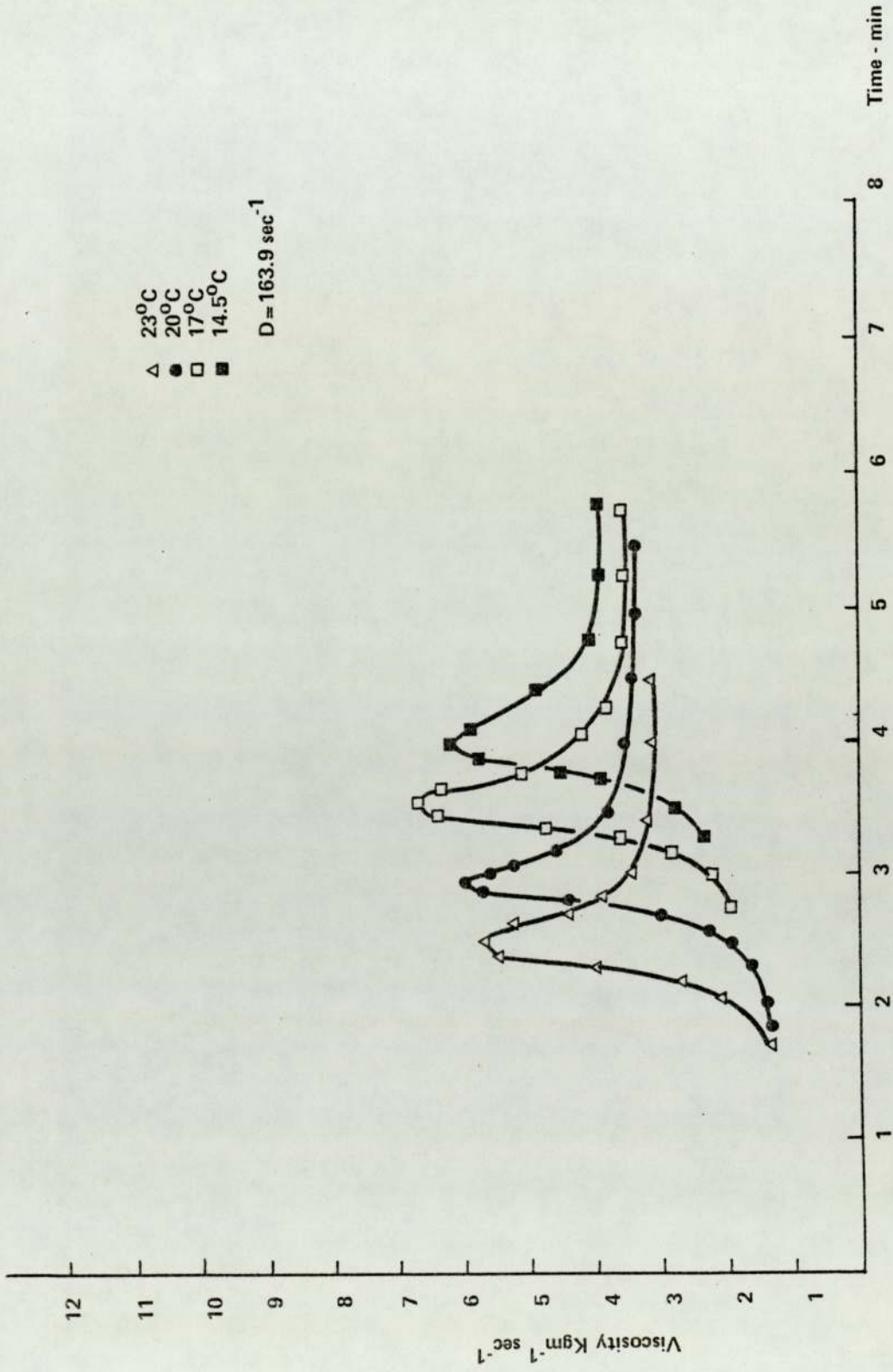
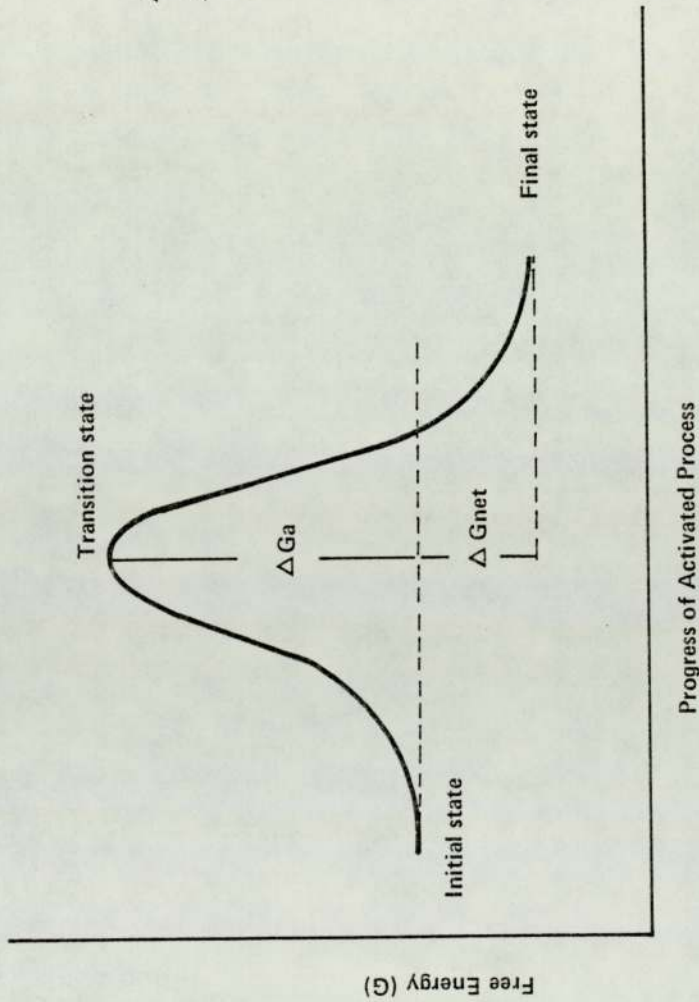


Figure 3.21 Effect of mixing temperature on the consistency of sear cement pastes of water-cement ratio 1.00



$\Delta G_a$  = activation free energy  
 $\Delta G_{net}$  = net free energy change

Figure 3.22 Energy of Activation

Temperature °C	T °C+273.15	$\frac{1}{T} \times 10^{-3}$	Penetration Test		Viscometer					
			Fondu pastes 0.55		Fondu pastes 0.55		Fondu pastes 0.60		Secar pastes 1.00	
			tmax ± -1 min	$\log_{10} \frac{1}{t_{max}}$						
14.5	287.65	3.476	6.25	-.796	5.70	-.756	6.40	-.806	4.00	-.602
17	290.15	3.446	5.25	-.720	5.00	-.699	5.50	-.740	3.55	-.550
20	293.15	3.411	4.25	-.628	4.20	-.623	4.70	-.672	2.95	-.470
23	296.15	3.377	3.50	-.544	3.50	-.544	3.90	-.591	2.50	-.398

Table 3.2 Data of plots of  $\log_{10} \left( \frac{1}{t_{max}} \right)$  against  $\left( \frac{1}{T} \right)$

Slope of the line	Penetration Test		Viscometer	
	Fondu pastes 0.55		Fondu pastes 0.60	
	- 2508		- 2254	
Energy of activation $\Delta G_a$ KJ/mole	$48 \pm 1$		$43 \pm 1$	

Table 3.3 Activation energy values

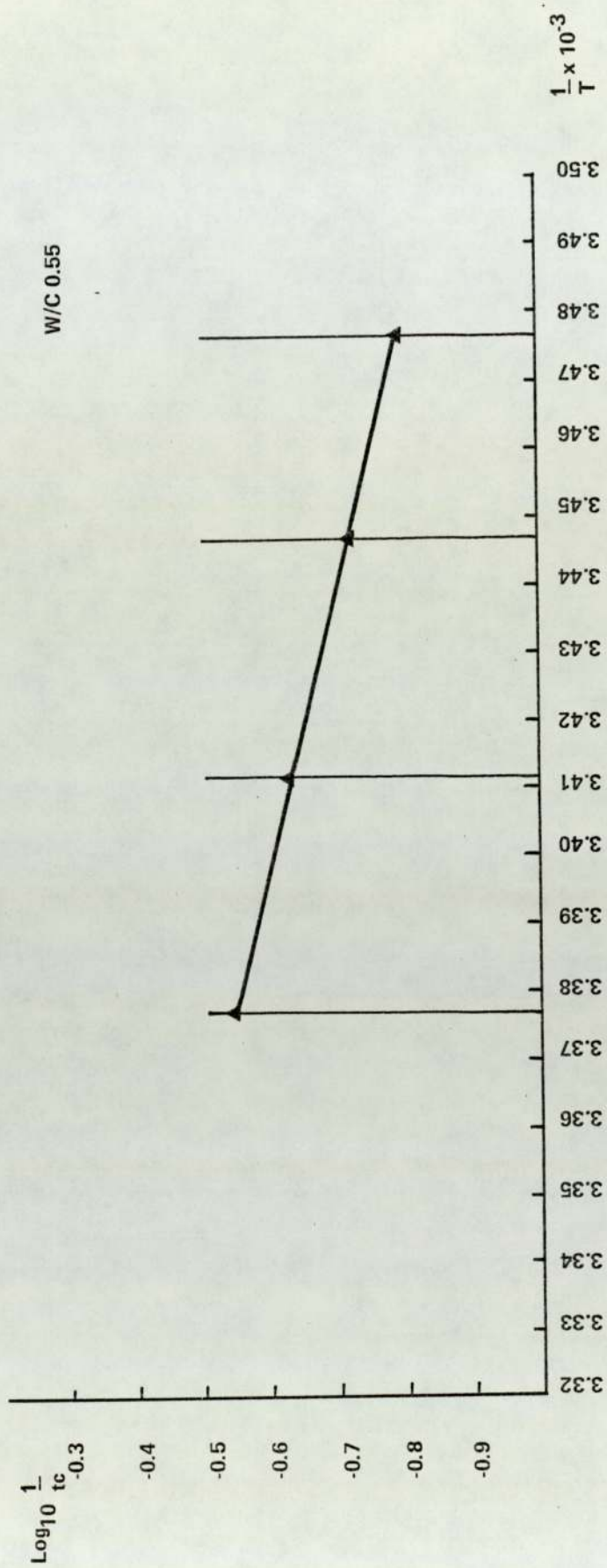


Figure 3.23 Development of Thixotropic structure of Fondu cement pastes (Penetration test results)

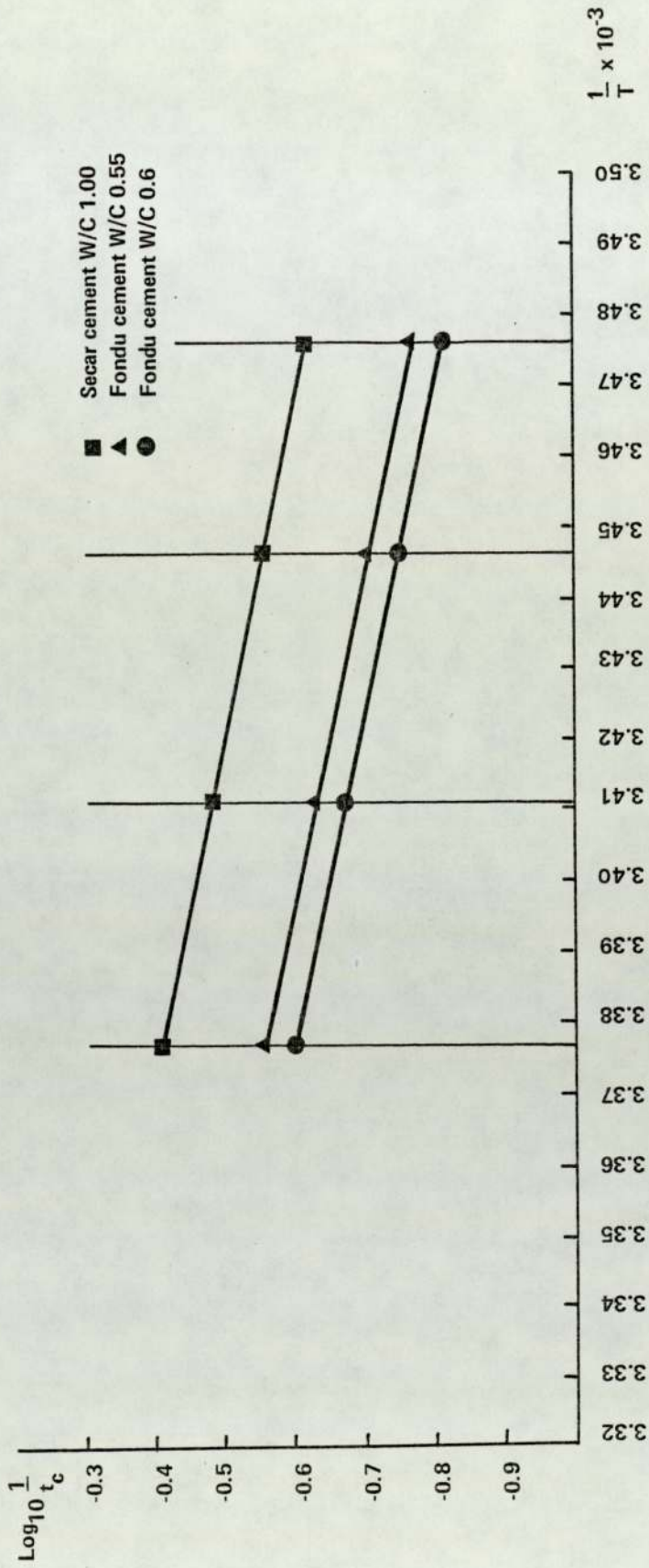


Figure 3.24 Development of Thixotropic structure of Fondu and Secar cement pastes (Viscometric Results)

## CHAPTER 4

### THE EFFECT OF MIXING, CURING AND TESTING CONDITIONS ON SUBSEQUENT RESULTS

In the previous chapter, various unexpected observations which made the study of the rheological characteristics of fresh aluminous cement pastes essential were reported. Before reaching a conclusion in this chapter about the mixing procedure it is necessary to mention other sources of discrepancy which acted jointly with the variations in paste consistency to cause a marked scatter in the measurements.

#### 4.1 HEAT OF HYDRATION

In the early stages of this research, pastes were initially cured at 20°C for 1 day before further exposure to higher temperatures. At the end of the initial curing period, pastes cylinders of water-cement ratio 0.25 were cut, as was explained in section (2.3), and were found to contain large visible cracks. Attempts were made to modify the time of mixing and the vibration variables, but no significant improvement was attained as a result of these changes. However, it was found that if the initial curing was carried out at 10°C instead of 20°C, the specimens developed no cracks. This suggested that these cracks were in fact thermal cracks which resulted from the sudden temperature rise leading to differential expansion within the paste during the hardening period at the higher temperature.

It was thus apparent that if reliable and reproducible specimens are required at such low water-cement ratios then the initial curing should be carried out at 10°C or lower.

To determine the dependence of the effect of heat of hydration on the initial curing temperature, measurements were made of the temperature rise during the first 24 hours at three different curing temperatures. Briefly, two containers were used; the larger was airtight with a hole in its lid through which a mercury thermometer was inserted. A small container was fitted inside the larger one, and a glass tube containing the fresh cement paste was placed in it, Figure 4.1. The space between the two containers was filled with water to saturate the air over the sample. The thermometer was placed vertically through the lid inside the paste after spraying its bulb with a mould release agent and covering it with very thin plastic material. This was meant to separate the thermometer glass from the hardened cement and enable it to be easily removed after the experiment. The readings were taken every 15 minutes and sometimes every 2 minutes depending on the rate of temperature rise. Figure 4.2 shows that the maximum temperature reached was in each case approximately twice the temperature of curing, thus the figures were 16, 39 and 79°C for specimens tested at 10, 22 and 37°C respectively.

Even after standardizing the initial curing temperature at 10°C to avoid thermal cracks in pastes of water-cement ratio 0.25, the temperature rise effect was manifested by pastes at the other water-cement ratios. This was concluded when a comparison was made between the compressive strength of pastes initially cured at 10°C then at higher temperatures. It was expected to obtain one strength-time relationship at each temperature, but, although the specimens were

well prepared, two different curves were observed instead of one. The reason for this discrepancy could be traced to the number of cement cylinders initially cured at a time, since curing (as mentioned in section 2.2) was carried out at 100% R.H. in airtight plastic boxes in which a number of cylindrical specimens were allowed to harden during the first 24 hours at 10°C. This is shown in Figure 4.3 in which curves A and B represent curing at 45°C and 35°C respectively. In each case, lower strength results are associated with the curing of six cylinders than with the curing of four cylinders in a box, and the temperature rise in this closed environment is to be held responsible for this behaviour. Hence for further experiments it was decided to limit the number of paste cylinders cured in a box of dimensions 120 mm x 240 mm x 80 mm to four at a time.

#### 4.2 SURFACE MOISTURE

Another discrepancy in the compressive strength results was found to occur according to whether the cylindrical specimens were immediately tested after cutting or allowed to dry in air before testing. Although the cutting procedure was essential prior to testing (section 2.3), its undesirable effect was the introduction of water in the specimens.

With pastes cured at 100% R.H, the strength was considerably influenced if the measurements were taken without any delay after cutting. However, if the specimens were allowed to dry for at least 4-6 hours, reproducible results were obtained, provided that the other sources of variations were eliminated. In contrast, specimens cured

in water and tested while wet gave consistent results. Table 4.1 summarises the results obtained with pastes of water-cement ratio 0.4 after 2 days of curing at 10°C.

Having considered these two sources of discrepancy, it is now possible to show the part played by the rheological properties of the fresh pastes in the variations of the strength and degree of conversion measurements.

The influence of mixing time on the one day strength at 10°C for a paste of a water-cement ratio of 0.6 is given in table 4.2. After 2 minutes of mixing at 20°C, the cement suspension produced can be considered as a dispersed suspension. Subsequent settlement, which is high, reduces the interparticle distance between cement grains to produce a very dense sediment with relatively high strength. After 7 minutes of mixing, or after complete breakdown of the flocculated structure, pastes were cast easily without settlement due to the sudden build-up as soon as the mixing ceased. This case can be considered as a thixotropic state for which strength results had the minimum scatter and were as expected with this water-cement ratio. Between 2 and 7 minutes of mixing a great deal of variation was obtained due to the formation of the flocculated structure.

The effect of insufficient mixing ( $\approx 2$  min) appeared during the degree of conversion measurements on a cement paste of water-cement ratio 0.6 cured at 45°C for 10 days. The cylindrical specimen was

sliced and samples were analysed representing the top, middle and bottom of the paste. While the top slices were porous, the lower ones were very dense as a direct consequence of sedimentation. Figure 4.4 shows the noticeable difference in the DOC between the specimens from the three regions. When the specimens were sufficiently mixed ( $\approx 7$  min), analysis showed no sign of heterogeneity.

It is, therefore, evident that the ideal sample should be mixed for such a time as to allow it to pass the point of maximum consistency. Due to the build-up of a thixotropic structure as soon as the mixing ceased, it was necessary to mix the specimens individually, rather than mix a large quantity and then distribute it in a number of vials. The proportions of water and cement to make pastes of various water-cement ratios to be used in future experiments are shown in table 4.3

#### 4.3 CONCLUSIONS

The behaviour of HAC pastes is very sensitive to conditions under which mixing and storage are carried out. In order to produce specimens of highly reproducible performance, it is necessary to follow the recommendations outlined below:-

1. The mixing should be carried out on one specimen at a time.
2. Regardless of the mixing temperature, the mixing time should be such that the paste passes the point of maximum consistency.

3. A relatively high mixing temperature is preferable since it shortens the mixing period.
4. Initial curing should be carried out at 10°C or lower.
5. The cylinders should be cured in a large space during hardening so as to avoid overheating.
6. Specimens cured at 100% R.H. should be allowed to dry after cutting for at least 4 hours prior to compressive strength testing, while specimens cured in water should be tested wet.

These conclusions form the basis for the experimental conditions to be employed in subsequent chapters.

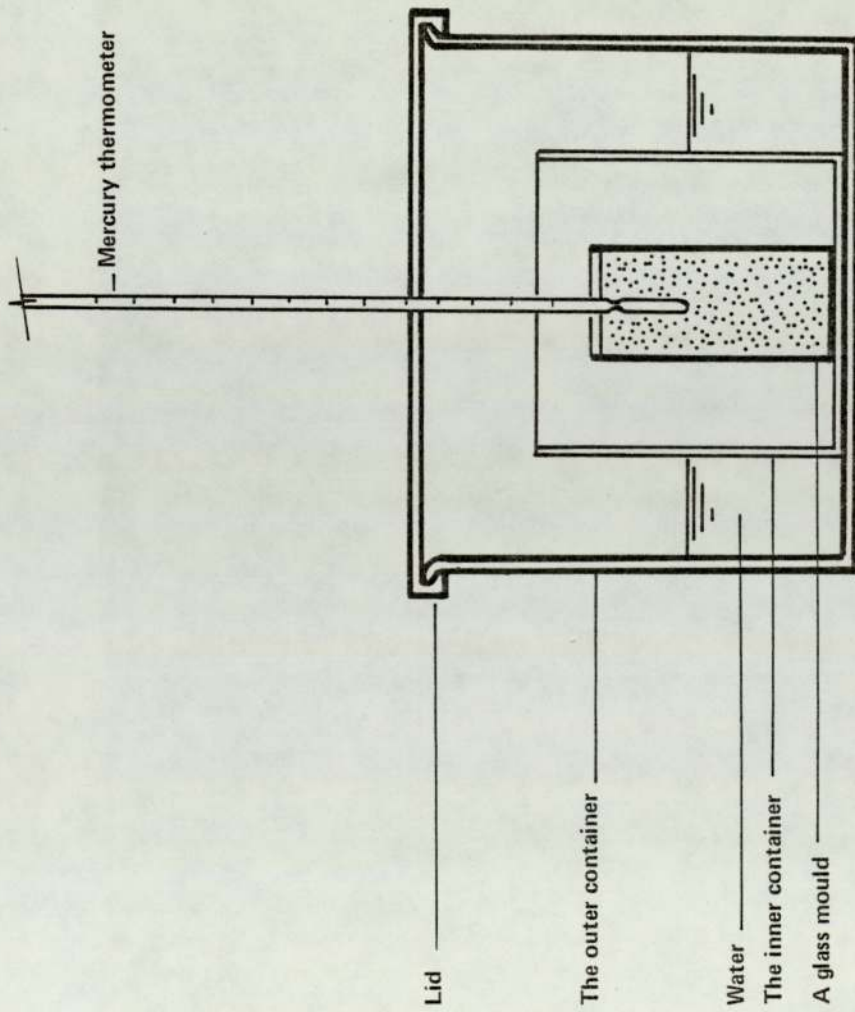


Figure 4.1 A method for monitoring the temperature changes within cement pastes during hardening

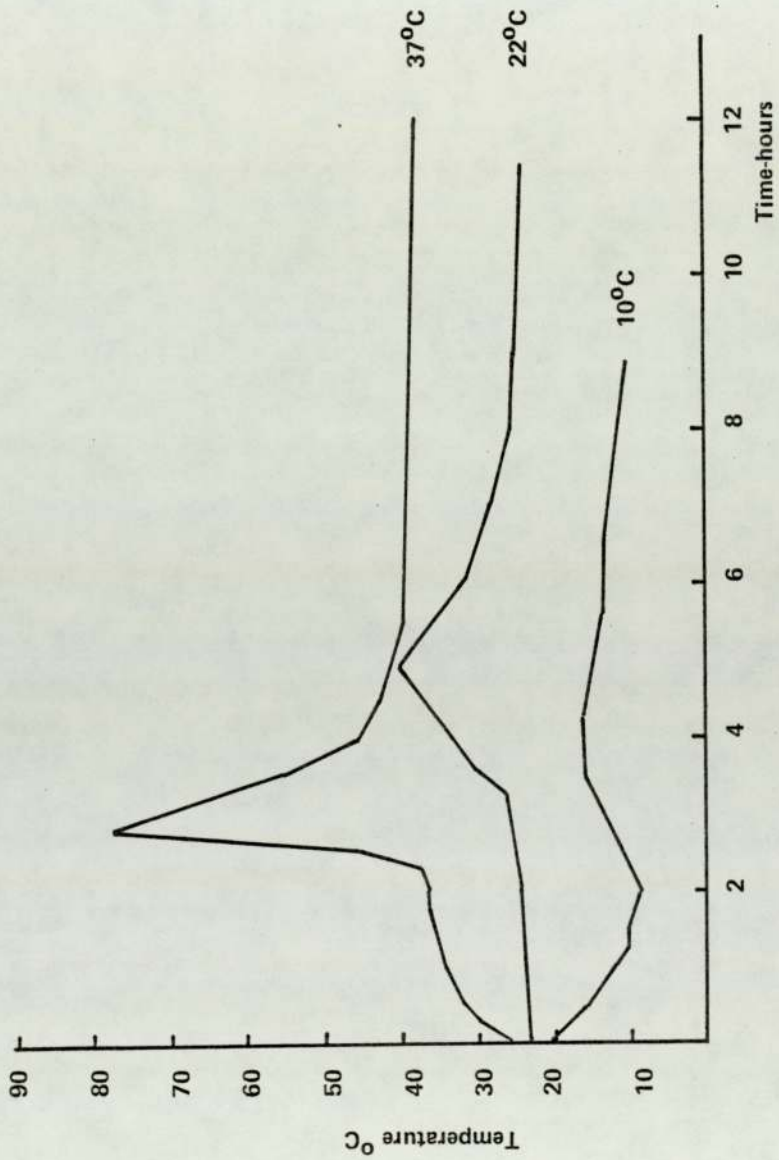


Figure 4.2 Time-temperature curves of HAC pastes during hardening at three different curing temperatures

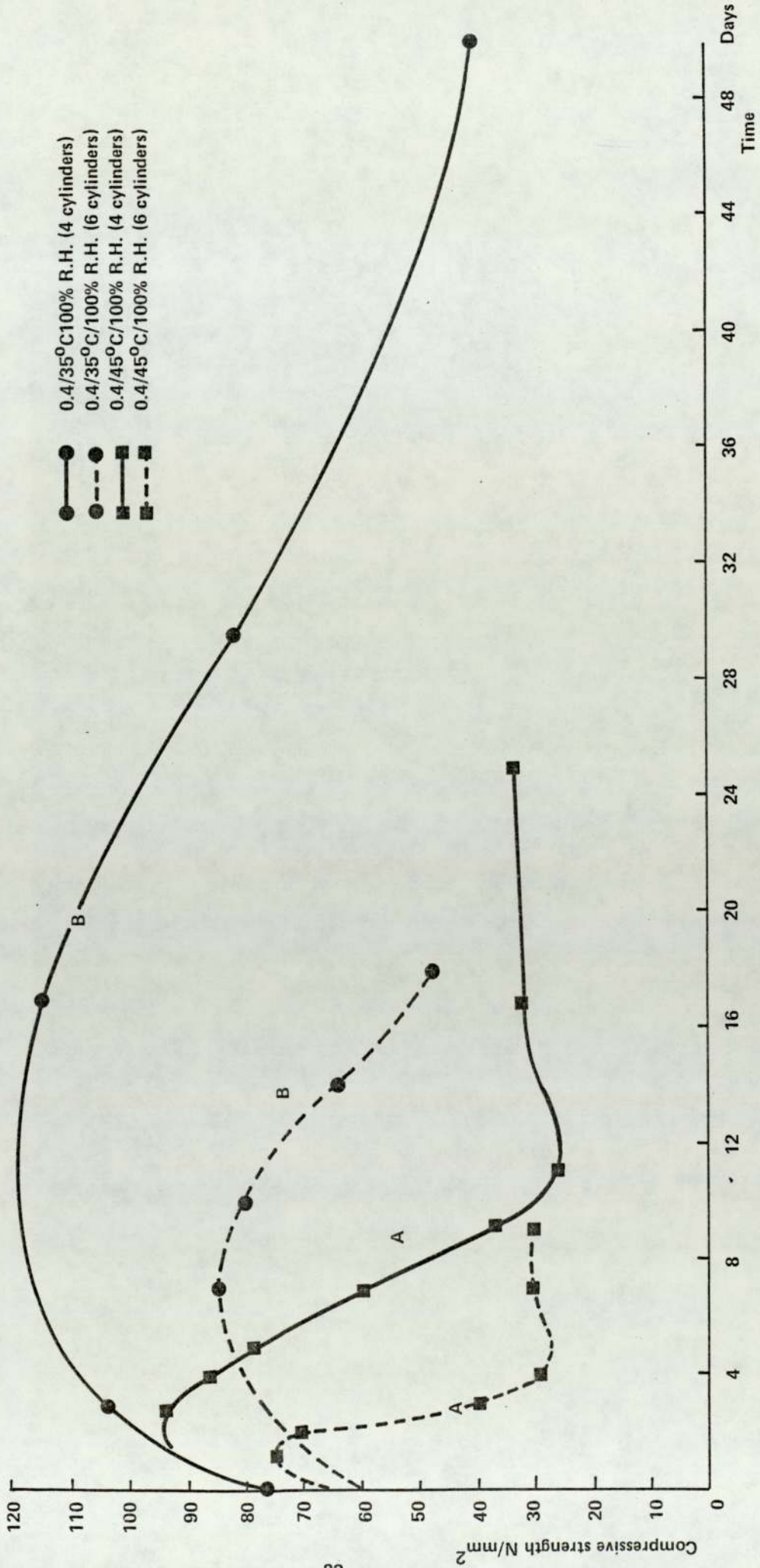


Figure 4.3 The effect of self-generated heat on the strength results

Curing	100% R.H.						Water					
Time of Test	Without drying			4 hr drying			Wet			4 hr drying		
Strength N/mm <sup>2</sup>	54	62	70	78	79	79	77	79	77	85	77	70

Table 4.1 The effect of surface moisture on the strength results

Mixing Time min	Strength N/mm <sup>2</sup>		
2	56	54	55
4.5	44	32	36
7	39	39.4	38.7

Table 4.2 The effect of mixing time on the strength results

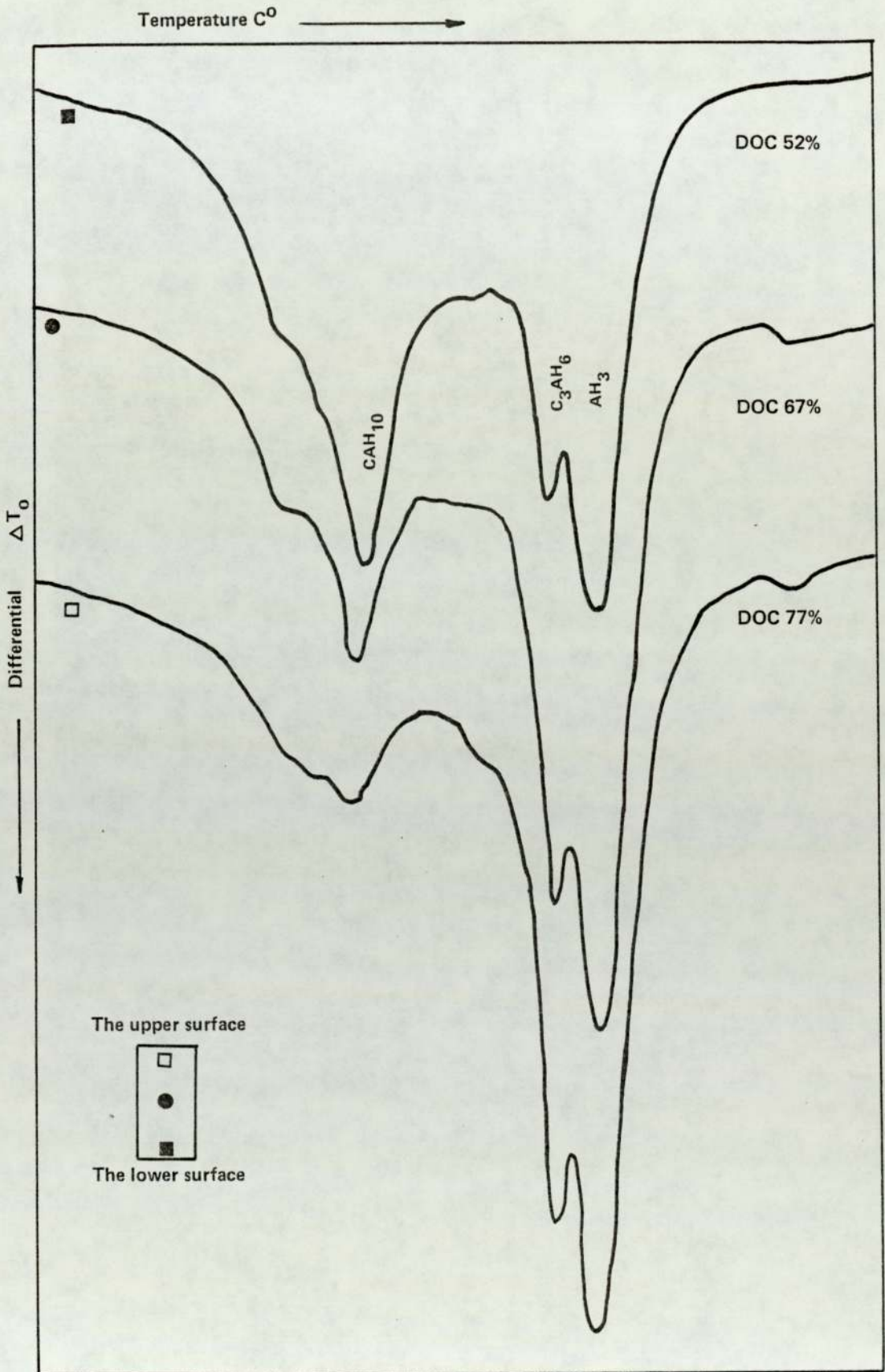


Figure 4.4 The effect of insufficient mixing on DTA measurements

W/C	Weight of Materials g	
	Cement	Water
0.25	40	10
0.4	35	14
0.55	30	16.5

Table 4.3 The proportions of HAC pastes mixes

## CHAPTER 5

### STRENGTH, MINERALOGY, AND PORE STRUCTURE OF SET HIGH ALUMINA CEMENT PASTES

#### 5.1 INTRODUCTION

The general consensus among workers who investigated hardened high alumina cement is that the increase in porosity is the unchallenged physical phenomenon directly responsible for the loss of strength accompanying conversion<sup>(11, 16, 44)</sup>. It must be emphasized, however, that this contention arose from a comparison between the various parameters in the unconverted and fully converted conditions, so that there was no study for the intermediate region between the two extremes in the strength-time curve. Therefore, the objective of this part of the research was to follow the change in the pore structure and the mineralogical properties throughout the conversion process in the hope that a pattern would emerge between strength and those two parameters. Before embarking on the experimental aspects of the study, a review is made of previous contributions relating the strength of various systems to their porosity.

#### 5.2 THE EFFECT OF POROSITY ON THE MECHANICAL PROPERTIES OF CEMENT PASTE AND RELATED MATERIALS

Hardened cement paste, in common with most constructional materials such as polycrystalline ceramics and gypsum, is porous. In general, porous materials tend to have heterogeneous microstructure involving a wide range of particle and pore sizes. The structure of hardened cement paste, which is a dispersion of unhydrated particles

in a matrix of hydration product, is a rather complex and highly variable system. The sizes and distribution of pores in such a structure are a function of water-cement ratio, the degree of hydration, and how the particles are aggregated and linked to each other. The fracture of all porous solids is very sensitive to the microstructure, depending on the presence of microscopic cracks, voids and other microstructural features. Thus to bridge the gap between the physical structure of such materials and the engineering aspects, the nature of the void spaces should be taken into consideration as well as the solid part. The influence of porosity on the mechanical properties of porous solids has been investigated extensively and a number of empirical and semi-empirical expressions, which relate the strength of brittle polycrystalline materials to the total porosity, have been proposed by various investigators.

Ryshkewitch<sup>(88)</sup>, in his investigation of the effect of porosity on the compressive strength of porous sintered alumina and zirconia, found that, the lowest porosity has a significant detrimental effect on the strength of a ceramic body of this type; a body with only 3% porosity is approximately 20% lower in strength than a completely dense body. Figure 5.1 shows that the strength varies logarithmically with a linear change in porosity. Duckworth<sup>(89)</sup>, reporting his work on silicate porcelain, mentioned that bend and torsion tests gave essentially the same strength-porosity characteristic as a compression test and this characteristic agreed favourably with that found by Ryshkewitch. He expressed the semilogarithmic relation in its equation form as:

$$\sigma = \sigma_0 e^{-BP}$$

$\sigma$  = strength of porous body

$\sigma_0$  = strength of nonporous body of the same material

P = Porosity expressed as a fraction

B = an empirical constant (the negative slope of the  
ln  $\sigma$  vs P curve)

Knudsen<sup>(90)</sup>, in reviewing several reports containing data related to the porosity and strength of porous alumina<sup>(91)</sup>, porous sintered compacts of steel<sup>(92)</sup>, and iron<sup>(93)</sup>, found that these data could be reinterpreted and represented by the same general semilogarithmic form noted previously. He also reported that such an expression was more applicable than the expression  $\sigma = \sigma_0 D^m$  proposed earlier by Bal'shin<sup>(94)</sup> where

D = relative density;  $D = (1-P)$

m = an empirical constant

Spriggs<sup>(95)</sup> and Knudsen<sup>(96)</sup> suggested that the Young's modulus (E) and shear modulus (G) of polycrystalline refractory materials, particularly alumina, are exponentially dependent on porosity; the expressions for the effect of porosity on Young's modulus and shear modulus being of the type

$$E = E_0 e^{-BP}$$

$$G = G_0 e^{-BP}$$

where  $E_0$  &  $G_0$  are the Young's modulus and the shear modulus of non porous body of the same material

P = Porosity expressed as a fraction

B = an empirical constant

Data for porous magnesium oxide were compiled and were found to follow the same type of relation as those for alumina<sup>(97)</sup>. Trostel<sup>(98)</sup> observed that bodies composed of fine grains maintain strength to a higher porosity than materials made of large grains.

Spriggs<sup>(99)</sup> extended his original exponential equation

$$E = E_o e^{-BP}$$

to include the separate effects of open and closed porosity.

He proposed an equation of the type

$$E = E_o e^{-B_o P_o} - B_c P_c$$

where

$P_o$  &  $P_c$  = volume fraction of open and closed porosity respectively

$B_o$  &  $B_c$  = empirical constants

The simple empirical expression for the porosity dependence of the elastic moduli was criticized by Hasselman<sup>(100)</sup> because it does not satisfy the boundary conditions of  $E = 0$  for  $P = 1$ . He then proposed a general equation based on the expression presented by Hashin<sup>(101)</sup> to be used to express the porosity dependence of the elastic moduli, including Young's modulus, of such materials.

$$E = E_o \left( 1 + \frac{AP}{1-(A+1)P} \right) \quad A \text{ Constant}$$

Piatacik and Hasselman<sup>(102)</sup> modified this equation to include also the separate effect of open and closed pores; the modified form became

$$E = E_o \left( 1 - \frac{A_o P_o}{1+(A_o-1)P_t} - \frac{A_c P_c}{1+(A_c-1)P_t} \right)$$

where  $A_o$  &  $A_c$  = numerical constants  
 $P_o$  = volume fraction of open porosity  
 $P_c$  = volume fraction of closed porosity  
 $P_t$  =  $P_o + P_c$  = total porosity

Brown, Biddulph & Wilcox<sup>(103)</sup> demonstrated from a purely theoretical point of view that not only the total porosity but the pore shape and orientation are important factors affecting the strength. Knudsen<sup>(90)</sup> proposed that the relation of the strength ( $\sigma$ ) of brittle polycrystalline specimens to porosity ( $p$ ) and grain size ( $G$ ) can be approximated by the equation

$$\sigma = KG^{-a}e^{-bP} \quad \text{where } a \text{ \& } b \text{ are constants.}$$

However, data for the microhardness of porous samples of halite and selenite fitted well the simple exponential expression proposed by Duckworth in 1953<sup>(104)</sup>. Soroka and Sereda<sup>(105)</sup> found that, for porous polycrystalline solids such as gypsum, hardness and modulus of elasticity are related to porosity and the relation can be described empirically by the same expression. In this work, which helped to elucidate the nature of the interparticle bond, the gypsum paste preparations were varied and the difference in the behaviour of the various systems indicated that intergrowth and interlocking of crystals significantly affect the mechanical properties; at the same porosity, hardness and modulus of elasticity values were much lower in systems in which crystal intergrowth is not likely. Similarly, the same authors studied the structure of cement paste and showed that the mechanical properties vary logarithmically with a linear change in porosity, Figure 5.2. In contrast to the gypsum system, however, strength of ordinary portland cement paste is mainly derived from a

particular type of interparticle bond, and this bond was suggested to arise from solid to solid contact resulting from the bringing together of surfaces<sup>(29)</sup>.

Feldman and Beaudoin<sup>(106)</sup> studied several hydrated portland cement systems over a wide range of porosities and concluded that porosity is a major factor in controlling strength of such systems. Morphology, which involves crystal bonding and product density, is also important; poorly aligned and ill-crystallised materials have the best bonding properties, whereas bonding of well-crystallised material is very poor at high porosity.

Jambor<sup>(107)</sup> found that the relationship between compressive strength and porosity of ordinary portland cement varies according to the pastes being compared. Thus samples with constant water-cement ratios but with different curing periods exhibit a relation unlike the one shown by pastes with different water-cement ratio but with the same time of curing. At low water-cement ratios, strength increases without considerable decrease in the total porosity but depends mainly on the composition and properties of binding hydration products. In pastes with high water-cement ratio, strength development is chiefly dependent on reducing the capillary pores.

Cottin and Reif<sup>(44)</sup>, in their study of unconverted and fully converted high alumina cement pastes, concluded that the variations in compressive strength and penetration resistance are exclusively explained by variations in porosity. The latter is itself

a function of the water-cement ratio, the relation being of the simple exponential form reported earlier.

This part of the review shows clearly the effect of the total porosity on the mechanical properties of different solid systems. From this point onwards, attention will be focused on the effect of individual pore size on these characteristics.

### 5.3 THE INFLUENCE OF PORE SIZE ON STRENGTH

Hasselmann and Fulrath<sup>(108)</sup>, in their study on two-phase brittle-matrix ceramic composites postulated that the effect of pores, which may act as stress concentrators, on strength is governed by the relative size of the Griffith flaw and the volume of material over which the stress concentrations act. On this basis, the effect of porosity on strength can be divided into three distinct classes of behaviour,

Figure 5.3:-

1. When the pore size is much larger than the flaw (case I), under loading conditions flaws located near pores will be entirely within a stress concentration field. These flaws will nucleate fracture at average stress equal to the zero-porosity strength divided by the maximum value of the stress concentration factor. A precipitous decrease in strength would be expected with the introduction of the first pore into the loaded area.
2. As the size of the pore approaches the flaw size (case II), the flaws will not be entirely located in areas of high strength concentration.

A smaller decrease in strength would be expected than for (case I), but the decrease would still be precipitous.

3. When the pore size is much smaller than the flaw size (case III), the stress concentration field will no longer be large enough to affect the strength of the material appreciably. Only a monotonic decrease in strength with porosity should be observed with no precipitous drop. The amount of material available to carry the load will determine the strength in this case.

The hypothesis of Hasselman and Fulrath has been applied by Williamson<sup>(55)</sup> to study the fracture of hardened ordinary portland cement paste. He considered the origin of the weakness to lie in the spaces which have not been filled by hydration products and thus act as stress concentrators to cause failure to occur along the boundaries between various microstructural features. The stress-concentration approach has also been applied by Kayyali, Page and Ritchie<sup>(62)</sup> to explain the difference in strength between two pastes of similar total porosity but of different pore size distribution. Large crystals of portlandite surrounded by voids were considered responsible for loss of strength of the weaker paste.

The significance of the pore size distribution as seen from the last part of the review makes it the main aspect of the pore structure to be studied.

## 5.4 EXPERIMENTAL

In this investigation, two sets of experiments were carried out. The first set was meant to study the system in the unconverted and fully converted cases while the second set was intended to follow the strength-time curve.

In the primary set, the factors studied were the pore size distribution and the total porosity, which was evaluated by determination of the apparent density of the hydrated pastes and the specific gravity of the solids. Pastes of three water-cement ratios, viz. 0.25, 0.4 and 0.55, were tested after 1 day of curing at 10°C and after being fully converted at 45°C.

In the secondary set, the mineralogical changes and the variations in the pore size distribution were studied under different conditions of water-cement ratio and curing regime. The basic set of parameters was the water-cement ratio of 0.4 and exposure at 45°C and 100% R.H. after 1 day curing at 10°C. Three other sets were generated by changing one parameter at a time while keeping the others constant. Thus the three other sets were: 0.4/45°C/water curing, 0.4/35°C/100% R.H, and 0.55/45°C/100% R.H.

The experimental techniques used throughout this section were fully explained in chapter 2. The mixing procedure was covered in chapter 4, together with precautions concerning curing and testing conditions. *It should also be mentioned that the standard deviation of the strength results was not greater than 1.00 N/mm<sup>2</sup> for any of the sets of three specimens tested.*

## 5.5 RESULTS AND DISCUSSION

### 5.5.1 FIRST SET

The strength results of this set of experiments are presented as a function of water-cement ratio in Figure 5.4 which indicates the significant role of the water-cement ratio on the loss of strength. In Figure 5.5 the compressive strength of the fully converted cylinders expressed as a percentage of 1-day strength at 10°C are plotted versus water-cement ratio. The curve documents this role quantitatively; losses of 57% and 78% were observed with water-cement ratios 0.4 and 0.55 respectively, while no significant change took place at the water-cement ratio of 0.25. The results are thus in reasonable accord with earlier work on the loss of strength of fully converted HAC pastes<sup>(11, 44)</sup>.

The total porosity data presented in Figure 5.6 as a function of water-cement ratio, are calculated from specific gravity and apparent density measurements summarized in tables 5.1 and 5.2. This total porosity-water-cement ratio relationship is confirmed by the cumulative pore size distributions in Figures 5.7 and 5.8, which correspond to unconverted and fully converted pastes of various water-cement ratios. Total porosity data obtained by both methods are included in table 5.3, and a specimen calculation of all porosity calculations is given in Appendix I. The change from the concave or linear shape of the pore size distribution curves in Figure 5.7 to the convex curves of Figure 5.8 indicates a considerable increase in number of pores in the size range 0.3-2.2  $\mu\text{m}$ . It is also possible to notice the increase in the value of the volume-average pore diameter as a direct consequence of conversion. For example, the figure, which corresponds to 50% of the intruded porosity, increased from 0.04  $\mu\text{m}$  to 1.3  $\mu\text{m}$  and from 0.09  $\mu\text{m}$  to 0.6  $\mu\text{m}$  for pastes of water-cement ratios of 0.55 and 0.4 respectively. Moreover, the curves indicate that the 'threshold diameter', defined by Winslow and

Diamond<sup>(48)</sup> as a diameter above which there is comparatively little intrusion into the paste, and immediately below which the greatest portion of the intrusion commences, was displayed in all cases but was more apparent after conversion than before.

The method of presenting the pore size distribution in Figures 5.9, 5.10 and 5.11 clearly shows the extent of the change of porosity with conversion, the effect being quite noticeable at higher water-cement ratios. In contrast to the others, the paste of water-cement ratio of 0.25 in Figure 5.9 shows no significant change in the pore structure. This trend agrees favourably with that of the strength results which are plotted as a function of total porosity in Figure 5.12. Although the graph displays a semi-logarithmic relation between the compressive strength and the total porosity of unconverted pastes, the data obtained for converted pastes investigated do not fit a similar relationship. Likewise, a departure from linearity could be obtained by plotting Cottin's<sup>(44)</sup> compressive strength data of fully converted pastes on a logarithmic scale as a function of total porosity, Figure 5.13. This pattern reflects the dependence of the binding forces within the converted pastes on the water-cement ratio.

It can be concluded from the results already presented that the compressive strength of unconverted set high alumina cement pastes is exponentially dependent on total porosity, but data for converted pastes exhibit a departure from this semilogarithmic relation. The results also indicate that the change in the pore size distribution is better manifested at relatively high water-cement ratios ( $\geq 0.4$ ), with a noticeable increase in number of pores in the size range 0.3-2.2  $\mu$ m and

in the value of the volume average pore diameter. It is also shown that the pore size measurements carried out at pressures up to 50,000 psi ( $351 \text{ N/mm}^2$ ) are quite sufficient for reasonably accurate estimation of the total porosity. This view has also been expressed by Cottin<sup>(44)</sup> in his work on set HAC pastes.

### 5.5.2 SECOND SET

The results of this set are summarized in Figures 5.14 to 5.22. The strength-time curves shown in Figure 5.14 for the various conditions investigated are typical of the behaviour of HAC. Referring to curve 2 of Figure 5.14, it is seen that decreasing the curing temperature to  $35^\circ\text{C}$  resulted in a considerable reduction in the rate at which the pastes lost their strength. A noticeable feature of this curve is that the maximum strength is about 1.2 times that of the material of curve 1. When the temperature was kept at the original level of  $45^\circ\text{C}$  the strength of the material immersed in water (curve 3) was better at early stages than that of curve 1, but became worse after full conversion was attained. Increasing the water-cement ratio to 0.55 (curve 4) caused an overall decrease in the strength of the material compared with that of curve 1.

The monitoring of the mineralogical changes with time is shown in Figure 5.15 for the materials whose behaviour is depicted in the strength-time curves. The DOC data were calculated from the DTA thermograms, some of which are shown in Appendix 4. The results indicate that varying the parameters caused reduction in the rate of conversion, but this reduction was not the same for all pastes. Pastes with a water-cement ratio of 0.4 converted in saturated air at  $35^\circ\text{C}$  showed a remarkable deviation from similar pastes cured at  $45^\circ\text{C}$ . Immersing the pastes in water resulted also in some delay to the conversion process. The high

water-cement ratio pastes showed a slight delay compared to pastes with water-cement ratio of 0.4 cured in the same conditions. In an attempt to correlate the strength to the mineralogical changes, the strength values were plotted as a function of the degree of conversion, Figure 5.16. A linear relationship was found to exist only in the region of maximum to minimum strength corresponding to degrees of conversion from 25% to 55%. It is also essential to notice that the increase in the water-cement ratio causes the pastes to lose an increasing percentage of their strength at any given DOC. For example, in Figure 5.16, at a 50% DOC and for pastes cured under the same conditions, the strength was 20 and 47 N/mm<sup>2</sup> for pastes of water-cement ratio of 0.55 and 0.4 respectively. These values represent the loss of about 56 and 39% of the 1-day strength at 10°C.

In presenting the pore size distribution data, two groups of curves were drawn for each of the strength-time curves in Figure 5.14. Thus Figures (5.17 a, b), (5.18 a, b) and (5.19 a, b), and (5.20 a, b) represent curves 1, 2, 3 and 4 respectively in Figure 5.14. For purposes of comparison, values of the experimental data, i.e. DOC, strength, total porosity, and average pore diameter, are tabulated on each pore size distribution sheet.

As an example, refer to Figure 5.17(a) which shows the first stage of the conversion process; the porosity decreases with time up to 3 days, which is almost the point of maximum strength shown in Figure 5.14. The second stage of the conversion process from the maximum to the fully converted strength is covered in Figure 5.17(b) which shows a dramatic increase in porosity with time. A similar trend was observed for the

rest of the materials and treatment conditions, Figures (5.18 a, b), (5.19 a, b) and (5.20 a,b).

The difference between specimens cured in air and those cured in water can be noticed at low degrees of conversion. Comparing the air-cured and water-cured samples in Figures 5.17(b) and 5.19(b) at almost 30% conversion, it can be seen that the average pore diameter for the former is  $0.11 \mu\text{m}$  while for the latter it is  $0.014 \mu\text{m}$ . This indicates the presence of a large portion of small diameters in the water cured samples, which may be an explanation for the higher strength, in the region of linearity, of the water cured specimens (curve 3) than those of the air cured specimens (curve 1), Figure 5.14.

Another feature of the pore size distribution curves is that some materials which end with the same total porosity have different pore size distributions. The significance of this is appreciated when a comparison is made between the compressive strengths of such materials. An example is given by curves C and E in Figure 5.20(b). The total porosity for the materials of the two curves is about  $.23 \text{ Cm}^3/\text{g}$ , yet the strength associated with curve C is  $66 \text{ N/mm}^2$  while the corresponding figure for curve E is  $21 \text{ N/mm}^2$ . It should also be noted that the distribution of this volume of pores is different for the two curves since for curve C the volume average diameter is  $0.025 \mu\text{m}$ , while for curve E it is  $0.22 \mu\text{m}$ . The behaviour of these two pastes of 0.55 water-cement ratio suggests that, even if a relation exists between strength and total porosity, the two materials would not fit the same curve. The semilogarithmic plot of strength versus total porosity shown in Figure 5.21 proves this statement. In this figure, curves C and D

represent specimens of water-cement ratio 0.4 cured in saturated air and water respectively. It is seen that a single line fits the experimental data in each case, whereas two lines, E and F, were required to represent the first and second stages of the conversion process for pastes made of water-cement ratio of 0.55 which are in fact on the same time-strength curve (curve 4, Figure 5.14). The existence of lines E and F, on which points 1 and 2 represent the materials of curves C and E in Figure 5.20b respectively, is an indication that after passing the point of maximum strength, the conversion has an effect on the binding forces within the paste amounting to the equivalent of producing a new material with new properties.

It was noticed in the first set of experiments that the change from an unconverted paste with an equal distribution of pores to a converted one whose majority of pores are in the larger sizes is indicated by the change from linear to convex curves (Figure 5.10). In this set the intermediate region between the two extremes was observed as curves with two humps indicating a different trend. In Figure 5.22, the unconverted paste represented by curve A shows a linear distribution of pores in the range of  $.012 - 1 \mu m$ , while curve B, representing the fully converted paste, has the majority of pores between  $0.12$  to  $1 \mu m$ . At about 30% conversion, curve C shows a concentration of pores in two regions:  $.004 - .018 \mu m$  and  $0.07 - 0.35 \mu m$ .

Another indication of the effect of conversion on the pore structure of the hardened pastes is the variation of the volume average pore diameter, which increases considerably after passing the point of maximum strength. Refer to the experimental data tabulated on the pore size distribution sheets.

## 5.6 CONCLUSIONS

Decreasing the temperature results in a considerable delay to the conversion process and hence to the rate at which the pastes lose their strength. Increase in the water-cement ratio causes the pastes to lose an increasing percentage of their strength at any given degree of conversion. Similar results are obtained through monitoring the mineralogical changes in the paste. When strength was plotted versus the degree of conversion, a linear relationship was found in the region of maximum to minimum strength, corresponding to degrees of conversion from 25 to 55%.

The strength of pastes of constant water-cement ratio and the same curing conditions but with different degrees of conversion was found to be exponentially dependent on total porosity. A different semilogarithmic relation was found when the strength of unconverted pastes with different water-cement ratios was plotted versus total porosity data, but fully converted pastes exhibited a departure from this relation.

The pore size distribution curves are good indicators of conversion, since a considerable change in the volume-average pore diameter is associated with it. The change from linear and concave to convex pore size distribution curves and the appearance of more defined 'threshold diameters' are other means of detecting conversion.

*It should also be mentioned that the strength - porosity relationship (Figure 5.21) suggests that the strength might vary logarithmically with the degree of conversion as this is expected to control the porosity of the paste (see footnote to Figure 5.16)*

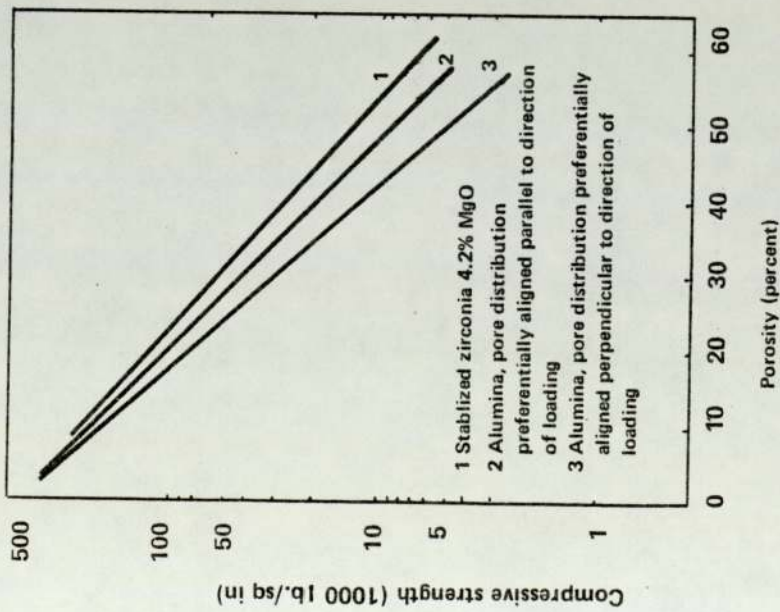


Figure 5.1 Effect of porosity on compressive strength of alumina and zirconia (88)

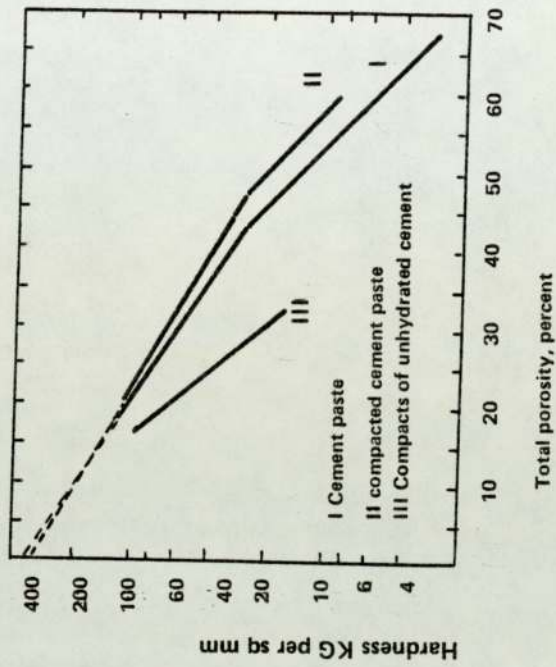


Figure 5.2 Hardness vs porosity for the cement systems (29)

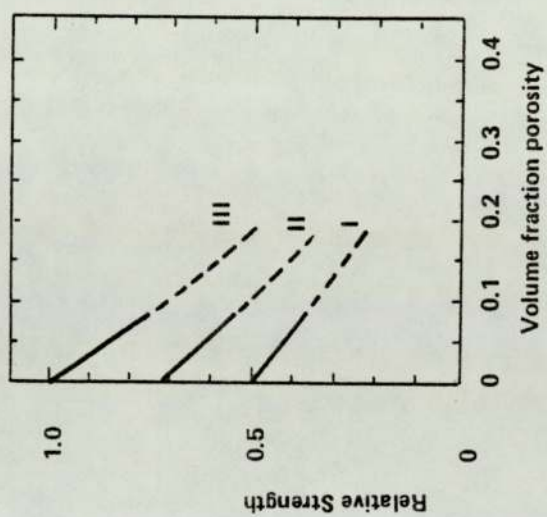


Figure 5.3 Proposed effect of micromechanical stress concentrations on the strength of a porous brittle material: Case I, flaw size  $\ll$  pore size; Case III, flaw size  $\gg$  pore size; and case II flaw size  $\approx$  pore size (108)

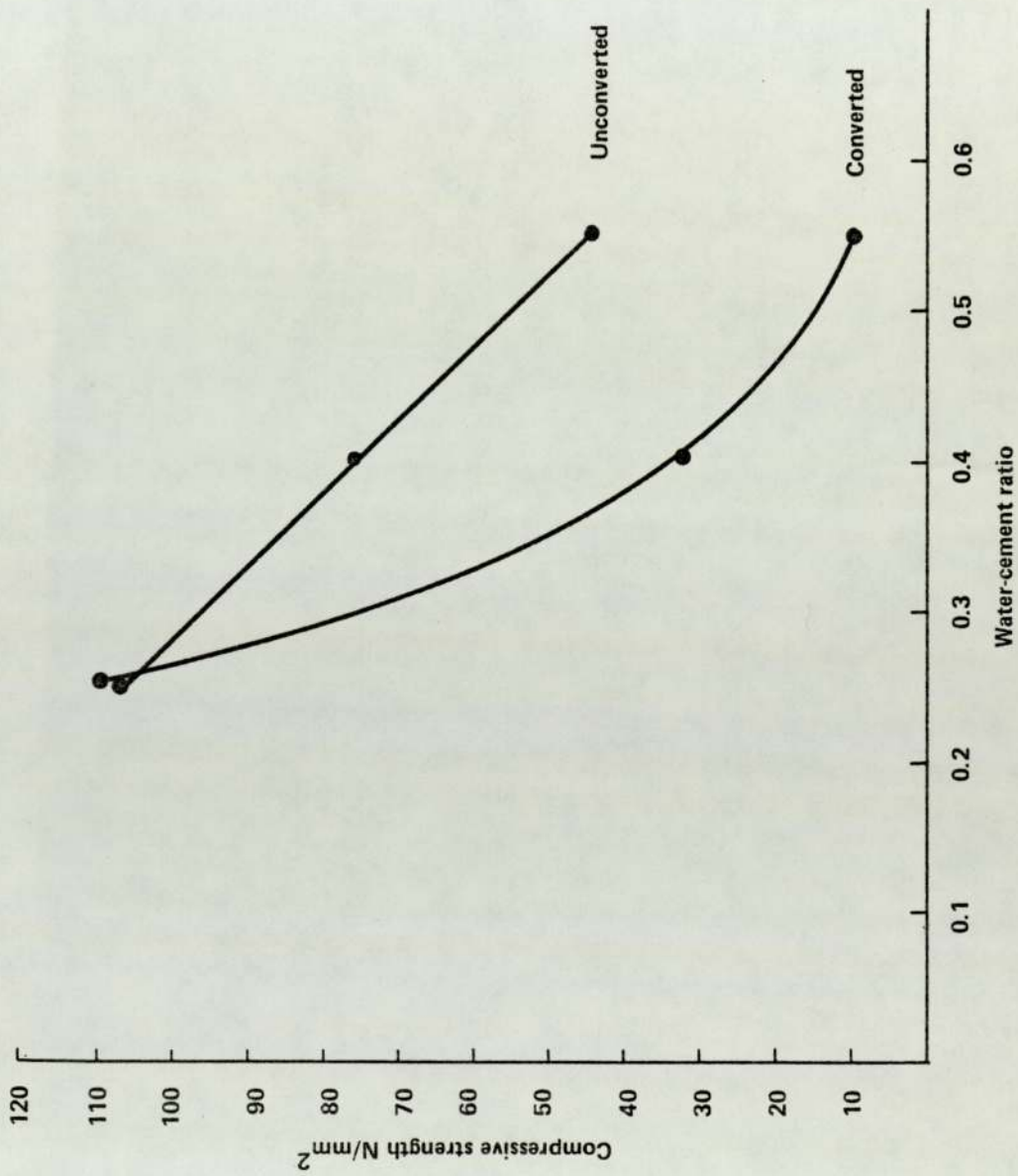


Figure 5.4 Strength of HAC paste as a function of water-cement ratio

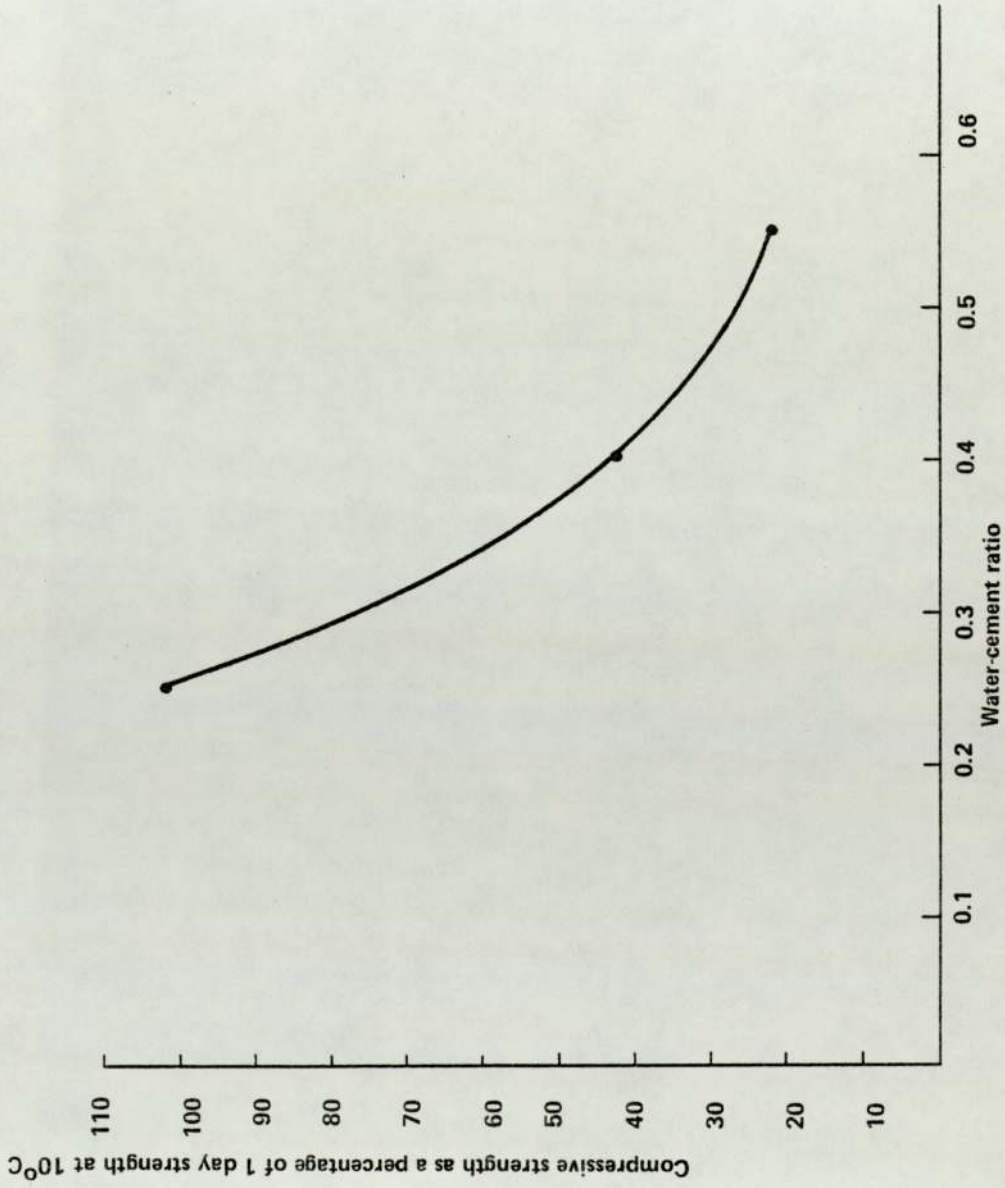


Figure 5.5 Influence of the water-cement ratio on the compressive strength of fully converted HAC paste expressed as a percentage of 1-day strength at 10°C

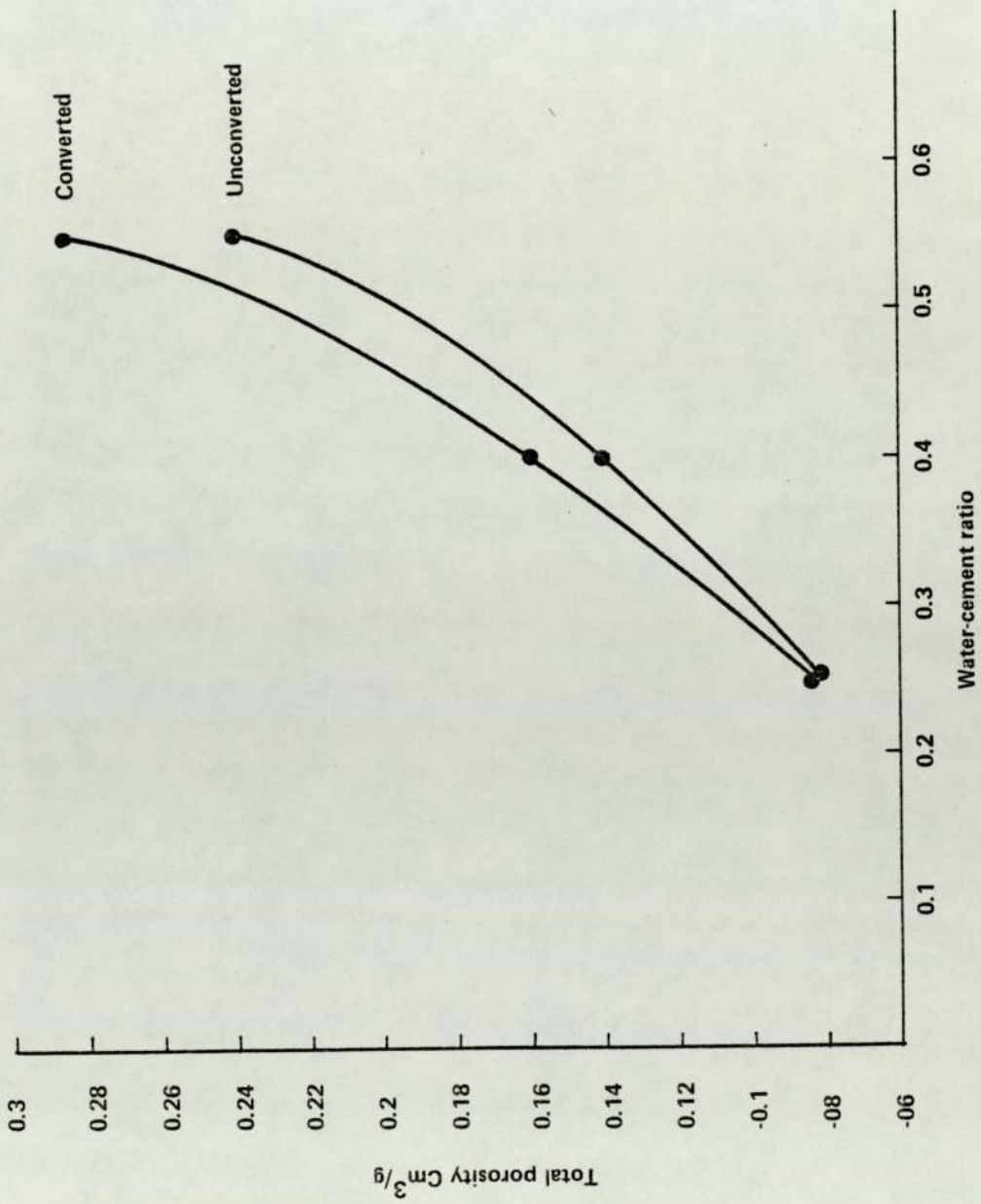


Figure 5.6 Porosity of HAC paste as a function of water-cement ratio

W/C	Specific gravity g/cm <sup>3</sup>	
	Unconverted	Converted
0.25	2.557	2.676
0.4	2.462	2.656
0.55	2.400	2.701

Table 5.1 Specific gravity of HAC pastes

W/C	Apparent density g/cm <sup>3</sup>	
	Unconverted	Converted
0.25	2.116	2.203
0.4	1.830	1.880
0.55	1.522	1.530

Table 5.2 Apparent density of HAC pastes

W/C	Total porosity cm <sup>3</sup> /g			
	Unconverted		Converted	
	T.P.	P.S.D	T.P.	P.S.D.
0.25	.082	.080	.081	.080
0.4	.140	.132	.160	.161
0.55	.240	.242	.286	.280

Table 5.3 Total porosity of HAC pastes

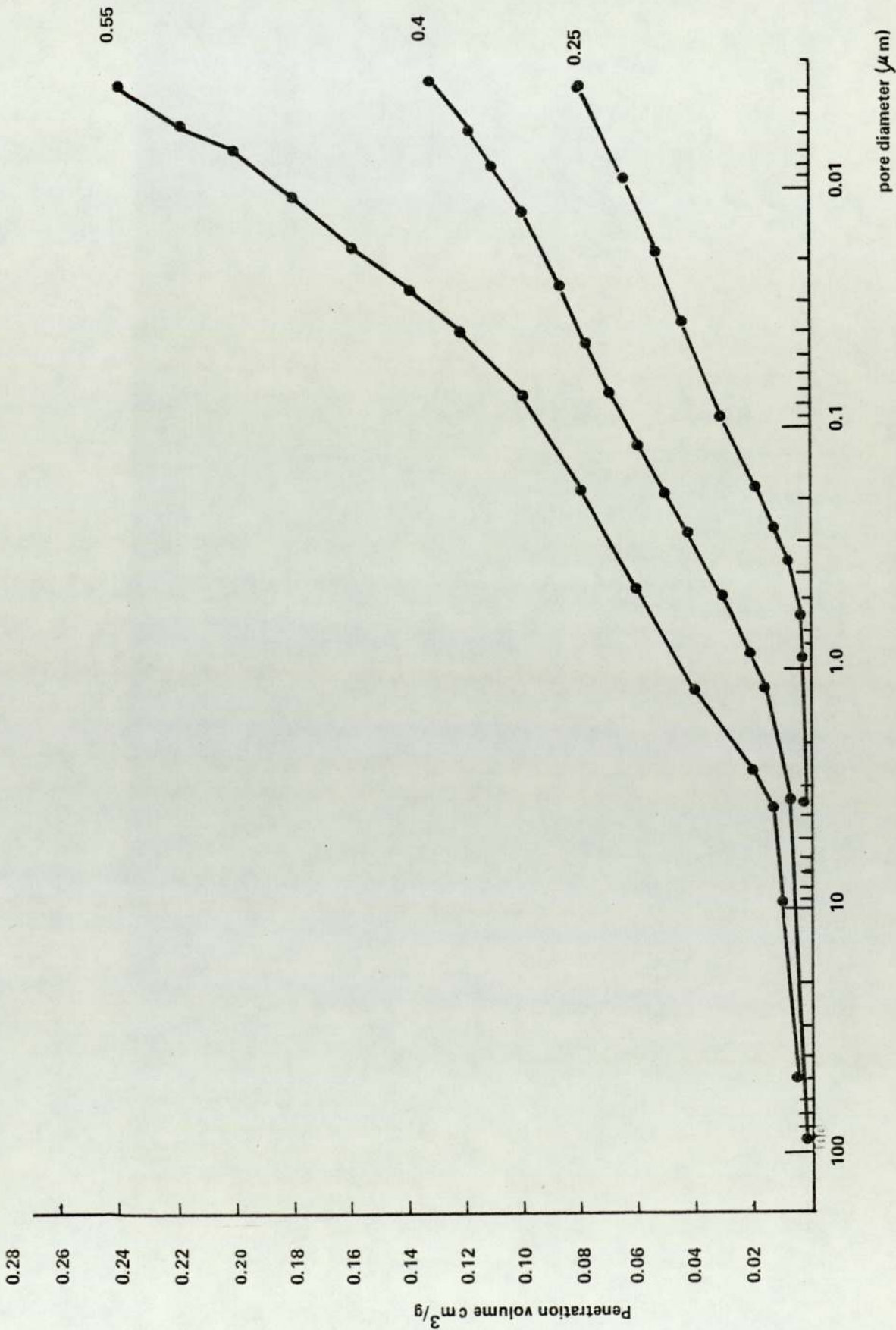


Figure 5.7 Pore size distribution curves of unconverted HAC cement pastes of various water-cement ratios

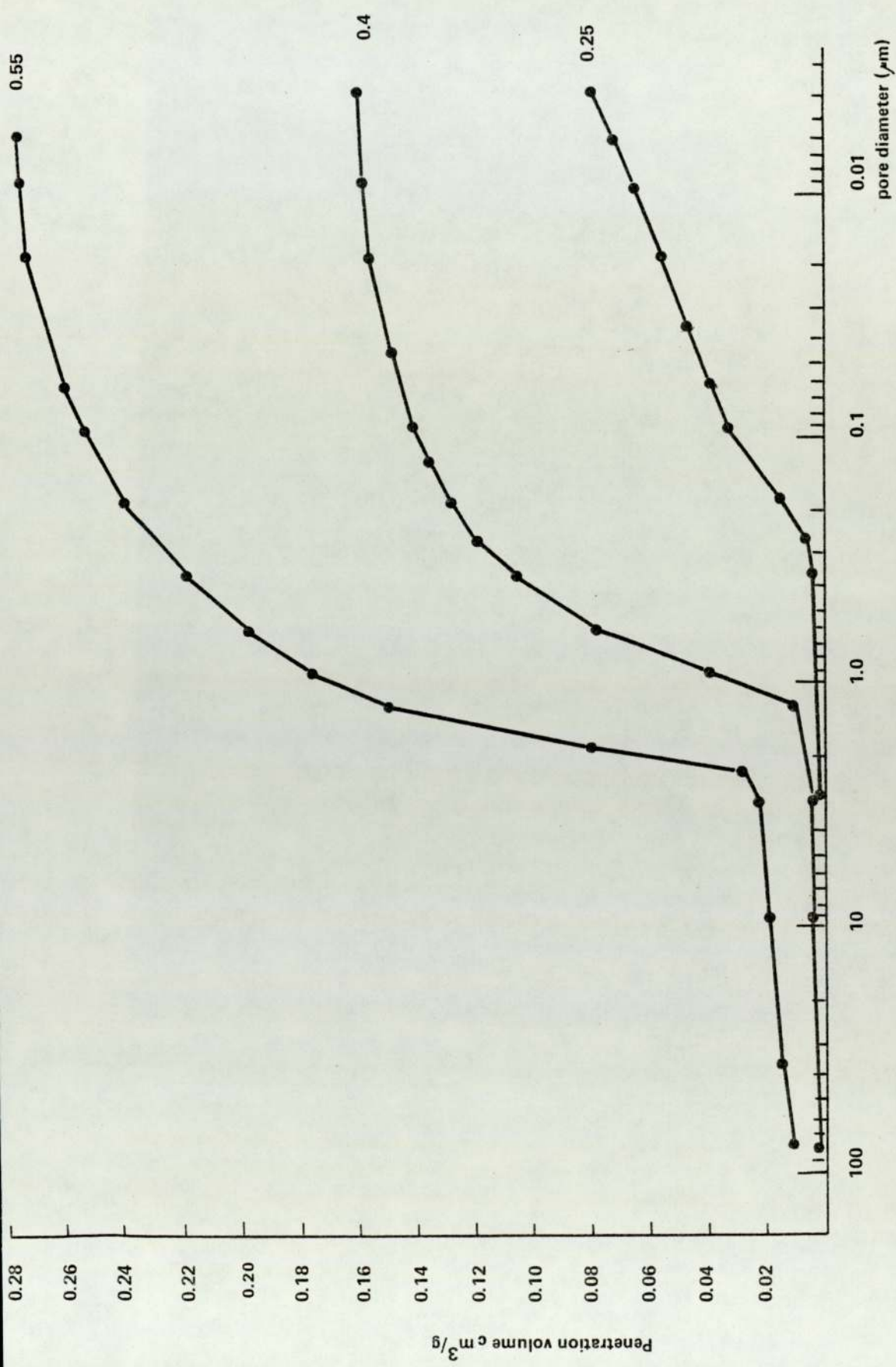


Figure 5.8 Pore size distribution curves of fully converted HAC cement pastes of various water-cement ratios

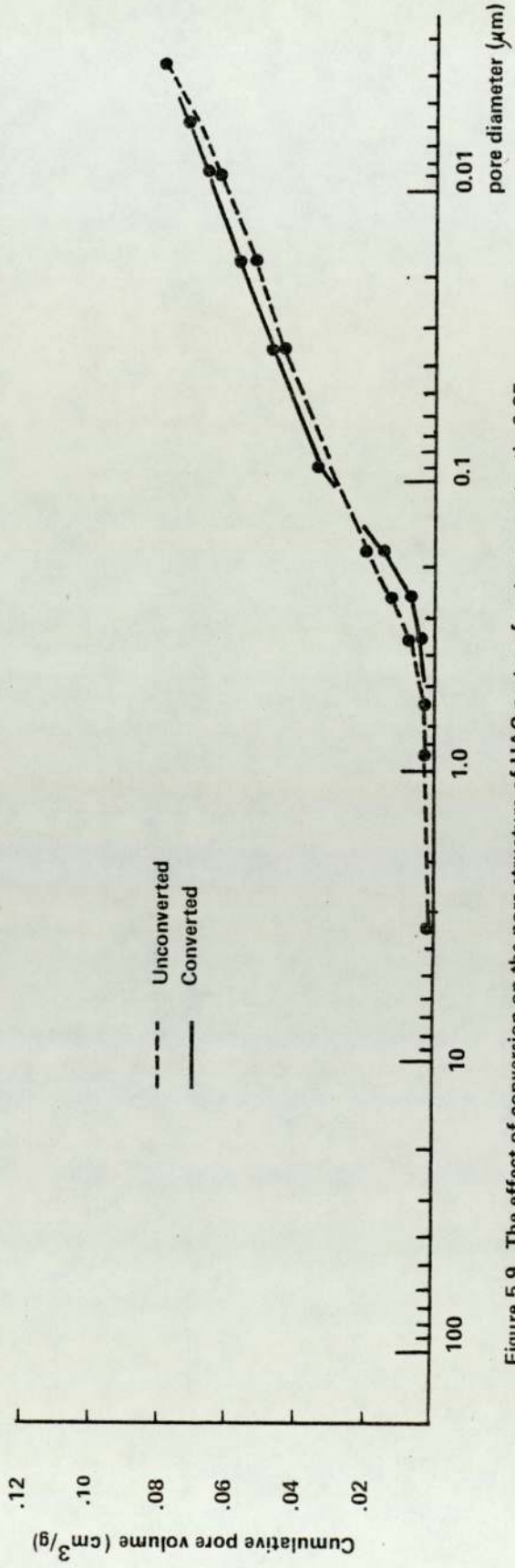


Figure 5.9 The effect of conversion on the pore structure of HAC pastes of water-cement ratio 0.25

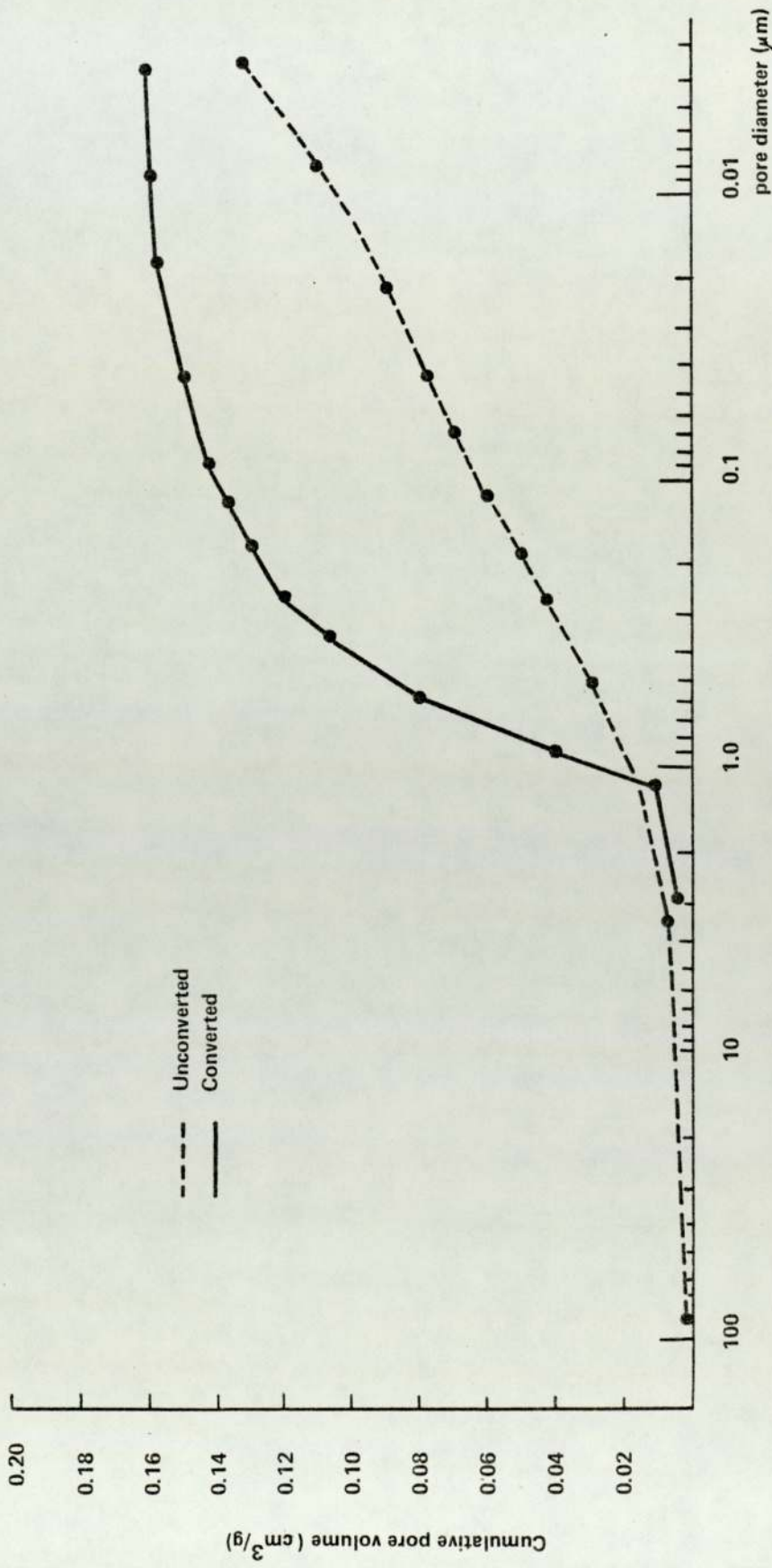


Figure 5.10 The effect of conversion on the pore structure of HAC pastes of water-cement ratio 0.4

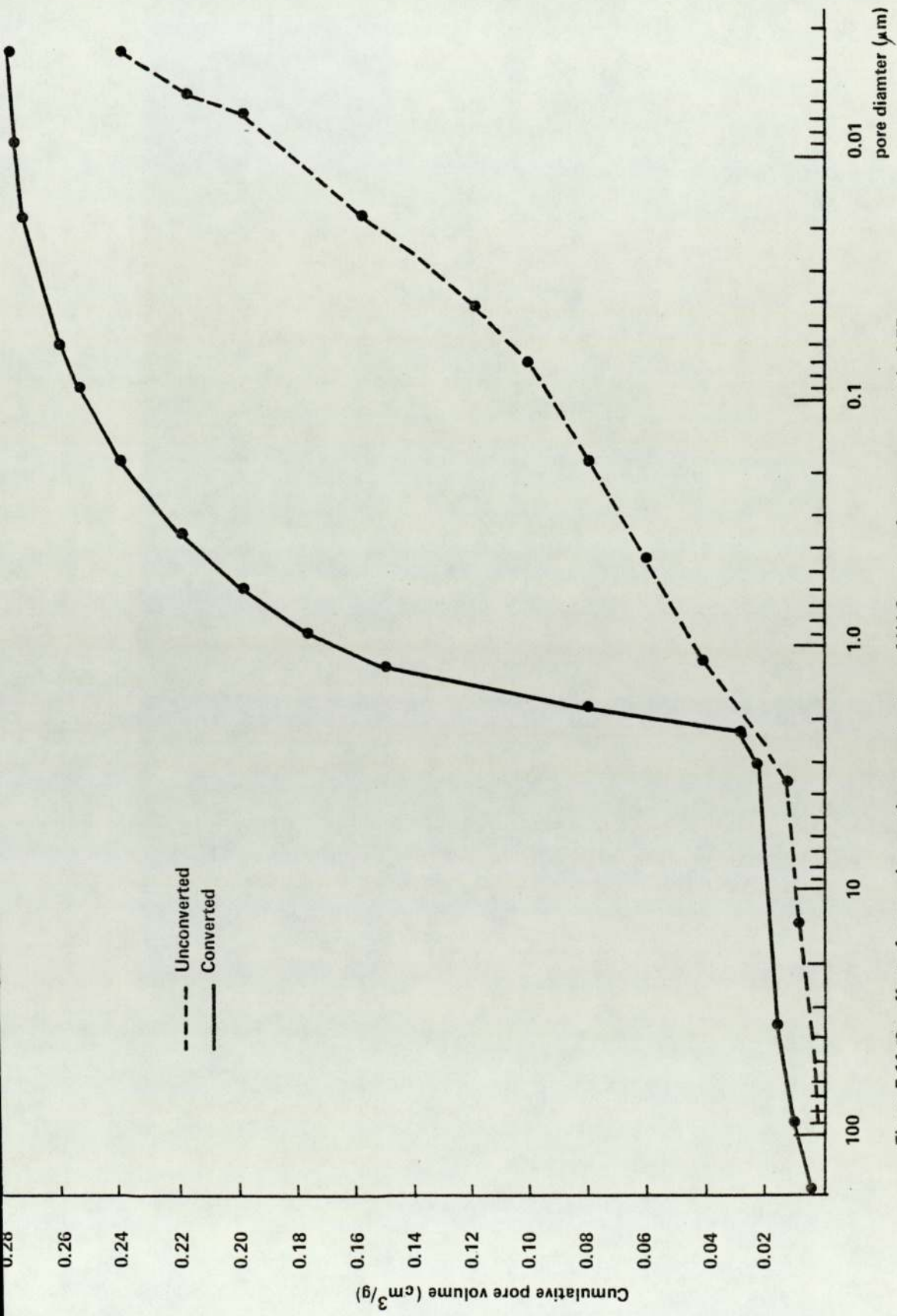


Figure 5.11 The effect of conversion on the pore structure of HAC pastes of water-cement ratio 0.55

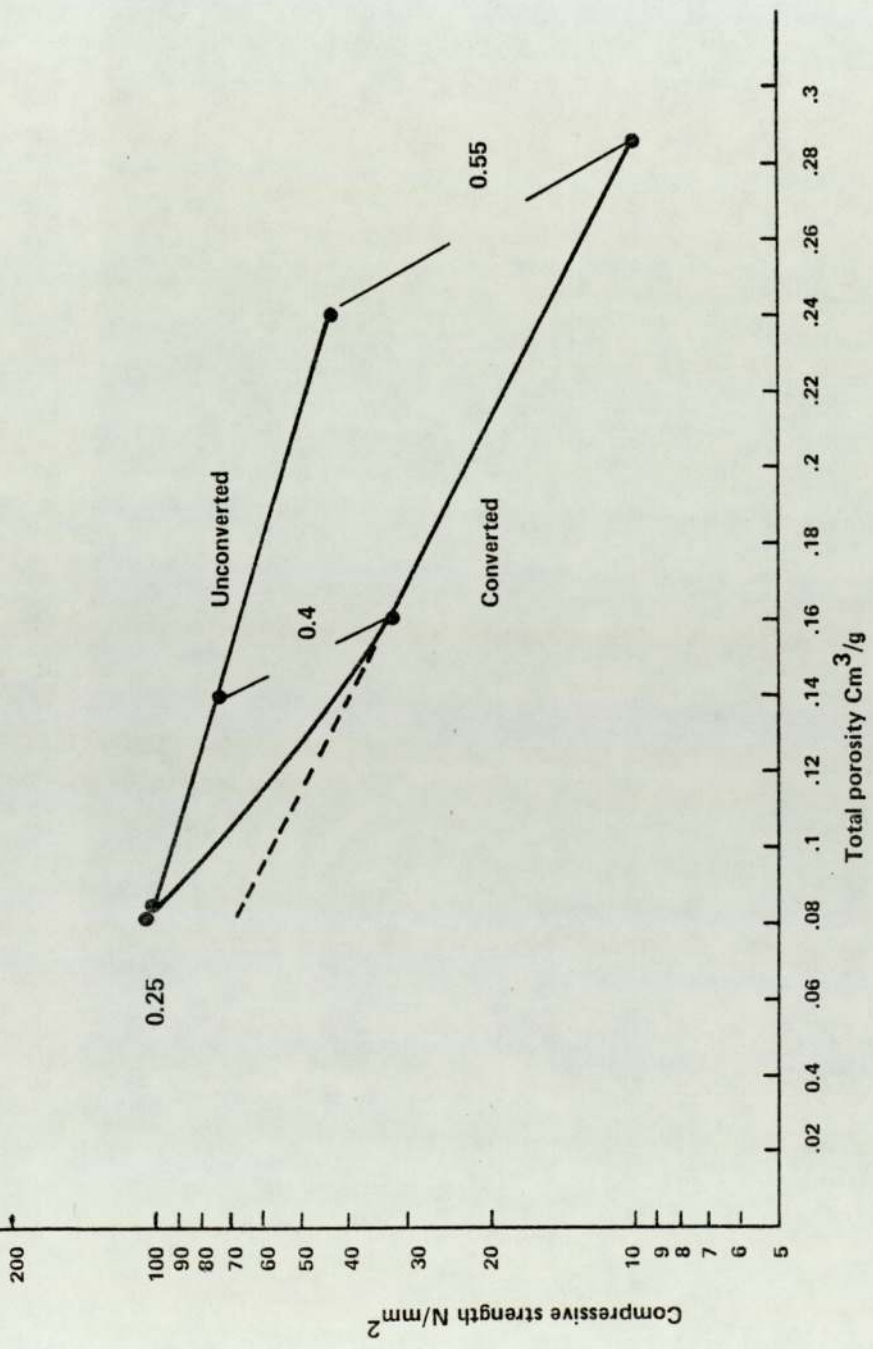


Figure 5.12 Strength of HAC paste as a function of total porosity

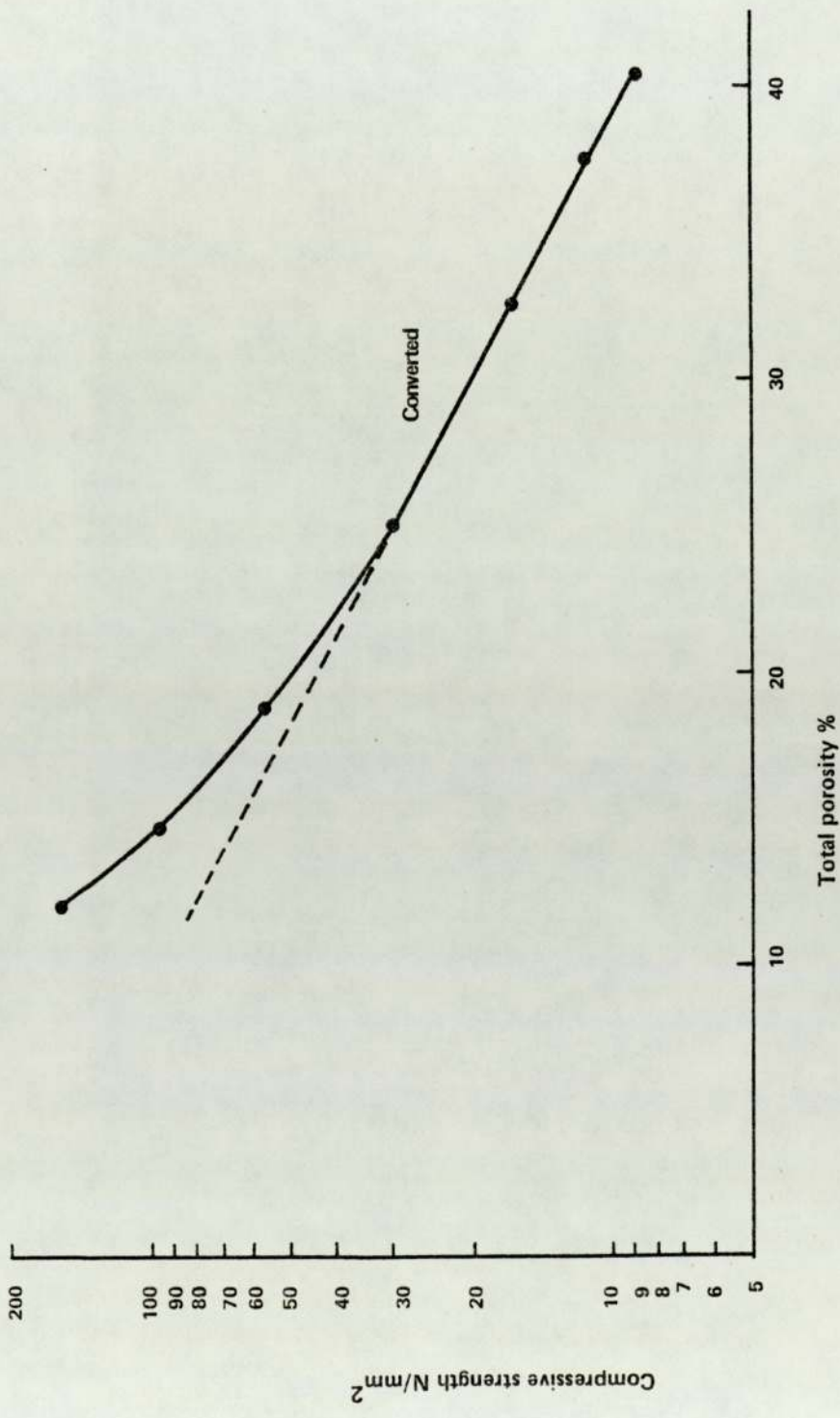


Figure 5.13 Strength of converted HAC paste as a function of total porosity (Cottin's results (44))

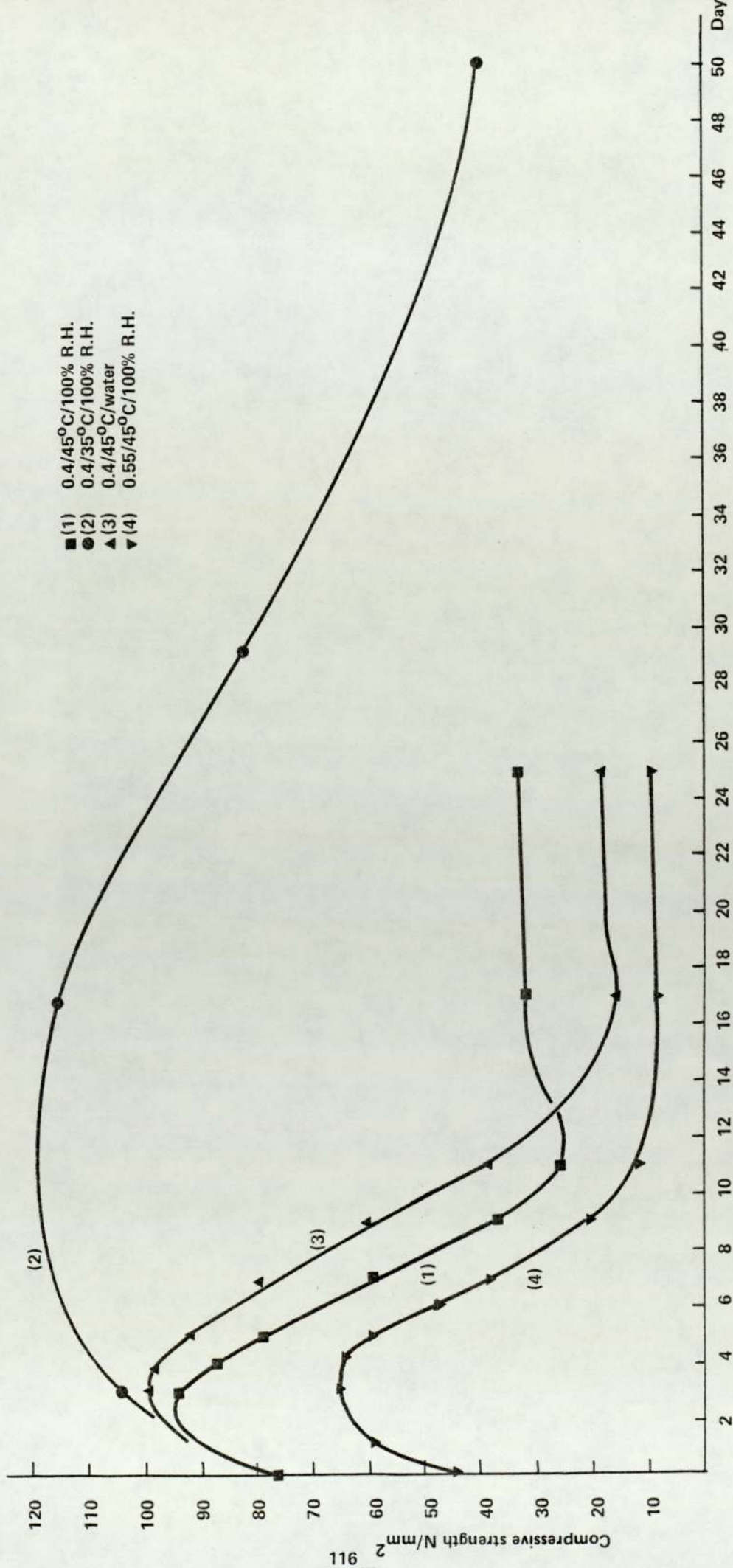


Figure 5.14 The Effect of water-cement ratio and curing conditions on the strength of HAC pastes

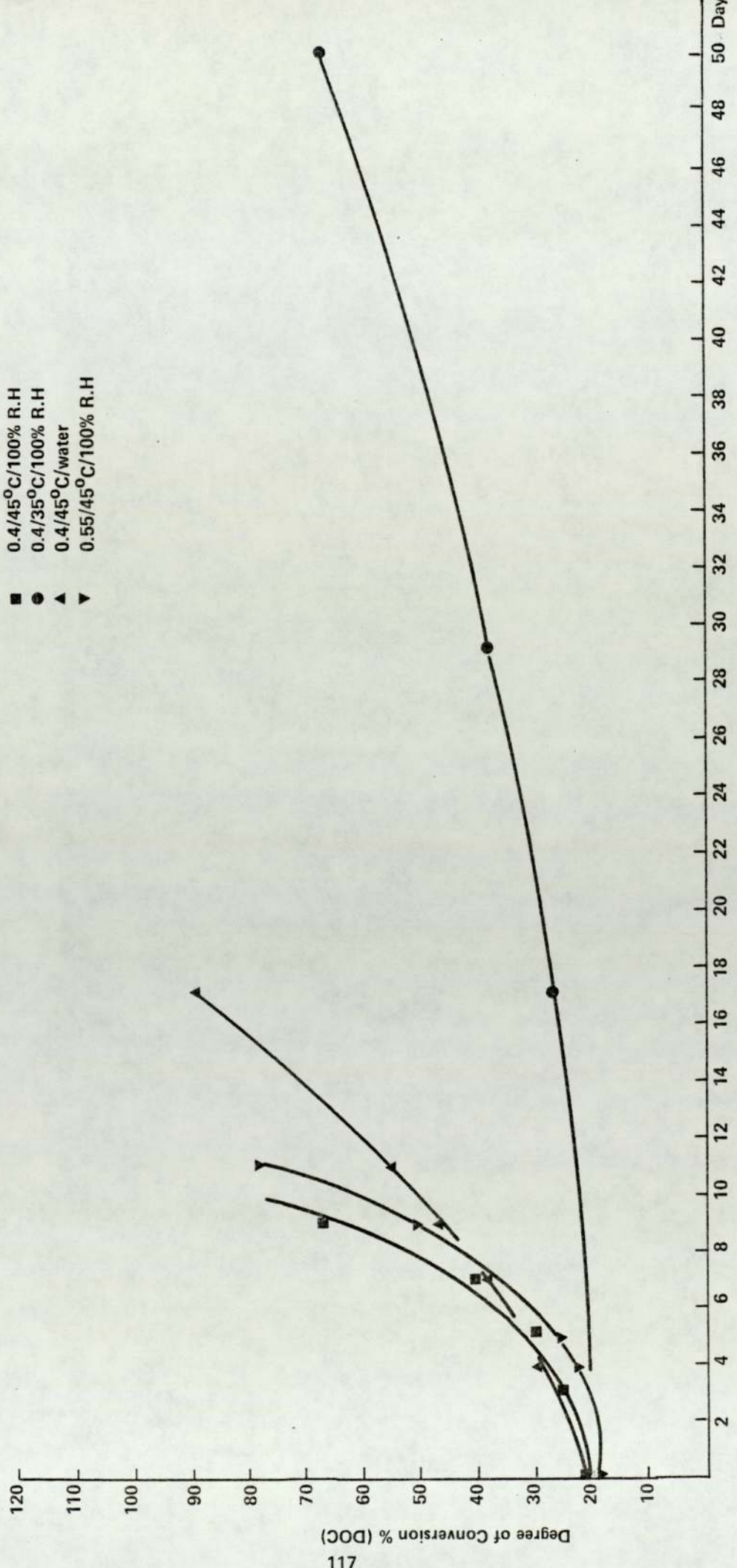


Figure 5.15 The effect of water-cement ratio and curing conditions on the mineralogy of HAC pastes

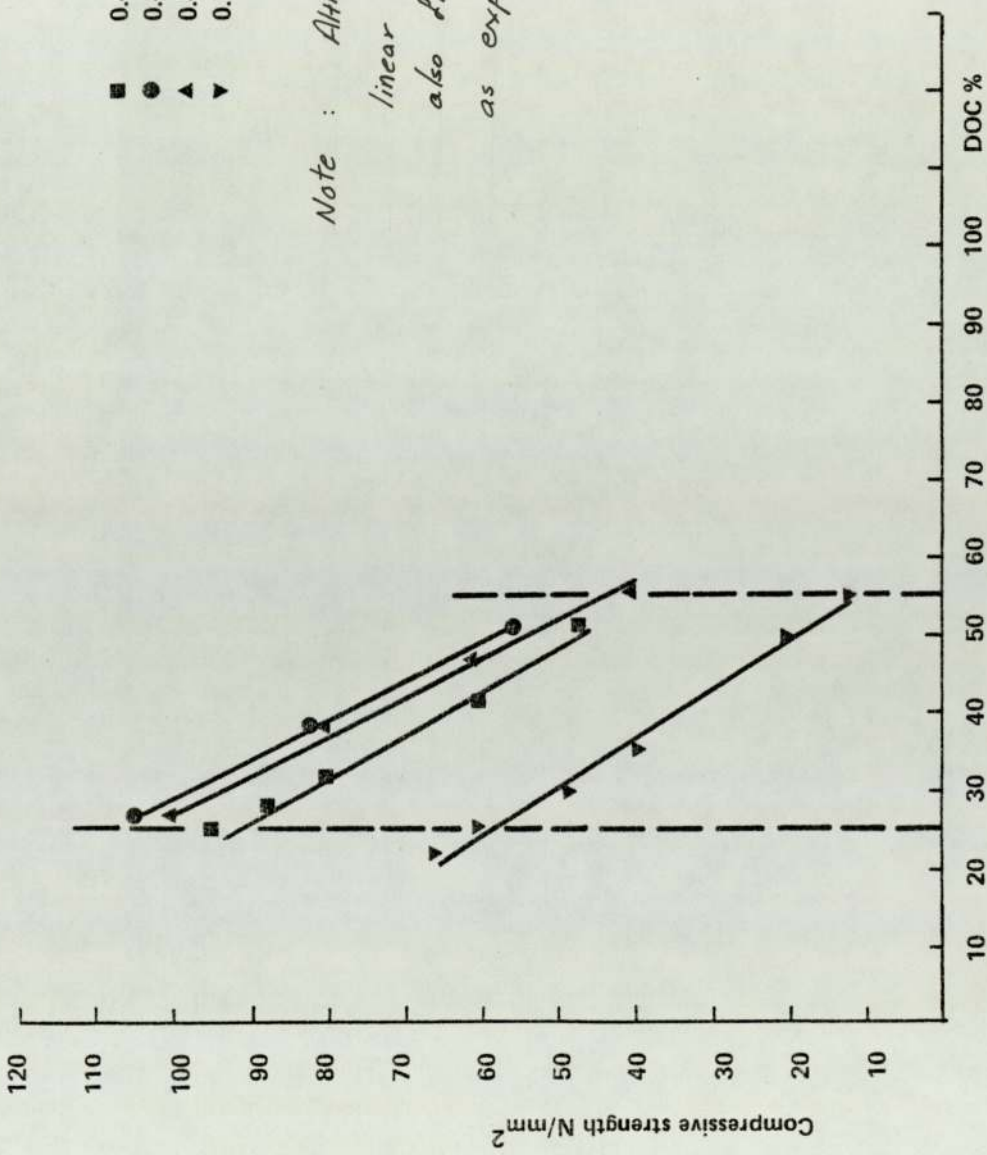


Figure 5.16 Strength of HAC paste as a function of degree of conversion

Note : Although the data apparently fit linear relationship reasonably, they also fit semilogarithmic relationships as expected (see discussion on page 102).

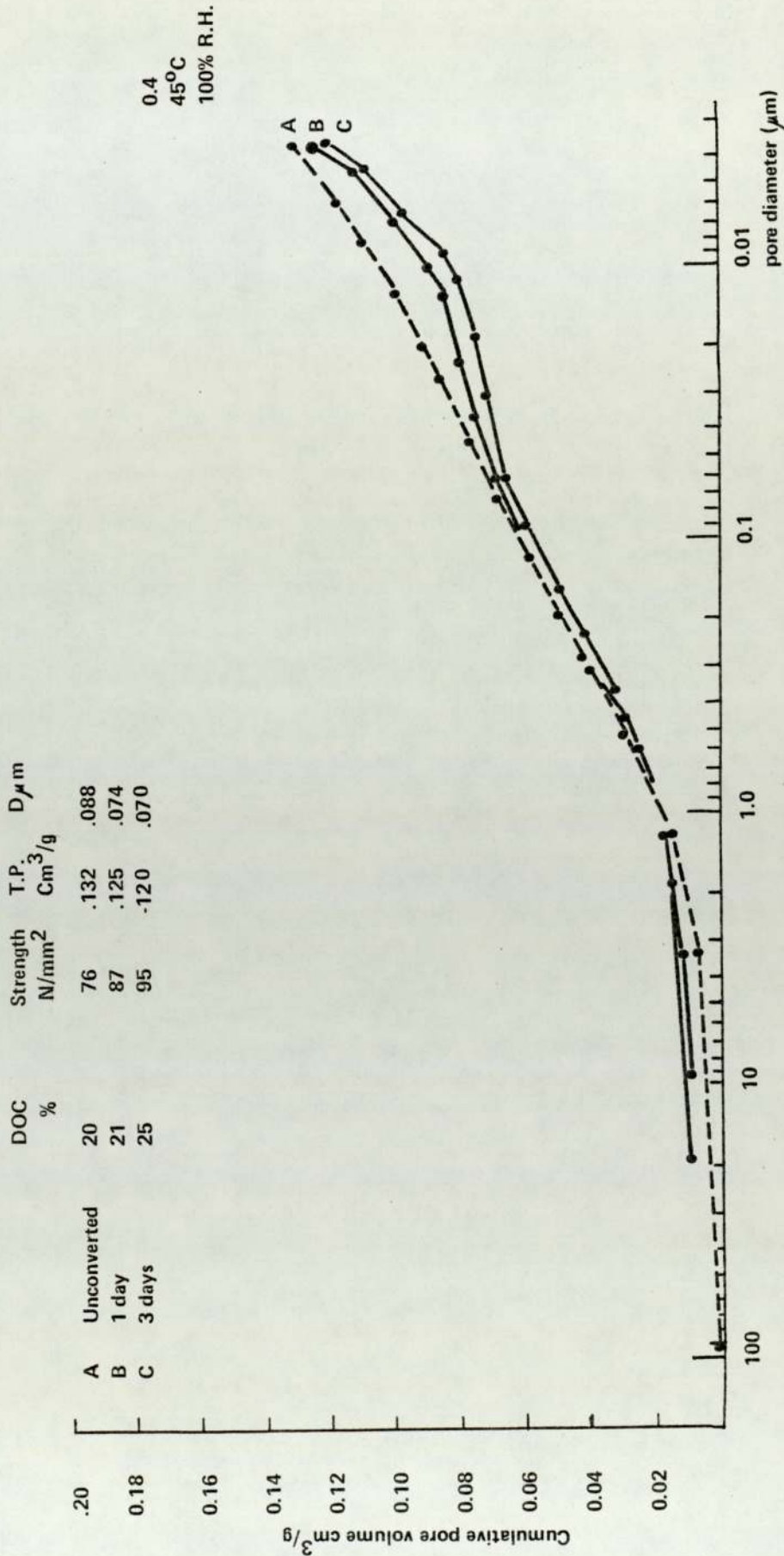


Figure 5.17(a) Pore size distribution curves of HAC pastes of water-cement ratio 0.4 during the first stage of the conversion process at 45°C and 100% R.H.

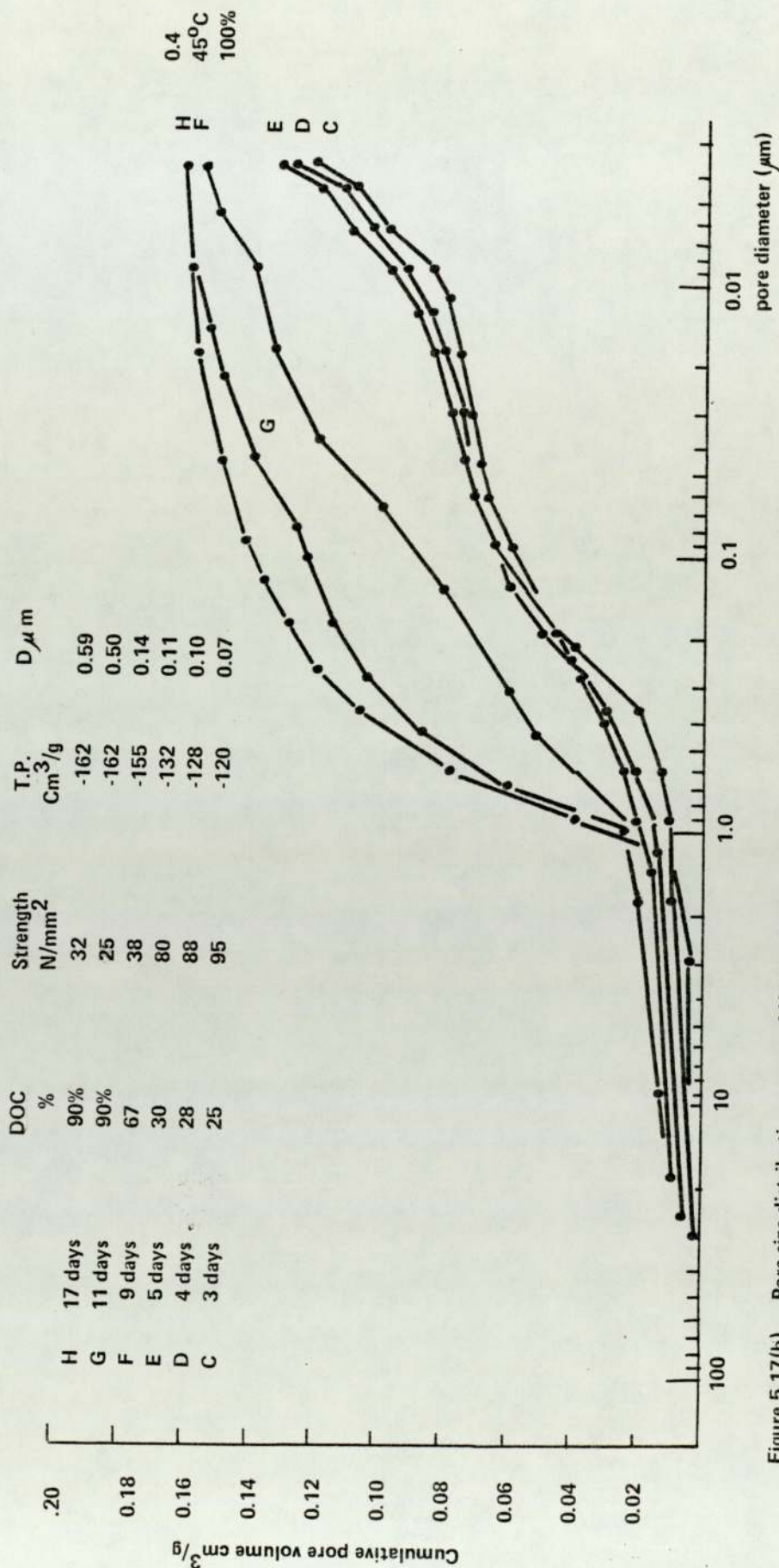


Figure 5.17(b) Pore size distribution curves of HAC pastes of water-cement ratio 0.4 during the second stage of the conversion process at 45°C and 100% R.H.

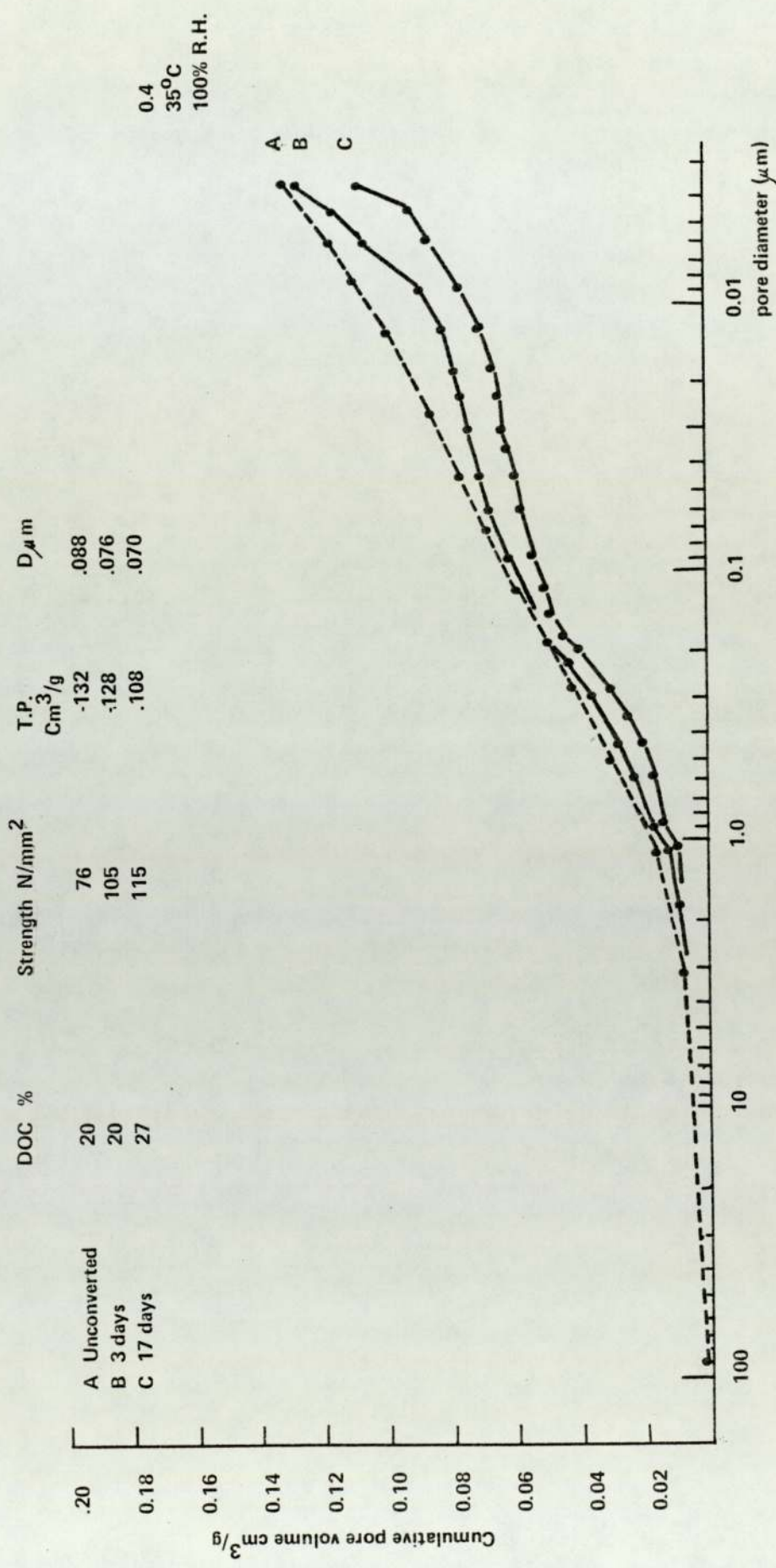


Figure 5.18(a) Pore size distribution curves of HAC pastes of water-cement ratio 0.4 during the first stage of the conversion process at 35°C and 100% R.H.

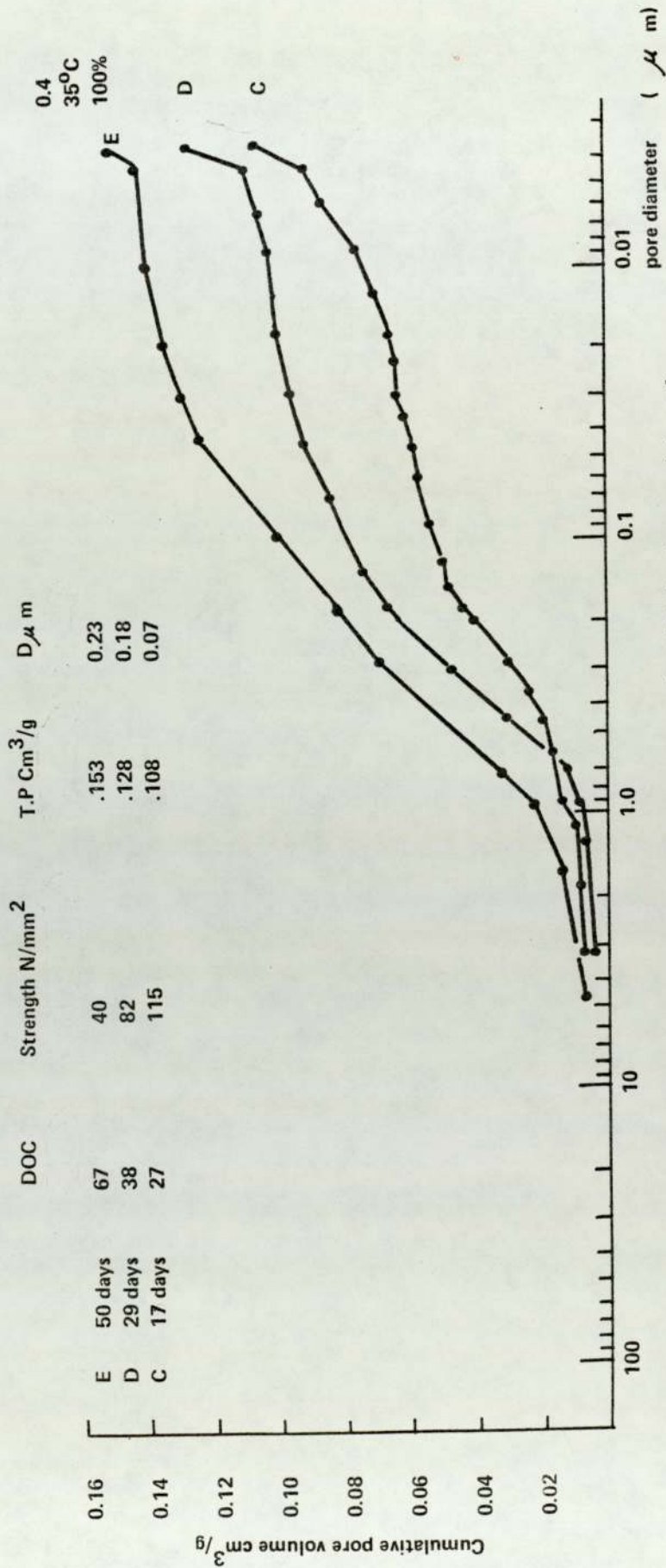


Figure 5.18(b) Pore size distribution curves of HAC pastes of water-cement ratio 0.4 during the second stage of the conversion process at 35°C and 100% R.H.

0.4  
45°C  
Water

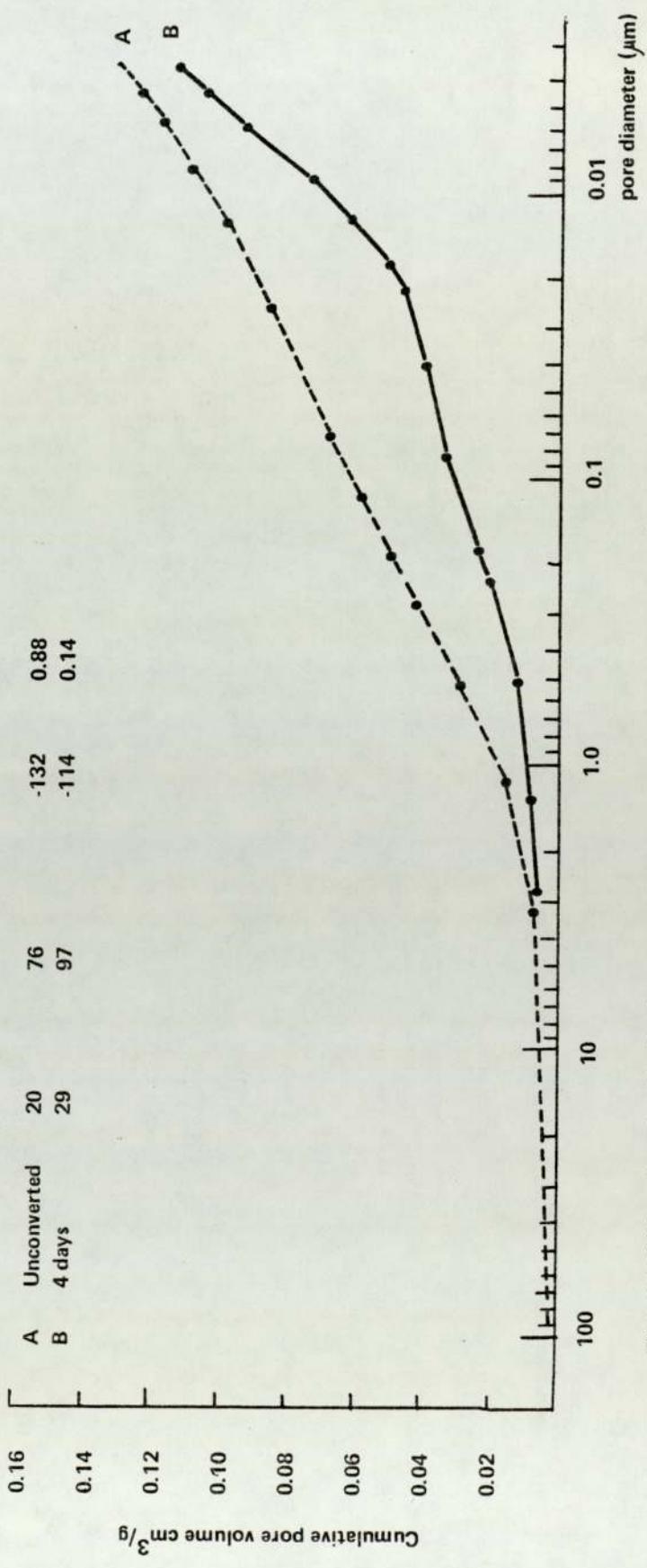


Figure 5.19(a) Pore size distribution curves of HAC pastes of water-cement ratio 0.4 during the first stage of the conversion process in water at 45°C

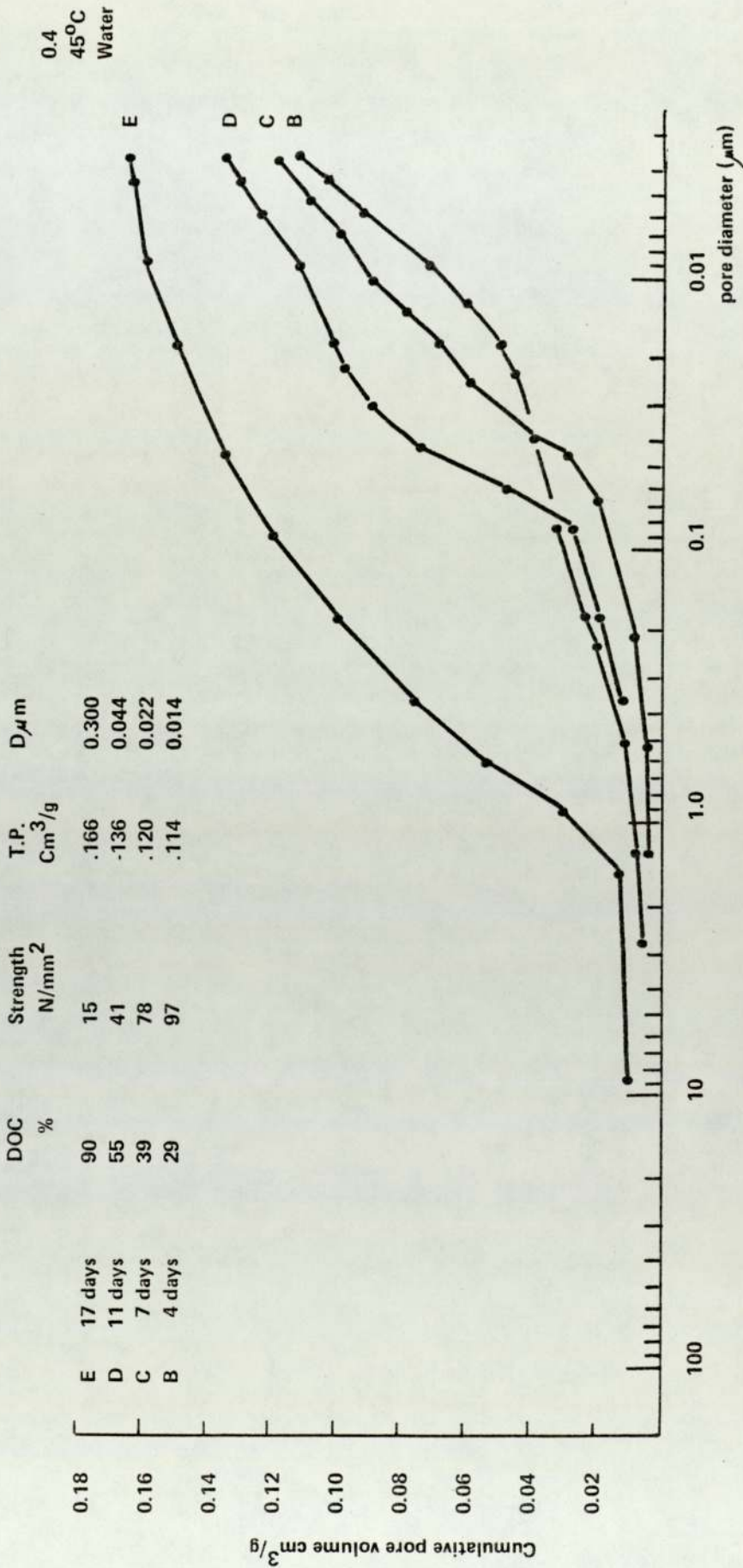


Figure 5. 19(b) Pore size distribution curves of HAC pastes of water-cement ratio 0.4 during the second stage of the conversion process in water at 45°C

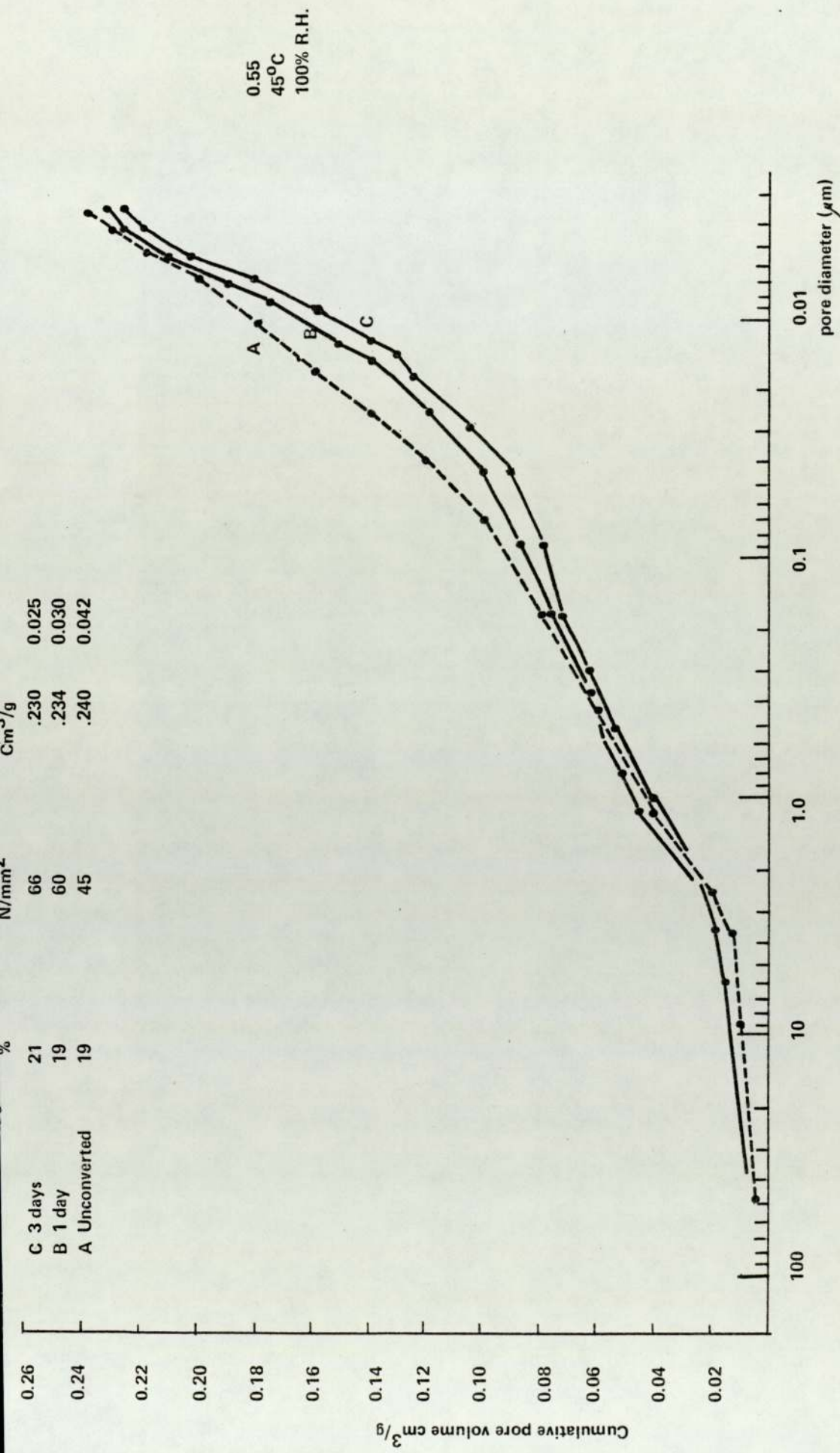


Figure 5.20(a) Pore size distribution curves of HAC pastes of water-cement ratio 0.55 during the first stage of the conversion process at 45°C and 100% R.H.

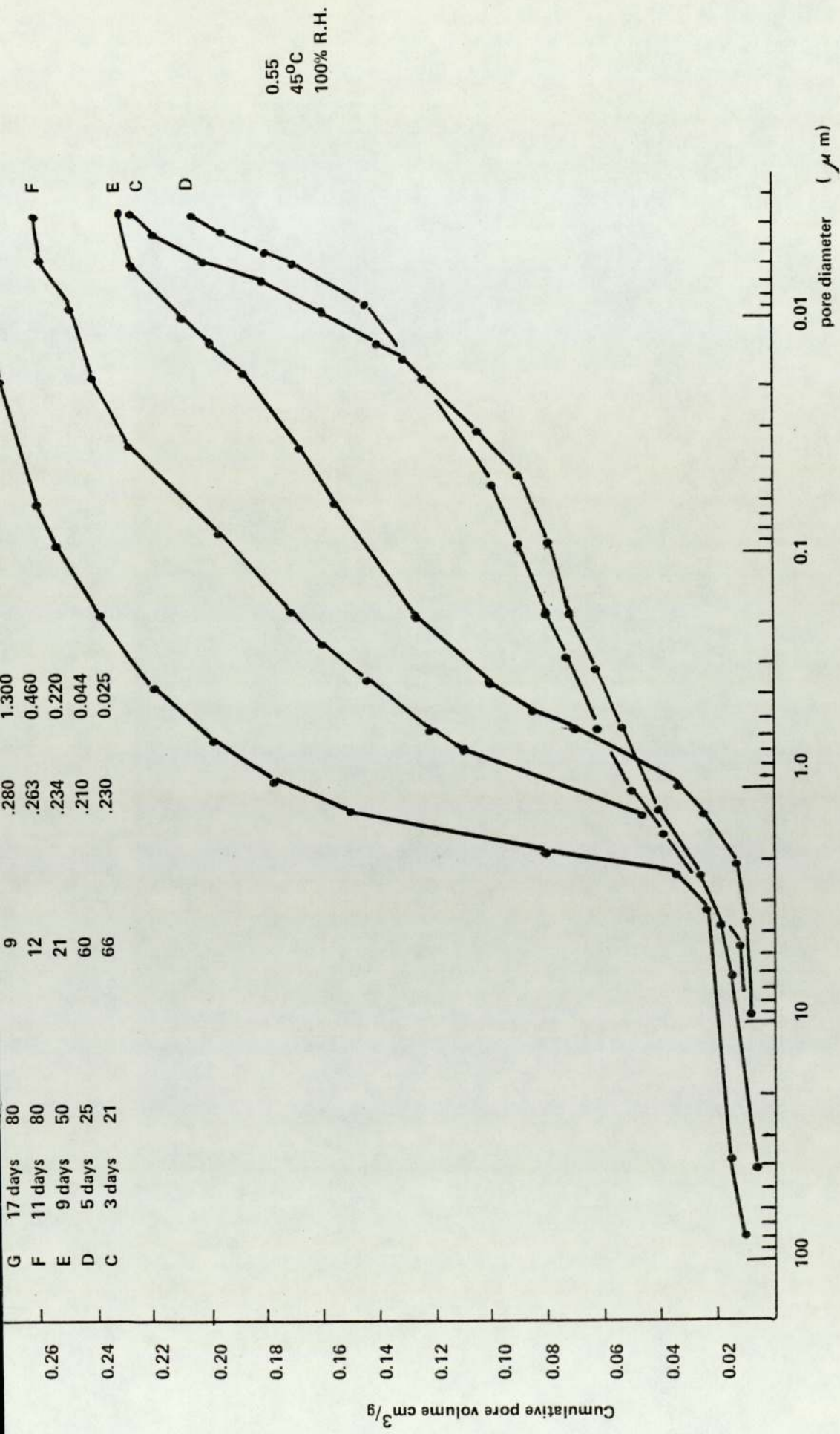


Figure 5.20(b) Pore size distribution curves of HAC pastes of water-cement ratio 0.55 during the second stage of the conversion process at 45°C and 100% R.H.

Line	X-intercept	Y-intercept	Slope
D	0.197	5754	-2.0
C	0.212	5248	-1.8
F	0.290	12589	-1.5
E	0.290	537031	-2.0

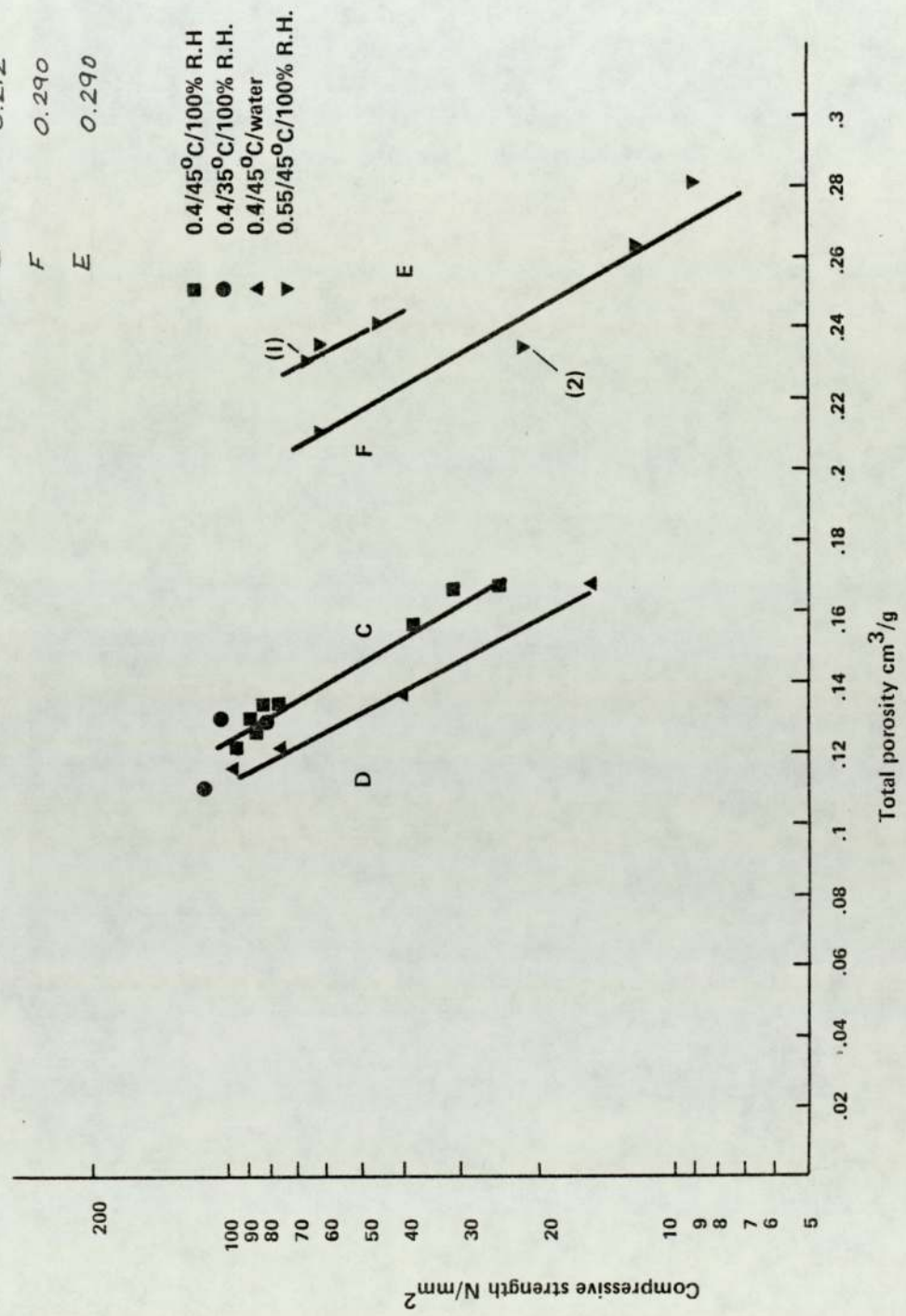


Figure 5.21 Relationship between strength and total porosity of HAC pastes with change in water-cement ratio and curing conditions

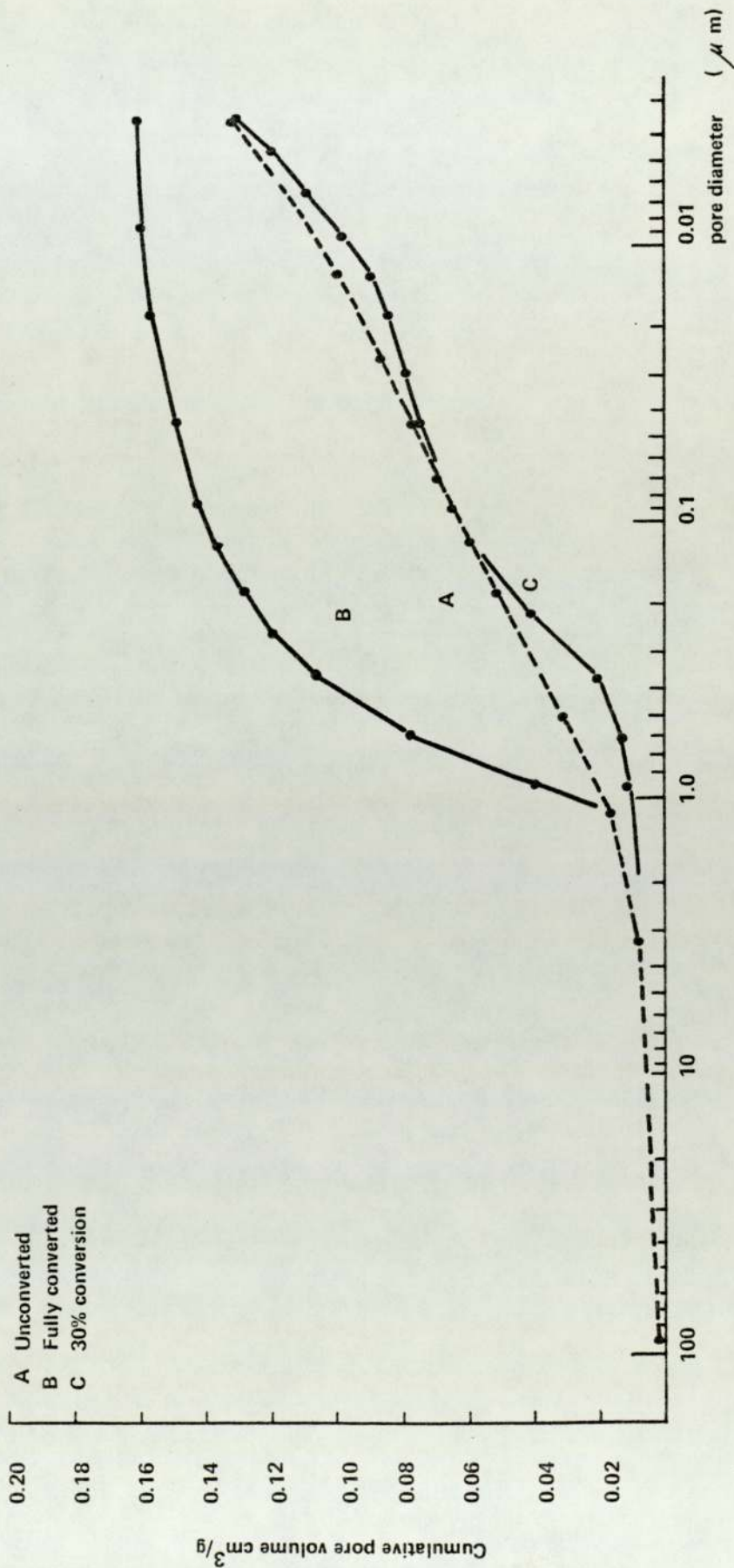


Figure 5.22 The effect of conversion on the shape of the pore size distribution curves of HAC pastes

## CHAPTER 6

### THE EFFECT OF CONVERSION ON THE CONTACT ZONE BETWEEN HIGH ALUMINA CEMENT PASTE AND EMBEDDED MATERIALS

#### 6.1 INTRODUCTION

The stability of high alumina cement concrete after a short period of initial treatment at suitably elevated temperature was studied by French, Montgomery and Robson<sup>(27)</sup>. In this investigation, tests were made using either siliceous aggregate or a synthetic cementitious aggregate, known as 'Alag'. It was found that concretes prepared from Alag aggregates tend to exhibit a higher compressive strength than otherwise similar concrete prepared from siliceous aggregate. The authors attributed the difference between the results to the hydration of Alag aggregate which, besides being a potentially hydratable material, is also chemically compatible with high alumina cement. It is also quite possible to suggest that the difference between the mineralogical composition of Alag and that of siliceous aggregate may lead to significant variations in the aggregate-cement bond, which seems to have a considerable influence on the mechanical characteristics of the concrete.

Much of the reported work dealing with the nature of adhesion set up between aggregates and cement and its influence on concrete strength has been reviewed by Alexander, Wardlaw and Gilbert in 1968<sup>(109)</sup> and in a more recent study by Swamy in 1971<sup>(110)</sup>. Various adhesive forces have been observed between the hydrated constituents of cement and aggregates according to their degree of reactivity towards the cementitious phases. The cement-aggregate bond in concretes made from a completely inert aggregate may be purely physical due to adhesion and mechanical interlock, depending on the type of cement, the water content, and the

mineralogical nature, the shape and surface texture of the aggregate. On the other hand, with most common aggregates that show some degree of activity, physical and chemical forces may act jointly between the cementitious phases and aggregates, depending on the nature, specific surface, and the extent of chemisorption of the aggregate surface. Apart from these forces, epitaxial overgrowth, which may result in a continuity of crystal structure between the hydration products and aggregates can form only where the lattice structure of the paste and aggregate crystals are compatible. However, it has been reported that the presence of such epitaxial bond does not necessarily imply strength and stiffness which could still be a consequence of purely physical or a weak chemical interaction<sup>(110)</sup>.

Whatever may be the type of bond involved, it has recently been found that the bond between various cementitious phases and different embedded materials is closely related to the microstructural characteristics of the interfacial zones developed between them; these zones have been the subject of many investigations since Farran's classic work in 1956<sup>(22)</sup>. Farran, in an attempt to analyse the mechanism of aggregate-cement bond used optical microscopy and X-ray diffraction to study the nature and the geometrical form of the hydrated constituents of various types of cements which are formed at the surfaces of several substrates. This author investigated the hydration products of high alumina cement, portland cement, portland-blast furnace slag cement and supersulphated cement at their contact layer with polished sections of calcite, dolomite, quartz, flint, feldspar and mica as well as glass (in the form of slides) and stainless steel.

It was found, with high alumina cement tested at 15<sup>o</sup>C, that the composition of the hydrated phases near the various surfaces is significantly altered with time and according to whether such surfaces are active or inert. Initially, and with all substrates except calcite, an interfacial film presenting the appearance of gel was formed which was expected to produce few capillary fissures at the interface and reasonably good bonding due to capillary attraction and mechanical interlock. The presence of monocalcium aluminate hydrate was detected by X-ray diffraction after 24 hours. After a few weeks, these crystals started to appear in the optical microscope in the shape of small roses which later increased in size and accumulated to produce different shapes, resulting in a significant reduction of the area of contact. After six months, the contact area was considerably reduced and was limited to the crystal edges. Occasionally, small quantities of bayerite (AH) in the form of very fine grains were observed.

On the other hand, it was shown that calcite may participate in chemical interaction with high alumina cement paste. X-ray studies showed initially the presence of hydrated monocalcium aluminate in large quantities, as seems to be the case with inert surfaces. After 48 hours, the formation of a solid solution of tetra-calcium aluminate and carboaluminate of lime was also observed. After a month, the contact layer was found to be composed only of this solid solution of  $C_4AH_{12}$  and  $C_3A \cdot CaCO_3 \cdot H_{11}$ . Farran attributed the adhesion between aluminous cement paste and calcite, manifested by a clear pitting on the polished aggregate surface, to the superficial dissolution of the calcareous surface. He was reserved in considering epitaxial overgrowth due to the absence of sufficient information about the crystal structure.

However, he was able to postulate that the bond between calcite and portland cement paste was epitaxial. The formation of a solid solution intermediate between the calcareous surface and calcium hydroxide deposited on the aggregate provided a continuity of crystal structure between the two, thus promoting the setting up of adhesion of the epitaxial type.

Farran's work on various types of portland cement was continued and refined by several investigators<sup>(58-60, 111-114)</sup>, but as far as the present author is aware, no similar study on high alumina cement was published since 1956. Therefore, it was considered essential to study the effect of conversion on the microstructural features of the interface between various aggregate materials and HAC pastes and to deduce its effect on the paste-aggregate bond. A scanning electron microscope equipped with a KEVEX energy dispersive X-ray analysis unit, which proved useful in related investigations, was employed throughout this part of the research. Differential thermal analysis (DTA) was also used.

## 6.2 EXPERIMENTAL PROCEDURES

### 6.2.1 SUBSTRATE PREPARATION

Four types of substrates were used, viz glass, Alag, granite, and limestone aggregates. The glass was in the form of microscope slides while aggregate sections were prepared from large pieces of their various materials. The aggregate sections, shown in Figure 6.1, were initially sawn using a diamond wheel and then ground against wet emery papers. The ground sections were then polished flat using a 6  $\mu$  m diamond lapping compound and were finally washed in acetone. Sections of low porosity limestone were immersed in water for a few hours and then surface dried prior to casting in order to minimise absorption of the water in the cement paste.

## 6.2.2 SPECIMEN PREPARATION AND TEST CONDITIONS

Pastes made at 0.4 water-cement ratio were mixed for 3.5 minutes using deionised water and cast directly on to the horizontal surfaces of the various substrates. To prevent the top face from crumbling after surface drying, a glass slide was placed on the paste and 'blu-tac' was used to form spacers between the slide and the various substrates (Figure 6.2). The specimens were then placed at 10°C in sealed plastic containers together with a commercial CO<sub>2</sub> adsorbent and allowed to hydrate at 100% R.H. for 24 hours, when they were either prepared for testing as 'unconverted specimens' or transferred to similar curing conditions but at 45°C. Specimens prepared with glass were tested after 2, 4, 6 and 10 days to monitor the changes in the interfacial region with subsequent exposure to high temperatures. After one month of curing at 45°C, specimens prepared with all substrates were investigated, as 'fully converted specimens'.

## 6.2.3 PASTE SEPARATION AND ANALYSIS

After curing for the desired length of time, the specimens were immediately transferred to a vacuum desiccator and continuously evacuated over a liquid nitrogen trap for 2 days. At the end of the drying process, the lower substrate section and the upper glass slide were separated and the paste was removed. A small piece of each specimen was prepared for SEM and elemental analysis as described in section 2.6. Thermal analysis was carried out on some specimens to determine the chemical composition of the contact zones. Thin layers were scraped with a razor and the resulting powder from each layer (0.05g) was diluted with alumina and tested as described in section 2.4. Specimens from a 20 year old concrete bridge made of HAC were also available for similar tests. Pieces of

concrete were broken and internal fragments from regions of interest were collected.

## 6.3 RESULTS AND DISCUSSION

### 6.3.1 UNCONVERTED SPECIMENS

This set of results deals with the interfacial zone developed between cement paste and various substrates after 1 day of curing in moist air at 10<sup>o</sup>C.

Figure 6.3 shows the typical features of the paste side of the interface with glass slides, while Figure 6.4 shows the X-ray spectrum obtained from this surface. Even at high magnification, as seen in Figure 6.5, this film which usually has the same gloss as the glass on which it was originally deposited still appears smooth with visible cracks. Although the contact zone was almost completely removed with the paste, small fragments which adhered to the glass surface resulted in holes, or 'windows' through which the detailed microstructural features of this region were observed. Figures 6.6, 6.7 and 6.8 which show these fractured areas at various magnifications indicate that the bulk of the contact zone is a porous body made up of thin platelets stacked together. Figures 6.9 and 6.10 show the EDXA analysis of the white platelets and the dark background in Figure 6.8. The analysis of these platelets, which is quite different from that of the underlying material, indicates a C/A ratio of about 2 and the presence of some iron (Figure 6.4). Although this may be at odds with the finding of Farran<sup>(22)</sup> who reported the C/A ratio to be unity in similar conditions, yet it seems to agree with what was stated by Lea<sup>(115)</sup> that plates of C<sub>2</sub>(AF)H<sub>8</sub> were, among other compounds, formed on the hydration of high

alumina cement on a microscope slide. However, when this interfacial layer was thermally analysed the hydrates which should have normally been detected at this curing temperature (i.e. alumina gel,  $CAH_{10}$ , or  $C_2AH_8$ ) were absent. The formation of this zone may have started by the deposition of a solid solution on the glass surface, which rapidly precipitated in the form of platelets whose dimensions seem to be of the order of one half to one  $\mu m$  across.

In general, similar phenomena were observed with polished sections of Alag and granite aggregates, but significant departure from the pattern was noted with the type of limestone used in this investigation. The interfacial film was substituted by a discontinuous layer with a higher calcium content and small quantities of sulphur (Figures 6.11 and 6.12). In isolated regions, however, limestone exhibited an interfacial film similar to the other three in continuity, but lacking their smoothness, and this is clear in Figures 6.13 and 6.14. In addition to the variations observed on the paste side of the interface with limestone, a relatively large proportion of cement matrix with traces of sulphur was seen adhering to the aggregate surface which showed similar traces. Figure 6.15 shows the general appearance of the aggregate side of the interface whose elemental analyses are provided in Figure 6.16 which refers to the adhering film, and Figure 6.17 which refers to the aggregate surface.

In spite of the differences encountered with limestone, there was a good contact between the unconverted paste and all the substrates against which it has been placed, indicating a solid to solid bond.

### 6.3.2 FULLY CONVERTED SPECIMENS

The results reported in this section are mainly for specimens similar to those discussed in section 6.3.1, but after being exposed to saturated air at 45°C for 1 month. Analytical and morphological studies on the interfacial zone developed between the converted mortar and aggregates or steel in a demolished 20 year old HAC concrete bridge are also reported.

In presenting the results, those for the cement-glass interface will be dealt with first and will be followed by those for the other substrates and the bridge.

#### 6.3.2.1 CEMENT-GLASS INTERFACE

Figure 6.18 which shows the general features of the paste side of the interface with a glass slide indicates the formation of large *regular* crystals surrounding, in some regions, pools of smaller crystals. Both types of crystals seen at higher magnification in Figures 6.19 and 6.20 are, as indicated by the EDXA analysis, crystallised alumina (Figure 6.21).

X-ray mapping was also made to trace the concentration of aluminium and calcium in the contact zone. The vertical edge<sup>(LHS)</sup> in Figure 6.22 shows the paste side of the interface with a glass slide while the rugged horizontal plane<sup>(RHS)</sup> represents the bulk of the converted paste. Figures 6.23 and 6.24 indicate that the interfacial zone is mainly composed of aluminium, while the elemental distribution in the bulk of the paste roughly corresponds to that of  $C_3AH_6$ . The spectra relating to the two regions are shown in Figures 6.25 and 6.26. Figure 6.27 shows the preparation of the specimen and its orientation in the SEM. The same

was used to estimate the thickness of the crystallised alumina layer by tilting the specimen until the interface was hidden as shown in Figure 6.28. X-ray maps were then made, in Figure 6.29, for calcium and aluminium distribution, the idea being that the retreat of the calcium away from the specimen's edge may give an estimate of the thickness of the alumina layer, which in the case of Figures 6.30 and 6.31 was found to be about  $8\mu\text{m}$ . The thickness was verified by an alternative procedure in which the electron beam was caused to travel across the alumina layer until the calcium region was reached. The thickness after which the calcium started to appear was about  $10\mu\text{m}$ .

This alumina was thermally analysed and found to be gibbsite ( $\text{AH}_3$ ). This is clear from Figure 6.32 in which the change in hydrate composition was monitored in the successive layers. The DTA curves indicate a sequence from the paste's interface gibbsite followed by a mixture of  $\text{C}_3\text{AH}_6$  and  $\text{AH}_3$ , the normal conversion products, whereas the EDXA results show a Ca-rich layer intermediate between the gibbsite crystals and the interior of the converted paste. This is illustrated in Figure 6.33 which shows the elemental analysis of the underlying material seen in Figure 6.34. It is significant to state that the gibbsite layer, which had a dark grey colour, was found to be much stronger than the fully converted bulk. This was observed during scraping for DTA samples.

On the other side of the interface, the glass surface, which is represented by the black regions in Figures 6.35-6.37, was sometimes almost bare of any hydrate but in most cases a thin film rich in calcium was found adhering to the glass with crystallised alumina loosely

scattered on top. The elemental analysis of this film is shown in Figure 6.38, in which the dotted peak represents Si X-rays originating from the glass.

### 6.3.2.2 CEMENT-AGGREGATE INTERFACE

Figures 6.39-6.41 show the general features of the paste side of the interface with Alag, granite and limestone aggregates, while in Figure 6.42, a spectrum typical of those obtained with all surfaces indicates a marked degree of similarity with  $AH_3$  crystals observed earlier in the case of glass. However, closer views of these surfaces reveal the crystallised alumina in various shapes and sizes. Figures 6.43-6.46 show the crystals obtained with Alag aggregate while Figures 6.47 and 6.48 show those obtained with granite and limestone aggregates respectively.

In contrast with this similarity on the paste side of the interface, the aggregates behaved differently in retaining hydrated phases of various composition, with granite having the least retention.

Alag aggregate showed a marked degree of overall superficial chemical interaction. To appreciate this, reference is made to Figures 6.49 and 6.50. The dry, polished surface of the aggregate in Figure 6.50 shows grey prismatic  $CaO \cdot Al_2O_3$  and white, highly reflecting, iron constituents as identified by Lea<sup>(116)</sup>. EDXA analysis of both areas are shown in Figures 6.51 and 6.52. Comparison with Figures 6.53 and 6.54 for the Alag surface separated from the converted paste reveals apparent swelling of the white area and etching of the grey area, with a deposition of crystallised alumina which in some cases is seen occupying considerable areas of the surface as in Figure 6.55.

The elemental analysis for the aggregate surface is shown in Figure 6.56. In a few cases, a thin layer indicated by a triangle in Figure 6.57 was seen on the aggregate. More rarely still, fragments from this layer were seen on the top of the crystallised alumina on the paste side, Figure 6.58. EDXA analysis of this thin layer is shown in Figure 6.59.

With limestone, well characterised ettringite ( $3\text{CaO} \cdot \text{Al}_2\text{O}_3 \cdot 3\text{CaSO}_4 \cdot 30\text{-}32\text{H}_2\text{O}$ ) needles, which may be prepared by the treatment of monocalcium aluminate solution with  $\text{CaO}$  and  $\text{CaSO}_4 \cdot 2\text{H}_2\text{O}^{(117)}$ , were seen projecting from the aggregate surface with some attached alumina crystals, Figures 6.60-6.62. The high content of sulphur in this growth is confirmed by the elemental analysis in Figure 6.64, while the same sulphur traces, found on the aggregate surface before conversion remained unchanged Figure 6.65. However, the fan shape of these needles in Figure 6.61 suggests that their base is in fact in the limestone. Part of these ettringite needles were observed sprinkled on the paste side of the interface, Figure 6.63. It is important to state that the contact between the ettringite's top and gibbsite is an indication of the space between the substrate and the paste.

The bare granite surface shown in Figure 6.66, whose elemental analysis is in Figure 6.67, is another piece of evidence indicating the absence of direct contact between the substrates and the bulk of the paste.

The results obtained with the various substrates suggest that when the contraction happened on crystallization, the paste lost contact with the surface against which it was placed except for tiny

chips whose further development is strongly influenced by the type of substrates. Further crystallization takes place away from the substrate, eventually resulting, in all cases, in gibbsite crystals of high variability of shape and size. On rare occasions, small parts of the fragments developed on the substrates' surface were seen on the paste side of the interface.

Another example of the absence of direct contact between the substrates and the converted paste and the formation of intermediate phases between the two materials is shown in Figures 6.68-6.71 which are for the paste side of specimens from a 20 year old HAC concrete bridge. In these photographs, the alumina is seen, in some regions, covered with a white lime rich layer. Figures 6.72 and 6.73 show the elemental analysis of the crystallised alumina and the lime layer respectively. On the other side of this interface, the aggregate surface shown in Figures 6.74 and 6.75 is largely covered in lime. Thermal analysis of the paste side of the interface with steel or aggregate in the same bridge shows without any doubt the formation of gibbsite (see Figure 6.76). In this figure, curve 2, representing the cement-aggregate interface, shows an endothermic effect with a peak at  $740^{\circ}\text{C}$  which could have resulted from decarbonation of  $\text{CaCO}_3$ , since this compound is known to give a peak at  $800^{\circ}\text{C}$ <sup>(118)</sup>. This may explain the presence of a lime rich layer between the aggregate and the converted paste.

### 6.3.3 THE CONVERSION PROCESS AT THE INTERFACE

The similarity between the paste side with different substrates in the fully converted case prompted monitoring of the formation of the crystallised alumina at 45<sup>o</sup>C over periods of 2, 4, 6 and 10 days using glass slides as substrate.

#### 6.3.3.1 MORPHOLOGICAL ANALYSIS

After 2 days (Figures 6.77 and 6.78)

---

The smooth surface of Figure 6.3 lost its gloss and irregular granules 1-2  $\mu$ m across were observed.

After 4 days (Figures 6.79 and 6.80)

---

Crystallization was well underway, and the crystals were becoming more regular and larger in size, the size being 2-4  $\mu$ m across.

After 6 days (Figures 6.81 and 6.82)

---

*Regular* crystals 3-4  $\mu$ m across were observed covering most of the surface.

After 10 days (Figures 6.83 and 6.84)

---

Practically the only change was the increase in the size of the crystals, which extended to about 6  $\mu$ m.

#### 6.3.3.2 ELEMENTAL ANALYSIS

As indicated in Figure 6.87, the crystallised phase after 6 days was purely alumina. However whilst calcium was noted in the crystals

at early stages (Figures 6.85 and 6.86), this was probably due to the small size of the alumina crystals which allowed Ca X-rays to be collected from the background as this contained a high proportion of calcium (Figure 6.88).

#### 6.4 CONCLUSIONS

Examination of the paste side of the cement-glass interface, formed at 10°C, indicates that the interfacial zone between the two materials is made up of platelets <sup>which are thought to be composed</sup> of  $C_2(A,F)H_8$ . In general, similar phenomena were observed with Alag and granite aggregates but significant departure from the pattern was noted with the type of limestone used in this investigation. However, a good contact between the unconverted paste and all the substrates against which it had been placed was observed, which may signify a solid to solid bond.

A second group of experiments showed that the interfacial film initially developed between cement paste and the various substrates at relatively low temperatures was considerably influenced by further exposure to higher temperatures. Regardless of the substrate used, the paste side of the interfacial zone was found to convert to crystallised alumina which was proved to be gibbsite ( $AH_3$ ) of high variability of shape and size.

On the other side of the interface, the substrates behaved differently in retaining hydrated phases of various composition, with granite having the least retention. It is suggested that when contraction happened on crystallization, the paste lost contact with the surface against which it was placed except for tiny chips whose further development was strongly influenced by the type of substrate. Specimens

obtained from a demolished 20 year old HAC concrete bridge confirmed the findings of the fully converted case.

The absence of direct contact between the substrates and the bulk of the paste indicates a considerable loss of bond strength, and the presence of scattered alumina crystals on very limited areas of the substrates should in no way be taken as a sign of strength. However, the etching, swelling, and the presence of a dense gibbsite region on the Alag surface can result in different bonding characteristics which may contribute to the relatively high strength of converted Alag concretes previously discussed in section 6.1.



Limestone

Granite

Alag

Glass

Figure 6.1 The Different types of substrates

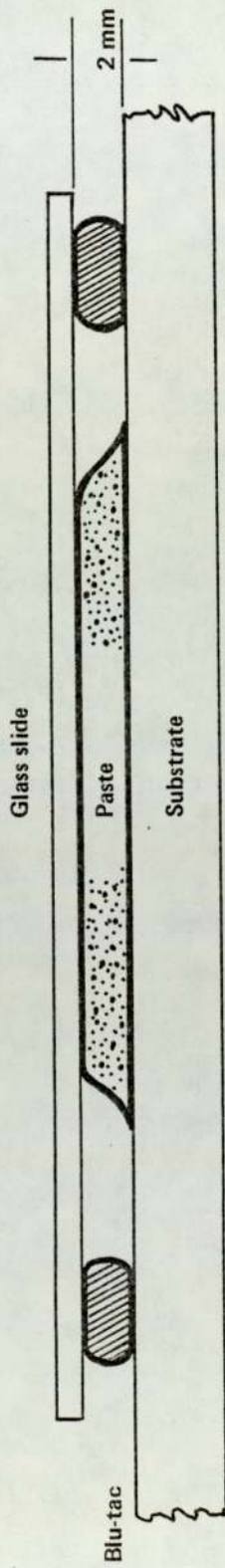


Figure 6.2 Specimen preparation for morphological studies



Figure 6.3 The general features of the unconverted paste side of the interface with a glass slide

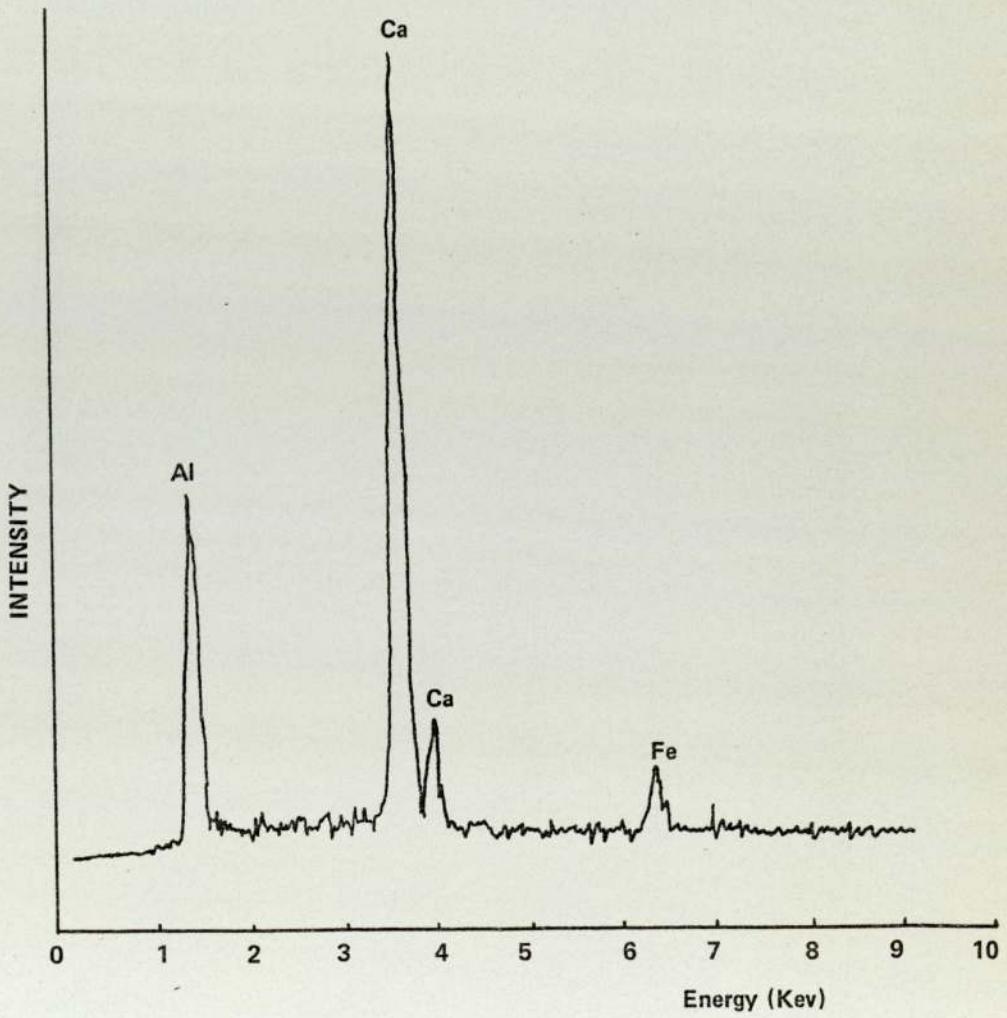


Figure 6.4 X-ray spectrum of the surface in Figure 6.3.



Figure 6.5 A higher magnification of the interfacial film in Figure 6.3



Figure 6.6 The general features of a window observed on the unconverted paste side of the interface with a glass slide

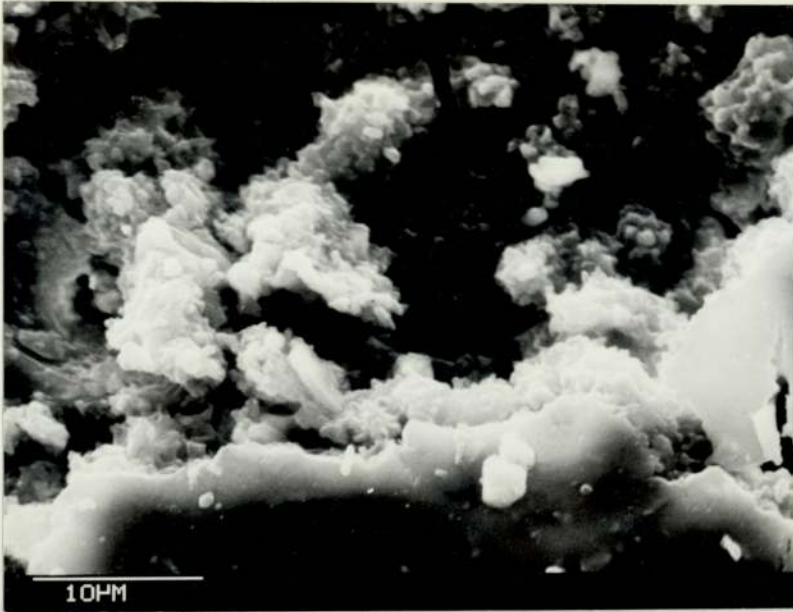


Figure 6.7 A higher magnification of a window similar to that of Figure 6.6.

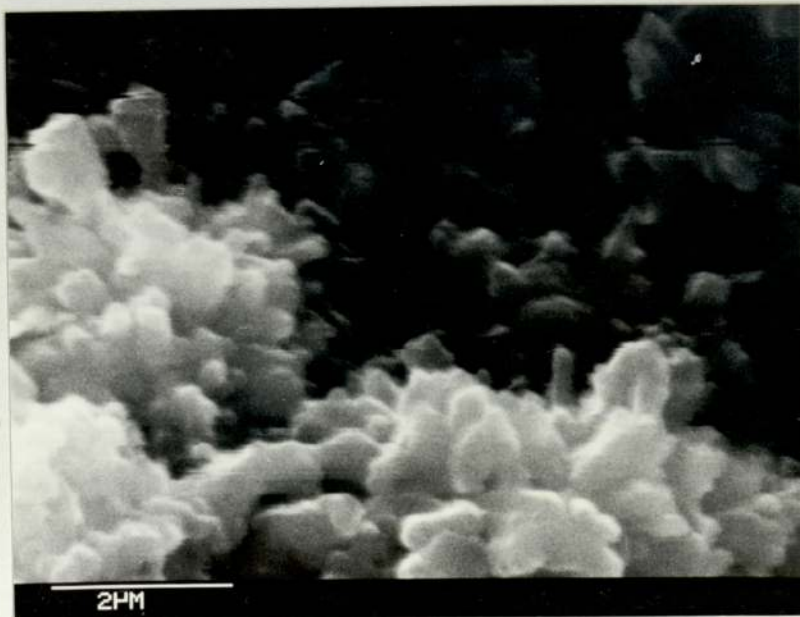


Figure 6.8 Small platelets of the unconverted paste side of the interface with glass

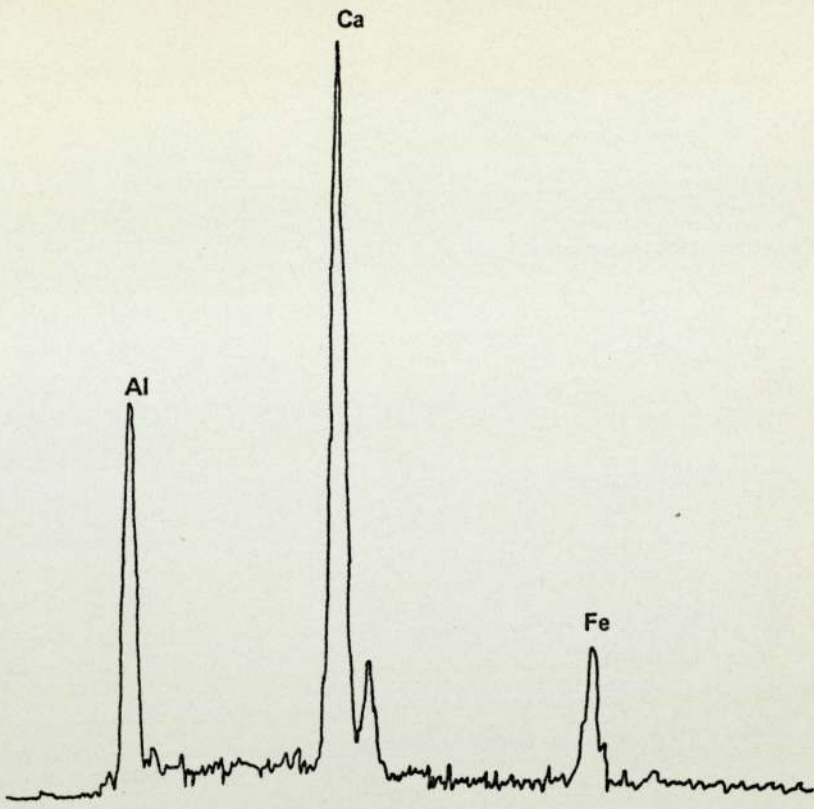


Figure 6.9 X-ray spectrum of the white platelets in Figure 6.8

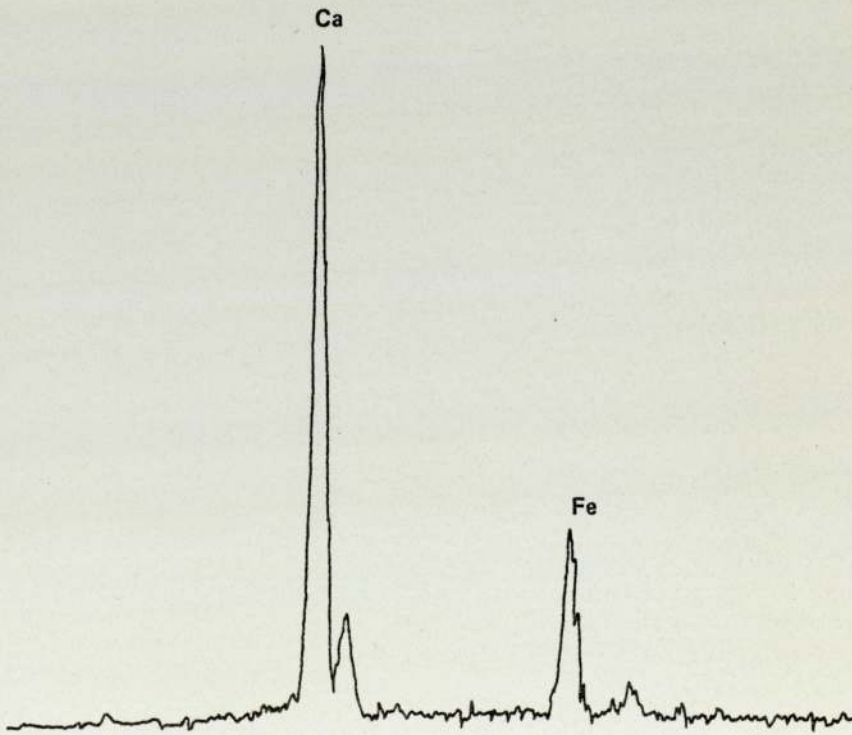


Figure 6.10 X-ray spectrum of the dark background in Figure 6.8

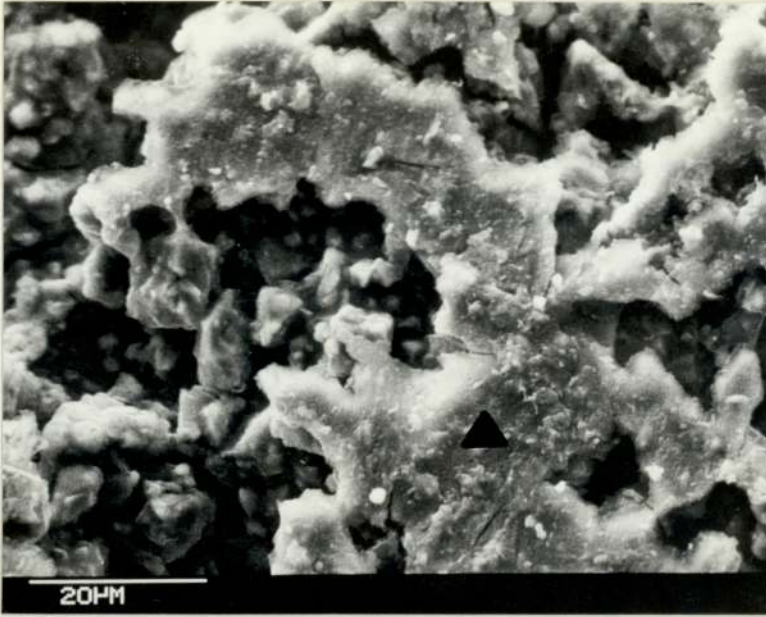


Figure 6.11 The general features of the unconverted paste side of the interface with a polished section of limestone

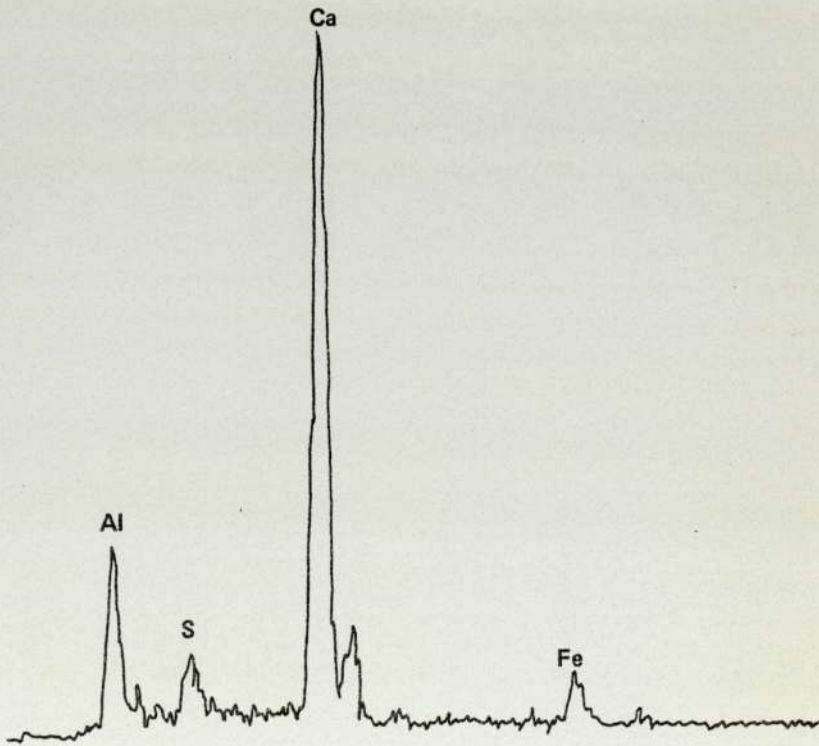


Figure 6.12 X-ray spectrum of the area marked by a triangle in Figure 6.11

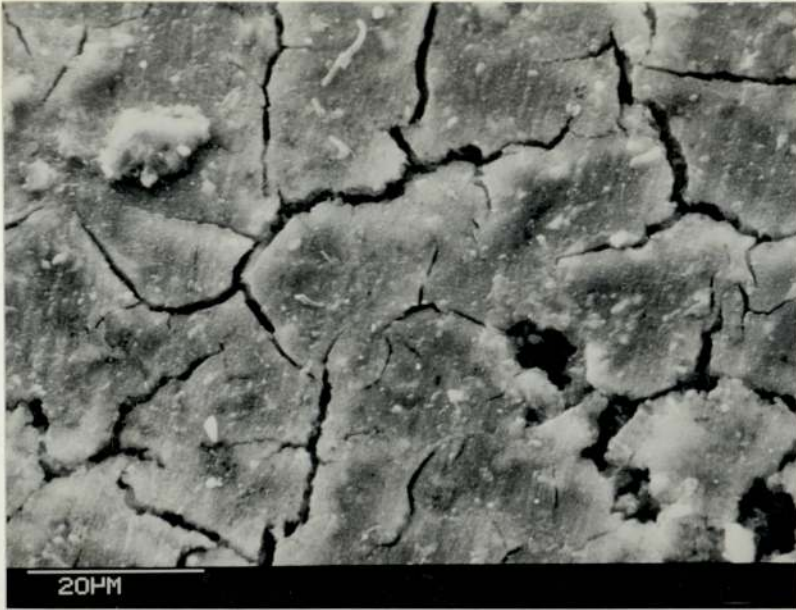


Figure 6.13 Typical features of the continuous regions observed on the unconverted paste side of the interface with limestone



Figure 6.14 A close-up of the surface shown in Figure 6.13

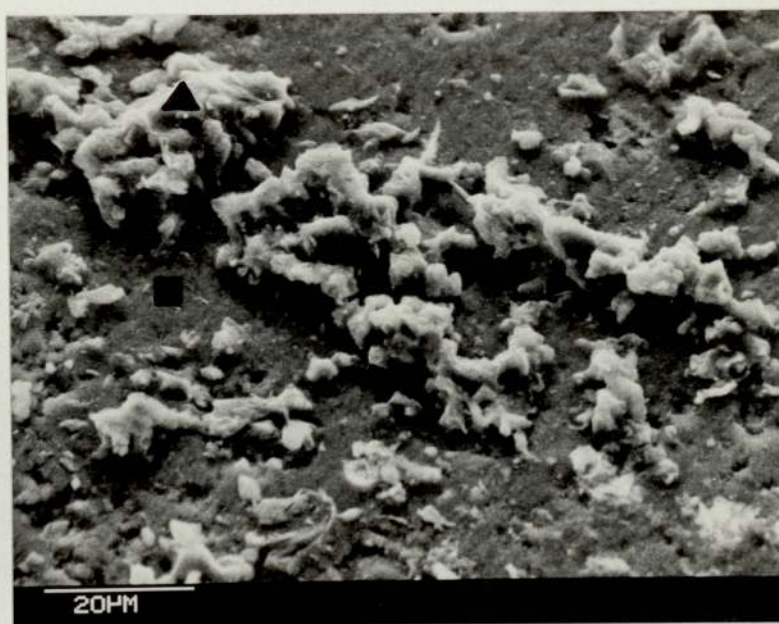


Figure 6.15 The general appearance of the limestone side of the interface with an unconverted paste

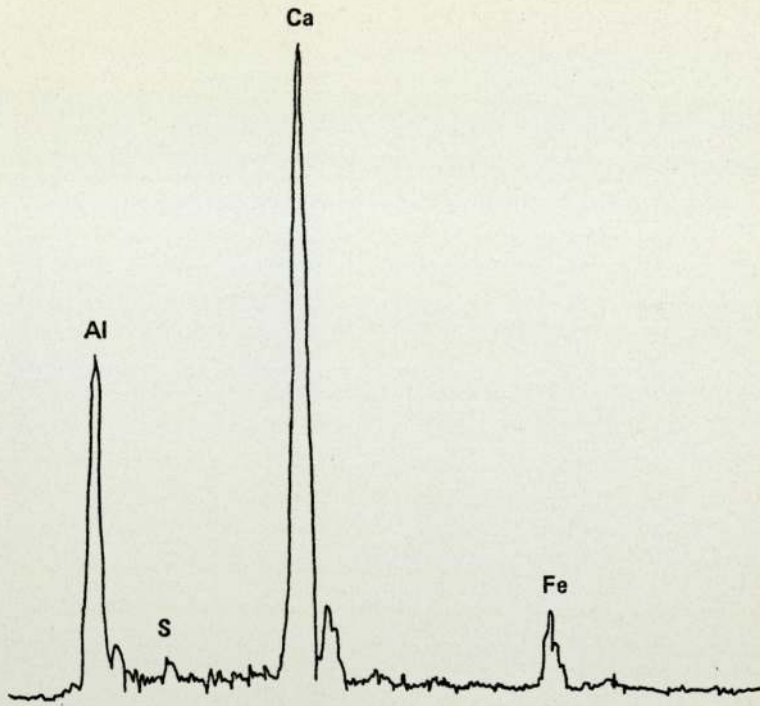


Figure 6.16 X-ray spectrum of the area marked by a triangle in Figure 6.15

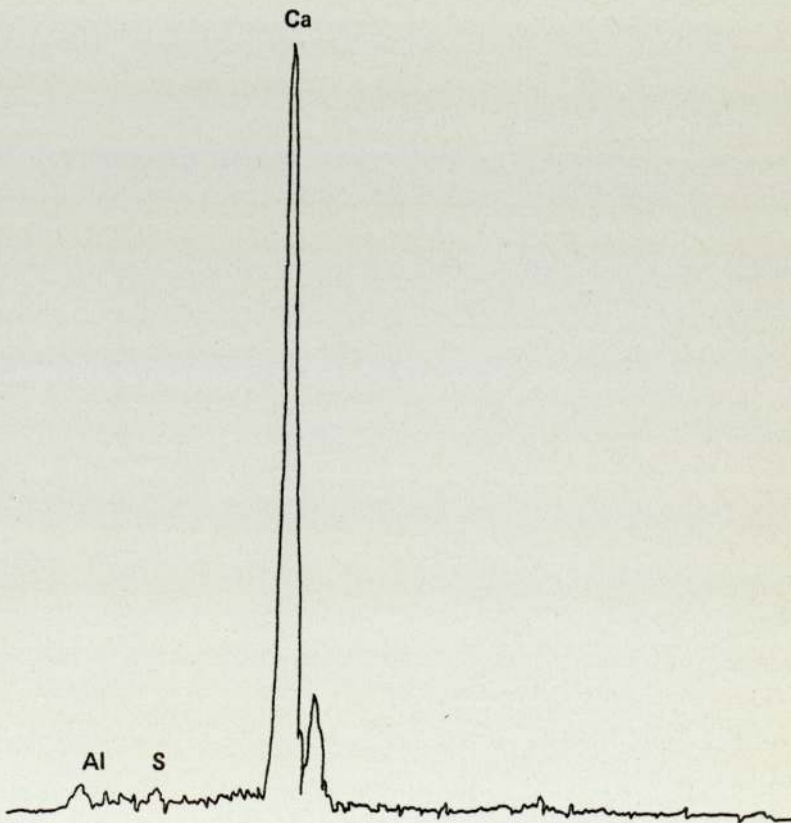


Figure 6.17 X-ray spectrum of the area marked by a square in Figure 6.15



Figure 6.18 The converted paste side of the interface with a glass slide

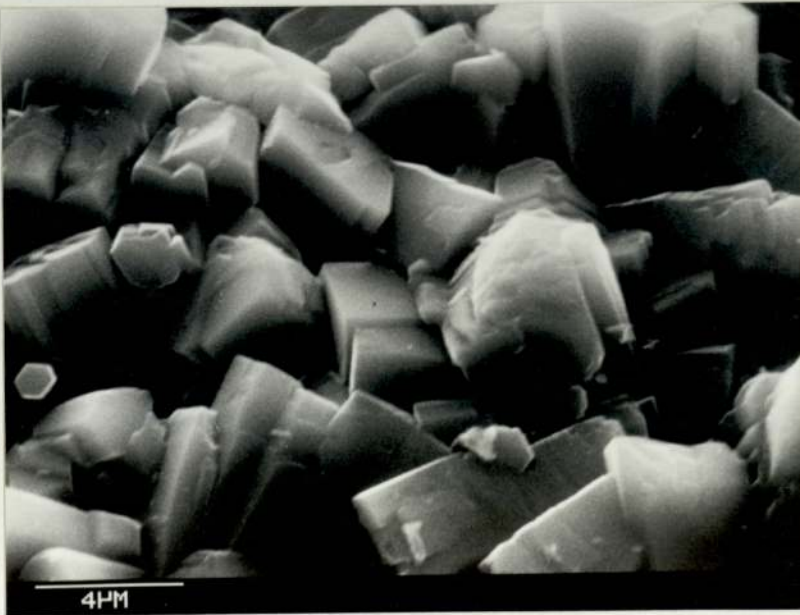


Figure 6.19 A close-up of the large crystals in Figure 6.18

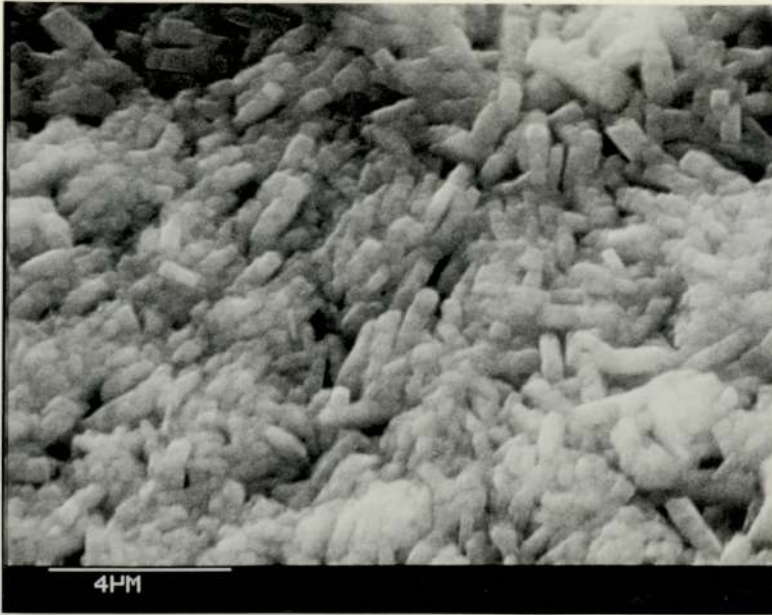


Figure 6.20 A close-up of the small crystals in Figure 6.18

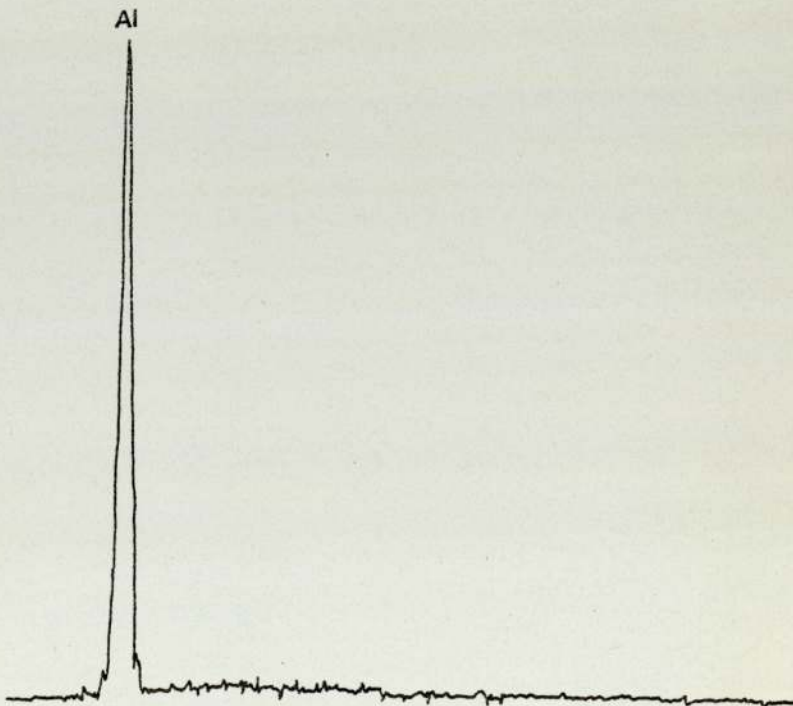


Figure 6.21 X-ray spectrum of the crystallised alumina in Figure 6.18

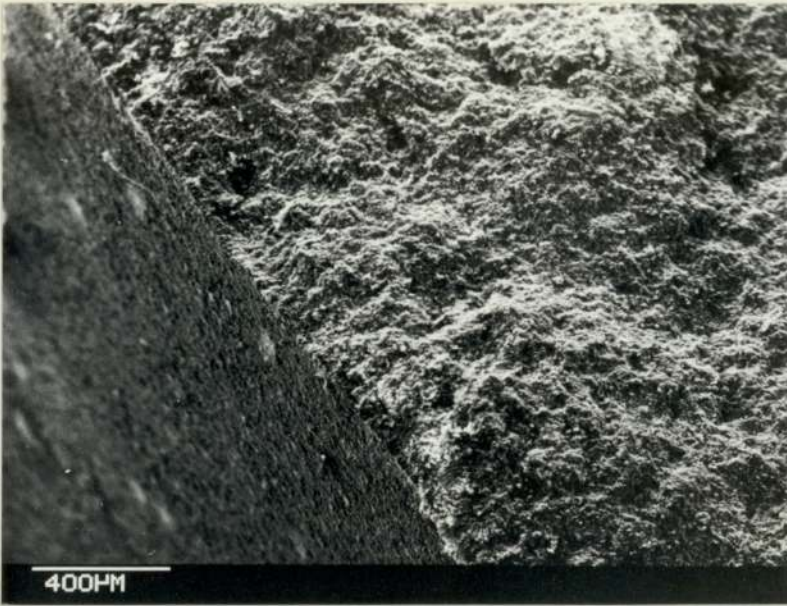


Figure 6.22 Scanning electron micrograph of the specimen in Figure 6.27



Figure 6.23 The distribution of aluminium on the two surfaces of Figure 6.22



Figure 6.22 Scanning electron micrograph of the specimen in Figure 6.27

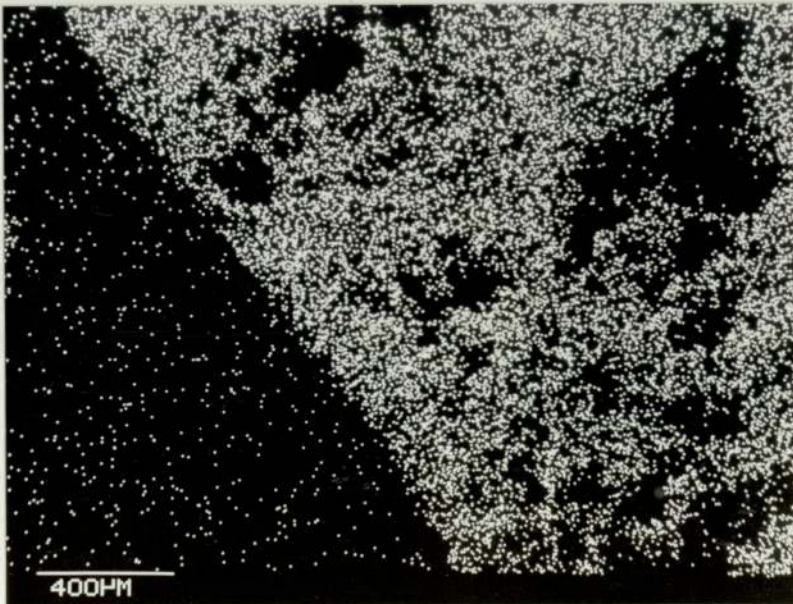


Figure 6.24 The calcium distribution for the two surfaces of Figure 6.22

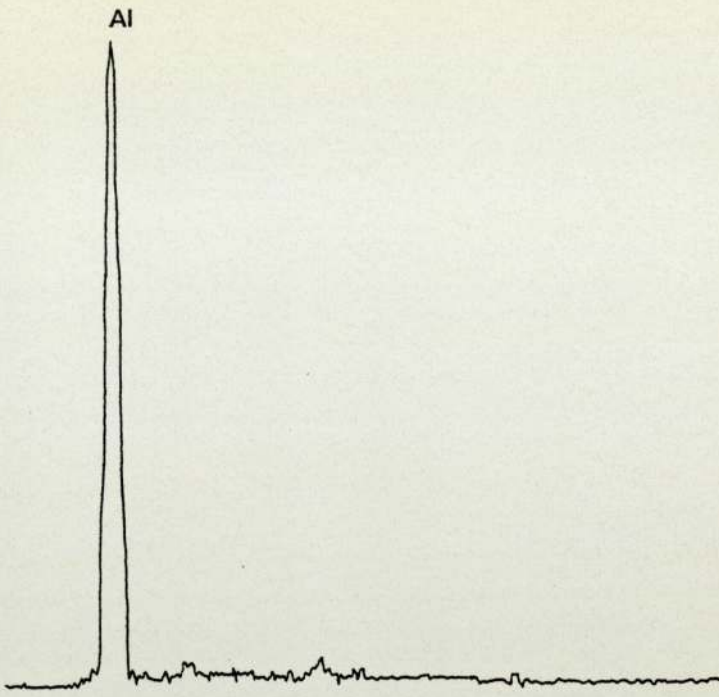


Figure 6.25 X-ray spectrum of the vertical edge in Figure 6.22

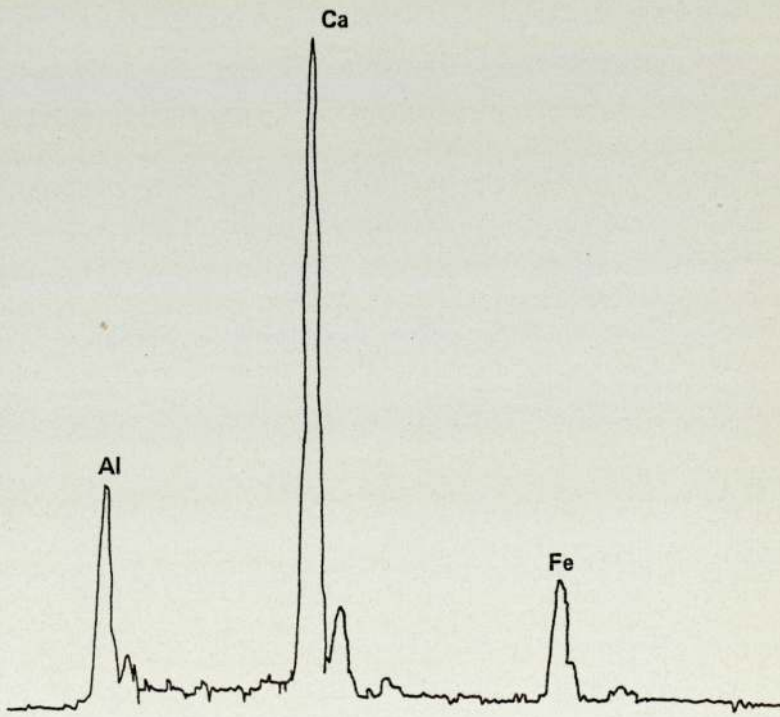


Figure 6.26 X-ray spectrum of the fractured paste in Figure 6.22

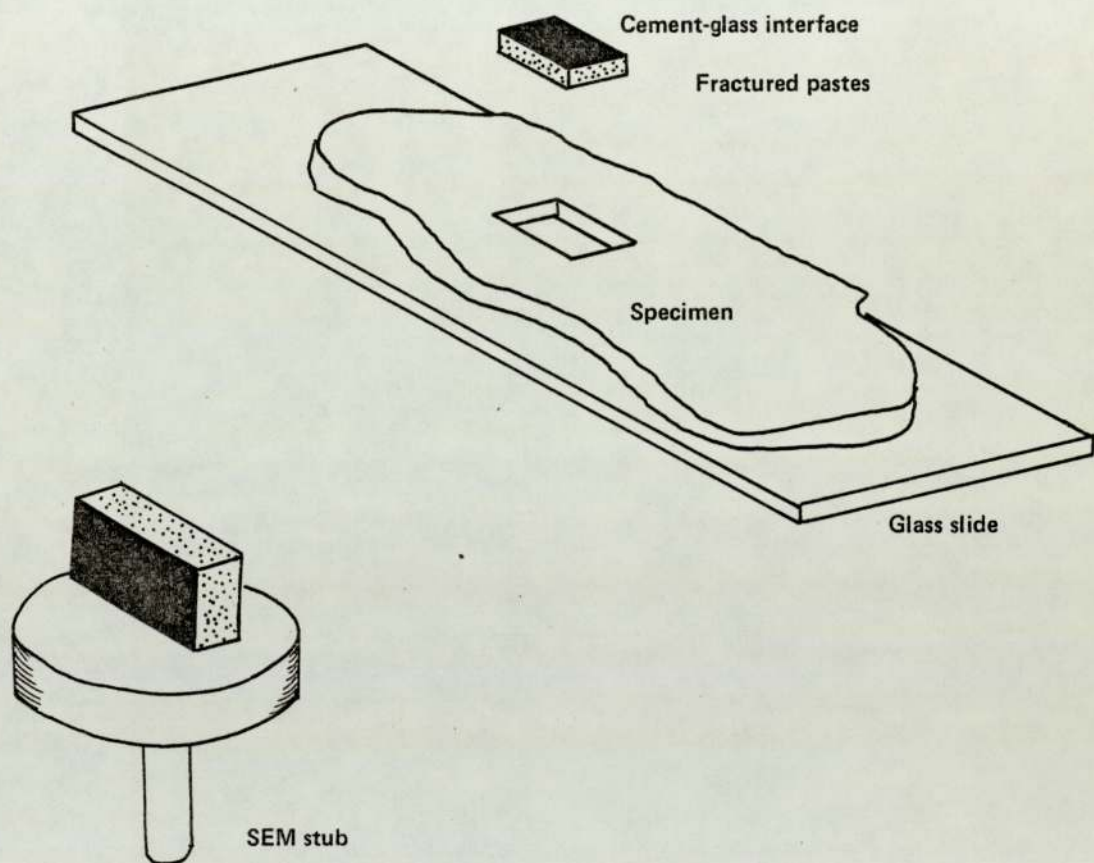


Figure 6.27 Preparation of the cross-section specimen and its orientation in the SEM



Figure 6.28 The edge of the fractured surface in Figure 6.22



Figure 6.29 A higher magnification of Figure 6.28

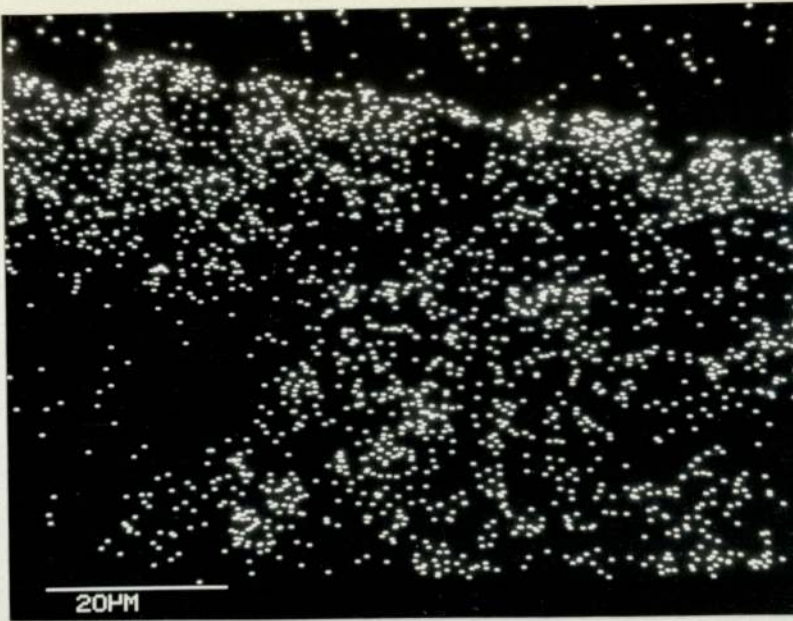


Figure 6.30 The aluminium distribution for the fractured surface of Figure 6.29



Figure 6.31 The calcium distribution for the fractured surface of Figure 6.29

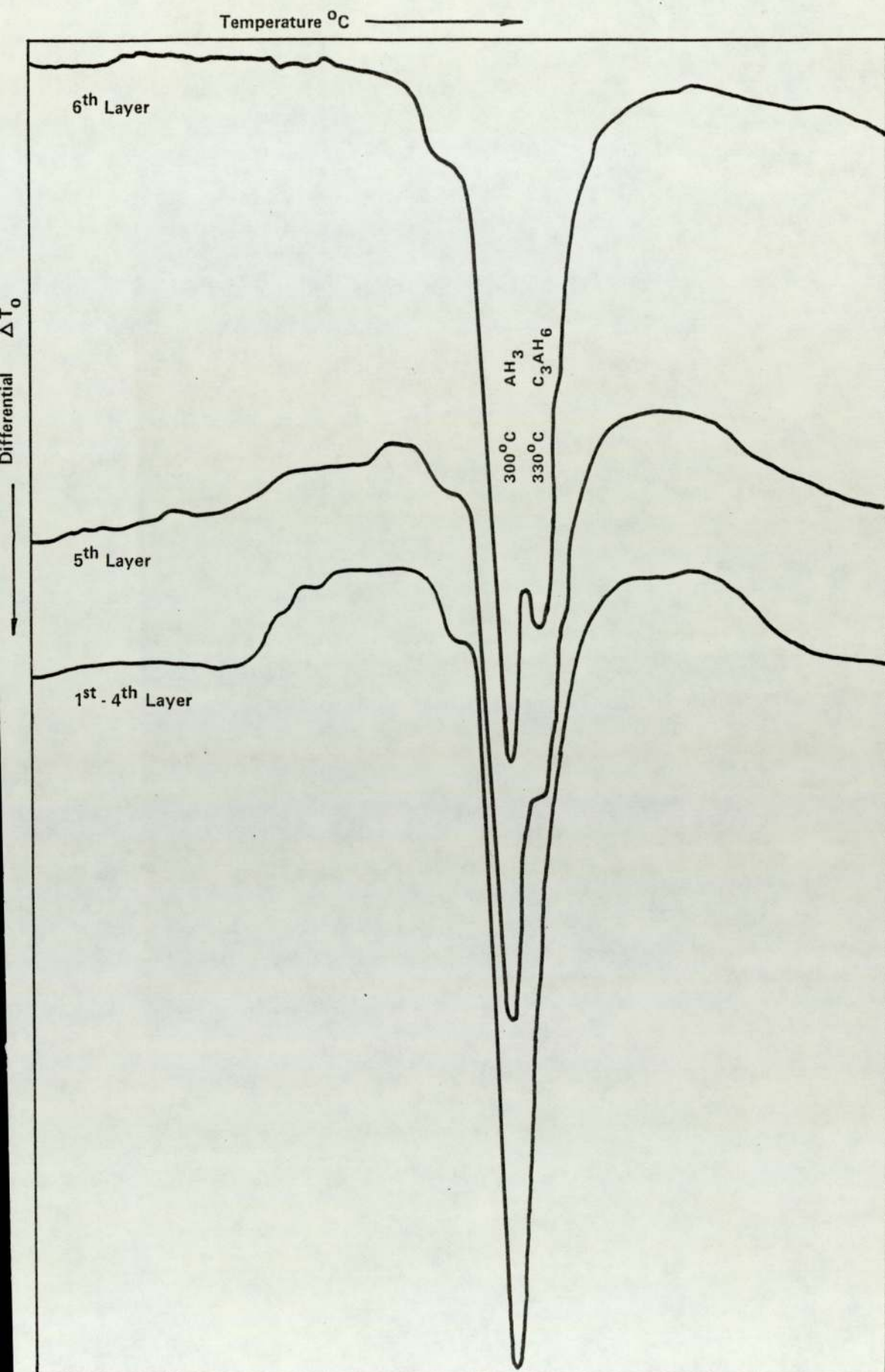


Figure 6.32 DTA thermograms of the converted paste side of the interface with a glass slide

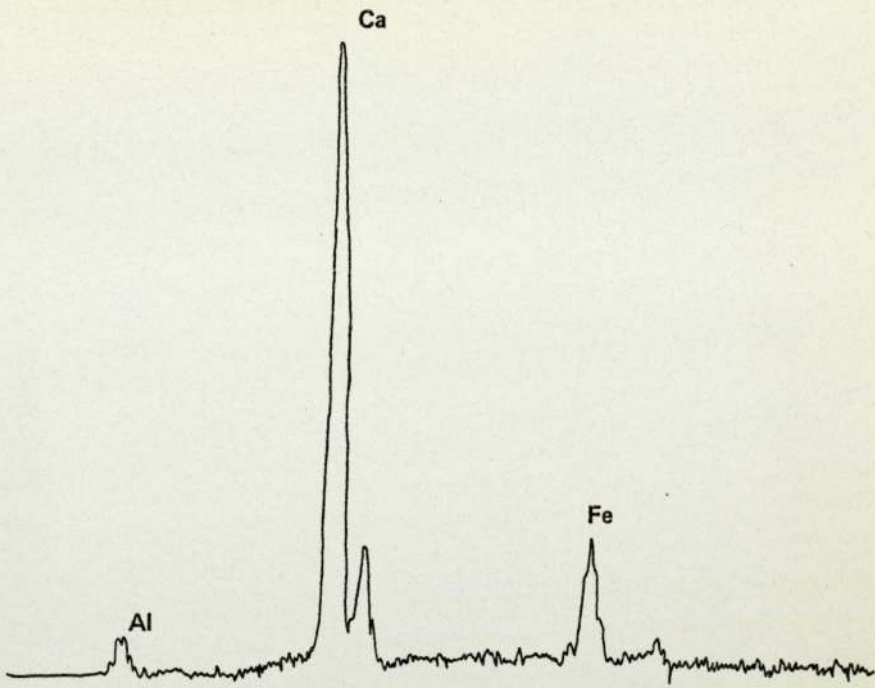


Figure 6.33 X-ray spectrum of the area marked by a triangle in Figure 6.34

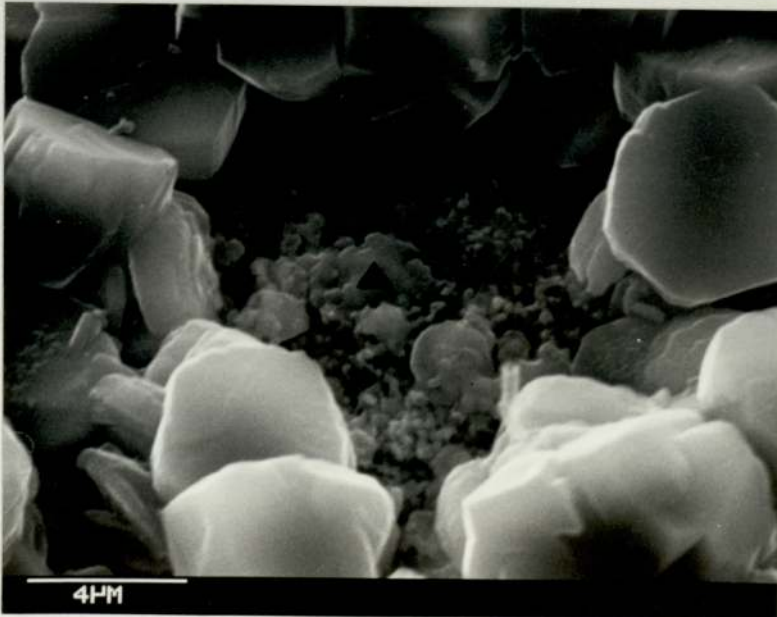


Figure 6.34 A close-up of the converted paste side of the interface with a glass slide

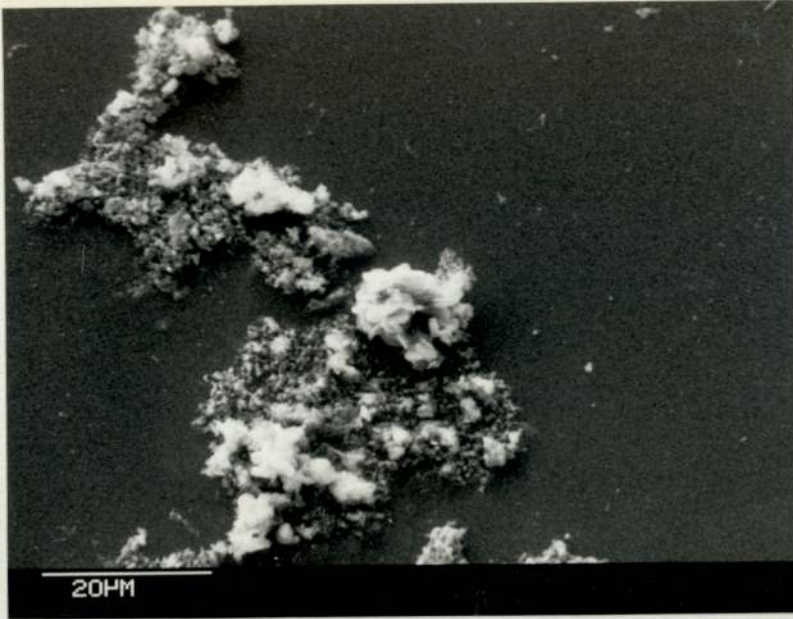


Figure 6.35 The glass side of the interface with a fully converted paste

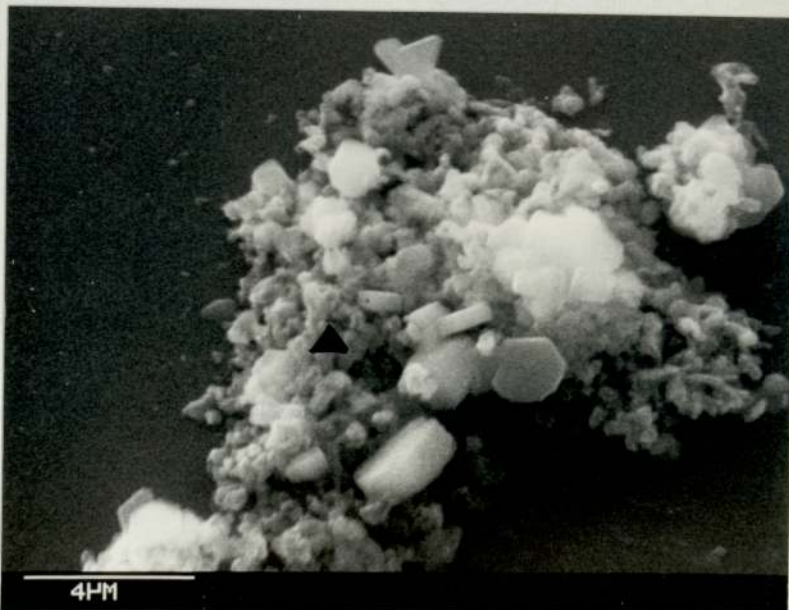


Figure 6.36 A higher magnification of the adhering film in Figure 6.35

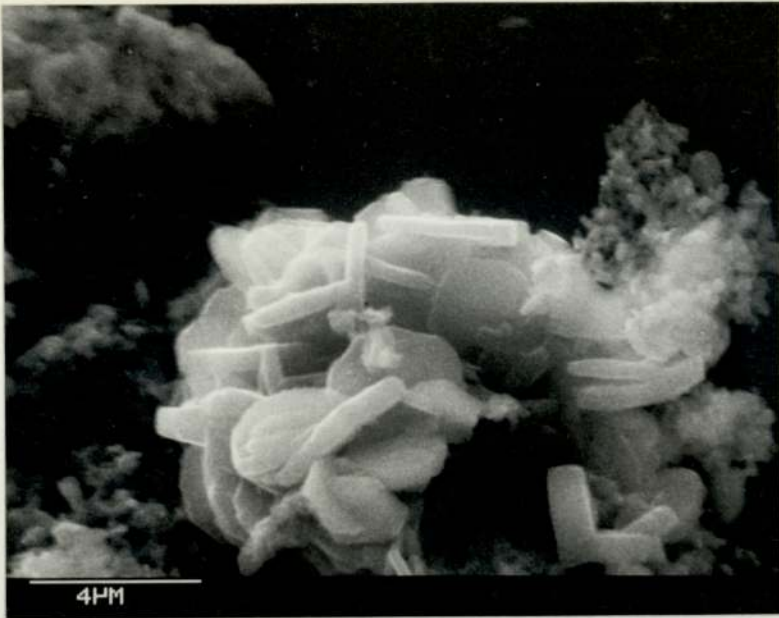


Figure 6.37 Crystallised alumina scattered on the top of the film adhering to the glass surface

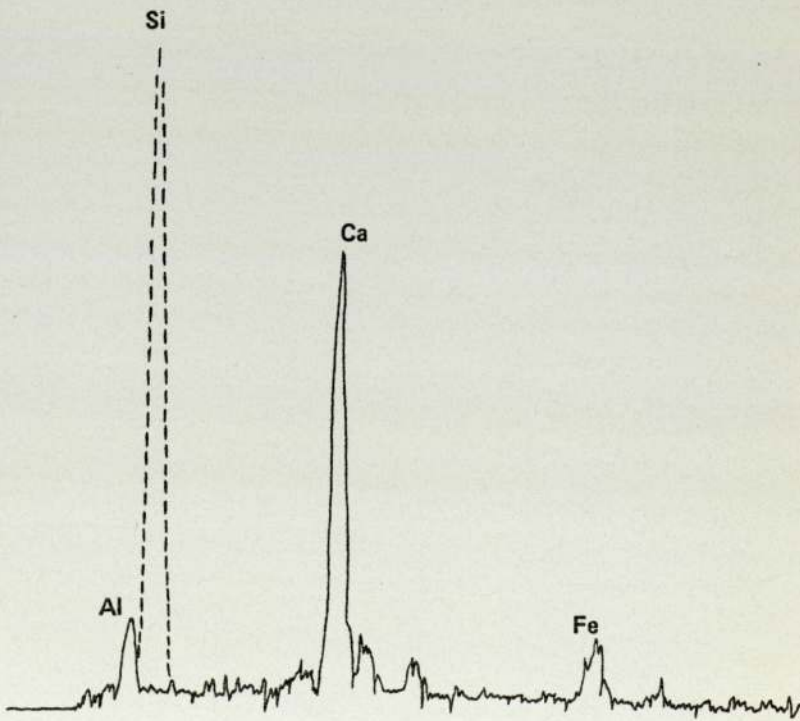


Figure 6.38 X-ray spectrum of the area marked by a triangle in Figure 6.36

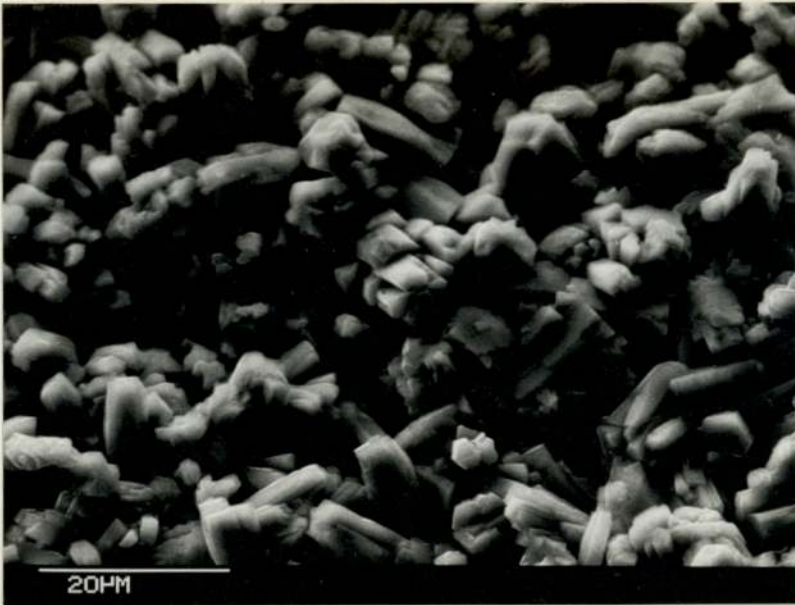


Figure 6.39 The general features of the converted paste side of the interface with Alag aggregate

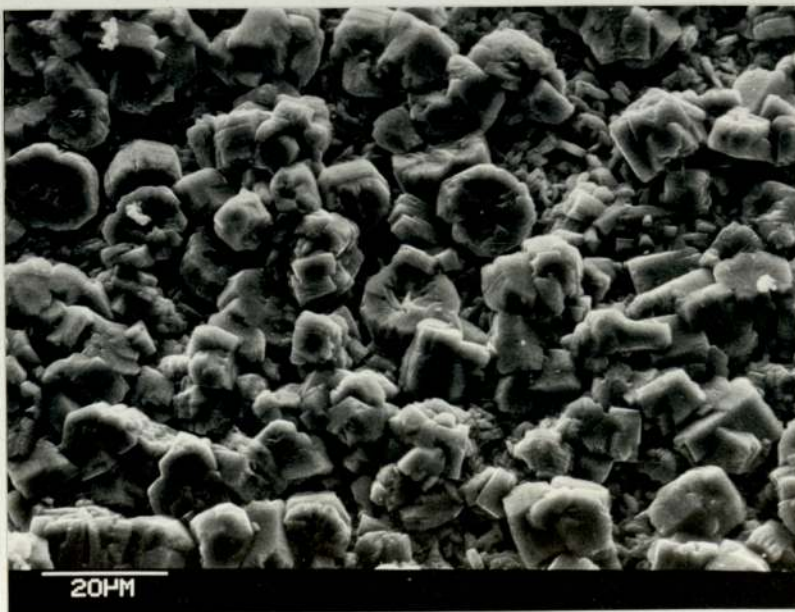


Figure 6.40 The general features of the converted paste side of the interface with granite

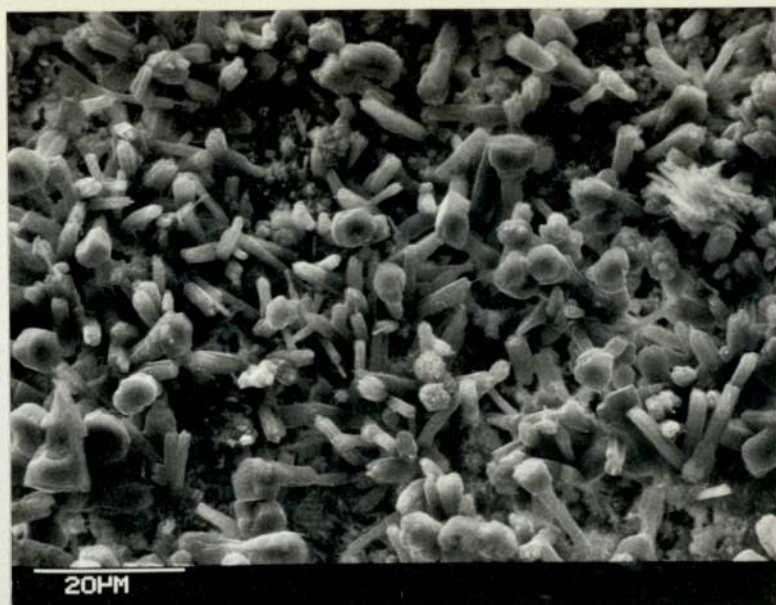


Figure 6.41 The general features of the converted paste side of the interface with limestone

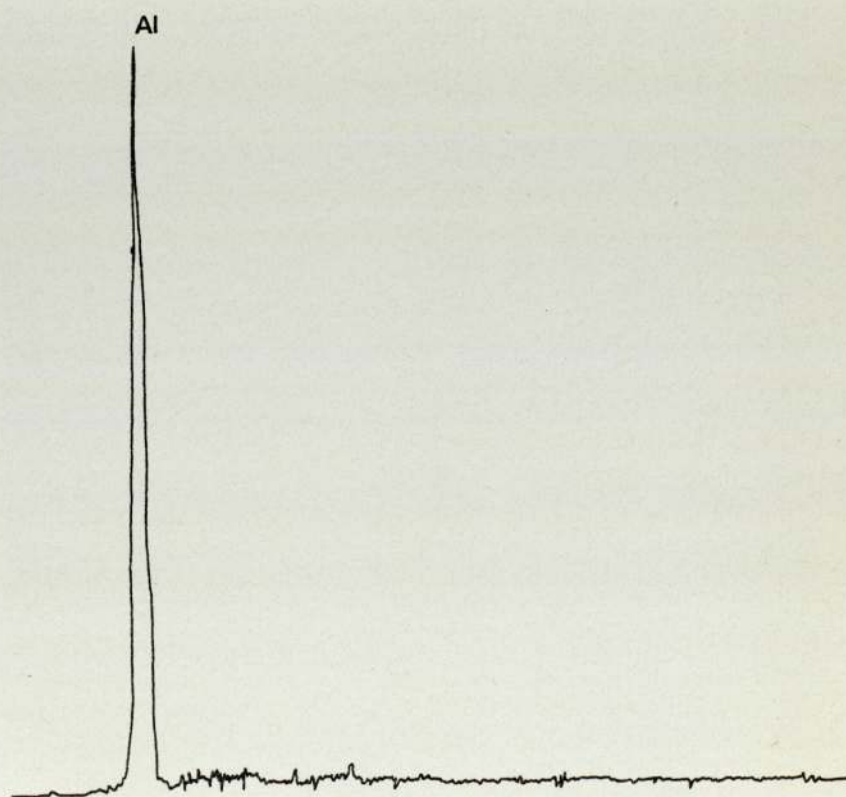


Figure 6.42 X-ray spectrum of the converted paste side of the interface with aggregates



Figure 6.43 One of the shapes of gibbsite crystals on the converted paste side of the interface with Alag aggregate

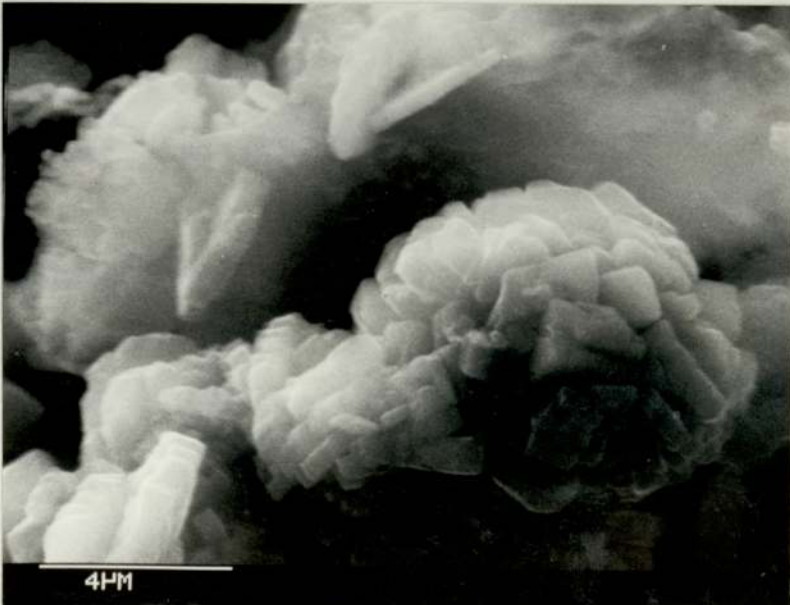


Figure 6.44 Another shape of gibbsite on the converted paste side of the interface with Alag aggregate

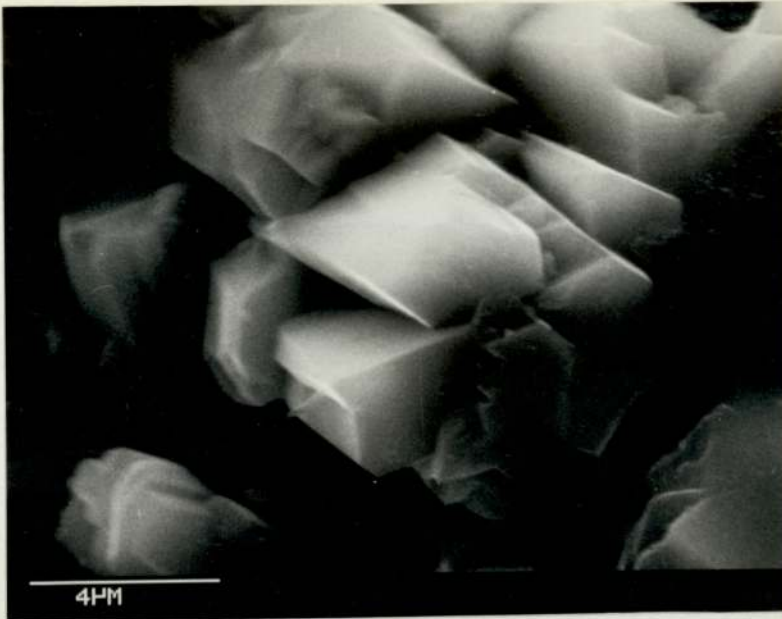


Figure 6.45 A close-up of the center of Figure 6.39

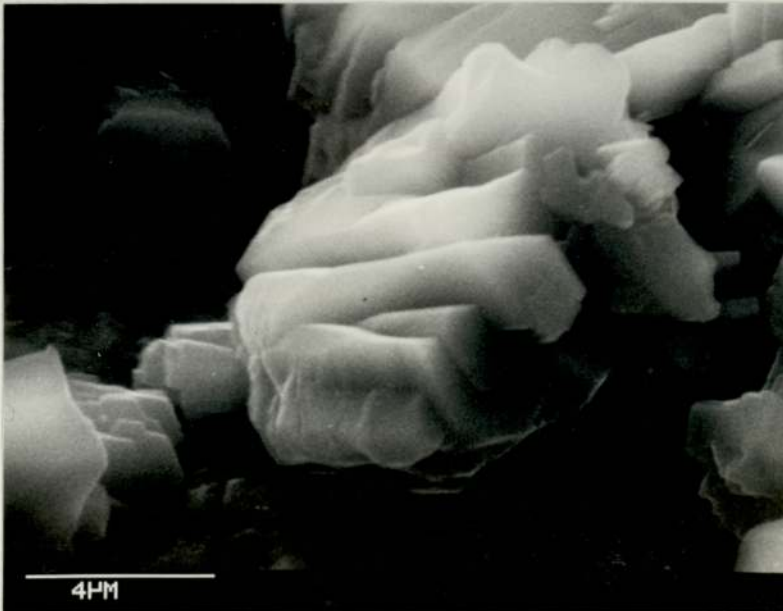


Figure 6.46 A different shape of gibbsite on the converted paste side of the interface with Alag aggregate

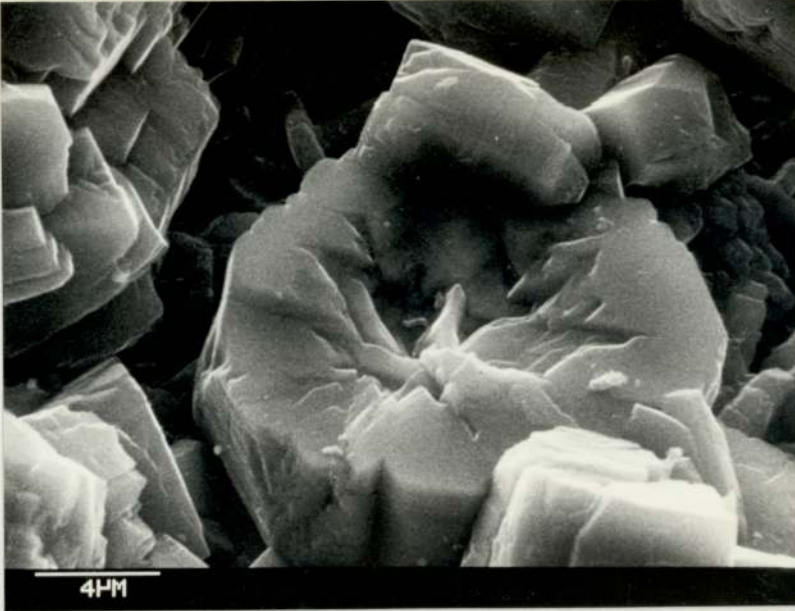


Figure 6.47 A close-up of the center of Figure 6.40

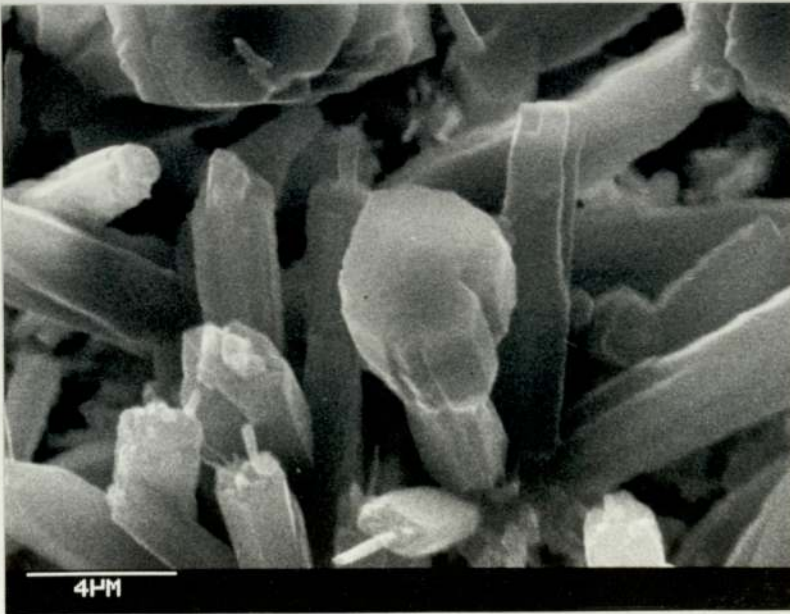


Figure 6.48 A close-up of the center of Figure 6.41

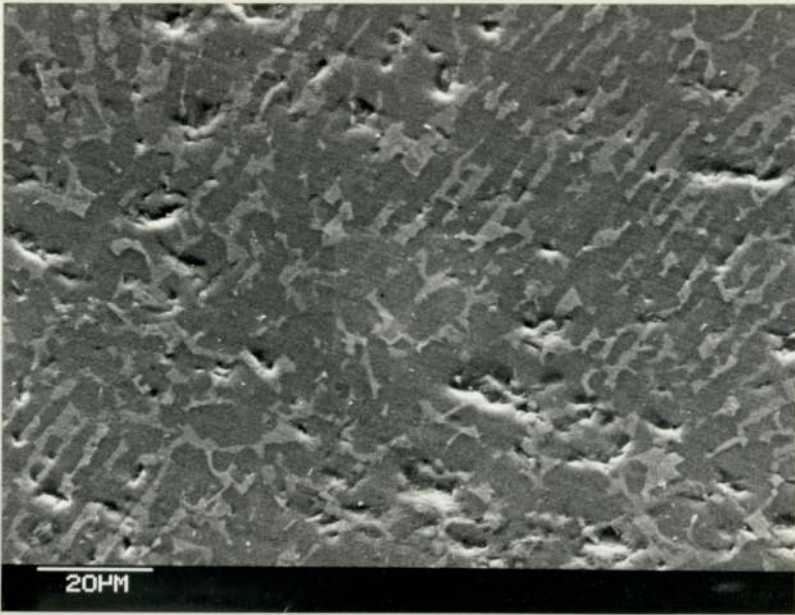


Figure 6.49 The general features of a polished surface of Alag aggregate



Figure 6.50 A higher magnification of the Alag surface in Figure 6.49

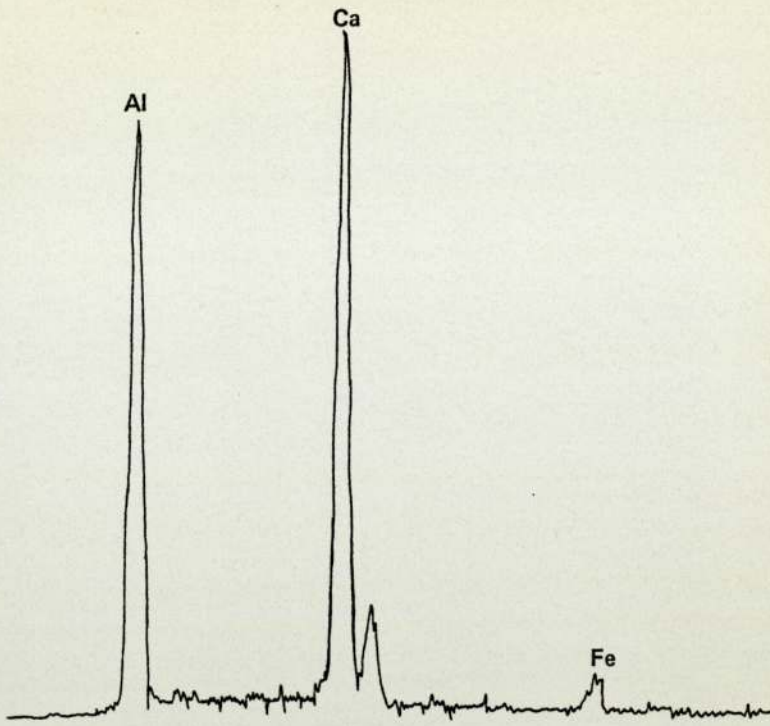


Figure 6.51 X-ray spectrum of the area marked by a triangle in Figure 6.50

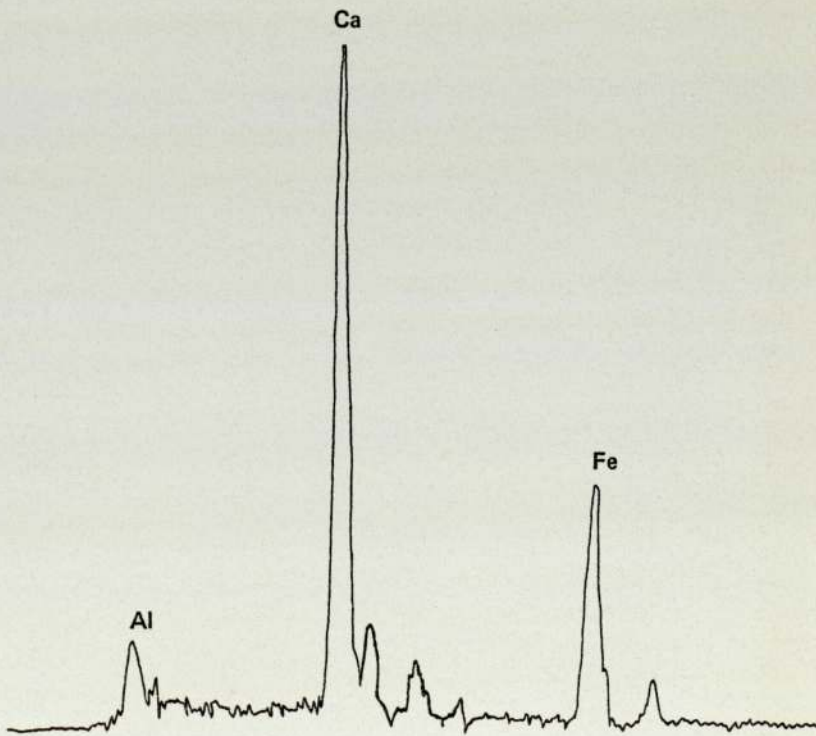


Figure 6.52 X-ray spectrum of the area marked by a square in Figure 6.50

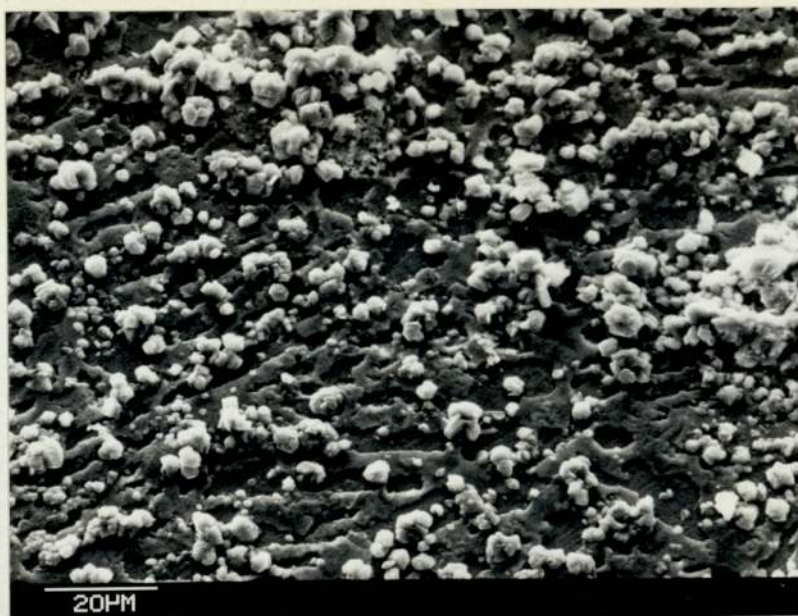


Figure 6.53 Alag side of the interface with a fully converted paste

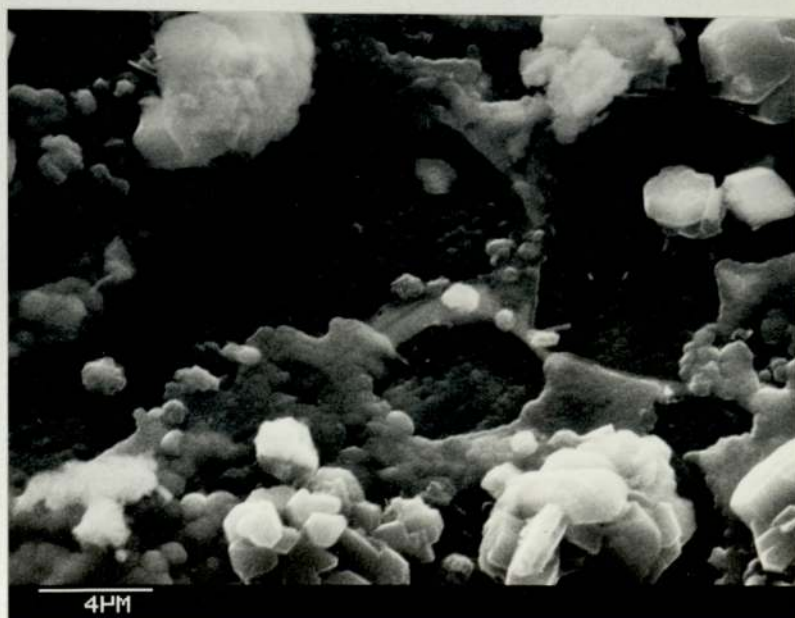


Figure 6.54 A close-up of the Alag side of the interface with a fully converted paste in Figure 6.53

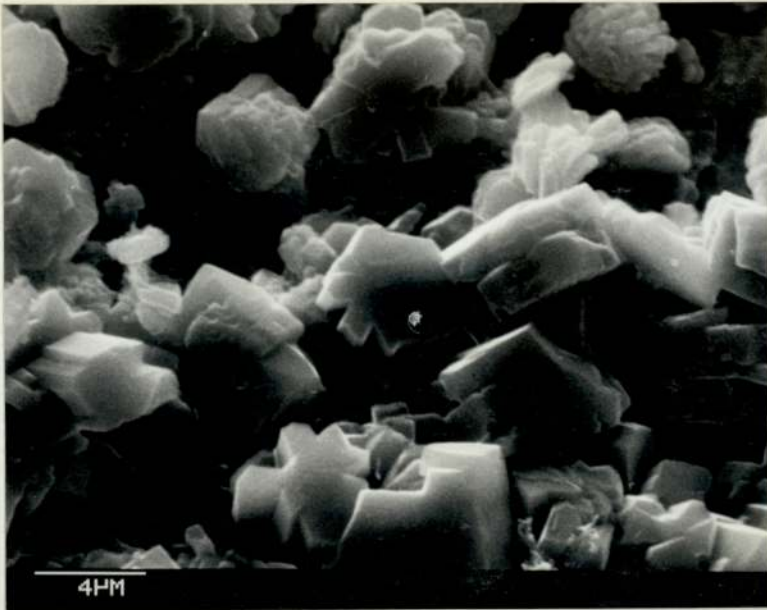


Figure 6.55 Crystallised alumina on the Alag side of the interface with a fully converted paste

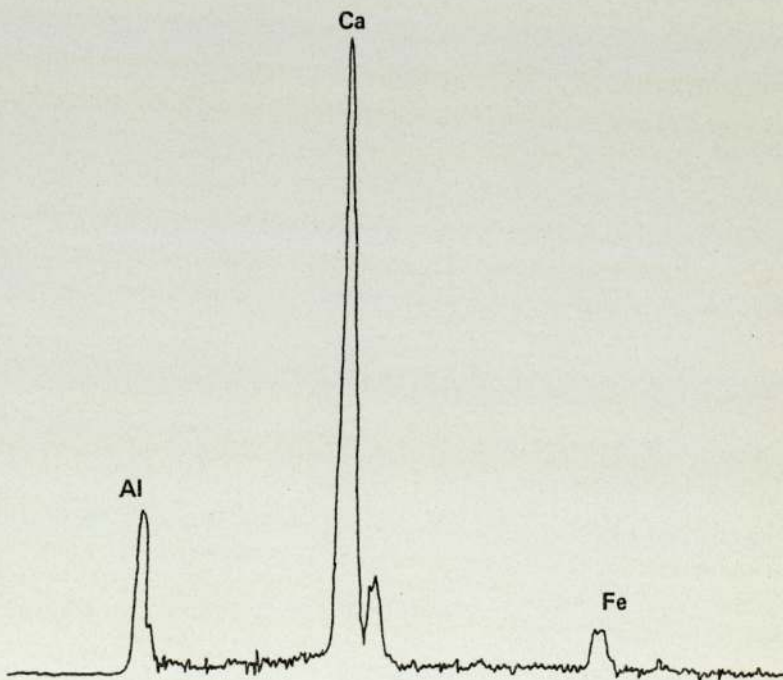


Figure 6.56 X-ray spectrum of the Alag side of the interface with a fully converted paste

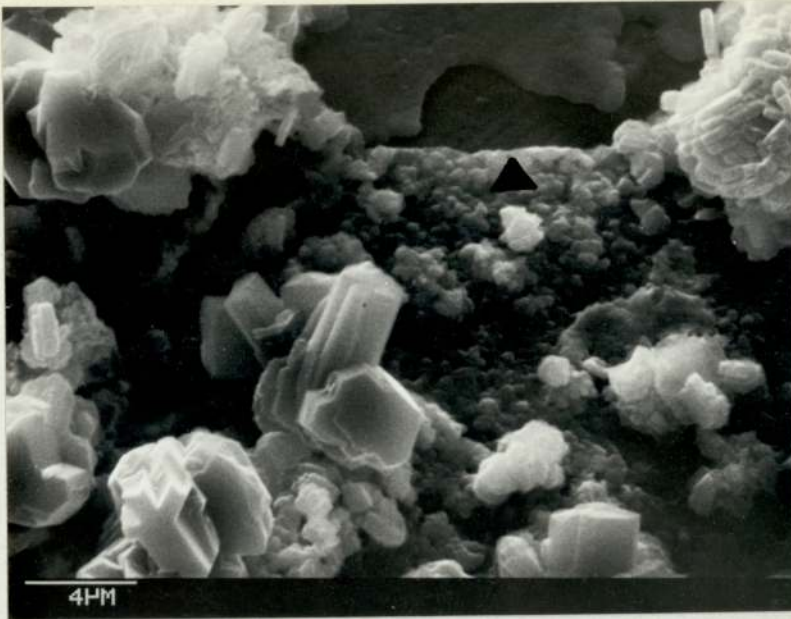


Figure 6.57 Different features of the Alag side of the interface with a fully converted paste

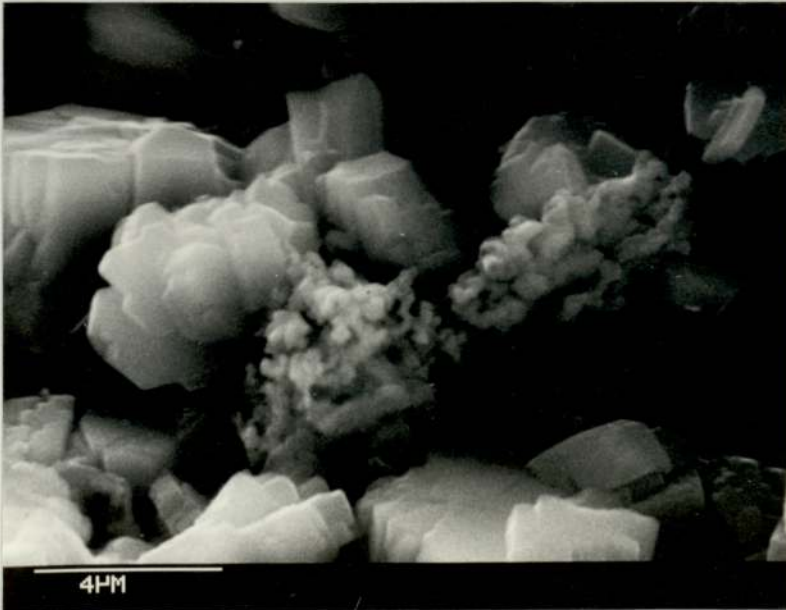


Figure 6.58 Fragments from the layer marked by a triangle in Figure 6.57 on the paste side of the interface with Alag aggregate

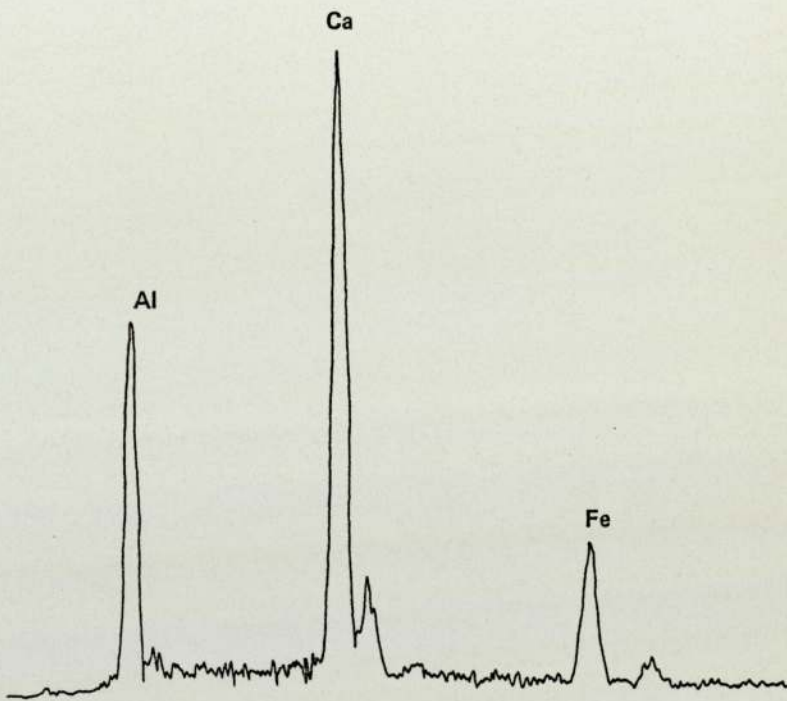


Figure 6.59 X-ray spectrum of the area marked by a triangle in Figure 6.57

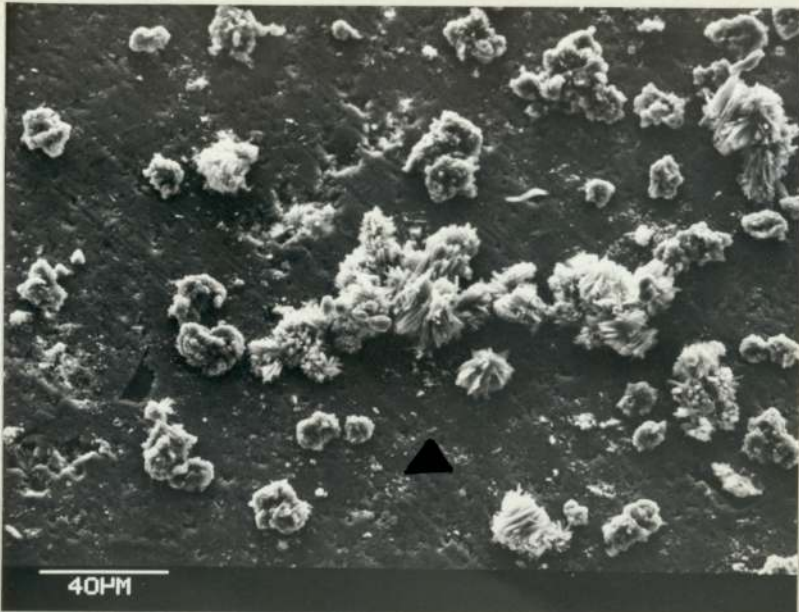


Figure 6.60 The general features of the limestone side of the interface with a fully converted paste



Figure 6.61 A close-up of the ettringite needles on the limestone surface

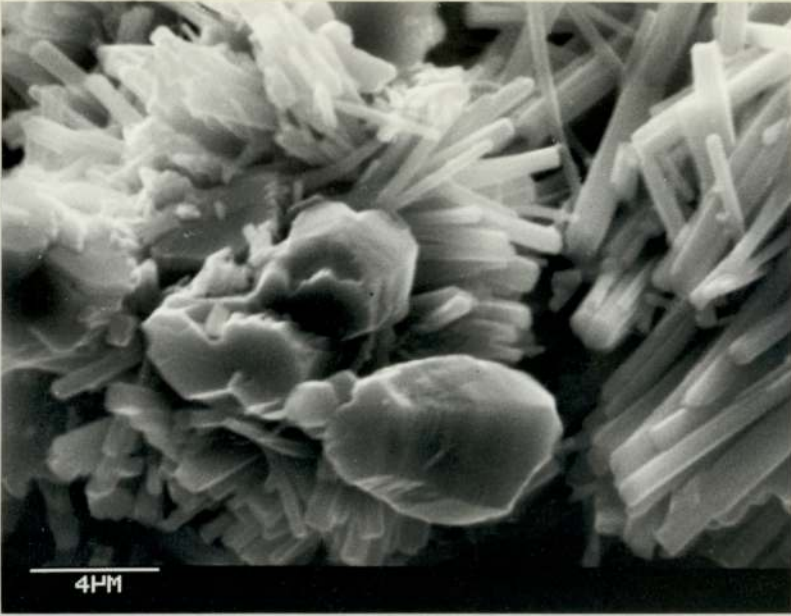


Figure 6.62 Attached crystallised alumina on the ettringite needles



Figure 6.63 Needles of ettringite on the converted paste side of the interface with limestone

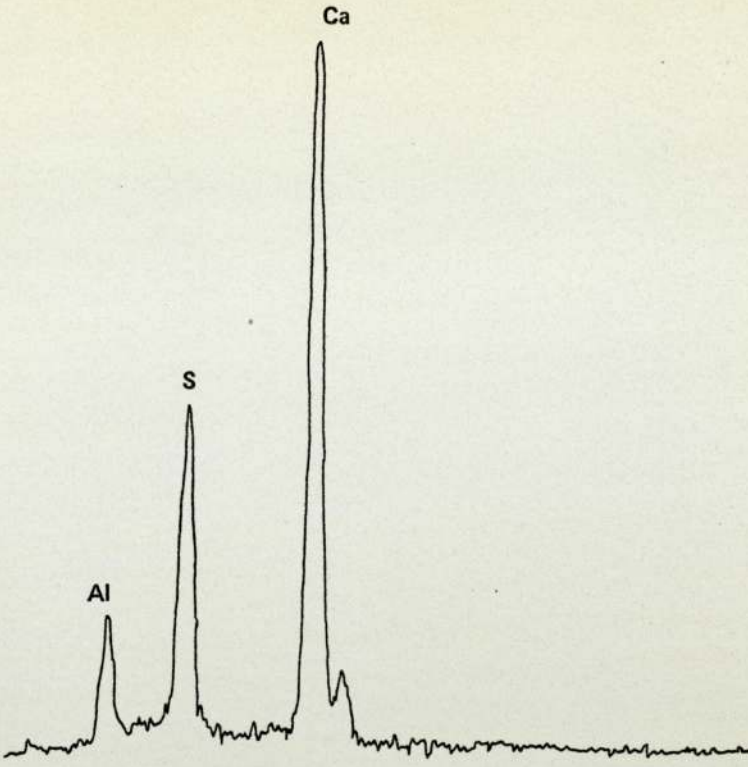


Figure 6.64 X-ray spectrum of ettringite needles

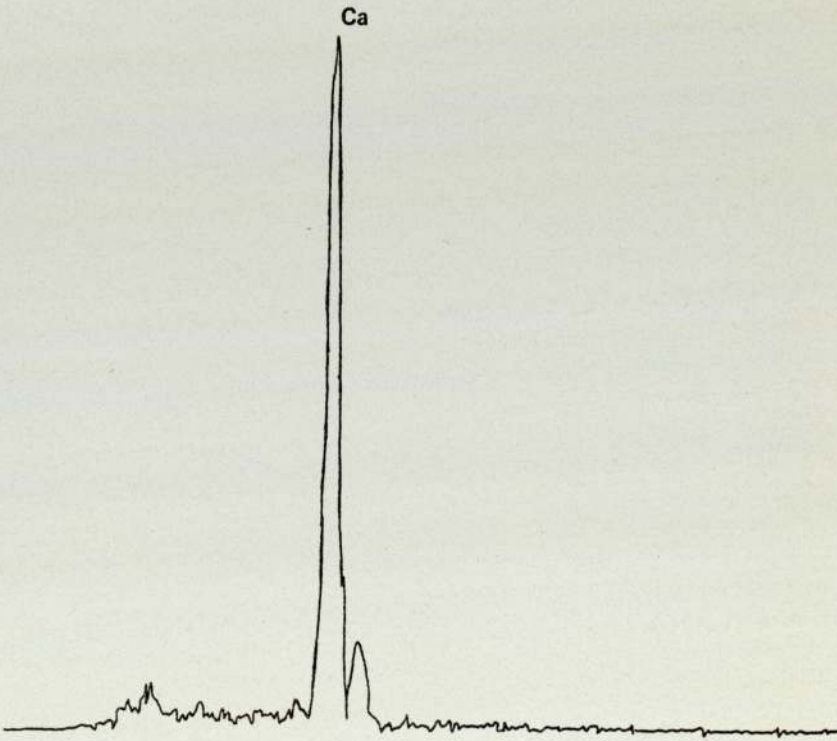


Figure 6.65 X-ray spectrum of the area marked by a triangle in Figure 6.60

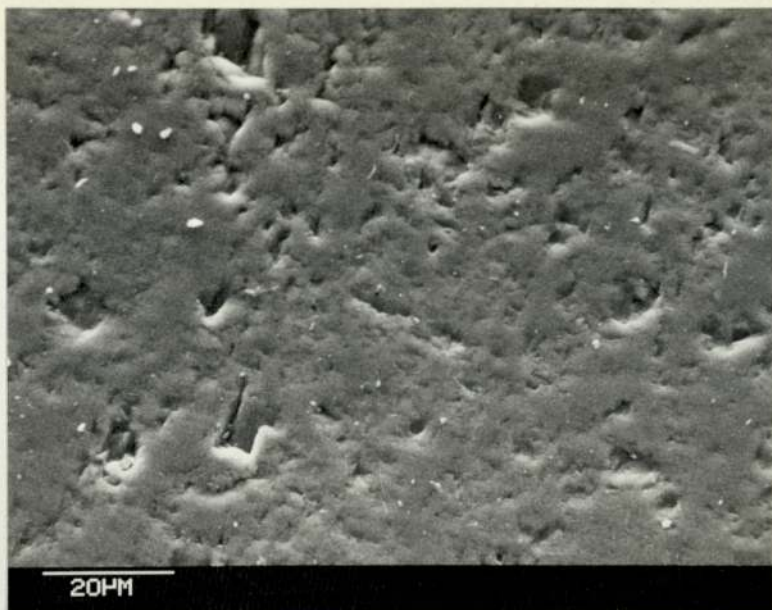


Figure 6.66 The granite side of the interface with a fully converted paste

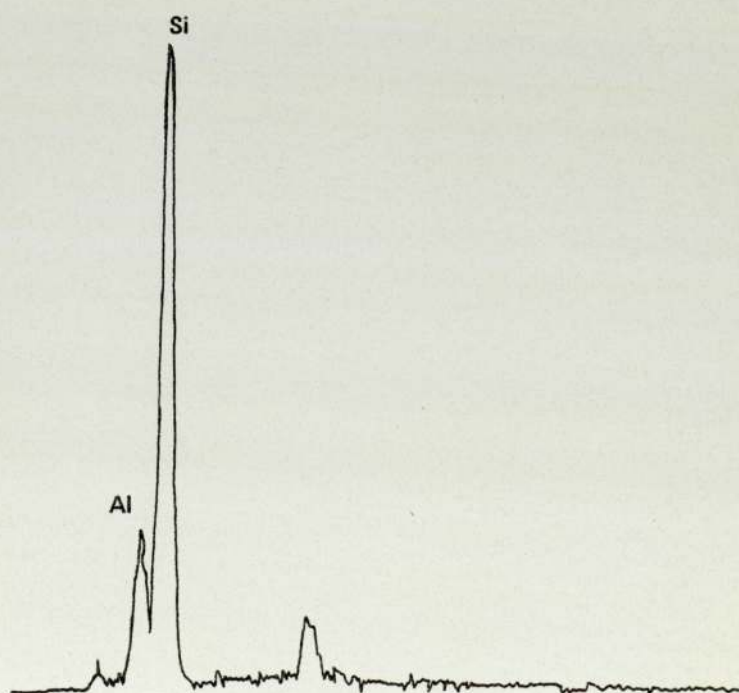


Figure 6.67 X-ray spectrum of the granite surface



Figure 6.68 The converted paste side of the interface of a specimen from a 20 year old HAC concrete bridge

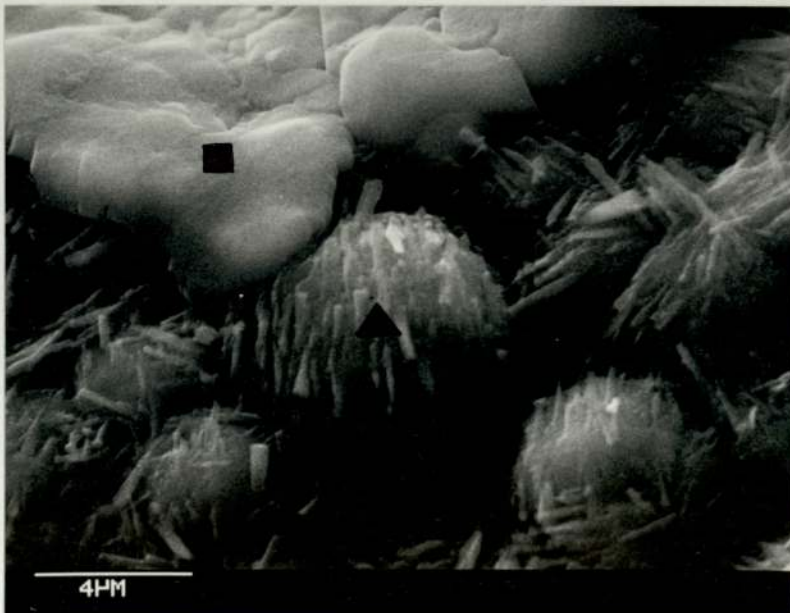


Figure 6.69 A close-up of the paste side of the interface in Figure 6.68

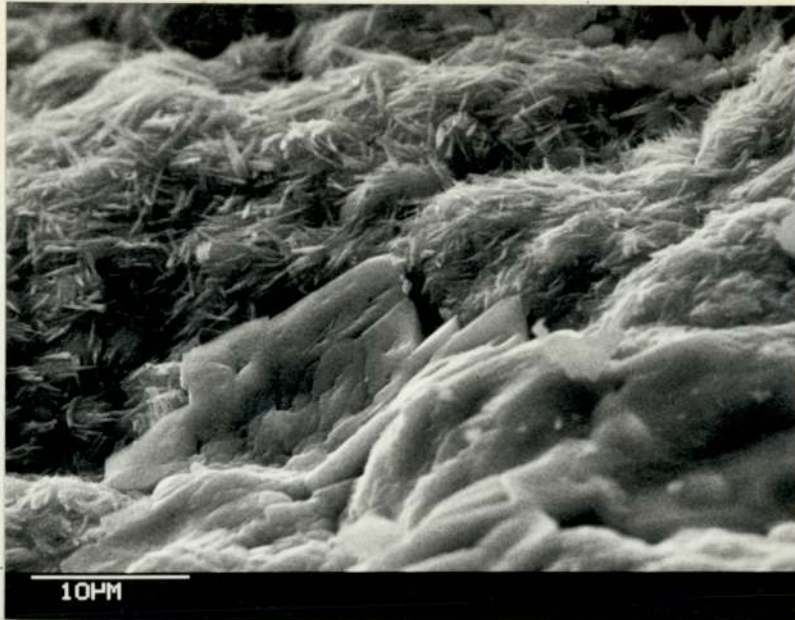


Figure 6.70 Another area of the paste side of the interface shown in Figure 6.68

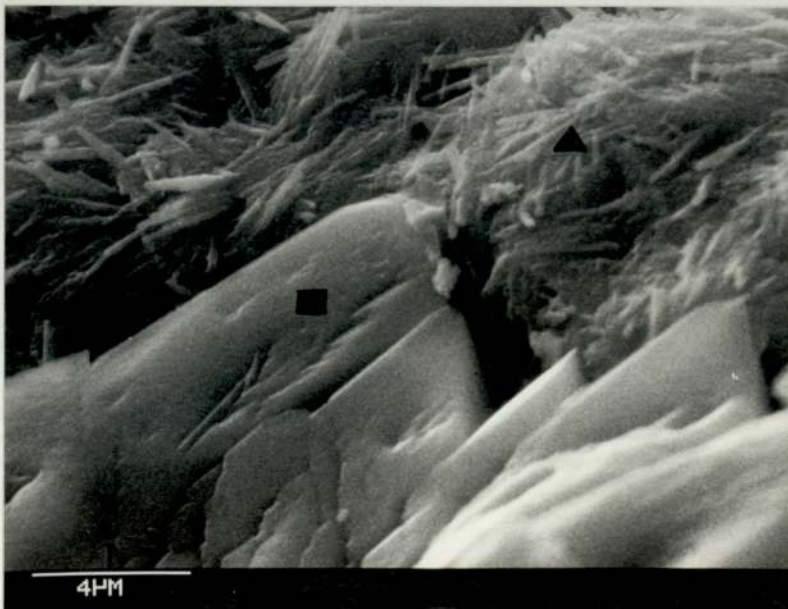
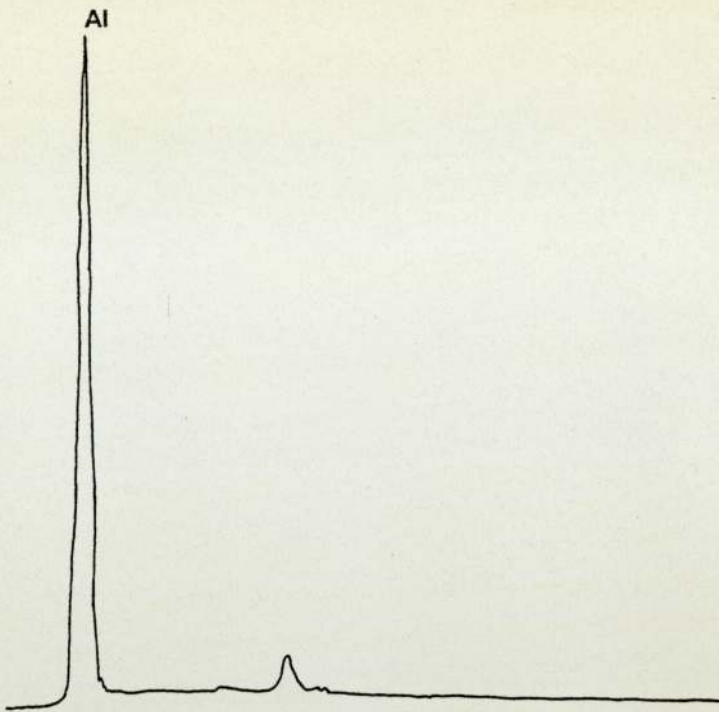
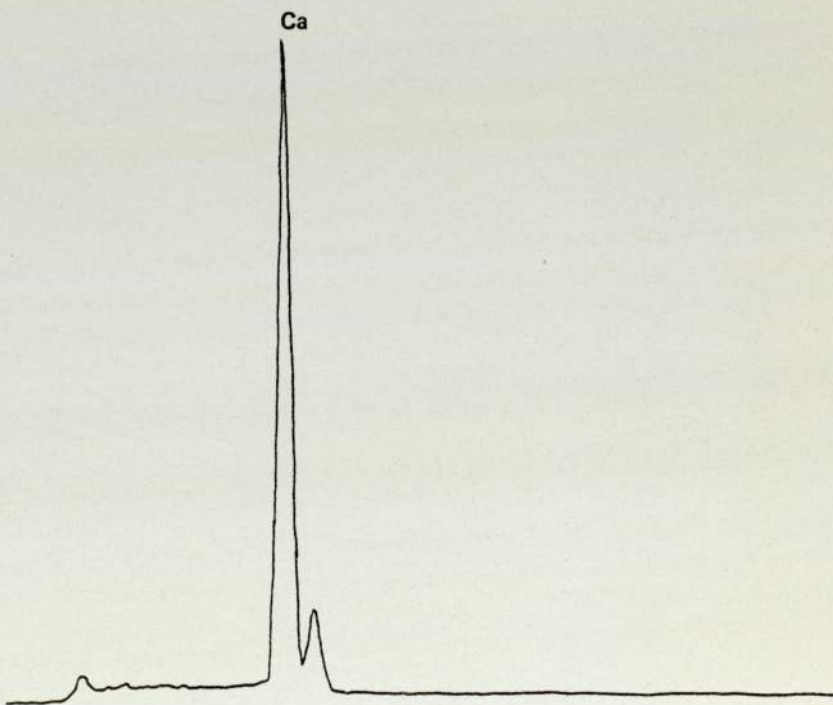


Figure 6.71 A close-up of the paste side of the interface in Figure 6.70  
( Typical of the areas and marked areas on Figure 6.69 )



*typical*  
Figure 6.72 X-ray spectrum of the area marked by a triangle in  
Figures 6.69 and 6.71



*typical*  
Figure 6.73 X-ray spectrum of the area marked by a square in  
Figures 6.69 and 6.71



Figure 6.74 The aggregate side of the interface with a converted paste in a 20 year old HAC concrete bridge



Figure 6.75 A close-up of the center of Figure 6.74

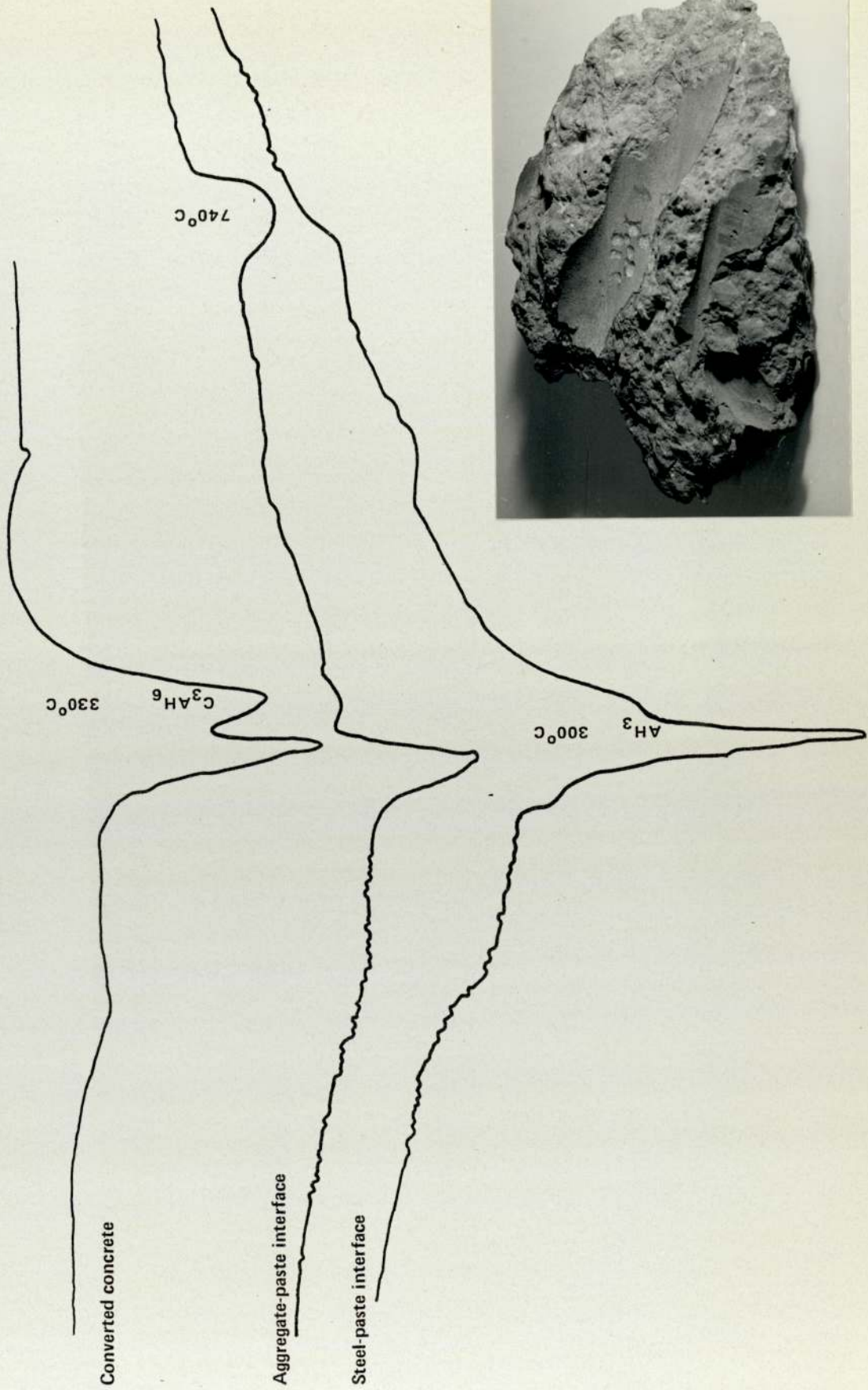


Figure 6.76 DTA thermograms of the paste side of a specimen from a 20 year old HAC concrete bridge



Figure 6.77 The morphology of the paste side of the interface with a glass slide after 2 days of curing at 45°C.

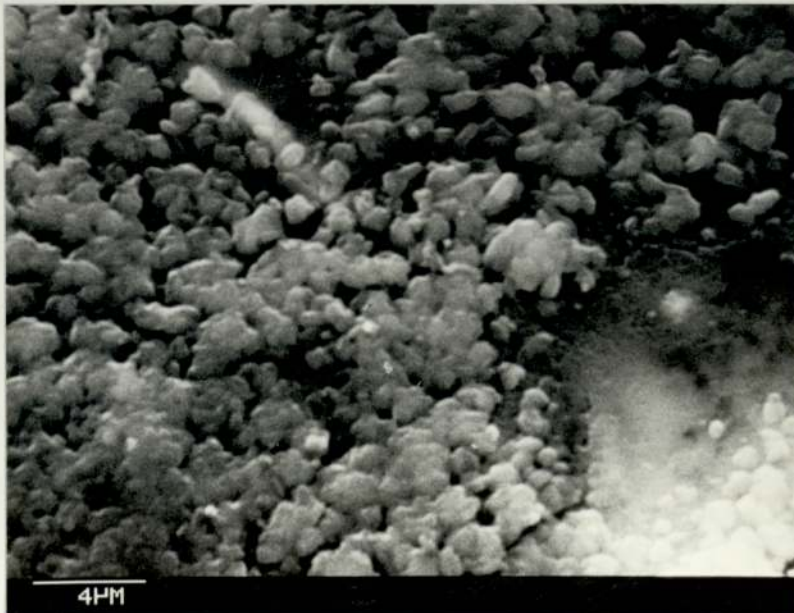


Figure 6.78 A close-up of the interfacial film in Figure 6.77

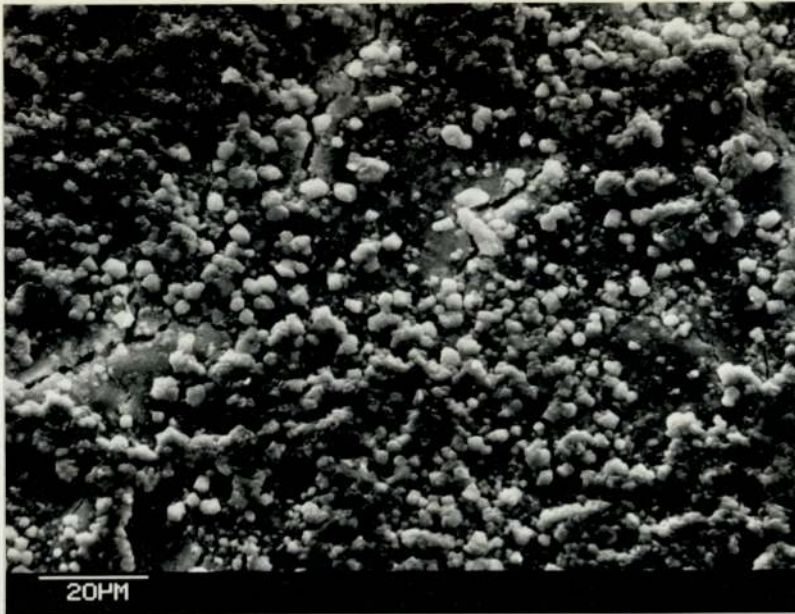


Figure 6.79 The general features of the paste side of the interface with a glass slide after 4 days of curing at 45°C

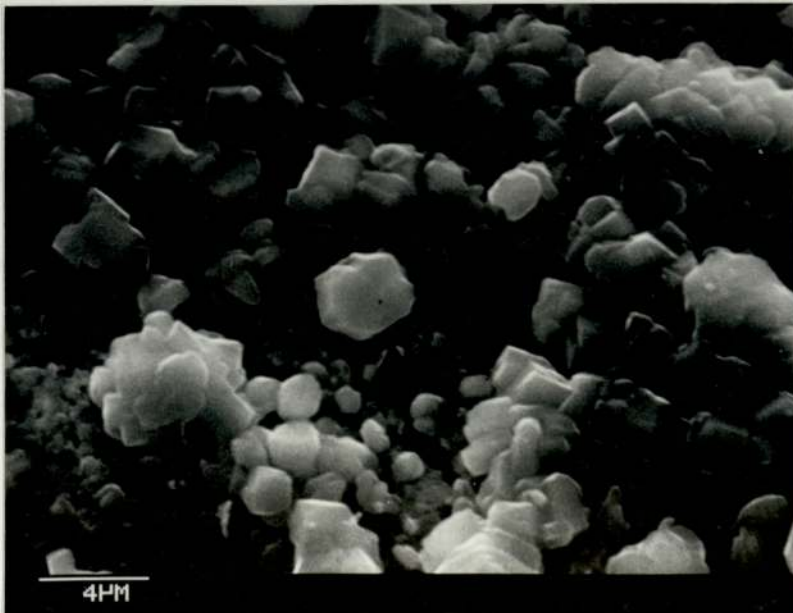


Figure 6.80 A close-up of the crystals in Figure 6.79

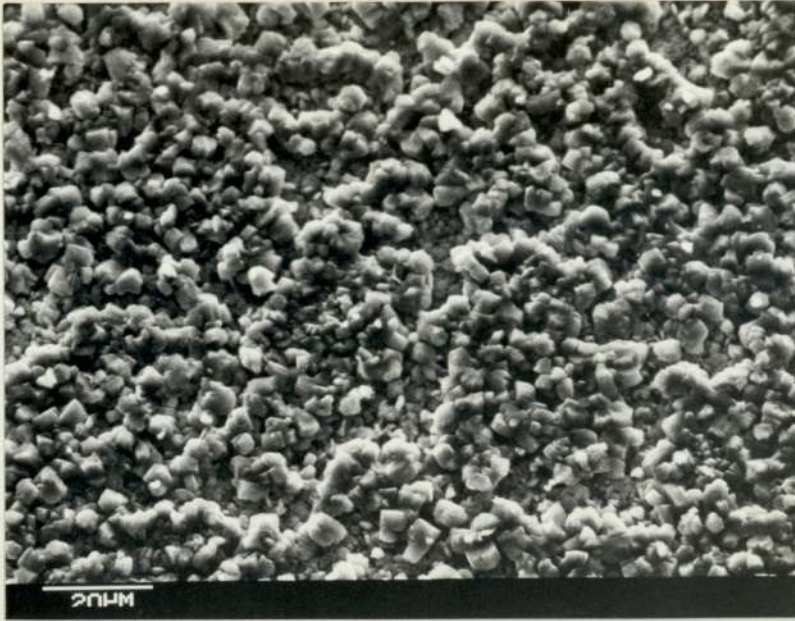


Figure 6.81 The general appearance of the paste side of the interface with a glass slide after 6 days of curing at 45°C.

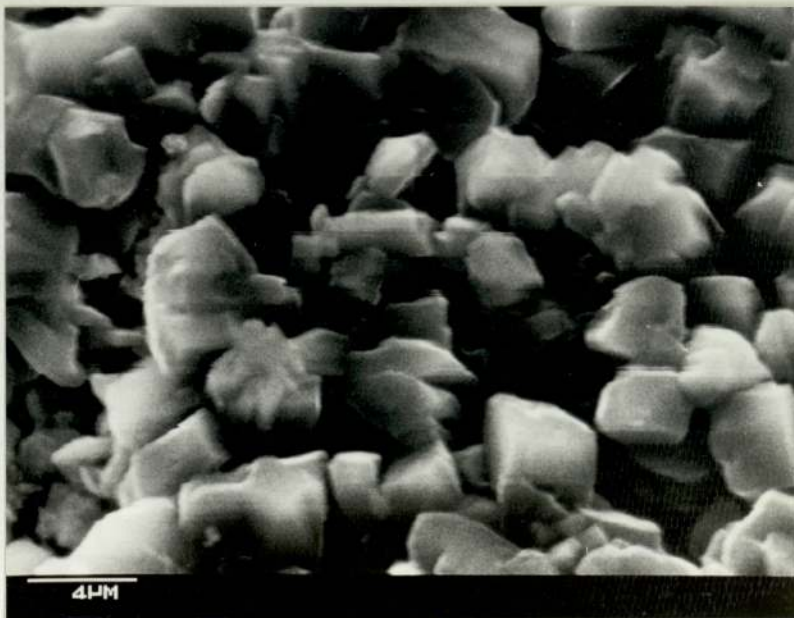


Figure 6.82 A close-up of the gibbsite crystals in Figure 6.81

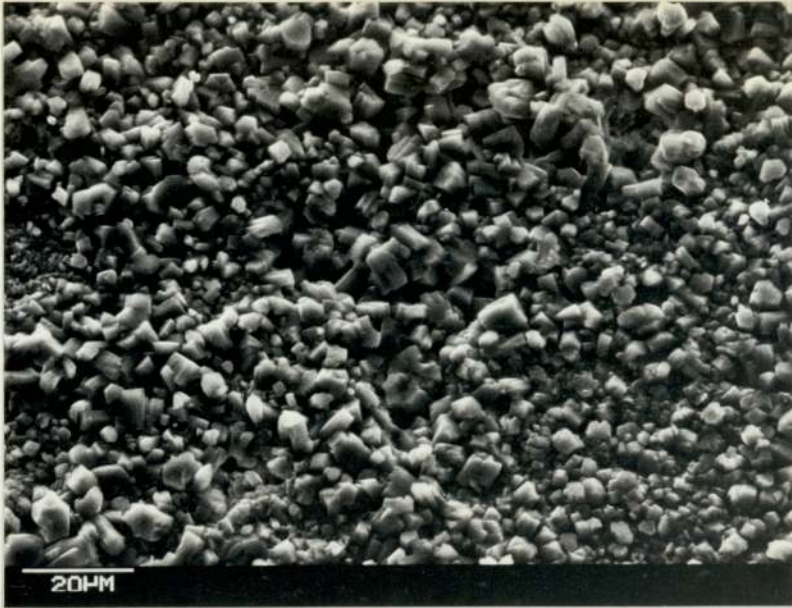


Figure 6.83 The morphology of the paste side of the interface with a glass slide after 10 days of curing at 45°C

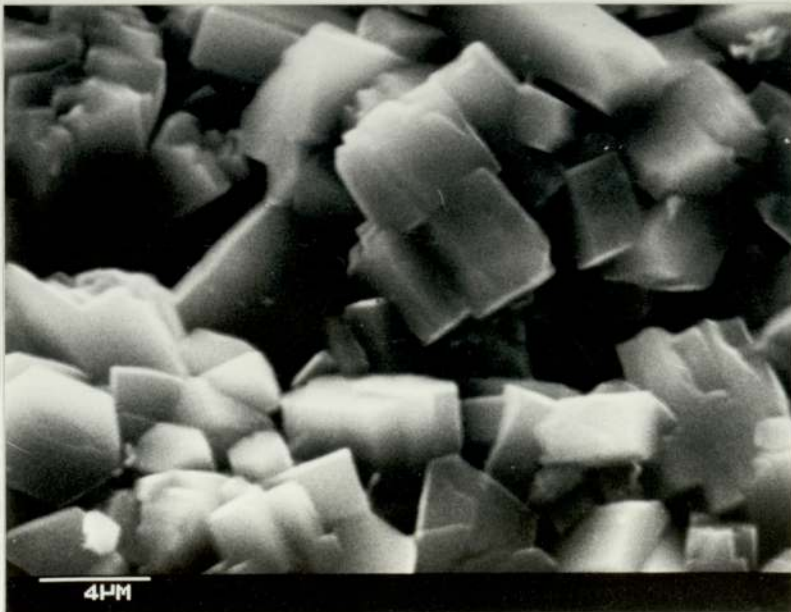


Figure 6.84 A close-up of the gibbsite crystals in Figure 6.83

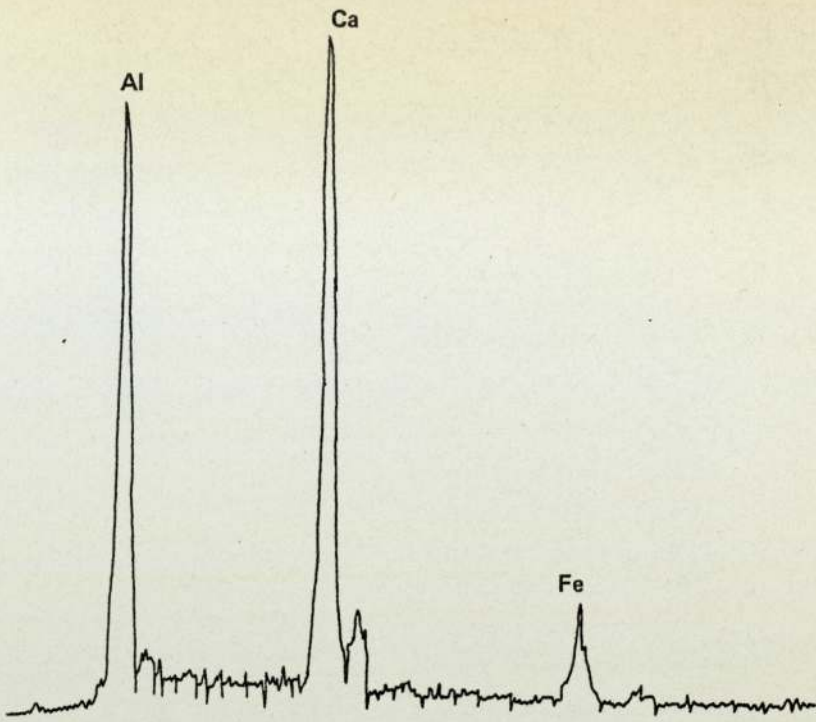


Figure 6.85 X-ray spectrum of the crystals in Figure 6.78

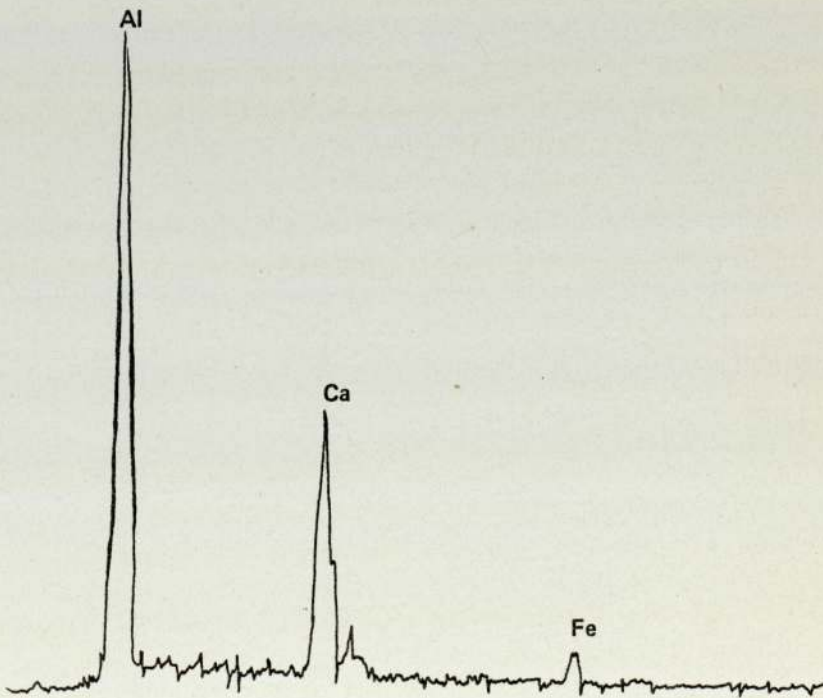


Figure 6.86 X-ray spectrum of the crystals in Figure 6.80

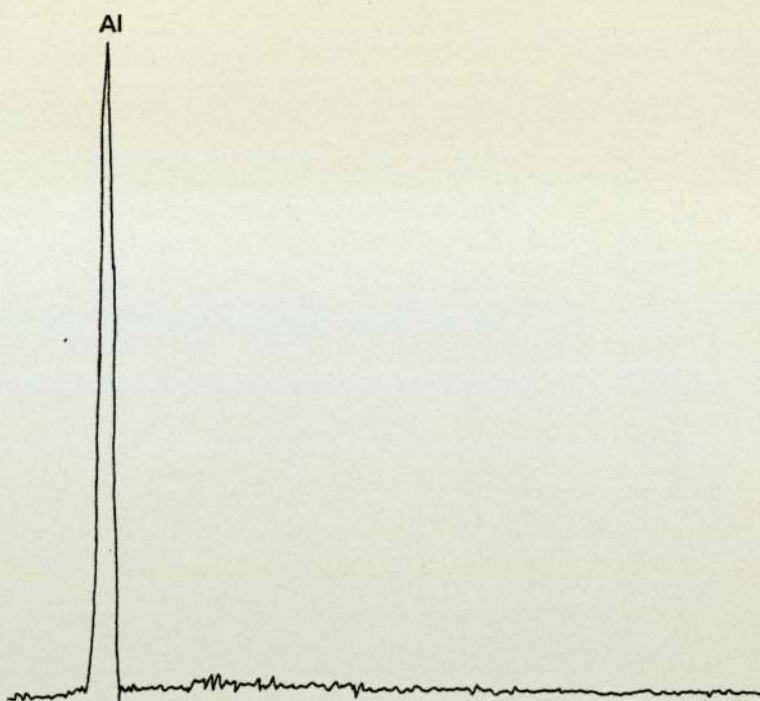


Figure 6.87 X-ray spectrum of the crystals in Figure 6.82

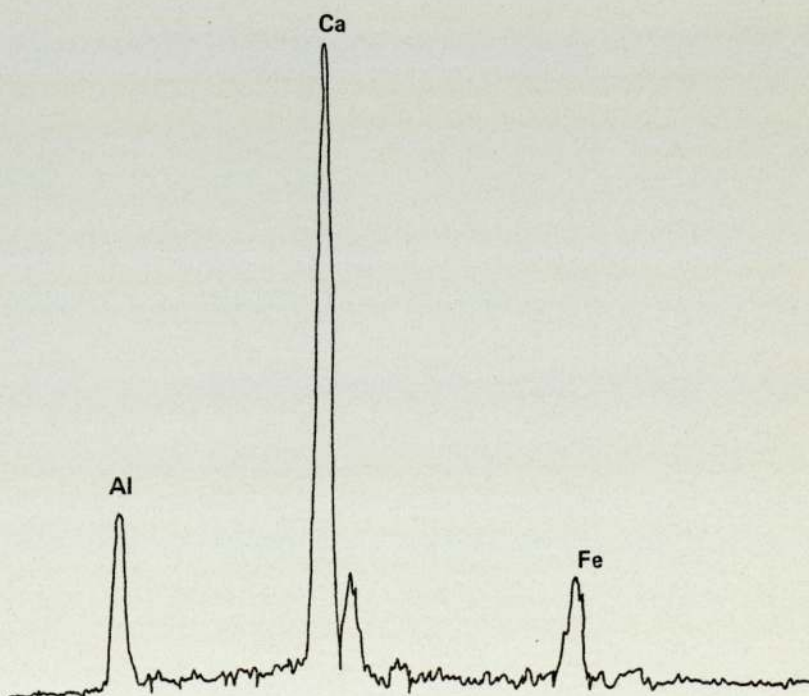


Figure 6.88 X-ray spectrum of the area marked by a triangle in Figure 6.80

## CHAPTER 7

### PHOSPHOGYPSUM AS AN ADDITIVE TO HIGH ALUMINA CEMENT PASTES

#### 7.1 INTRODUCTION

Many attempts were made to modify the hydration and hardening of HAC so as to avoid the adverse effect associated with conversion. One approach for solving this problem was the use of additives which would prevent or retard the formation of the cubic hydrate, or those which substitute the calcium aluminate hydrates with more stable phases. The additives of the first type are covered by Robson<sup>(23)</sup> who questioned their retarding effect. The second category is the one which has direct relation to the line of this investigation and hence will be considered in more detail.

Budnikov<sup>(26)</sup> investigated the effect of introducing gypsum or anhydrite (obtained by firing gypsum at about 600-700°C) into aluminous cement. He found that at the first stage of hydration calcium aluminates, dissolving in water, begin to interact with calcium sulphate with the formation of the complex compound calcium sulphoaluminate,  $C_3A \cdot 3CaSO_4 \cdot 31H_2O$ . According to him, anhydrite is a more active additive to aluminous cement than gypsum. Normally-cured aluminous cement containing 25% of anhydrite showed a considerable increase in its mechanical strength when exposed to a high temperature (60°C).

Sulphated high alumina cement (SHAC) consisting of 1 part calcium sulphate to 3 parts HAC was recommended by Hughes and Middleton<sup>(25)</sup> for use in grouting operations. It was concluded that its performance, when combined with an appropriate proportion and type of additive, has proved comparable with that for unconverted HAC grouts, but without any of the problems caused by subsequent loss in strength.

In the two previous attempts the stable sulphoaluminate hydrate was produced during hardening. A different approach, however, was used by Mehta<sup>(24)</sup> who added a previously prepared calcium sulphoaluminate ( $4\text{CaO} \cdot 3\text{Al}_2\text{O}_3 \cdot \text{SO}_3$ ) to HAC. His conclusion was that the presence of this additive at 5% level did not interfere with the initial hydration rate of the cement, and it also ensured that no loss in compressive strength resulted when concrete containing this additive was exposed to hot-wet conditions.

Due to the high cost of HAC, however, applications which would involve its use with additives are economically unattractive unless the additives themselves are cheap. For this reason, it was considered worthwhile to examine the feasibility of utilising calcium sulphate in the form of the industrial by-product, phosphogypsum.

Over 2 million tonnes / year of by-product phosphogypsum are produced in the UK alone, the major source by far being the manufacture of wet-process phosphoric acid. The second important source is the manufacture of hydrofluoric acid. Calcium sulphate obtained as a by-product is crystallised in one of three forms: anhydrite ( $\text{CaSO}_4$ ), hemihydrate ( $\text{CaSO}_4 \cdot \frac{1}{2}\text{H}_2\text{O}$ ), or gypsum ( $\text{CaSO}_4 \cdot 2\text{H}_2\text{O}$ ). However, phosphate and fluoride impurities, which are the main significant contaminants in phosphogypsum, can cause difficulties when this type of calcium sulphate is used as a substitute for natural gypsum<sup>(119)</sup>. The influence of the phosphogypsum impurities on the setting time and compressive strength of portland cement mortars and concretes was investigated by Tabikh and Miller<sup>(120)</sup> who reviewed various purification procedures adopted for minimizing the deleterious effects of such impurities.

Hence, the main objective of this part of the research was to explore the possibility of using phosphogypsum as a cheap additive in HAC.

## 7.2 EXPERIMENTAL

Three types of phosphogypsum supplied from different sources (section 2.1) and natural gypsum were investigated.

In the first set of experiments, phosphogypsum was added in crude form, or after washing with water (W), or after being initially washed with water followed by treatment with limewater (W.L). Water washing was performed at room temperature in large plastic troughs; phosphogypsum was washed with pressurised water issuing from a hose until the trough was full. The turbulence caused by the water assisted in stirring the contents which were then left to settle and the contaminated water was poured out. This procedure was repeated until the water was clear of any visible contaminant. Treatment with limewater was carried out by preparing a saturated solution of lime in which the water-washed phosphogypsum was placed, stirred, and left for 1 hr. At the end of this period, the phosphogypsum was transferred to limewater placed in large plastic containers and left there for 3 days.

The purified phosphogypsum was dried on steel trays in an oven at 60°C. The dry product was hand sieved on a 150 $\mu$  m screen and the fraction that passed was used in the test. In this set natural gypsum was used as a control.

In the second set of experiments, which was intended to compare the anhydrite derived from phosphogypsum with the natural anhydrite, the crude phosphogypsum was fired at 600°C (600), or fired after being washed with water and limewater (WL 600).

In preparing the pastes, one part by weight of the additive was added to three parts of HAC, and the water-solid ratio of 0.4 was used throughout.

After casting, the pastes were initially cured in saturated air at 10°C until they were hard enough to be placed in water at the same temperature. The time required to achieve this state was taken as an indication of the setting time. This initial curing lasted for 4 days with the first set, while it required 2 days with the second set before the specimens were exposed to water curing at 60°C. The curing at 60°C for both sets lasted for 3 days, which was sufficient for HAC pastes made with the same water-*Solid* ratio to attain minimum strength. The composition and strength of the pastes were determined before and after exposure to hot-wet curing.

## 7.3 RESULTS AND DISCUSSION

### 7.3.1 SETTING TIME

Table 7.1 shows that the addition of natural or by-product anhydrite has no significant influence on the setting time of HAC pastes at 10°C (12 hrs). The addition of natural gypsum resulted in a noticeable increase in the setting time (36 hrs), while no sign of hardening was observed with crude phosphogypsum even after 5 days. However, phosphogypsum washed with water caused the pastes to harden after about

60 hrs. The nearest setting time to natural gypsum was obtained with phosphogypsum washed initially in water and then in limewater (48 hrs).

The change in the setting behaviour was attributed to the acidity of the different systems, since it is known that acids have a very powerful retarding effect on HAC pastes<sup>(121)</sup>. To provide evidence for this conclusion, pH determinations were carried out. Approximately 1 g of sample was shaken up in 25 ml of deionised water, and the pH measured. As would be expected, after water washing the pH of the phosphogypsums approached that of the gypsum control, and after washing in limewater they became alkaline, table 7.2.

In addition, visual inspection showed that the colour of the crude materials was a dark cream, whereas those washed in water or in limewater were much lighter in colour, indicating that some material was removed during washing. The effect of aqueous washing is the dissolution of surface-adsorbed contaminants, while treatment with limewater converts acid phosphates into  $\text{Ca}_3(\text{PO}_4)_2$  and complex fluoroanions into  $\text{CaF}_2$  and insoluble silicates and aluminates<sup>(120)</sup>.

### 7.3.2 COMPRESSIVE STRENGTH

Pastes containing either natural gypsum or purified phosphogypsum showed the same trend on strength-time curves, Figure 7.1. The pattern was that of low strength after 4 days of initial curing at 10°C followed by gradual increase on subsequent exposure to higher temperature. The result indicates the reliability of the calcium sulphoaluminate system under hot-wet conditions, but it also shows that the system lacks the rapid hardening properties of HAC at low ambient temperatures.

In contrast, the addition of anhydrite derived from phosphogypsum or natural gypsum resulted in reasonable strength after 2 days of curing at 10°C, but caused a considerable loss of strength at 60°C, Figure 7.2. This is in disagreement with the findings of Budnikov<sup>(26)</sup> concerning the reactivity of anhydrite with HAC.

### 7.3.3 THERMAL ANALYSIS

Thermal analysis was performed to determine the change in the composition of the pastes at various stages.

At the end of the initial curing at 10°C, it was found that the inclusion of phosphogypsum or natural gypsum in HAC pastes resulted in two endothermic peaks at 130°C and 260°C (curve 1 Figure 7.3). The endothermic effects can be attributed to the stable high sulphate calcium sulphoaluminate, C<sub>3</sub>A. 3CaSO<sub>4</sub>. 31-32 H<sub>2</sub>O and the unstable low sulphate calcium sulphoaluminate, C<sub>3</sub>A. CaSO<sub>4</sub>. 12H<sub>2</sub>O. This is based on the fact that these two compounds were detected in the system CaO - Al<sub>2</sub>O<sub>3</sub> - CaSO<sub>4</sub> - H<sub>2</sub>O<sup>(122)</sup>, and were found to exhibit an endothermal peak anywhere in the range 120°-180°C and 200 - 250°C respectively<sup>(123)</sup>. Exposure to curing at 60°C resulted in a slight decrease in the quantity of the stable compound, but the unstable compound peak at 260°C was substituted by two endothermic peaks at 200°C and 270°C (curve 2 Figure 7.3). These two peaks could be correlated with the formation of a compound of composition C<sub>3</sub>A. CaSO<sub>4</sub>. 7H<sub>2</sub>O which loses 4 molecules at 190°C and the remaining water at 260°C<sup>(124)</sup>.

Thermal analysis in Figure 7.4 indicates that the addition of natural or chemical anhydrite to HAC a little effect on the hydration process of the cement, since <sup>alumina</sup> gel and  $CAH_{10}$  were detected at the end of initial curing period at  $10^{\circ}C$  (curve 1) and the presence of  $C_3AH_6$  and  $AH_3$  was evident after 3 days of curing at  $60^{\circ}C$  (curve 2).

#### 7.4 CONCLUSIONS

The results of this brief attempt at an assessment of phosphogypsum as an additive to HAC indicate that:

1. Crude phosphogypsum is unsuitable because of its impurities.
2. Aqueous washing was sufficient to reduce the acidity to nearly the level found in gypsum, but subsequent washing with limewater removed the remaining acidity.
3. The addition of gypsum or purified phosphogypsum resulted in a cementitious material of slow setting properties at relatively low ambient temperatures ( $\approx 10^{\circ}C$ ), but its reliability at higher temperatures ( $\approx 60^{\circ}C$ ) was evident. This may be attributed to the formation of various forms of calcium sulphoaluminate hydrates.
4. Anhydrite derived from phosphogypsum or natural gypsum was almost an inert additive, since it did not interfere with the hydration process of HAC, and this was compatible with the results for the mechanical strength of HAC pastes containing this type of additive.

Addition		Setting time (hrs)
Group 1	Gypsum	36
	S	No hardening
	S.W	60
	S.W.L	48
	F	No hardening
	F.W.	65
	F.W.L	48
	IC	No hardening
	IC.W	60
	IC.W.L	48
Group 2	Gypsum+600°C	12
	S 600	12
	S.W.L. 600	12
	F. 600	15
	F.W.L. 600	12
	IC. 600	12
	IC.W.L. 600	12
HAC	(No addition)	12

Table 7.1 Effect of additions on the setting time of HAC pastes

Phosphogypsum	Cleaning stage	pH
F	————— (Crude)	3.25
S	—————	3.30
IC	—————	3.80
F	W (Water washing)	5.50
S	W	6.15
IC	W	5.90
F	W.L (Water + limewater)	8.30
S	W.L	8.70
IC	W.L	8.00
N GYPSUM		6.40

Table 7.2 Effect of washing on phosphogypsum

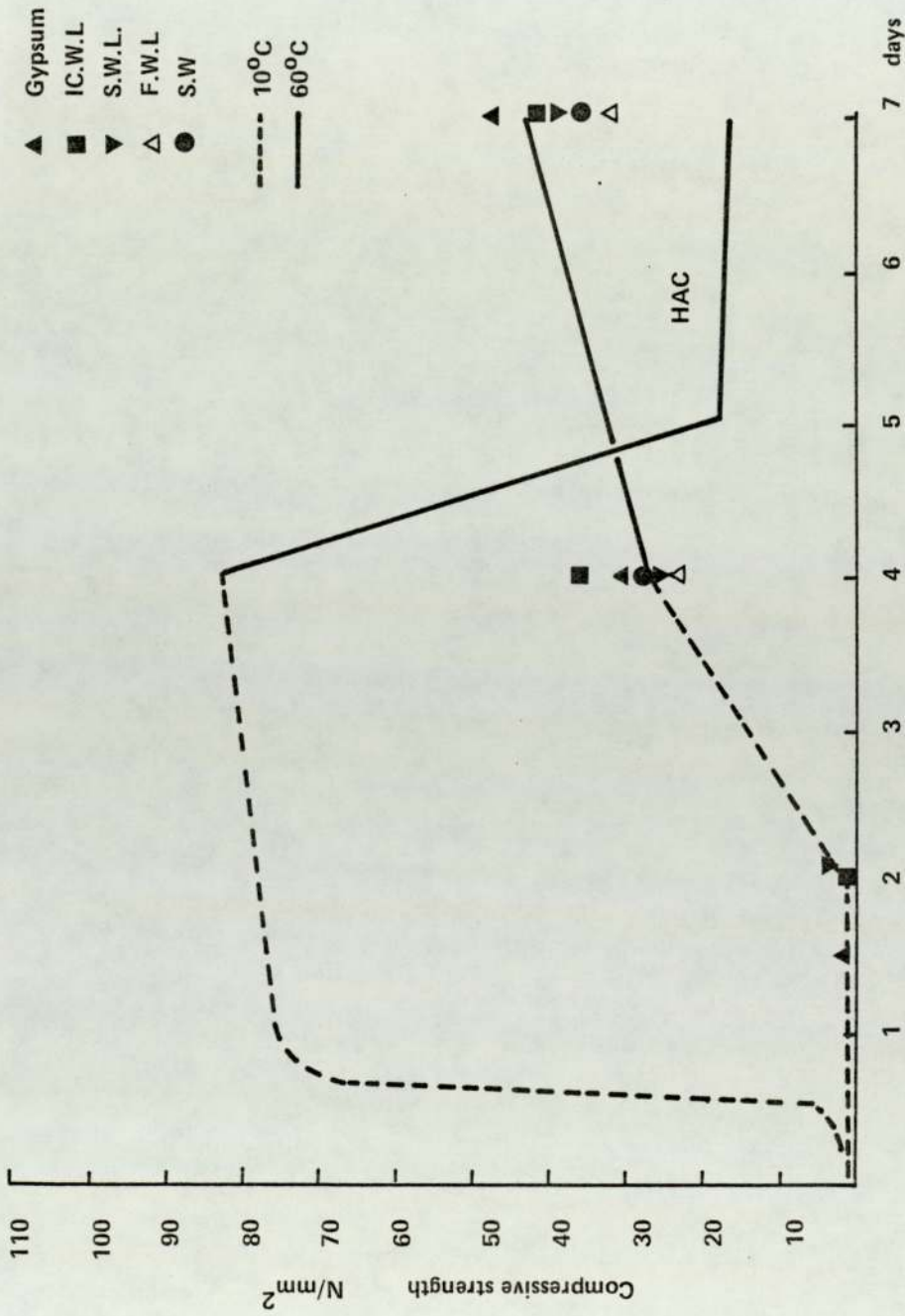


Figure 7.1 The effect of adding gypsum or purified phosphogypsum on the strength of HAC pastes

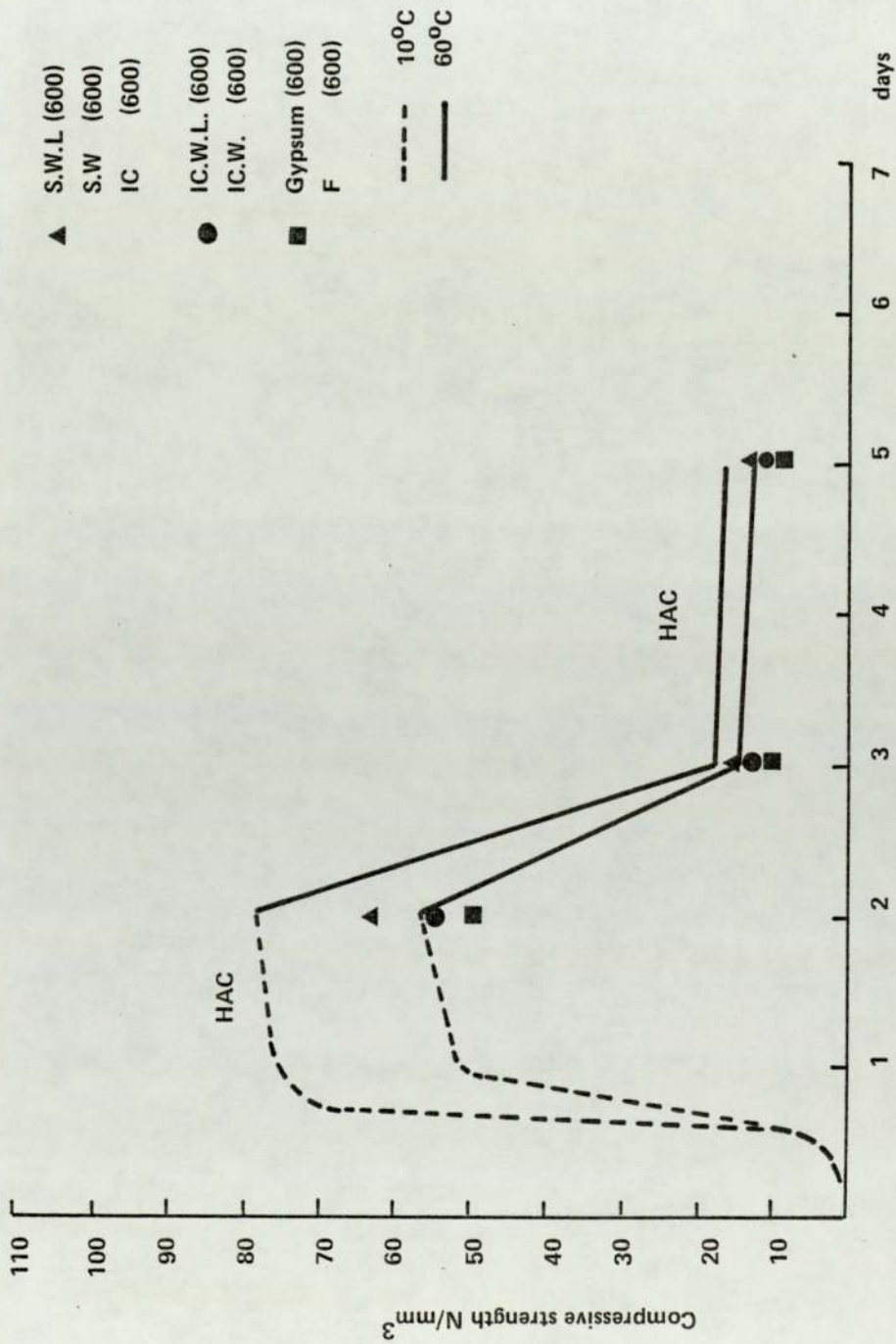


Figure 7.2 The effect of adding natural or chemical anhydrite on the strength of HAC pastes

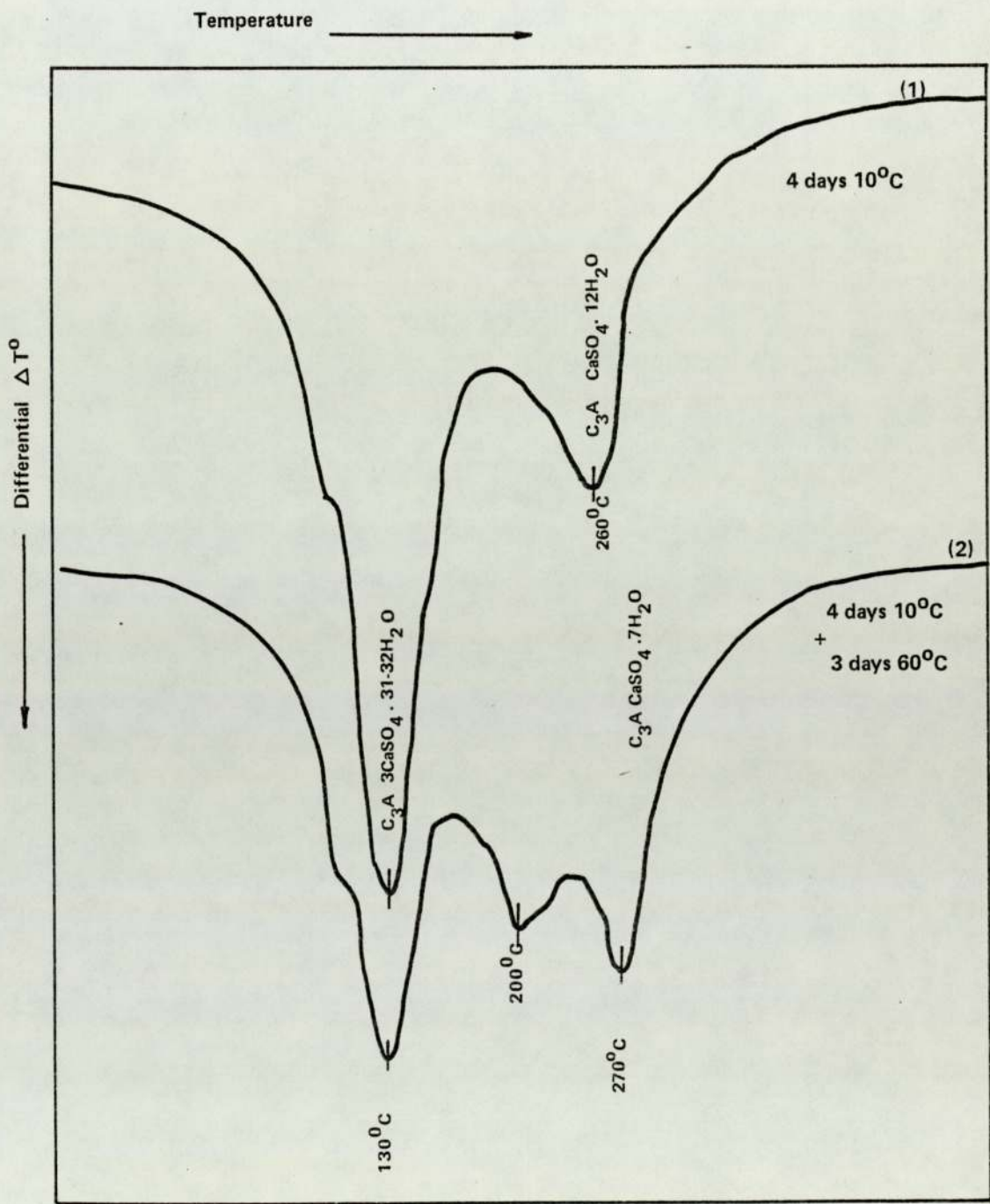


Figure 7.3 DTA of HAC with additions of gypsum or purified phosphogypsum

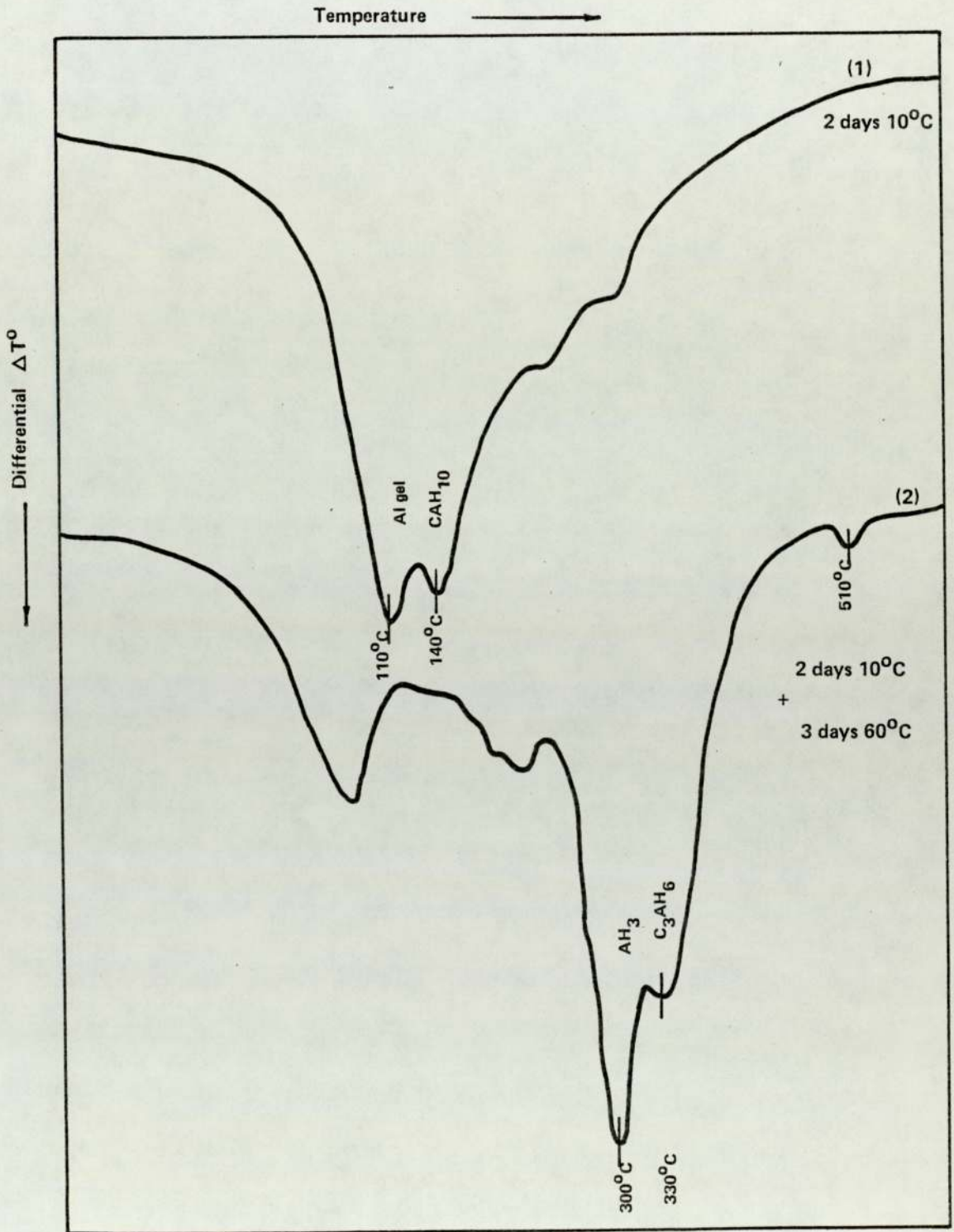


Figure 7.4 DTA of HAC with additions of natural or chemical anhydrite

## CHAPTER 8

### GENERAL CONCLUSIONS AND RECOMMENDATIONS FOR FURTHER WORK

#### 8.1 GENERAL CONCLUSIONS

The behaviour of HAC pastes is very sensitive to conditions under which mixing and storage are carried out.

It was observed that the consistency of the fresh pastes is highly dependent on mixing time as well as on the temperature of mixing. It was clear that, under continuous mixing, the viscosity of aluminous cement pastes increased as mixing time increased until it reached a maximum value; this was followed by a gradual decrease towards a steady plateau. The results also showed that the lower the water content the higher the consistency and the shorter the time required to reach the most viscous condition. However, it was evident that varying the mixing shearing rate has no significant effect on the time required to reach this state.

It was also found that, under the action of mixing, aluminous cement pastes eventually acquired reproducible thixotropic properties, but this condition was not achieved unless mixing was continued beyond the point of highest consistency: It was apparent that the mixing time required to achieve the maximum consistency tended to increase considerably with decrease in the mixing temperature. The dependence of the rate of stiffening of the paste on temperature indicated that the development of the thixotropic structure might involve a thermally activated process such as the dissolution of counter ions into the electrolyte to reduce the zeta potential, thus promoting flocculation of the cement particles. This process, whose activation energy was

estimated to be  $43 \pm 1$  KJ/mole, was not apparently influenced by changing the water-cement ratio or the type of cement.

Understanding these characteristics which determine the location of the unhydrated particles in the paste, proved to be essential in achieving homogeneous specimens with minimum sediment; otherwise inexplicable variability in results would have been unavoidable.

Other sources of discrepancy that acted jointly with the variations in paste consistency to cause a marked scatter in the results of early experiments were spotted. Self-generated heat, which is a function of the curing temperature at the time of hardening, was found to result in thermal cracks in pastes made of low water-cement ratio and in a serious reduction in the strength of the rest of the pastes. It was also observed that the surface moisture of the specimens prior to compressive strength measurements was an important factor during testing.

These observations together with the anomalous behaviour of fresh HAC pastes made it essential to follow certain stringent procedures in order to produce specimens of highly reproducible performance.

Mineralogical and pore size distribution studies on hardened cement pastes have revealed certain relationships between these two factors and the strength of the material.

A linear relationship which was found to exist between strength and the degree of conversion was limited to the region of maximum to minimum strength corresponding to degrees of conversion from 25% to 55%.

This relation indicates that the increase in the water-cement ratio causes the pastes to lose an increasing percentage of their strength at any given DOC.

The strength of pastes of constant water-cement ratio and the same curing conditions, but with different degrees of conversion was found to be exponentially dependent on total porosity. A different semilogarithmic relation was found when the strength of unconverted cement pastes with different water-cement ratios was plotted versus total porosity data, but fully converted pastes exhibited a departure from this relation. These relationships indicate that conversion may produce a different material of weaker binding capacity and higher fraction of pores. This effect is more pronounced at relatively higher water-cement ratios.

Pore size distribution curves are a suitable means for estimating the total porosity of aluminous cement pastes, and they also proved valuable in explaining the variations in the strength of two materials of the same water-cement ratio and the same total porosity. The weaker paste had a considerably higher fraction of large pores than the stronger paste. These pores which are believed to act as stress concentrators are responsible, together with the modified binding characteristics within the paste, for the loss of strength in the former case.

Pore size distribution curves can also be used to indicate the state of the strength of the paste. Unconverted as well as strong pastes showed either an equal distribution of pores represented by almost linear curves or a large fraction of small pores represented by concave

curves. In contrast, fully converted pastes can be identified by a sharp increase in the number of pores in the range of larger diameters as is evident from the convex shape of the curves.

The volume average pore diameter, which corresponds to 50% of the intruded porosity, is another good indicator of the mechanical and mineralogical conditions of the material; highly converted or weak specimens showed an increasing size of this parameter.

Analytical and morphological studies on the interfacial zone developed between aluminous cement pastes and various substrates indicated that this zone is seriously affected by the conversion process.

At relatively low temperatures, the contact zone between the hydrated constituents of the cement and the different materials, with the exception of limestone, was made up of small platelets which are thought to be composed of  $C_2(AF)H_8$ . However, this film which usually mirrors the surface on which it was originally deposited, was substituted, in the case of limestone, by a discontinuous layer with a higher calcium content and small quantities of sulphur.

In spite of the differences encountered with limestone at low temperature, exposure to higher temperatures resulted in the conversion of the paste side of the interface with all substrates to crystallised alumina of high variability of size and shape. This alumina layer was thermally analysed and proved to be gibbsite; its thickness was estimated to be 8-10  $\mu$ m.

Although there was a similarity in the behaviour of the paste side of the interface, the substrates behaved differently in retaining hydrated phases of various compositions, with granite having the least retention. In addition, evidence of superficial chemical interaction was observed only on the Alag surface, while well characterised ettringite needles were seen projecting from the limestone surface. With glass, however, a thin layer rich in calcium was occasionally observed attached to the surface.

These observations, together with those obtained from analysing a demolished 20 year old HAC concrete bridge, indicated the absence of direct contact between the substrates and the converted pastes due to the contraction of the interfacial film on crystallisation. This indicates a considerable loss in the aggregate-cement bond, which is believed to have a significant influence on the strength of the converted concrete.

The possibility of using by-product calcium sulphate (phosphogypsum) as a cheap additive in HAC pastes was briefly examined.

Crude phosphogypsum was found to be unsuitable because of its powerful retarding effect on the cement hydration.

Purified phosphogypsum was comparable to natural gypsum in that the addition to HAC of either resulted in a cementitious material of slow setting properties at relatively low temperatures. However, this material showed a gradual increase in strength at higher temperatures.

The hydration process of HAC pastes was not significantly influenced by the addition of anhydrite derived from phosphogypsum or natural gypsum.

## 8.2 RECOMMENDATIONS FOR FURTHER WORK

1. The temperature-dependent stiffening process observed with aluminous cement pastes requires further investigation, and in particular, the fact that Secar 250 cement which contains a high proportion of alumina produced suspensions more viscous than those obtained with ordinary HAC merits detailed examination. Promising lines of approach are offered by electrokinetic studies, particularly zeta potential measurements on the fresh pastes in the presence of different kinds of electrolyte and analytical studies on the composition of the solution formed under the action of mixing. This work should be supplemented by the study of the effects of temperature and time of mixing on the consistency of concrete mixes which are expected to be influenced by the rheological characteristics of the fresh paste.

2. Practical difficulties associated with the available methods for determining or indicating the strength of HAC concretes in existing buildings limit the usefulness of such methods. However, pore size distribution measurements on this type of concrete may prove adequate in indicating the strength of the material. This looks promising since the shape of the curves obtained with pastes was directly related to the mechanical and mineralogical conditions of the hardened cement. Therefore, it would be valuable to extend the present work on the pore structure of HAC pastes to cover a wider range of water-cement ratios and treatment conditions and to carry out similar studies on different concrete mixes. A method should be developed to take into consideration the effect of aggregates on the results.

3. The composition of the interfacial zone developed between HAC pastes and various substrates at low temperatures needs to be determined

precisely, for example by using X-ray diffraction. Since all experiments carried out on the cement/aggregate interface were conducted at 100% R.H, work on specimens immersed in water might reveal a different morphology. Direct measurements are also needed for the bond strength between HAC pastes and different materials, together with studies on the long term durability of embedded steel in the converted matrix.

4. It is considered desirable to launch a comprehensive programme for the study of the mechanical properties of sulphated aluminous cement containing various ratios of by-product phosphogypsum. However, suitable additives are required to accelerate the hardening of this type of cement at relatively low temperatures.

## APPENDIX 1

### POROSITY MEASUREMENTS

#### A.1.1 EXAMPLE OF TOTAL POROSITY DETERMINATION

The determination of the total porosity involves the measurements of the apparent density ( $\rho_A$ ) and the true density ( $\rho_T$ ) of the material.

##### A.1.1.1. THE APPARENT DENSITY

DATA: Sample: Paste of water-cement ratio 0.4 cured for 1 day  
at 10°C.

Weight of the dry sample ( $W_s$ ) = 3.3580g

Weight of mercury displaced by the sample =  
24.9559g

The volume of this weight of mercury is equal to the volume of the dry sample ( $V_T$ ). Hence the apparent density of the paste is

$$\rho_A = \frac{W_s}{V_T} = \frac{3.3580}{24.9559/13.6} = 1.8300\text{g/cm}^3$$

where 13.6 g/cm<sup>3</sup> is the density of mercury

##### A.1.1.2 THE TRUE DENSITY

DATA:  $W_1$  = weight of the pycnometer = 41.3805g

$W_2$  = weight of the pycnometer + sample = 46.8661g

$W_3$  = weight of the pycnometer + paraffin = 82.3190g

$W_4$  = weight of the pycnometer + sample + paraffin = 85.9841g

The weight of the solids  $W_s = W_2 - W_1 = 5.4856\text{g}$

$$\text{The volume of the solids} = V_s = \frac{W_3 - (W_4 - W_2) - W_1}{.817} = 2.2280 \text{ cm}^3$$

where  $.817 \text{ g/cm}^3$  is the density of the paraffin. The true density of the solid  $= \frac{5.4856}{2.2280} = 2.4620 \text{ g/cm}^3$

### A.1.1.3 TOTAL POROSITY

The total porosity may be expressed as a percentage

$$\text{T.P} = \left(1 - \frac{\rho_A}{\rho_T}\right) \times 100 = \left(1 - \frac{1.8300}{2.4620}\right) \times 100 = 25.7\%$$

or as the volume of pores per unit weight of the dry sample.

The calculation procedure is as follows:

$$\text{The apparent density } \rho_A = \frac{W_s}{V_s + V_v} = \frac{5.4860}{2.228 + V_v} = 1.8300 \text{ g/cm}^3$$

or

$$1.8300 (2.2280 + V_v) = 5.4860$$

thus

$$V_v = .7698 \text{ cm}^3$$

$$\text{The total porosity} = \frac{V_v}{W_s} = \frac{.7698}{5.4860} = 0.14 \text{ cm}^3/\text{g}$$

### A.1.2 CALCULATION OF PORE SIZE DISTRIBUTION

$$p = - \frac{4 \gamma \cos \theta}{d} \quad (\text{see Appendix 2})$$

$\gamma$  for mercury = 485 dynes/cm ( $485 \times 10^{-6} \text{ N/mm}$ )

$\theta$  is the contact angle between vacuum dried cement paste and mercury =  $130^\circ$

In the Micromeritics Instrument Corporation porosimeter, the pressure P was given in psi, while the diameter of pore d was to come out in microns, thus

$$d = \frac{176.6}{P}$$

The calculations for a paste of water-cement ratio 0.4 cured for 1 day at 10°C are presented in the following table.

Specimen weight (W <sub>s</sub> ) 3.2025 g Cell factor .000790 cm <sup>3</sup> /count				
A Applied Pressure psi	B Penetration Counter Indication	C Corrected Counter Indication (B-'Blank' Result)	D Pore Diameter (130° Contact Angle) (176.6 ÷ A) microns	E cm <sup>3</sup> /g Volume of Pores of Indicated Diameter and Larger C (Factor ÷ W <sub>s</sub> )
1	3	3	176.6000	0.0007
50	37	37	3.5320	0.0091
200	81	81	0.8830	0.0199
750	171	171	0.2355	0.0422
1000	212	211	0.1766	0.0520
2000	271	268	0.0883	0.0661
4000	325	320	0.0442	0.0789
6000	355	377	0.0294	0.0856
8000	380	369	0.0221	0.0910
10000	401	388	0.0177	0.0957
12000	417	401	0.0147	0.0989
14000	429	410	0.0126	0.1010
16000	442	420	0.0110	0.1036
18000	454	430	0.0098	0.1060
20000	465	438	0.0088	0.1080
24000	486	453	0.0074	0.1117
28000	505	467	0.0063	0.1152
32000	522	478	0.0055	0.1179
36000	543	494	0.0049	0.1218
40000	565	510	0.0044	0.1258
48000	600	534	0.0037	0.1317

## APPENDIX 2

### THE WASHBURN FORMULA OF THE INTRUSION OF A NON-WETTING LIQUID INTO A SPHERICAL PORE

The penetration of a non-wetting liquid, such as mercury, into a pore of a circular cross-section requires the application of an external force in order to overcome the surface tension of the liquid ( $\gamma$ ) which acts along the perimeter.

The force opposing entry normal to the plane of contact is

$$F_o = -\pi d \gamma \cos \theta$$

where  $d$  is the diameter of the pore and  $\theta$  the contact angle the liquid makes with the material.

The external force, which must be applied to the non-wetting liquid to make it enter the pore is given by the equation

$$F_a = \pi \frac{d^2}{4} p$$

where  $p$  is the applied external pressure. At equilibrium

$$\pi \frac{d^2}{4} p = -\pi d \gamma \cos \theta$$

which gives

$$p = -\frac{4 \gamma \cos \theta}{d}$$

This is the relationship describing the intrusion of a non-wetting liquid into a spherical pore.

### APPENDIX 3

#### THE REINER AND RIWLIN EQUATION OF PLASTIC FLOW IN A ROTATIONAL VISOMETER

In the rotational viscometer, the material is placed between an outer cylinder of radius  $R_c$  and an inner cylinder of radius  $R_b$  and of height  $h$ . The outer cylinder is rotated at an angular speed  $\Omega$  and the torque on the inner cylinder  $T$  is measured.

At equilibrium, for a cylindrical surface of radius  $r$  (between  $R_b$  and  $R_c$ ), the moment of internal forces must be equal to  $T$  and is given by

$$T = F \times 2\pi r \times r \quad (1)$$

or

$$F = \frac{T}{2\pi r^2 h} \quad (2)$$

where  $F$  is the shearing force per unit area.

The velocity at a distance  $r$  from the axis is  $rw$ , where  $w$  is the angular velocity. Then the velocity at a distant  $dr$  beyond that point is

$$(r + dr)(w + dw) = rw + wdr + rdw + (dr)(dw) \quad (3)$$

The last term can be neglected, being of the second order. The increase in velocity in passing from  $r$  to  $r + dr$  is

$$dv = wdr + rdw \quad (4)$$

and the velocity gradient is

$$\frac{dv}{dr} = w + r \frac{dw}{dr} \quad (5)$$

Introducing the second term of this expression, which represents the shearing motion, into Bingham's law of plastic flow gives

$$r \frac{dw}{dr} = \frac{1}{\mu} (F - \mathcal{T}_0) \quad (6)$$

where  $\mathcal{T}_0$  is the yield value and  
 $\mu$  is the plastic viscosity

Substituting 2 in Equation 6 gives

$$r \frac{dw}{dr} = \frac{1}{\mu} \frac{T}{2\pi r^2 h} - \frac{1}{\mu} \mathcal{T}_0$$

then,

$$\mu \frac{dw}{dr} = \frac{T}{2\pi r^3 h} - \frac{\mathcal{T}_0}{r}$$

Integrating between  $r = R_b$  and  $r = R_c$

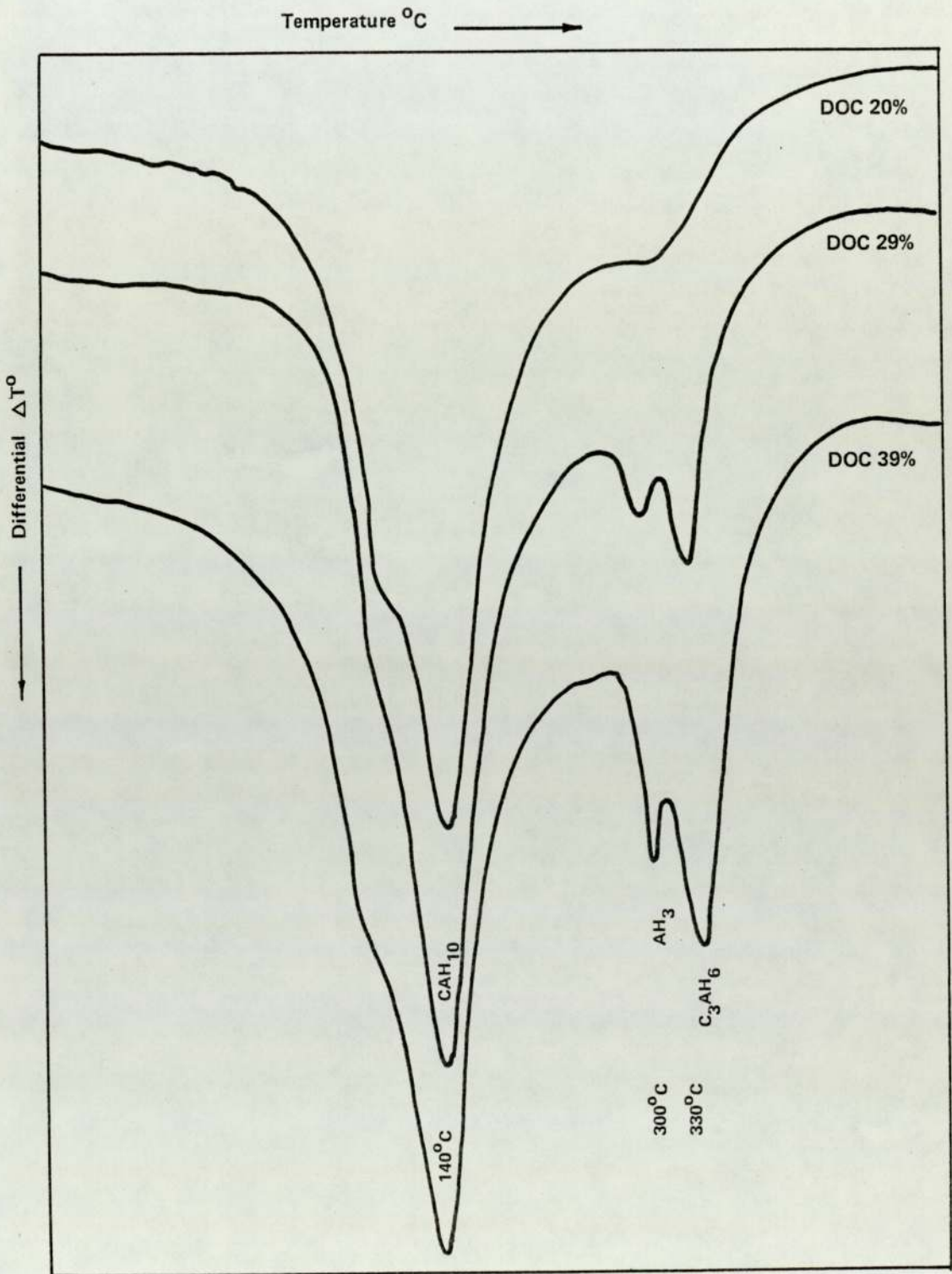
$$\mu \int_0^{\Omega} dw = \int_{R_b}^{R_c} \left[ \frac{T}{2\pi h} \cdot \frac{1}{r^3} - \frac{\mathcal{T}_0}{r} \right] dr$$

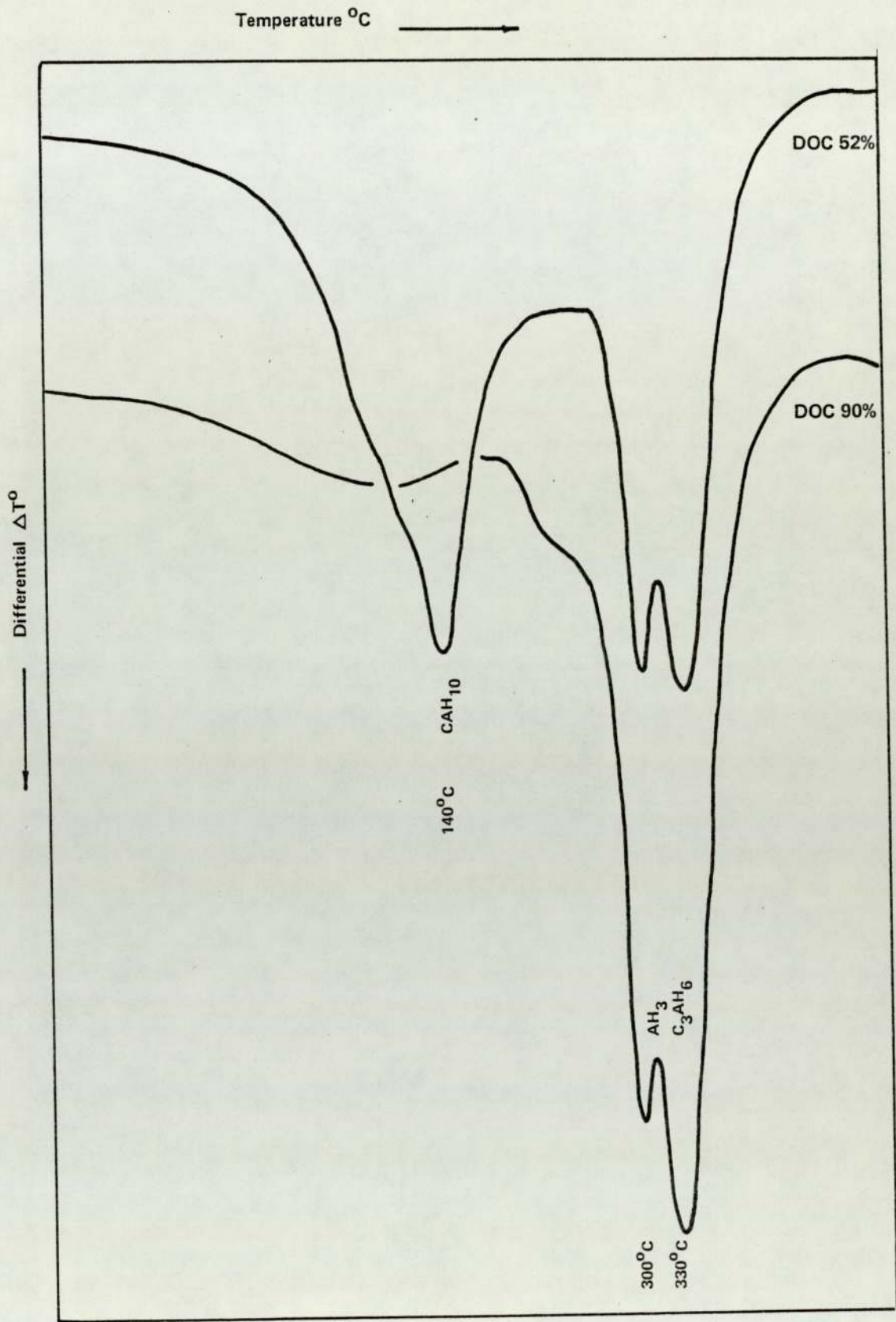
then,

$$\Omega = \frac{T}{4\pi\mu h} \left( \frac{1}{R_b^2} - \frac{1}{R_c^2} \right) - \frac{\mathcal{T}_0}{\mu} \ln \frac{R_c}{R_b}$$

This is the Reiner and Rivlin equation of plastic flow in a rotational viscometer.

## DIFFERENTIAL THERMAL ANALYSIS THERMOGRAMS





## REFERENCES

1. British Standards Institution. High Alumina Cement. BS 915: 1947, p. 4.
2. T. D. Robson. High Alumina Cements and Concretes. Contractors Records Ltd., London, 1962, pp. 190-194.
3. F. M. Lea. The Chemistry of Cement and Concrete. Third Edition. Edward Arnold Ltd., London, 1970, p. 490.
4. A. M. Neville. High Alumina Cement Concrete. The Construction Press Ltd., Lancaster, 1975, p. 23.
5. O. J. Masterman. High Alumina Cement Concrete with Data Concerning Conversion. Civil Engineering and Public Works Review, Vol. 56, 1961, pp. 483-486.
6. British Standard Institution. The Structural Use of Concrete. Code of Practice CP110: Part I: 1972, p. 133.
7. N. Davey. Influence of Temperature upon the Strength Development of Concrete. Building Research Technical Paper, No. 14, 1933, p. 76.
8. A. M. Neville. High Alumina Cement Concrete. The Construction Press Ltd., Lancaster, 1975, pp. 86-110.
9. Building Research Station. High Alumina Cement in Buildings. Current Paper, CP 34/75, 1975, pp. 23-45.
10. A. M. Neville. High Alumina Cement Concrete. The Construction Press Ltd., Lancaster, 1975, pp. 146-159.
11. H. G. Midgley. The Mineralogy of Set High Alumina Cement. Transactions, British Ceramic Society, Vol. 66, 1967, pp. 161-187.
12. C. Bradbury, P. M. Callaway and D. D. Double. The Conversion of High Alumina Cement/Concrete. Materials Science and Engineering, Vol. 23, 1976, pp. 43-53.
13. V. S. Ramachandran and R. F. Feldman. Hydration Characteristics of Monocalcium Aluminate at a Low Water-Solid Ratio. Cement and Concrete Research, Vol. 3, 1973, pp. 729-750.
14. T. M. Kula, M. D. Meiser and R. E. Tressler. Curing Temperature and Humidity Effects on the Strength of an Aluminous Cement. Cement and Concrete Research, Vol. 10, 1980, pp. 491-499.
15. P. K. Mehta. Retrogression in Hydraulic Strength of Calcium Aluminate Cement Structures. Minerals Processing, Vol. 2, 1964, pp. 16-19.

16. P. K. Mehta and G. Lesnikoff. Conversion of  $\text{CaO} \cdot \text{Al}_2\text{O}_3 \cdot 10\text{H}_2\text{O}$  to  $3\text{CaO} \cdot \text{Al}_2\text{O}_3 \cdot 6\text{H}_2\text{O}$ . *Journal of the American Ceramic Society*, Vol. 54, 1971, pp. 210-212.
17. H. G. Midgley and K. Pettifer. Electron Optical Study of Hydrated High-Alumina Cement Pastes. *Transactions, British Ceramic Society*, Vol. 71, 1972, pp. 55-59.
18. D. C. Teychenne. Long-Term Research into the Characteristics of High Alumina Cement Concrete. *Magazine of Concrete Research*, Vol. 27, 1975, pp. 78-102.
19. T. D. Robson. High Alumina Cements and Concretes. *Contractors Record Ltd.*, London, 1962, p. 103.
20. H. G. Midgley and A. Midgley. The Conversion of High Alumina Cement. *Magazine of Concrete Research*, Vol. 27, 1975, pp. 59-77.
21. A. M. Neville. Further Tests on the Strength of High Alumina Cement Concrete under Hot Wet Conditions. *RILEM International Symposium on Concrete and Reinforced Concrete in Hot Climates*, Haifa, 1960, p. 22.
22. J. Farran. Mineralogical Contribution to the Study of Adhesion between the Hydrated Constituents of Cement and the embedded material. *Revue des Matériaux de Construction*, Vol. 490-491, 1956, pp. 155-172.
23. T. D. Robson. High Alumina Cements and Concretes. *Contractors Record Ltd.*, London, 1962, pp. 105-107.
24. P. K. Mehta. Successful Prevention of Loss of Strength in Concrete made with High Alumina Cement. *Proc. of the Fifth International Symposium on the Chemistry of Cement*, Tokoyo, 1968, pp. 148-152.
25. B. P. Hughes and C. I. Middleton. High Strength Grouts. *Concrete*, No. 10, 1975, pp. 31-32.
26. P. P. Budnikov. Role of Gypsum in the Hardening of Hydraulic Cements. *Proc. of the Fourth International Symposium on the Chemistry of Cement*, Washington, 1960, pp. 469-477.
27. P. J. French, R. G. J. Montgomery and T. D. Robson. High Concrete Strength within the Hour. *Concrete*, No. 5, 1971, pp. 3-8.
28. A. M. Neville. *Properties of Concrete*. Second Edition. Pitman Publishing, 1973, pp. 460-521.
29. I. Soroka and P. J. Sereda. The Structure of Cement Stone and the Use of Compacts as Structural models. *Proc. of the Fifth International Symposium on the Chemistry of Cement*, Vol. III, 1968, pp. 67-73.

30. R. F. Feldman and V. S. Ramachandran. Differentiation of Interlayer and Adsorbed Water in Hydrated Portland Cement by Thermal Analysis. *Cement and Concrete Research*, Vol. I, 1971, pp. 607-620.
31. V. S. Ramachandran and R. F. Feldman. Significance of low water-solid Ratio and Temperature on the Physical-mechanical Characteristics of hydrates of Tricalcium Aluminate. *Journal of Chemical Technology & Biotechnology*, Vol. 23, 1973, pp. 625-633.
32. J. Gebauer and R. W. Coughlin. Preparation, Properties and Corrosion Resistance of Composites of Cement Mortar and Organic Polymers. *Cement and Concrete Research*, Vol. I, 1971, pp. 187-210.
33. J. M. Coldrey and M. J. Purton. Application of Thermal Analysis in investigations on Calcium Silicate Bricks. *Journal of Applied Chemistry*, Vol. 18, 1968, pp. 353-360.
34. V. S. Ramachandran. Application of Thermal Analysis in Cement Chemistry. Chemical Publishing Company, New York, 1969.
35. C. M. George. The Hydration Kinetics of Refractory Aluminous Cements. Presented at the Refractories Division Meeting of the American Ceramic Society at Cincinnati, Ohio, May 1976.
36. Recommendations for the Testing of High Alumina Cement Concrete Samples by Thermoanalytical Techniques. HAC committee of the Thermal Methods Group of the Analytical Division of the Chemical Society, 1975.
37. D. W. Lewis, W. L. Dolch and K. B. Woods. Porosity determination and the significance of pore Characteristics of Aggregates. *Proceedings of the American Society for Testing materials, ASTM*, Vol. 53, 1953, pp. 949-958.
38. ASTM Standards, Method of Test for Specific Gravity of Solids, D854-52, Part 3, 1952, p. 1447.
39. A. Wheeler. *Catalysis*, Vol. 2. Reinhold, New York, 1955, p. 118.
40. E. E. Bodor, J. Skalny, S. Brunauer, J. Hagymassy and M. Yudenfreund. Pore structure of hydrated Calcium Silicates and Portland Cement by Nitrogen Adsorption. *Journal of Colloid and Interface Science*, Vol. 34, 1970, p. 560.
41. J. Hagymassy, I. Odler, M. Yudenfreund, J. Skalny and S. Brunauer. Pore Structure Analysis by water vapour adsorption. III. Analysis of hydrated Calcium Silicate and Portland Cement. *Journal of Colloid and Interface Science*, Vol. 38, 1972, p. 20.
42. S. Diamond. A critical comparison of mercury Porosimetry and Capillary condensation pore size distributions of Portland Cement Pastes. *Cement and Concrete Research*. Vol. I. 1971, pp. 531-445.

43. R. Tsukayama. Effect of Conversion on properties of Concrete using high aluminous cement. Proc. of the Fifth International Symposium on the Chemistry of Cement, III, Tokyo, 1968, pp. 316-327.
44. B. Cottin and P. Reif. Physical parameters governing the mechanical properties of neat aluminous cement pastes. Revue des Matériaux de Construction, No. 661, 1970, pp. 293-305.
45. E. W. Washburn. Proceeding, National Academy of Sciences, PNAS, Vol. 7, 1921, p. 112.
46. F. M. Lea. The Chemistry of Cement and Concrete. Third Edition. Edward Arnold Ltd., London, 1970, p. 207.
47. S. Chatterji and J. W. Jeffery. Microstructure of Set High Alumina Cement Pastes. Transactions, British Ceramic Society, Vol. 67, 1968, pp. 171-183.
48. D. N. Winslow and S. Diamond. A mercury porosimetry study of the evolution of porosity in Portland Cement. Journal of Materials Vol. 5, 1970, pp. 564-585.
49. J. F. Young. Capillary porosity in Hydrated Tricalcium Silicate pastes. Powder technology, Vol. 9, 1974, pp. 173-179.
50. D. H. Bager and J. Sellevold. Mercury Porosimetry of Hardened Cement Paste, the influence of particle size. Cement and Concrete Research. Vol. 5, 1975, pp. 171-178.
51. V. S. Ramachandran. Calcium Chloride in Concrete, Science and Technology. Applied Science Publishers Ltd., London 1976, p. 31.
52. H. Le. Chatelier. Thesis 1887: Recherches Experimentals sur la Constitution des Moitiers Hydrauliques (1904). Second Edition Paris (English translation) McGraw-Hill Publishing Company, 1905.
53. L. S. Brown and R. W. Carlson. Petrographic studies of hydrated cements. Proceedings of the American Society for testing materials. Vol. 36, 1936, pp. 332-350.
54. P. Terrier and M. Moreau. Research on the Pozzolanic action of fly ash in cement. Ciments et Betons, Oct-Nov, 1966, pp. 613-614.
55. R. B. Williamson. Solidification of Portland Cement. Progress in Materials Science, Vol. 15, 1972, pp. 189-285.
56. S. Chatterji and J. W. Jeffery. Three dimensional arrangement of hydration products in set cement paste. Nature, Vol. 209, 1969, pp. 1233-1234.
57. R. B. Williamson. Portland Cement: pseudomorphs of original cement grains observed in hardened pastes. Science, Vol. 164, 1969, pp. 549-551.

58. S. Chatterji and J. W. Jeffery. The Nature of the bond between different types of aggregates and Portland Cement. Indian Concrete Journal. Vol. 45, 1971, pp. 346-349.
59. M. N. Al Khalaf and C. L. Page. Steel/Mortar Interface, Microstructural features and mode of failure. Cement and Concrete Research. Vol. 9, 1979, pp. 197-208.
60. B. D. Barnes, S. Diamond and W. L. Dolch. The Contact zone between Portland Cement paste and glass 'aggregate' surface. Cement and Concrete Research, Vol. 8, 1978, pp. 233-244.
61. S. Diamond. Identification of hydrated cement constituents using a scanning electron microscope-energy dispersive X-ray spectrometer combination. Cement and Concrete Research, Vol. 2, 1972, pp. 617-632.
62. O. A. Kayyali, C. L. Page and A. G. B. Ritchie. The effects of Freezing and Thawing Cycles on the microstructure and strength of Portland Cement paste. Hydraulic cement pastes: their structure and properties. Proceedings of a conference held at University of Sheffield, 8-9 April 1976, Cement and Concrete Association, pp. 204-218.
63. T. D. Ciach, J. E. Gillott, E. G. Swenson and P. J. Sereda. Microstructure of Calcium Silicate hydrates. Cement and Concrete Research, Vol. I, 1971, pp.13-25.
64. T. D. Ciach and E. G. Swenson. Morphology and microstructure of hydrating Portland Cement and its constituents, V. Cement and Concrete Research, Vol. I, 1971, pp. 515-530.
65. S. Diamond. Cement Paste Microstructure - An overview at several levels. Hydraulic cement pastes: their structure and properties. Proceedings of a conference held at University of Sheffield, 8-9 April 1976, Cement and Concrete Association, pp. 2-30.
66. H. Mori, K. Minegishi, T. Ohta and T. Akiba. The effect of alkali on the microstructure of hardened  $3\text{CaO} \cdot \text{SiO}_2$  paste. Review of the 25th General Meeting, Cement Association of Japan, 1971, pp. 33-37.
67. R. L. Berger, J. F. Young and F. V. Lawrence. Discussion of the paper Morphology and Surface properties of hydrated tricalcium silicate paste by M. Collepardi and B. Marchese. Cement and Concrete Research, Vol. 2, 1972, pp. 633-636.
68. K. Newman. Design of Concrete mixes with high-alumina Cement. Reinforced Concrete Review, Vol. 5, 1960, pp. 269-294.
69. D. J. Shaw. Introduction to Colloid and Surface Chemistry. Butterworths. London 1966, p. 4.
70. S. Glasstone and D. Lewis. Elements of Physical Chemistry. Second edition. Macmillan Press Ltd., London, 1976, pp. 579-584.

71. T. C. Powers. The properties of fresh concrete. John Wiley & Sons Inc. New York, 1968, pp. 423-434.
72. E. H. W. Verwey and J. T. G. Overbeek. Theory of the Stability of Lyophobic Colloids. Elsevier (1948).
73. M. Daimon and D. M. Roy. Rheological properties of cement mixes. Cement and Concrete Research. Vol. 8, 1978, pp. 753-764.
74. D. J. Shaw. Introduction to Colloid and Surface Chemistry. Butterworths. London 1966, p. 173.
75. H. Green. Industrial Rheology and Rheological Structures. John Wiley & Sons Inc, 1949, p. 201.
76. British Standards Institution. BS 5168: 1975. Glossary of rheological terms. London. p. 18.
77. G. H. Tattersall. The workability of Concrete. Cement and Concrete Association. A viewpoint Publication, 1976.
78. T. E. R. Jones, G. Brindley and B. C. Patel. A study of the Rheological properties of cement pastes. Hydraulic cement pastes: their structure and properties. Proceedings of a Conference held at University of Sheffield 8-9 April 1976, C & CA Publication, 1976, pp. 134-149.
79. T. E. R. Jones and S. Taylor. A mathematical model relating the flow curve of a cement paste to its water/cement ratio. Magazine of concrete research, Vol. 29, 1977, pp. 207-212.
80. M. Ish-Shalom and S. Greenberg. The Rheology of Fresh Portland Cement pastes. Proceedings of the Fourth International Symposium on the Chemistry of cement, Washington, 1960, pp. 731-748.
81. S. A. Greenberg, R. Jarnutowski, and T. N. Chang. The Rheology of Silica Suspensions. Portland Cement Association Serial No 1045, 1963.
82. H. Green. Industrial Rheology and Rheological Structures. John Wiley & Sons Inc, 1948, p. 50.
83. C. R. Dimond and G. H. Tattersall. The Use of the Coaxial Cylinders Viscometer to measure the Rheological properties of cement pastes. Hydraulic cement pastes: their structure and properties. Proceeding of a conference held at University of Sheffield 8-9 April 1976. C & CA publication, 1976, pp. 118-133.
84. G. H. Tattersall. Structural breakdown of cement paste at constant rate of shear. Nature, Vol. 176, 1955, p. 166.
85. H. Green. Industrial Rheology and Rheological Structures. John Wiley & Sons Inc, 1949, p. 35.

86. H. Green. *ibid*, p. 130.
87. S. Glasstone, K. J. Laidler and H. Eyring. *The Theory of rate processes*. McGraw-Hill Book Co, New York, 1941.
88. E. Ryshkewitch. Compression Strength of porous Sintered alumina and zirconia. *Journal of the American ceramic society*. Vol. 2, 1953, pp. 65-68.
89. W. Duckworth. Discussion of Ryshkewitch paper. *Journal of the American Ceramic Society*, Vol. 2, 1953, p. 68.
90. F. P. Kundsen. Dependence of Mechanical Strength of Brittle polycrystalline specimens on porosity and grain size. *Journal of the American Ceramic Society*, Vol. 8, 1959, pp. 376-387.
91. R. L. Coble and W. D. Kingery. Effect of porosity on physical properties of sintered alumina. *Journal of the American Chemical Society*, Vol. 11, 1956, pp. 377-385.
92. P. O. L. Duwez and H. E. Martens. Powder Metallurgy of porous metals and alloys having a controlled porosity. *Transactions, American institute of mining & Metallurgical engineers. Institute of metals division*. Vol. 12, 1948, pp. 848-874.
93. A. Squire. Density relationship in Iron-powder compacts. *Transactions, American Institute of mining & Metallurgical engineers*. Vol. 9, 1947, pp. 485-503.
94. M. Yu. Bal'shin. Relation of mechanical properties of powder metals and their porosity and the ultimate properties of porous metal-ceramic materials. *Doklady. AKAD SCI USSR*, Vol. 5, 1949, pp. 831-834.
95. R. M. Spriggs. Expression for the effect of porosity on elastic modulus of polycrystalline refractory materials, particularly alumina Oxide. *Journal of the American Ceramic Society*, Vol. 12, 1961, pp. 628-629.
96. F. P. Knudsen. Effect of porosity on Young's modulus of Alumina. *Journal of The American Ceramic Society*. Vol. 2, 1962, pp. 94-95.
97. R. M. Spriggs, L. A. Brissette and T. Vasilos. Effect of porosity on elastic and shear moduli of polycrystalline magnesium oxide. *Journal of The American Ceramic Society*, Vol. 8, 1962, p. 400.
98. L. J. Trostel. Strength and Structure of refractories as a function of pore content. *Journal of the American Ceramic Society*, Vol. 9, 1962, pp. 563-564.
99. R. M. Spriggs. Effect of open and closed pores on elastic moduli of polycrystalline alumina. *Journal of the American Ceramic Society*, Vol. 9, 1962, p. 454.

100. D. P. H. Hasselman. On the porosity dependence of the elastic moduli of polycrystalline refractory materials. *Journal of The American Ceramic Society*, Vol. 9, 1962, p. 452.
101. Z. Hashin, Elastic moduli of heterogeneous materials. *Journal of Applied Mechanics*, Vol. 1, 1962, pp. 142-150.
102. R. S. Piatasik and D. P. H. Hasselman. Effect of open and closed pores on Young's modulus of polycrystalline Ceramics. *Journal of the American Ceramic Society*, Vol. 1, 1964, pp. 50-51.
103. S. D. Brown, R. B. Biddulph and P. D. Wilcox. A strength Porosity relation involving different pore geometry and orientation. *Journal of The American Ceramic Society*, Vol. 7, 1964, pp. 320-322.
104. P. J. Sereda. Significance of microhardness of porous inorganic materials. *Cement and Concrete Research*, Vol. 2, 1972, pp. 717-729.
105. I. Soroka and P. J. Sereda. Interrelation of hardness, modulus of elasticity and porosity in various gypsum systems. *Journal of The American Ceramic Society*, Vol. 6, 1968, pp. 337-340.
106. R. F. Feldman and J. J. Beandoin. Microstructure and strength of hydrated cement. *Cement and Concrete Research*, Vol. 6, 1976, pp. 389-400.
107. J. Jambor. Influence of water-cement ratio on the structure and strength of hardened cement pastes. *Hydraulic cement pastes: their structure and properties. Proceeding of a conference held at University of Sheffield 8-9 April 1976. C & CA publications.* pp. 175-188.
108. D. P. H. Hasselman and R. M. Fulrath, Micromechanical stress concentration in two-phase Brittle matrix ceramic composites. *Journal of The American Ceramic Society*, Vol. 8, 1967, pp. 399-404.
109. K. M. Alexander, J. Wardlaw and D. J. Gilbert. Aggregate-cement bond, cement paste strength and the strength of concrete. *Proceedings of International Conference on the Structure of concrete. London, September 1965, Published by Cement and Concrete Association, 1968, pp. 59-81.*
110. R. N. Swamy. Aggregate - matrix interaction in concrete systems. *Proceeding of Conference on structure, Solid Mechanics and Engineering Design, University of Southampton, April 1969, Published by Wiley-interscience, 1970, pp. 301-315.*
111. D. W. Hadley. The nature of the paste - aggregate interface. *PhD Thesis, School of Civil Engineering, Purdue University, 1972.*
112. B. D. Barnes. Morphology of the paste-aggregate interface. *PhD Thesis, School of Civil Engineering, Purdue University, 1975.*

113. M. N. Al-Khalaf. Bonding between metals and Portland Cement. PhD Thesis. Department of Civil Engineering, The University of Strathclyde, 1976.
114. B. D. Barnes, S. Diamond and W. L. Dolch. Micromorphology of the interfacial zone around aggregates in Portland Cement mortar. Journal of The American Ceramic Society, Vol. 62, 1979, pp. 21-24.
115. F. M. Lea. The Chemistry of Cement and Concrete. Third edition. Edward Arnold Ltd., London, 1970, p. 506.
116. F. M. Lea. *ibid*, p. 466.
117. F. M. Lea. *ibid*, p. 223.
118. V. S. Ramachandran. Application of Thermal Analysis in Cement Chemistry. Chemical Publishing Company, New York, 1969, p. 95.
119. W. Gutt and M. A. Smith. Utilisation of by-product calcium sulphate. Chemistry and Industry, 1973, pp. 610-619.
120. A. A. Tabikh and F. M. Miller. The Nature of phosphogypsum impurities and their influence on cement hydration. Cement and Concrete Research, Vol. 1, 1971, pp. 663-678.
121. T. W. Parker. The constitution of aluminous cement. Proceedings of the Third International Symposium on the Chemistry of Cement, London, 1952, pp. 485-515.
122. F. E. Jones. The Quaternary System  $\text{CaO} - \text{Al}_2\text{O}_3 - \text{CaSO}_4 - \text{H}_2\text{O}$  at  $25^\circ\text{C}$ . The Journal of physical chemistry, Vol. 48, 1944, pp. 311-355.
123. V. S. Ramachandran. Application of Thermal Analysis in Cement Chemistry. Chemical Publishing Company, New York, 1969, p. 142.
124. V. S. Ramachandran. *ibid*, p. 151.